Progress in liquid crystal chemistry

Edited by Sabine Laschat

Imprint

Progress in liquid crystal chemistry

Sabine Laschat

Since their discovery in 1888 by the botanist Friedrich Reinitzer, who studied the melting behavior of cholesteryl benzoates, liquid crystals have developed from a mere curiosity to a highly interdisciplinary research field, with LC displays being the most important application to date [1,2]. However, besides the use of thermotropic liquid crystals for display technology many other applications will probably be on the market in the near future, such as organic light emitting diodes, photovoltaic devices, organic field effect transistors, gas sensors etc. [3-8]. One of the major issues in liquid crystal research today is still the poor knowledge of structure-property relationships and thus the synthesis of whole series of structurally related compounds is required in order to allow the design of liquid crystalline and other physical properties. It is the goal of this thematic series "Progress in Liquid Crystal Chemistry" to give the reader of *Beilstein Journal of Organic Chemistry* a flavor of the synthetic challenges of liquid crystal research, as well as interdisciplinary aspects from material science, physics, physical and theoretical chemistry. It is a great pleasure to serve as a guest editor for this thematic series, where leading experts from all over the world have contributed original research papers and accounts that deal with diverse topics such as phthalocyanine-fullerene hybrid materials for photovoltaic devices, functional metallomesogens, coaxial electrospinning of liquid crystal-containing microfibers, banana-discotic hybrid systems, ionic liquid crystals, relations between molecular length distribution and formation of smectic phases, nematic phase engineering by using V-shaped molecules, saddle-shaped columnar systems displaying anomalous odd-even effects, theoretical studies on the origin of chirality transfer in liquid crystalline host-guest systems, liquid crystalline carboranes and dyes and discotic phenanthrene quinones. Many new exciting discoveries in this diverse research area are to be expected in the near future and our aim with this Thematic Series is to attract a new audience to this topic.

Sabine Laschat

Guest Editor

References

1. Reinitzer, F. *Monatsh. Chem.* **1888,** *9,* 421–441.
   doi:10.1007/BF01516710
2. Sluckin, T. J.; Dunmur, D. A.; Stegemeyer, H. *Crystals that flow: Classic papers from the history of liquid crystals;* Taylor & Francis: London, 2004.
3. Sergeyev, S.; Pisula, W.; Geerts, Y. H. *Chem. Soc. Rev.* **2007,** *36,* 1902–1929. doi:10.1039/b417320c
4. Tschierske, C. *Chem. Soc. Rev.* **2007,** *36,* 1930–1970.
   doi:10.1039/b615517k
5. Donnio, B.; Bruce, D. W. *Struct. Bonding* **1999,** *95,* 193–247.
   doi:10.1007/3-540-68118-3_5

6. Laschat, S.; Baro, A.; Steinke, N.; Giesselmann, F.; Hägele, C.;
   Scalia, G.; Judele, R.; Kapatsina, E.; Sauer, S.; Schreivogel, A.;
   Tosoni, M. *Angew. Chem.* **2007,** *119,* 4919–4973.
   Angew. Chem. Int. Ed. **2007**, *46*, 4832–4887.
   doi:10.1002/anie.200604203.

7. Kato, T.; Yasuda, T.; Kamikawa, Y.; Yoshio, M. *Chem. Commun.* **2009,**
   729–739. doi:10.1039/b816624b

8. Simpson, C. D.; Wu, J.; Watson, M. D.; Müllen, K. *J. Mater. Chem.*
   2004, *14,* 494–504. doi:10.1039/b312789c

Synthesis of mesogenic phthalocyanine-C$_{60}$ donor–acceptor dyads designed for molecular heterojunction photovoltaic devices

Yves Henri Geerts[*1], Olivier Debever[1], Claire Amato[1] and Sergey Sergeyev[*1,2]

Abstract

A series of phthalocyanine-C$_{60}$ dyads **2a–d** was synthesized. Key steps in their synthesis are preparation of the low symmetry phthalocyanine intermediate by the statistical condensation of two phthalonitriles, and the final esterification of the fullerene derivative bearing a free COOH group. Structural characterization of the molecules in solution was performed by NMR spectroscopy, UV–vis spectroscopy and cyclic voltammetry. Preliminary studies suggest formation of liquid crystalline (LC) mesophases for some of the prepared dyads. To the best of our knowledge, this is the first example of LC phthalocyanine-C$_{60}$ dyads.

Introduction

Among sustainable energy technologies, photovoltaic (PV) conversion of solar energy is considered as a promising solution. Although currently the market is dominated by inorganic PV devices, development of organic PV materials is driven by their compatibility with solution processing and hence the potentially low cost of large-scale production by printing technologies [1-3]. One of the most popular concepts in the design of organic PV devices is the "bulk heterojunction" architecture, featuring blends of the two immiscible materials: a donor and an acceptor of electrons [4-7]. After absorption of a photon, an initially formed exciton is dissociated at the donor/acceptor interface into a positive charge (hole) and a negative charge (electron), which are transported to the electrodes. Hence, a critical issue in bulk heterojunction PV devices is the control of morphology of materials, in order to provide both the efficient exciton generation and the rapid charge carrier transport. The logical step in the development of this architecture is "molecular heterojunction", that is, creation of covalent link-

ages between donor and acceptor components [6]. The main idea is that in material well-organized on the molecular level, donor and acceptor moieties will create the separate pathways for the transport of holes and electrons, respectively. One can intuitively expect that for such high order of self-organization, liquid crystalline (LC) materials will be beneficial, because they combine order and fluidity, which allows the self-healing of structural defects [8].

One of the most widely used molecules in the bulk heterojunction PV devices is fullerene C_{60}, firstly in the pristine form and later as easily soluble derivatives such as phenylcyclopropa[6,6]C_{60}-butanoic acid methyl ester (PCBM, **1**, Figure 1) [9-12]. It has been used in a combination with a plethora of conjugated polymers [13-18] as well as small molecules [19-21]. Furthermore, a number of C_{60}-containing covalent ensembles were studied within the "molecular heterojunction" concept [22-29].

Phthalocyanines (Pc) have found a number of industrial applications as dyes and pigments due to their bright blue or green colors combined with extraordinary thermal and photochemical stability [30]. Phthalocyanines bearing flexible peripheral substituents form columnar mesophases [8,31], which demonstrate very efficient charge transport along the columns [32,33]. A unique combination of properties makes phthalocyanines excellent candidates as active materials for photovoltaic devices.

Within the concept of a "molecular heterojunction", a number of phthalocyanine-fullerene dyads and triads were synthesized [34-38] and long-lived photoinduced charge transfer was demonstrated in these type of materials [39]. Although examples of mesogenic fullerene derivatives have been previously reported [40-44], mesogenic Pc-C_{60} dyads are unknown, most probably due to the tedious purification of the unsymmetrically substituted phthalocyanines bearing long peripheral substituents. A possible elegant solution to this problem was demonstrated by Torres and co-workers, who obtained LC mesophases of several phthalocyanine-C_{60} dyads by blending them with a mesogenic phthalocyanine derivative [45]. In this paper we report the synthesis of the first example, to the best of our knowledge, of mesogenic phthalocyanine-fullerene dyads.

Results and Discussion

The structure of dyads **2a–d** is depicted in Figure 1. We decided to combine in one molecule the phenylcyclopropa[6,6]C_{60} moiety of PCBM as an acceptor and a phthalocyanine bearing three swallow-tail alkoxy groups as a donor. The choice of the substituents on the phthalocyanine core was dictated by the previous finding that the pseudosymmetrical phthalocyanine **3** bearing four such substituents is very soluble in many organic solvents, forms columnar mesophases over a broad temperature range and, at the same time, possesses a reasonably low clearing point (ca. 180 °C) [46]. Finally, a critical issue in obtaining a mesogenic phthalocyanine-C_{60} dyad can be a difficulty in accommodating a bulky C_{60} molecule in the columnar LC
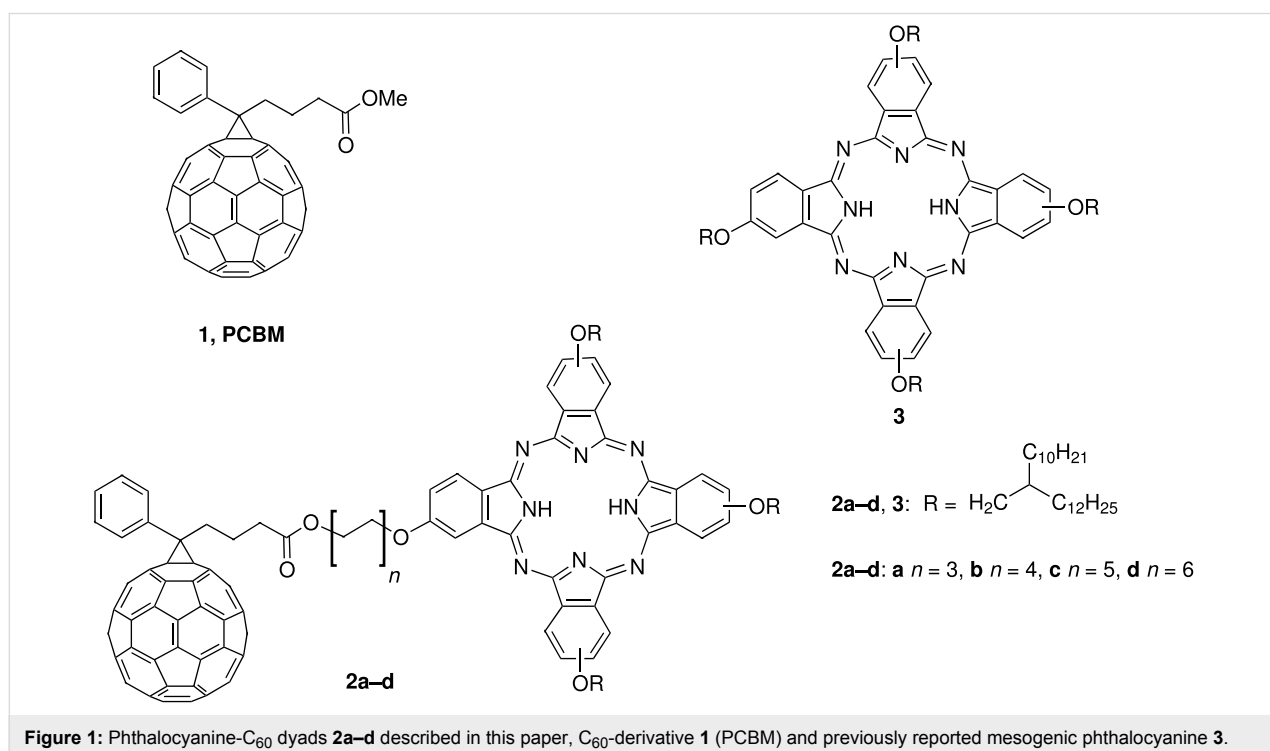

Figure 1: Phthalocyanine-C_{60} dyads **2a–d** described in this paper, C_{60}-derivative **1** (PCBM) and previously reported mesogenic phthalocyanine **3**.

mesophases [45]. To this end, we envisaged the variation of the linker between the fullerene and the phthalocyanine unit.

The synthesis of dyads **2a–d** is summarized in Scheme 1 and Scheme 2. The key step, which also represents a bottle-neck in terms of yield (see below), is the preparation of the low-symmetry phthalocyanines **4a–d**. To this end, we originally decided to explore the statistical condensation of phthalonitriles **5** and **6a–d** (Scheme 1). Previously, synthesis of 4-alkoxy-phthalonitriles such as **5** via aromatic nucleophilic substitution in 4-nitrophthalonitrile with the corresponding alcohols in the presence of LiOH in DMSO was reported [46]. However, the yields of phthalonitriles **5** were moderate (below 50%) and their separation from multiple side products was cumbersome. Hence, we preferred to prepare **5** (80% yield) by Williamson reaction between phenol **7** and bromide **8**. The latter was synthesized from the corresponding commercially available alcohol by the well-known general method (CBr$_4$/PPh$_3$) [47]. A similar procedure was then used to synthesize phthalonitriles **6a–d** (80–86% yield) starting from the corresponding commercially available ω-bromoalcohols.

Several strategies for the synthesis of low-symmetry A$_3$B phthalocyanines (where A and B refer to the chemically different isoindole units comprising the phthalocyanine core) were reported earlier, including expansion of subphthalo-

cyanines or solid-phase synthesis on polymer supports [48]. However, operationally simplest and shortest route is the statistical condensation of the two different phthalonitriles. This method inevitably produces a mixture of the desired A$_3$B phthalocyanines with the products of compositions A$_4$, A$_2$B$_2$, AB$_3$ and B$_4$. In theory, 3 : 1 molar ratio of the two dinitriles is required to access A$_3$B products. However, using larger excess of one of dinitriles (often 9 : 1 stoichiometry is used) is more practical. Although the amount of the A$_4$ phthalocyanine in the reaction mixture grows, the formation of cross-condensation products other than A$_3$B is essentially suppressed (see Figure SI2 in the Supporting Information for the graphical presentation of the product distribution). Hence, the isolation of the desired A$_3$B is limited to the separation from the A$_4$. Another factor that facilitates the separation by chromatography is rather different polarity of the substituents on A and B units. In our case, the oligomethylene linker with a terminal OH group is much more polar than the bulky swallow-tail alkyl group, and we did not expect difficulties in the separation of condensation products.

However, attempted condensation of **5** and **6a–d** gave no desired phthalocyanine derivative. We reasoned that the unprotected OH group in one of the reaction components may affect the condensation, and converted alcohols **6a–d** into acetals **9a–d** (84–93% yield) by treatment with an excess of meth-

Scheme 1: Synthesis of low-symmetry phthalocyanines **4a–d**.

Scheme 2: Synthesis of dyads **2a–d**.
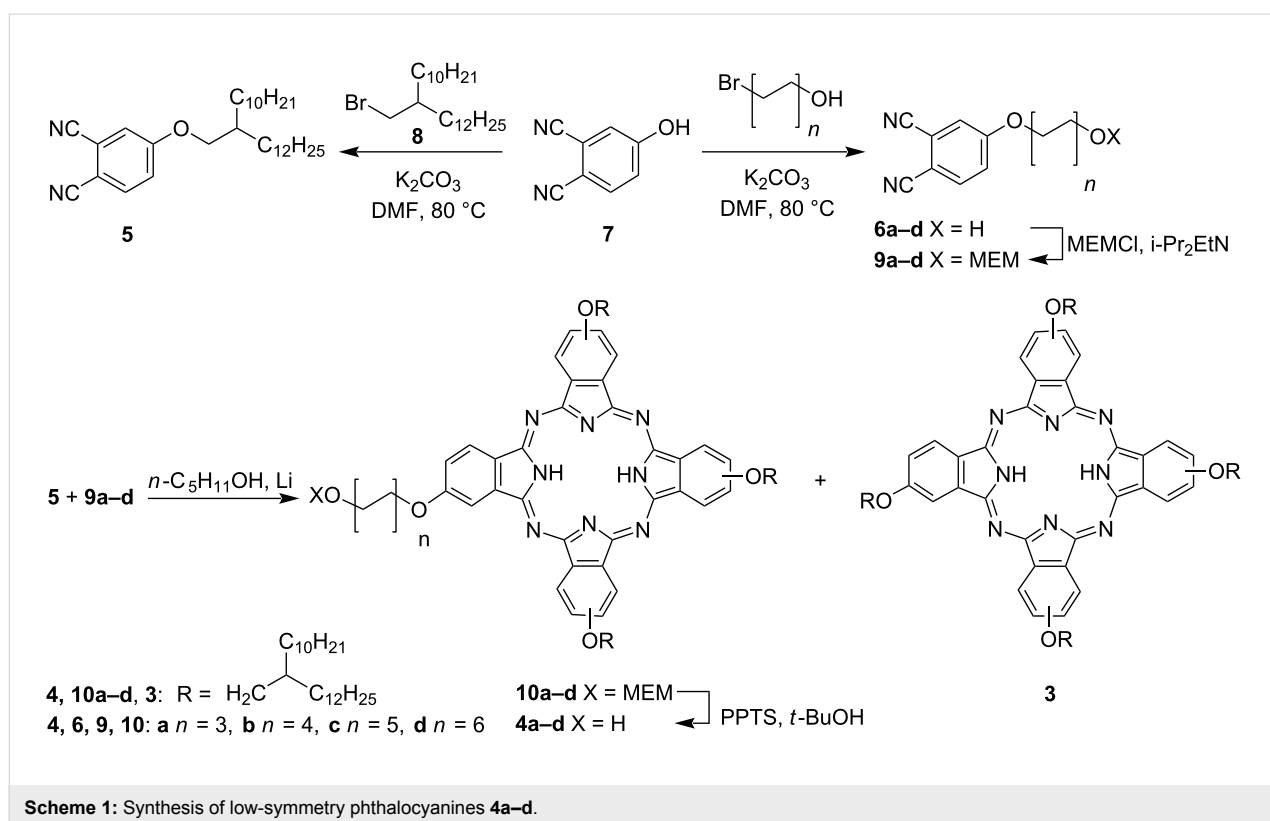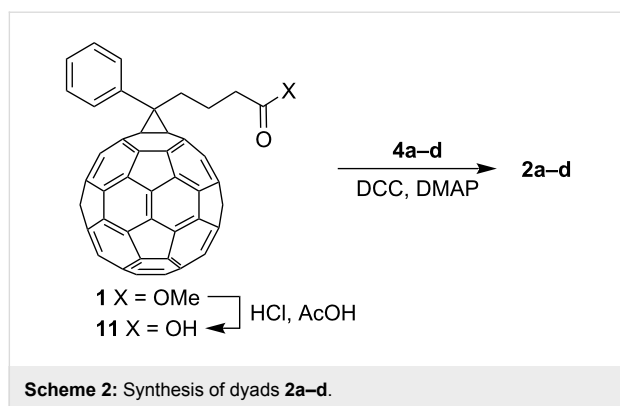
oxyethoxymethyl chloride (MEMCl) in the presence of *i*-Pr$_2$EtN as a base. The general choice of acetal as a protective group was dictated by its excellent stability in the presence of the strong bases, required for the cyclotetramerization of phthalonitriles. Among various popular acetal protective groups, the relatively polar MEM moiety was chosen to facilitate the chromatographic separation of the unsymmetrical phthalocyanines **10a–d** from the major side product **3**: the latter bears only relatively apolar, bulky swallow-tail alkoxy groups. In addition, the signal of the terminal methyl group of the MEM moiety serves as a convenient "marker" in rather complex ^{1}H NMR spectra of phthalocyanines **10a–d** (see below). Condensation of **5** and **9a–d** in *n*-C$_5$H$_{11}$OH/*n*-C$_5$H$_{11}$OLi upon reflux afforded the desired A$_3$B phthalocyanines **10a–d** (13–24% after column chromatography) together with pseudo-symmetrical A$_4$ phthalocyanine **3** (35–51%). The seemingly modest yields of **10a–d** actually correspond to those reported earlier for other A$_3$B-type phthalocyanines: yields higher than 20% are rare in such reactions [45,49-51]. The MEM protective group in **10a–d** was then quantitatively removed to give **4a–d** upon treatment with pyridinium tosylate (PPTS) in *t*-BuOH according to previously reported general method [52].

The structure of the phthalocyanines **4a–d** was confirmed by ^{1}H and ^{13}C NMR, and HR-MALDI mass spectrometry. ^{1}H NMR spectra of low-symmetry phthalocyanines **4a–d** and **10a–d** in CDCl$_3$ closely resemble those of **3** and feature a series of three unstructured multiplets from the protons of 1,2,4-substituted benzene rings. Inner-core protons in **4a–d** and **10a–d** are observed as a broad and concentration-sensitive high-field signal. It should be noted that **3** (as well as any phthalocyanine derivative prepared from a 4-substituted phthalonitrile) represents a mixture of four regioisomers [48,53], while lower-symmetry **4a–d** and **10a–d** are actual mixtures of as many as eight regioisomers each. This greatly complicates their NMR spectra (see Supporting Information). Furthermore, each regioisomer is a mixture of different diastereoisomers due to the presence of the asymmetric carbon atom in every peripheral

substituent. However, although 2-decyltetradecyl substituents in **3** and **10a–d** are formally chiral, they should actually be treated as pseudo-achiral since the difference between the two of the substituents at the asymmetric carbon (the two linear alkyl groups of different length) is very small. As was shown previously, the complex diastereochemical composition does not influence the behavior of phthalocyanines bearing similar swallow-tail branched alkyl chains [46,54-57]. UV–vis absorption spectra of **4a–d** (Figure 2) are characteristic for metal-free phthalocyanine derivatives: they feature two intense long-wave absorption bands (termed Q-bands).

In the final synthetic step, reaction between **4a–d** and the acid **11** (prepared by acid-catalyzed hydrolysis of the commercially available methyl ester **1**, PCBM) [10,58] afforded the corresponding dyads **2a–d** (Scheme 2). Although in general esterification appears as a trivial synthetic transformation, esterification of **11** is greatly complicated by its poor solubility in virtually all organic solvents. After some experimenting, we found that the classical dicyclohexylcarbodiimide/*N*,*N*-dimethylamino-pyridine (DCC/DMAP) protocol gives the best results, provided the acid **11** was first sonicated in *o*-dichlorobenzene for two hours prior to reaction, and then an alcohol **4a–d**, DCC and DMAP were added to the reaction mixture. After purification by column chromatography, the dyads **2a–d** were isolated in yields up to 45%. Again, the relatively modest yields are comparable with or superior to those previously reported for the esterification of poorly soluble acid **11** with various alcohols [22,50,59].

The structure of dyads **2a–d** was confirmed by NMR, MALDI MS and UV–vis absorption spectroscopy. ^{1}H NMR spectra of the dyads **2a–d** essentially correspond to the superposition of the spectra of the phthalocyanine **4a–d** and PCBM (**1**), with the exception of the signal of C*H*$_2$OC=O in dyads **2a–d** (ca. 4.10 ppm), which is shifted downfield vs. the signal of C*H*$_2$OH in phthalocyanines **4a–d** (ca. 3.80 ppm). ^{13}C NMR spectrum of the dyad **2c** also essentially represents a superposition of the spectra of phthalocyanine **4c** and PCBM (**1**). However, its detailed interpretation is greatly complicated because of a large number of signals, broadening of the signals due to the complex isomeric composition of phthalocyanine (see above), and overlaps of signals (see Supporting Information for the original NMR spectra). For this reason, only selected ^{13}C chemical shifts are given in the Experimental Part. UV–vis absorption spectra of the dyads **2a–d** also appear as superposition of the spectra of **4a–d** and **1**: next to the intense Q-band (maxima at 670 and 707 nm) and B-band (between ca. 300 and ca. 450 nm) of phthalocyanine moiety, very strong high energy absorption of the cyclopropanated C$_{60}$ derivative with the maximum at ca. 260 nm is observed (Figure 2).
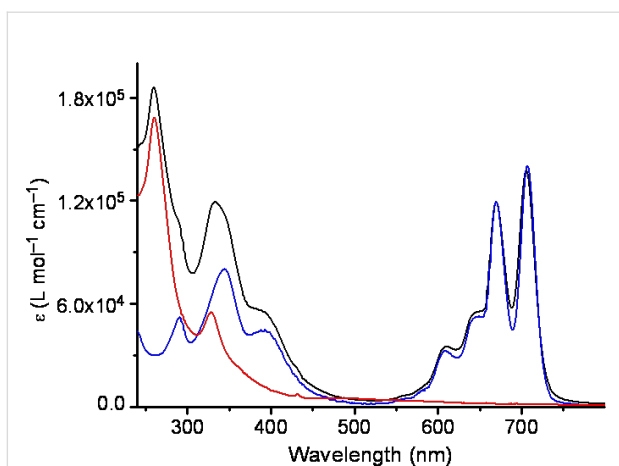
Figure 2: UV–vis absorption spectra of **2a** (black), **4a** (blue) and **1** (red) in CH_2Cl_2.

Table 1: Experimental values of reduction potentials $E^i_{red} = (Ep^i_c + Ep^i_a)/2$ of **1**, **2a,d** and **3**, vs. SCE, in CH_2Cl_2 ($c = 10^{-4}$ M), scan rate 100 mV s^{-1}.

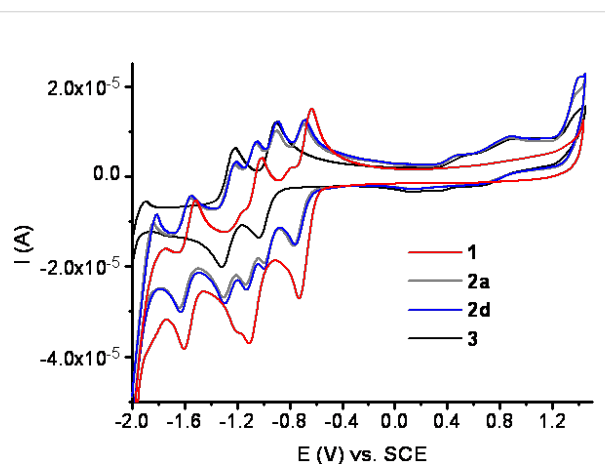|	E^1_{red}, V	E^2_{red}, V	E^3_{red}, V	E^4_{red}, V	E^5_{red}, V
1	−0.68		−1.06		−1.67
2a	−0.73	−0.94	−1.09	−1.26	−1.60
2d	−0.71	−0.94	−1.09	−1.25	−1.59
3		−0.96		−1.27	

Figure 3: Cyclic voltammograms of **1** (red), **2a** (grey), **2d** (blue) and **3** (black) in CH_2Cl_2 ($c = 10^{-4}$ M), scan rate 100 mV s^{-1}.

Cyclic voltammetry measurements of dyads **2a** and **2d** in CH_2Cl_2 produced essentially identical results. Wave potentials do not change upon elongation of the spacer between the donor and the acceptor (Table 1). Furthermore, the voltammograms effectively correspond to the superposition of those for PCBM (**1**) and the phthalocyanine **3**, and do not display supplementary waves (Figure 3). The reduction part of the voltammograms of **2a**,**d** displays five quasi-reversible reduction waves, three due to the C_{60} moiety and two due to the phthalocyanine fragment. In the oxidation part of the voltammograms of **2a**,**d**, several poorly resolved waves identical to those of phthalocyanine **3** are observed at potentials up to +1.6 V vs. saturated calomel electrode (SCE). These observations, together with UV–vis spectra, suggest the absence of intramolecular charge transfer in the ground state for dyads **2a–d**.

Preliminary investigation of the dyads **2a–d** by polarized optical microscopy (POM) showed that the length of the spacer between the phthalocyanine and the fullerene moieties significantly affects the thermotropic properties of the material. Dyads **2a,b** are liquid at room temperature, while dyads **2c,d** display at room temperature fluidic birefringent textures confirming the occurrence of liquid crystalline (LC) mesophases. Upon heating, transitions to isotropic liquid were observed at 120 °C and 90 °C for **2c** and **2d**, respectively. For **2c** this transition was only detectable by POM and not by differential scanning calorimetry (DSC), while for **2d** DSC on heating revealed an endothermic peak at 90 °C [enthalpy 2.7 kJ/mol] in perfect agreement with POM observation. The small enthalpy value supports the transition from LC mesophase to isotropic liquid. However, assignment of the nature of LC mesophases for **1c,d** from the available data was not obvious, since the textures observed by POM were not characteristic. The major conclusion is nonethe-

less that the length of the spacer in **2a–d** between the C_{60} fragment and the mesogenic phthalocyanine moiety decisively affects the supramolecular structure of the material.

Conclusion

We report the first example, to the best of our knowledge, of mesogenic phthalocyanine-C_{60} dyads. The key step in their synthesis is the preparation of the low-symmetry phthalocyanines, bearing three mesogenic swallow-tail substituents and an OH-terminated polymethylene linker. These key intermediates were synthesized by experimentally simple statistical condensation of two phthalonitriles, giving comparatively high yields (up to 24%) for this type of reaction. Upon the favorable combination of the length of the linker with the length of peripheral substituents on the phthalocyanine, bulky C_{60} moiety can be accommodated in the LC mesophase. Detailed analysis of this supramolecular organization, as well as deeper insight in the structure-property relationships of dyads **2**, will be the subject of a separate publication. Other objectives of our ongoing research include: studies of macroscopic alignment in films of dyads **2**, studies of charge carrier mobility in aligned films, and fabrication and evaluation of photovoltaic devices.

Experimental

General details. All chemicals were purchased from Aldrich, Acros or TCI and used without further purification. Acid **11** was prepared according to the published procedure [10]. TLC was performed on precoated plates with silica gel 60 F_{254} (Merck), visualization with UV (λ = 254 nm). Column chromatography was performed on silica gel (0.040–0.063 mm, Macherey–Nagel). ^{1}H NMR and ^{13}C NMR spectra were recorded on Bruker Avance 300 or Varian VNMRS 400 spectrometers; chemical shifts are given in ppm relative to Me_4Si (internal standard); coupling constants *J* are given in Hz. MALDI mass spectra were recorded on a Waters MALDI-QTOF Premier, using a 350 mW laser with dithranol (1,8-dihydroxy-10*H*-anthracen-9-one) as matrix for phthalocyanines and with DCB (*trans*-2-[3-(4-tert-butylphenyl)-2-methyl-2-propenylidene]malonitrile) as matrix for fullerene derivatives; EI and ESI mass spectra were recorded on a Waters AutoSpec 6. UV–Visible absorption spectra were recorded on a HP 8453 spectrophotometer in a quartz cell (optical path of 1 cm). For POM experiments, a NIKON Eclipse 80i microscope equipped with a digital camera DS Camera Head D5-5M was used; temperature was controlled by a Linkam Scientific Instruments GS350 hot stage. For DSC, a Perkin Elmer Diamond DSC calorimeter was used.

Electrochemistry. Cyclic voltammetry experiments were performed with a computer controlled Autolab potentiostat. Measurements were carried out at room temperature in a three-electrode single-compartment cell (10 mL), in CH_2Cl_2 solutions (concentration 10^{-4} M), containing Bu_4NPF_6 (0.1 M) as supporting electrolyte, at a scan rate of 100 mV s^{-1}. A glassy carbon, polished by a slurry-suspension of alumina on microcloth and washed by Milli-Q water before each experiment, was used as a working electrode. A spiral platinum wire was employed as counter electrode and an Ag/AgCl/KCl(sat) used as reference electrode was connected to the cell solution via a salt bridge containing a saturated aqueous KCl solution. The Ag/AgCl electrode was checked against the ferrocene/ferrocinium (Fc/Fc$^+$) couple (E°$_{Fc/Fc+}$ = 0.425 V vs. Ag/AgCl) before and after each experiment. All potentials are reported versus saturated calomel electrode (SCE) (E°$_{Fc/Fc+}$ = 0.405 V vs. SCE). Before each measurement, solutions were deaerated by 20 min nitrogen bubbling.

4-(2-Decyltetradecyloxy)phthalonitrile (5). To a solution of phenol **7** (1.80 g, 12.5 mmol) and bromide **8** (4.18 g, 10 mmol) in dry DMF (60 mL) was added dry K_2CO_3 (1.72 g, 12.5 mmol). The mixture was stirred at 90 °C under Ar for 7 h. After cooling to r.t., the mixture was poured into water (60 mL) and extracted with AcOEt (3 × 200 mL). The combined organic layers were washed with aqueous NaHCO$_3$ (5%), dried with

MgSO$_4$ and concentrated in vacuum. Column chromatography (SiO$_2$, CH_2Cl_2) afforded pure **5** as a light yellow solid (4.81 mg, 80%); R$_f$ 0.7 (CH_2Cl_2). Analytical data identical to those previously reported [46].

4-{10-[(2-Methoxyethoxy)methoxy]decyloxy}phthalonitrile (9c). A solution of phthalonitrile **6c** (570 mg, 1.47 mmol) and *i*-Pr$_2$EtN (0.77 mL, 4.5 mmol) in CH_2Cl_2 (30 mL) was treated dropwise with MEMCl (0.33 mL, 2.94 mmol) and the resulting mixture was stirred overnight at r.t. The mixture was then treated with aqueous saturated NaHCO$_3$ (35 mL); the organic layer was separated, the aqueous layer was extracted with CH_2Cl_2 (2 × 40 mL), combined organic layers were dried over MgSO$_4$ and evaporated. Column chromatography of the residue (CH_2Cl_2/AcOEt 4 : 1, R$_f$ 0.69) afforded **9c** (479 mg, 84%) as a light yellow solid; mp 43 °C; R$_f$ 0.64 (CH_2Cl_2/AcOEt 9 : 1); ^{1}H NMR (300 MHz, CDCl$_3$, 25 °C): δ = 7.68 (d, $^3J_{H,H}$ = 8.8 Hz, 1H), 7.24 (d, $^4J_{H,H}$ = 2.6 Hz, 1H), 7.14 (dd, $^3J_{H,H}$ = 8.8 Hz, $^4J_{H,H}$ = 2.6 Hz, 1H), 4.69 (s, 2H, OCH$_2$O), 4.03 (t, $^3J_{H,H}$ = 6.5 Hz, 2H, CH$_2$O), 3.68 (t, $^3J_{H,H}$ = 5.1 Hz, 2H, CH$_2$O), 3.52–3.60 (m, 4H, OCH$_2$CH$_2$O), 3.38 (s, 3H, MeO), 1.81 (quint, $^3J_{H,H}$ = 7.2 Hz, 2H), 1.26–1.64 (m, 14H); ^{13}C NMR (100 MHz, CDCl$_3$, 25 °C): δ = 162.2, 135.1, 119.5, 119.3, 117.4, 115.7, 115.3, 107.0, 95.5, 71.8, 69.3, 67.9, 66.7, 59.0, 29.7, 29.4, 29.4, 29.4, 29.2, 28.7, 26.2, 25.8; HR-MS (EI): *m/z* calcd. for C$_{22}$H$_{32}$N$_2$O$_4$ ([M]$^+$): 388.2362, found 388.2374.

2-{10-[(2-Methoxyethoxy)methoxy]decyloxy}-9(10),16(17),23(24)-tri(2-decyltetradecyloxy)-29H,31H-phthalocyanine (10c). Li (125 mg, 17.7 mmol) was dissolved under Ar in *n*-pentanol (10 mL) and the mixture was heated to reflux until Li was completely dissolved. After cooling to r.t., a solution of phthalonitriles **5** (3.41 g, 7.1 mmol) and **9c** (305 mg, 0.79 mmol) in *n*-pentanol (15 mL) was added dropwise and the mixture was heated to reflux overnight. After cooling to r.t., AcOH was added dropwise until pH 5–6 was reached. The green solid was filtered and extensively washed with MeOH. Column chromatography of the residue afforded first **3** (eluted with CH_2Cl_2, 1.76 g, 50%) and then **10c** (eluted with CH_2Cl_2/AcOEt 1 : 1, 347 mg, 24%). Green solid; R$_f$ 0.75 (CH_2Cl_2/AcOEt 1:1). ^{1}H NMR (300 MHz, CDCl$_3$, 25 °C): δ = 8.50–8.90 (m, 4H), 8.10–8.50 (m, 4H), 7.30–7.60 (m, 4H), 4.71 (s, 2H, OCH$_2$O), 4.25–4.50 (m, 8H, ArOC*H$_2$*), 3.65–3.80 (m, 4H, C*H$_2$*OCH$_2$OC*H$_2$*), 3.58–3.63 (m, 2H, OCH$_2$C*H$_2$*O), 3.36 (s, 3H, MeO), 2.10–2.23 (m, 5H, ArOCH$_2$C*H$_2$* + ArOCH$_2$C*H*), 1.15–1.90 (m, 134H), 0.85 (t, $^3J_{H,H}$ = 6.8 Hz, 18H), −2.84 (s, 2H, NH); ^{13}C NMR (100 MHz, CDCl$_3$, 25 °C): δ = 160.2 (br), 147.0 (br), 136.6 (br), 127.8 (br), 122.2 (br), 117.0 (br), 104.0 (br), 94.6 (OCH$_2$O), 70.9 (br, CH$_2$O), 70.7 (br, CH$_2$O), 67.4 (br, CH$_2$O), 66.9 (CH$_2$O), 65.7 (CH$_2$O), 58.0 (MeO), 37.5 (br), 30.5–31.0 (several CH$_2$), 28.3–29.4 (several CH$_2$), 26.3 (CH$_2$),

25.2–25.5 (several CH$_2$), 21.5–21.8 (several CH$_2$), 13.1 (Me); HR-MS (MALDI): *m/z* calcd. for C$_{118}$H$_{190}$N$_8$O$_7$ ([M]$^+$): 1831.4757, found 1831.4748.

2-(10-Hydroxy-decyloxy)-9(10),16(17),23(24)-tri(2-decyl-tetradecyloxy)-29*H*,31*H*-phthalocyanine (4c). A stirred solution of the phthalocyanine **10c** (275 mg, 0.15 mmol) and PPTS (188 mg, 0.75 mmol) in *t*-BuOH (20 mL) was heated to reflux overnight. After cooling to r.t., the reaction mixture was concentrated in vacuum. The resulting solid was suspended in MeOH (50 mL), then filtered, extensively washed with MeOH and dried to give **4c** (261 mg, 100%). Green solid; ^{1}H NMR (300 MHz, CDCl$_3$, 25 °C): δ = 8.90–9.20 (m, 4H), 8.45–8.80 (m, 4H), 7.50–7.75 (m, 4H), 4.35–4.55 (m, 8H, ArOC*H*$_2$), 3.72 (t, $^3J_{H,H}$ = 6.0 Hz, 2H, C*H*$_2$OH), 2.03–2.20 (m, 5H, ArOCH$_2$C*H*$_2$ + ArOCH$_2$C*H*), 1.10–1.95 (m, 134H), 0.80–0.93 (m, 18H), −3.07 (s, 2H, NH); ^{13}C NMR (100 MHz, CDCl$_3$, 25 °C): δ = 161.0 (br), 147.6 (br), 137.4 (br), 128.6 (br), 123.0 (br), 118.2 (br), 104.8 (br), 71.6 (br, CH$_2$O), 68.4 (br, CH$_2$O), 63.1 (CH$_2$O), 38.5 (br), 32.9 (br), 31.6–32.2 (several CH$_2$), 29.4–30.5 (several CH$_2$), 27.3 (CH$_2$), 26.3–26.6 (several CH$_2$), 25.9, 22.6–22.9 (several CH$_2$), 14.2 (Me); HR-MS (MALDI): *m/z* calcd. for C$_{114}$H$_{182}$N$_8$O$_5$ ([M]$^+$): 1743.4233, found 1743.4240.

Phthalocyanine-C$_{60}$ dyad 2c. A solution of the phthalocyanine **4c** (64 mg, 0.037 mmol) and the acid **11** (50 mg, 0.056 mmol) in *o*-dichlorobenzene (7 mL) was sonicated for 2 h. After cooling to 0 °C, DCC (31 mg, 0.15 mmol) and DMAP (18 mg, 0.15 mmol) were added, the mixture was allowed to reach r.t. and was stirred overnight. The resulting mixture was concentrated and the residue was purified by column chromatography (CH$_2$Cl$_2$/hexane 3 : 2) to give **2c** (46 mg, 47%). Green solid; R$_f$ 0.67 (CH$_2$Cl$_2$/hexane 3 : 2); ^{1}H NMR (300 MHz, CDCl$_3$, 25 °C): δ = 8.25–8.80 (m, 4H), 7.90–8.20 (m, 4H), 7.72 (d, $^3J_{H,H}$ = 7.4 Hz, 2H), 7.30–7.60 (m, 7H), 4.20–4.50 (m, 8H, ArOC*H*$_2$), 4.05–4.15 (m, 2H, COOC*H*$_2$), 2.67 (t, $^3J_{H,H}$ = 7.5 Hz, 2H, C*H*$_2$COO), 2.39 (t, $^3J_{H,H}$ = 7.0 Hz, 2H, PhCC*H*$_2$), 1.98–2.25 (m, 7H, ArOCH$_2$C*H*$_2$ + ArOCH$_2$C*H* + C*H*$_2$CH$_2$COO), 1.10–1.90 (m, 134H), 0.80–0.95 (m, 18H), −3.36 (s, 2H, NH); ^{13}C NMR (100 MHz, CDCl$_3$, 25 °C), selected signals: δ = 173.1 (C=O), 160.3 (br, arom. C–O), 79.7 (fullerene C(sp^3)), 71.8 (br, CH$_2$O), 68.4 (br, CH$_2$O), 64.7 (*C*H$_2$OC=O), 51.7 (Ph*C*), 33.5 and 34.0 (*C*H$_2$C=O and PhC*C*H$_2$); HR-MS (MALDI): *m/z* calcd. for C$_{185}$H$_{192}$N$_8$O$_6$ ([M]$^+$): 2621.4965 (M$^+$), found 2621.5530.

Supporting Information

Experimental procedures and analytical data for derivatives **2a,b,d**, **4a,b,d**, **6a–d**, **9a,b,d**, **10a,b,d**.

Supporting Information File 1
Experimental details
[http://www.beilstein-journals.org/bjoc/content/supplementary/1860-5397-5-49-S1.doc]

Acknowledgements

References

1. Spanggaard, H.; Krebs, F. C. *Sol. Energy Mater. Sol. Cells* **2004,** *83,* 125–146. doi:10.1016/j.solmat.2004.02.021
2. Pivrikas, A.; Sariciftci, N. S.; Juška, G.; Österbacka, R. *Prog. Photovoltaics* **2007,** *15,* 677–696. doi:10.1002/pip.791
3. Hoth, C. N.; Schilinsky, P.; Choulis, S. A.; Brabec, C. J. *Nano Lett.* **2008,** *8,* 2806–2813. doi:10.1021/nl801365k
4. Hiramoto, M.; Fujiwara, H.; Yokoyama, M. *Appl. Phys. Lett.* **1991,** *58,* 1062–1064. doi:10.1063/1.104423
5. Halls, J. J. M.; Walsh, C. A.; Greenham, N. C.; Marseglia, E. A.; Friend, R. H.; Moratti, S. C.; Holmes, A. B. *Nature* **1995,** *376,* 498–500. doi:10.1038/376498a0
6. Yu, G.; Gao, J.; Hummelen, J. C.; Wudl, F.; Heeger, A. J. *Science* **1995,** *270,* 1789–1791. doi:10.1126/science.270.5243.1789
7. Janssen, R. A. J.; Hummelen, J. C.; Sariciftci, N. S. *MRS Bull.* **2005,** *30,* 33–36.
8. Sergeyev, S.; Pisula, W.; Geerts, Y. H. *Chem. Soc. Rev.* **2007,** *36,* 1902–1929. doi:10.1039/b417320c
9. Wienk, M. M.; Kroon, J. M.; Verhees, W. J. H.; Knol, J.; Hummelen, J. C.; van Hal, P. A.; Janssen, R. A. J. *Angew. Chem., Int. Ed.* **2003,** *42,* 3371–3375. doi:10.1002/anie.200351647
10. Hummelen, J. C.; Knight, B. W.; LePeq, F.; Wudl, F.; Yao, J.; Wilkins, C. L. *J. Org. Chem.* **1995,** *60,* 532–538. doi:10.1021/jo00108a012
11. Janssen, R. A. J.; Hummelen, J. C.; Wudl, F. *J. Am. Chem. Soc.* **1995,** *117,* 544–545. doi:10.1021/ja00106a068
12. Yang, C.; Cho, S.; Heeger, A. J.; Wudl, F. *Angew. Chem., Int. Ed.* **2009,** *48,* 1592–1595. doi:10.1002/anie.200805228
13. Thompson, B. C.; Fréchet, J. M. J. *Angew. Chem., Int. Ed.* **2008,** *47,* 58–77. doi:10.1002/anie.200702506
14. Wienk, M. M.; Turbiez, M.; Gilot, J.; Janssen, R. A. J. *Adv. Mater.* **2008,** *20,* 2556–2560. doi:10.1002/adma.200800456
15. Yi, H.; Johnson, R. G.; Iraqi, A.; Mohamad, D.; Royce, R.; Lidzey, D. G. *Macromol. Rapid Commun.* **2008,** *29,* 1804–1809. doi:10.1002/marc.200800440
16. He, Y.; Wu, W.; Zhao, G.; Liu, Y.; Li, Y. *Macromolecules* **2008,** *41,* 9760–9766. doi:10.1021/ma801923c

17. Zhang, F.; Bijleveld, J.; Perzon, E.; Tvingstedt, K.; Barrau, S.; Inganäs, O.; Andersson, M. R. *J. Mater. Chem.* **2008,** *18,* 5468–5474. doi:10.1039/b811957k

18. Zhou, E.; Nakamura, M.; Nishizawa, T.; Zhang, Y.; Wei, Q.; Tajima, K.; Yang, C.; Hashimoto, K. *Macromolecules* **2008,** *41,* 8302–8305. doi:10.1021/ma802052w

19. Silvestri, F.; Irwin, M. D.; Beverina, L.; Facchetti, A.; Pagani, G. A.; Marks, T. J. *J. Am. Chem. Soc.* **2008,** *130,* 17640–17641. doi:10.1021/ja8067879

20. Kronenberg, N. M.; Deppisch, M.; Würthner, F.; Lademann, H. W. A.; Deing, K.; Meerholz, K. *Chem. Commun.* **2008,** 6489–6491. doi:10.1039/b813341g

21. Tamayo, A. B.; Walker, B.; Nguyen, T.-Q. *J. Phys. Chem. C* **2008,** *112,* 11545–11551. doi:10.1021/jp8031572

22. Schuster, D. I.; MacMahon, S.; Guldi, D. M.; Echegoyen, L.; Braslavsky, S. E. *Tetrahedron* **2006,** *62,* 1928–1936. doi:10.1016/j.tet.2005.07.127

23. Narutaki, M.; Takimiya, K.; Otsubo, T.; Harima, Y.; Zhang, H.; Araki, Y.; Ito, O. *J. Org. Chem.* **2006,** *71,* 1761–1768. doi:10.1021/jo051821v

24. Nakamura, T.; Araki, Y.; Ito, O.; Murata, Y.; Komatsu, K. *J. Photochem. Photobiol., A* **2006,** *178,* 242–250.

25. Fujitsuka, M.; Makinoshima, T.; Takamizawa, A.; Araki, Y.; Ito, O.; Obara, Y.; Aso, Y.; Otsubo, T. *Bull. Chem. Soc. Jpn.* **2006,** *79,* 1860–1868. doi:10.1246/bcsj.79.1860

26. Schuster, D. I.; Li, K.; Guldi, D. M.; Palkar, A.; Echegoyen, L.; Stanisky, C.; Cross, R. J.; Niemi, M.; Tkachenko, N. V.; Lemmetyinen, H. *J. Am. Chem. Soc.* **2007,** *129,* 15973–15982. doi:10.1021/ja074684n

27. Guldi, D. M.; Spänig, F.; Kreher, D.; Perepichka, I. F.; van der Pol, C.; Bryce, M. R.; Ohkubo, K.; Fukuzumi, S. *Chem.–Eur. J.* **2008,** *14,* 250–258. doi:10.1002/chem.200700837

28. Kawauchi, H.; Suzuki, S.; Kozaki, M.; Okada, K.; Islam, D.-M. S.; Araki, Y.; Ito, O.; Yamanaka, K.-i. *J. Phys. Chem. A* **2008,** *112,* 5878–5884. doi:10.1021/jp800716e

29. Guldi, D. M.; Illescas, B. M.; Atienza, C. M.; Wielopolski, M.; Martín, N. *Chem. Soc. Rev.* **2009,** *38,* 1587–1597. doi:10.1039/b900402p

30. Gregory, P. *J. Porphyrins Phthalocyanines* **2000,** *4,* 432–437. doi:10.1002/(SICI)1099-1409(200006/07)4:4<432::AID-JPP254>3.0.CO;2-N

31. Laschat, S.; Baro, A.; Steinke, N.; Giesselmann, F.; Hägele, C.; Scalia, G.; Judele, R.; Kapatsina, E.; Sauer, S.; Schreivogel, A.; Tosoni, M. *Angew. Chem., Int. Ed.* **2007,** *46,* 4832–4887. doi:10.1002/anie.200604203

32. Warman, J. M.; de Haas, M. P.; Dicker, G.; Grozema, F. C.; Piris, J.; Debije, M. G. *Chem. Mater.* **2004,** *16,* 4600–4609. doi:10.1021/cm049577w

33. Iino, H.; Hanna, J.; Bushby, R. J.; Movaghar, B.; Whitaker, B. J.; Cook, M. J. *Appl. Phys. Lett.* **2005,** *87,* 132102. doi:10.1063/1.2056608

34. Kahnt, A.; Guldi, D. M.; de la Escosura, A.; Martínez-Díaz, M. V.; Torres, T. *J. Mater. Chem.* **2008,** *18,* 77–82. doi:10.1039/b712751k

35. Guldi, D. M.; Zilbermann, I.; Gouloumis, A.; Vázquez, P.; Torres, T. *J. Phys. Chem. B* **2004,** *108,* 18485–18494. doi:10.1021/jp047105z

36. Guldi, D. M.; Gouloumis, A.; Vazquez, P.; Torres, T. *Chem. Commun.* **2002,** 2056–2057. doi:10.1039/b205620h

37. Gouloumis, A.; Liu, S.-G.; Sastre, A.; Vazquez, P.; Echegoyen, L.; Torres, T. *Chem.–Eur. J.* **2000,** *6,* 3600–3607. doi:10.1002/1521-3765(20001002)6:19<3600::AID-CHEM3600>3.3.CO;2-S

38. Isosomppi, M.; Tkachenko, N. V.; Efimov, A.; Vahasalo, H.; Jukola, J.; Vainiotalo, P.; Lemmetyinen, H. *Chem. Phys. Lett.* **2006,** *430,* 36–40. doi:10.1016/j.cplett.2006.08.107

39. Loi, M. A.; Denk, P.; Hoppe, H.; Neugebauer, H.; Winder, C.; Meissner, D.; Brabec, C.; Sariciftci, N. S.; Gouloumis, A.; Vazquez, P.; Torres, T. *J. Mater. Chem.* **2003,** *13,* 700–704. doi:10.1039/b212621d

40. Donnio, B.; Buathong, S.; Bury, I.; Guillon, D. *Chem. Soc. Rev.* **2007,** *36,* 1495–1513. doi:10.1039/b605531c

41. Nakanishi, T.; Shen, Y.; Wang, J.; Yagai, S.; Funahashi, M.; Kato, T.; Fernandes, P.; Möhwald, H.; Kurth, D. G. *J. Am. Chem. Soc.* **2008,** *130,* 9236–9237. doi:10.1021/ja803593j

42. Mamlouk, H.; Heinrich, B.; Bourgogne, C.; Donnio, B.; Guillon, D.; Felder-Flesch, D. *J. Mater. Chem.* **2007,** *17,* 2199–2205. doi:10.1039/b700460e

43. Lenoble, J.; Campidelli, S.; Maringa, N.; Donnio, B.; Guillon, D.; Yevlampieva, N.; Deschenaux, R. *J. Am. Chem. Soc.* **2007,** *129,* 9941–9952. doi:10.1021/ja071012o

44. Maringa, N.; Lenoble, J.; Donnio, B.; Guillon, D.; Deschenaux, R. *J. Mater. Chem.* **2008,** *18,* 1524–1534. doi:10.1039/b717105f

45. de la Escosura, A.; Martinez-Diaz, M. V.; Barbera, J.; Torres, T. *J. Org. Chem.* **2008,** *73,* 1475–1480. doi:10.1021/jo7022763

46. Tant, J.; Geerts, Y. H.; Lehmann, M.; de Cupere, V.; Zucchi, G.; Laursen, B. W.; Bjørnholm, T.; Lemaur, V.; Marcq, V.; Burquel, A.; Hennebicq, E.; Gardebien, F.; Viville, P.; Beljonne, D.; Lazzaroni, R.; Cornil, J. *J. Phys. Chem. B* **2005,** *109,* 20315–20323. doi:10.1021/jp054778o

47. Appel, R. *Angew. Chem., Int. Ed. Engl.* **1975,** *14,* 801–811. doi:10.1002/anie.197508011

48. de la Torre, G.; Claessens, C. G.; Torres, T. *Eur. J. Org. Chem.* **2000,** 2821–2830. doi:10.1002/1099-0690(200008)2000:16<2821::AID-EJOC2821>3.0.CO;2-2

49. Huang, X.; Liu, Y.; Wang, S.; Zhou, S.; Zhu, D. *Chem.–Eur. J.* **2002,** *8,* 4179–4184. doi:10.1002/1521-3765(20020916)8:18<4179::AID-CHEM4179>3.0.CO;2-L

50. Sastre, A.; Gouloumis, A.; Vázquez, P.; Torres, T.; Doan, V.; Schwartz, B. J.; Wudl, F.; Echegoyen, L.; Rivera, J. *Org. Lett.* **1999,** *1,* 1807–1810. doi:10.1021/ol991063t

51. Humberstone, P.; Clarkson, G. J.; McKeown, N. B.; Tracher, K. E. *J. Mater. Chem.* **1996,** *6,* 315–322. doi:10.1039/jm9960600315

52. Banwell, M. G.; Edwards, A. J.; Harfoot, G. J.; Jolliffe, K. A. *Tetrahedron* **2004,** *60,* 535–547. doi:10.1016/j.tet.2003.10.122

53. Rager, C.; Schmid, G.; Hanack, M. *Chem.–Eur. J.* **1999,** *5,* 280–288. doi:10.1002/(SICI)1521-3765(19990104)5:1<280::AID-CHEM280>3.0.CO;2-0

54. Sergeyev, S.; Pouzet, E.; Debever, O.; Levin, J.; Gierschner, J.; Cornil, J.; Gomez-Aspe, R.; Geerts, Y. H. *J. Mater. Chem.* **2007,** *17,* 1777–1784. doi:10.1039/b617856a

55. Sergeyev, S.; Debever, O.; Pouzet, E.; Geerts, Y. H. *J. Mater. Chem.* **2007,** *17,* 3002–3007. doi:10.1039/b704344a

56. Tylleman, B.; Gómez-Aspe, R.; Gbabode, G.; Geerts, Y. H.; Sergeyev, S. *Tetrahedron* **2008,** *64,* 4155–4161. doi:10.1016/j.tet.2008.03.004

57. Tylleman, B.; Gbabode, G.; Amato, C.; Buess-Herman, C.; Lemaur, V.; Cornil, J.; Gómez-Aspe, R.; Geerts, Y. H.; Sergeyev, S. *Chem. Mater.* **2009,** *21,* 2789–2797. doi:10.1021/cm900383c

58. Drees, M.; Hoppe, H.; Winder, C.; Neugebauer, H.; Sariciftci, N. S.; Schwinger, W.; Schäffler, F.; Topf, C.; Scharber, M. C.; Zhud, Z.; Gaudianad, R. *J. Mater. Chem.* **2005,** *15,* 5158–5163. doi:10.1039/b505361g

59. Giacalone, F.; Segura, J. L.; Martin, N. *J. Org. Chem.* **2002,** *67,* 3529–3532. doi:10.1021/jo020088u

License and Terms

Chiral amplification in a cyanobiphenyl nematic liquid crystal doped with helicene-like derivatives

Alberta Ferrarini[*1], Silvia Pieraccini[2], Stefano Masiero[2] and Gian Piero Spada[*2]

Abstract

The addition of a chiral non-racemic dopant to a nematic liquid crystal (LC) has the effect of transferring the molecular chirality to the phase organization and a *chiral nematic* phase is formed. This molecular chirality amplification in the LC provides a unique possibility for investigating the relationship between molecular structure, intermolecular interactions, and mesoscale organization. It is known that axially chiral or helical-shaped molecules with reduced conformational disorder are good candidates for high *helical twisting power* derivatives. In particular, biaryl derivatives are known to be efficient chiral inducers in biaryl nematic mesophases. In this paper, we focus on a new series of helicene-like molecules of known absolute configuration. We have integrated cholesteric pitch measurements with geometry optimization by DFT calculations and analysis of the twisting ability by the Surface Chirality model to shed light on the structural features responsible for the analogies and differences exhibited by these derivatives. The investigation of these dopants with well-defined geometry, by virtue of the low conformational freedom, and the substituents variously distributed around the core, allows us to extend our knowledge of the molecular origin of the chirality amplification in liquid crystals and to confirm the simple relationship "molecular *P*-helicity" → "cholesteric *P*-handedness" for helical-shaped helicene-like derivatives.

Introduction

Nematic liquid crystals (LCs) are fluid phases formed by anisometric molecules which, though free to rotate as in ordinary liquids, ar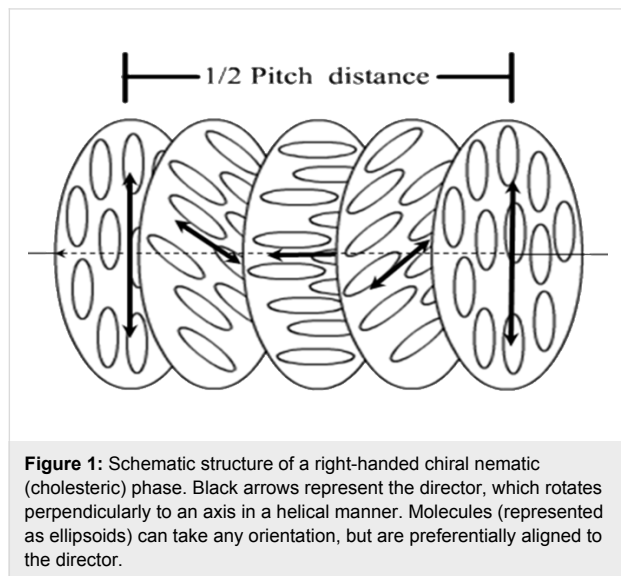e preferentially aligned along a common axis, called *director*. The addition of a chiral non-racemic dopant to a nematic liquid crystal has the effect of transferring the molecular chirality to the phase organization and a *chiral*

nematic (or *cholesteric*) phase is formed, in which the director rotates perpendicularly to an axis in a helical way (see Figure 1) [1].

Figure 1: Schematic structure of a right-handed chiral nematic (cholesteric) phase. Black arrows represent the director, which rotates perpendicularly to an axis in a helical manner. Molecules (represented as ellipsoids) can take any orientation, but are preferentially aligned to the director.

For a given nematic host, the handedness and magnitude of the pitch of the cholesteric helix depend on the structure, concentration, and enantiomeric purity of the dopant. Enantiomeric pairs induce oppositely handed cholesteric phases. At low concentration, the helix pitch is inversely proportional to the molar fraction of the dopant; the propensity of a dopant to induce a helical organization in the LC matrix is then quantified by its *helical twisting power* (HTP), which is defined as [2,3]:

$$HTP = (pcr)^{-1} \qquad (1)$$

where p is the helical pitch of the cholesteric phase and c and r are the concentration (molar fraction) and the enantiomeric excess of the dopant, respectively. The sign of HTP is taken as positive if the induced cholesteric phase is right-handed (P).

Cholesteric induction has attracted great interest in the field of material science [4]. Most applications (for example, for the development of reversible optical memories) [5] require chiral dopants with good solubility in the nematic host and high helical twisting power. Understanding of the mechanism behind chirality transfer from solute molecules to host nematic phases is essential for designing LC-based chiral devices; our and other research groups have investigated this issue (for a selection of papers, see refs [6-21]). Cholesteric induction has also been exploited for the assignment of the absolute configuration of chiral molecules, as a viable alternative or complement to more usual techniques such as Circular Dichroism [2,3] (for a general review on CD, see refs [22,23]).

From a more fundamental point of view, the molecular chirality amplification in LC gives a unique possibility for investigating the relationship between molecular structure, intermolecular interactions, and mesoscale organization. The phenomenon of cholesteric induction can be explained in general terms as the result of the competition between (i) a chiral force, which originates from the chirality of intermolecular interactions and promotes a twist of the nematic director and (ii) an elastic restoring force, which can be traced back to the anisotropy of intermolecular interactions and opposes director distortions [24]. Different theories [25-27] have contributed to elucidate the molecular mechanism behind cholesteric induction, as well as Molecular Dynamics simulations [28-30]; for the connection between structure of the chiral dopant and cholesteric organisation, the *Surface Chirality* (SC) model has been shown to be particularly useful [31,32]. This is a phenomenological mean field theory wherein the anisotropy and chirality of the interactions of the dopant with the surrounding molecules are parameterized on the basis of the geometric features of the molecular surface. The underlying assumption is that short-range intermolecular interactions, which are modulated by molecular shape, are mainly responsible for the organization of thermotropic LCs. A valuable feature of the SC model is its realistic account of molecular structure; a detailed representation of the molecular surface can be easily obtained, once the atomic coordinates are known. The availability of reliable molecular structures is a requirement for the quality of HTP predictions. Nowadays, good estimates of molecular geometry can be obtained at an affordable computational cost using standard Quantum Mechanical (QM) tools.

It is known that axially chiral or helical-shaped molecules with reduced conformational disorder are good candidates for high HTP derivatives [2,4,6]. In particular, biaryl derivatives have been described as efficient chiral inducers in biaryl nematic mesophases (as, for instance, the widely used commercial mixture E7 from BDH) [33-45] and this has been viewed as a consequence of their structural analogy and molecular recognition via core–core interactions with the host molecules [46,47].

To avoid confusion with the *P*/*M* stereochemical descriptors of chirality axes, planes, or helices according to IUPAC nomenclature [48], we use here pseudo-*P* and pseudo-*M* to indicate the handedness of the twist between the two (aromatic) planes (for example, a biphenyl, irrespective of the presence of the substituents, is designed as pseudo-*P* when the two phenyl rings are arranged in such a way that a clockwise rotation (<90°) of the ring closer to the observer is required to obtain the coplanarity of the two aromatic planes). In most cases, (pseudo-*P*)-biaryls induce (*P*)-cholesterics; however, the relationship between stereochemical descriptor of the molecular chirality

and handedness of the induced cholesteric phase is not straight-forward. Indeed, it has been found that homochiral molecules with similar structures may induce cholesteric phases of opposite handedness [7,49]. A striking example is homochiral oligonaphthalenes, which, despite the clear structural helicity and the similar orientational behavior, exhibit no trivial relationship between molecular stereochemical descriptor (a*R* or a*S*) and cholesteric handedness (*P* or *M*) [50]. Changes in the molecular geometry, arising from the presence of substituents or conformational equilibria, can have a dramatic effect on the twisting ability of a dopant [2]. Moreover, in the case of dopants with low twisting power, cholesterics of opposite handedness may be induced in different LC solvents [8]. However, for solutes with clearly defined helicity and alignment axes, a weak sensitivity to small changes in structure and environment is more often observed. This uniformity of behavior was observed for the helicenes investigated; in penta- and hexa- and carbo- and hetero-helicenes, the relationship between the molecular stereochemical descriptor and the cholesteric handedness was verified and interpreted [51]: (*P*)-helicenes induce (*P*)-cholesterics in all the cases investigated.

In this paper, we focus on a new series of helicene-like molecules of known absolute configuration (Figure 2). We have integrated cholesteric pitch measurements with geometry optimization by DFT calculations and analysis of the twisting ability by the SC method to shed light on the structural features responsible for the analogies and differences exhibited by these derivatives. The investigation of these dopants with well-defined geometry, by virtue of the low conformational freedom, and substituents variously distributed around the molecular core, allows us to extend our knowledge of the molecular origin of the chirality amplification in liquid crystals.

Results and Discussion

The enantioselective synthesis as well as the configuration assignment of enantiopure dihydro[5]helicene quinones or bisquinones **1–5** and of dihydro- (and tetrahydro-) [4]helicene quinones **6–8** has been described by Carreño, Urbano and coworkers [52-57].

The twisting powers of the helicenes under investigation measured in the nematic solvent E7 are reported in Table 1.

We can see that all compounds possessing, as a common feature, homochiral *P*-helicity (for helical-shaped molecules, *P* and *M* describe the sense of the twist of the helix: this is right-handed, and is denoted as *P*, if the sense of the twist is clockwise as one progresses along the helix axis [48]) follow the relationship "molecular *P*-helicity" → "cholesteric P-handed-ness" already reported for a series of carbo- and hetero-heli-
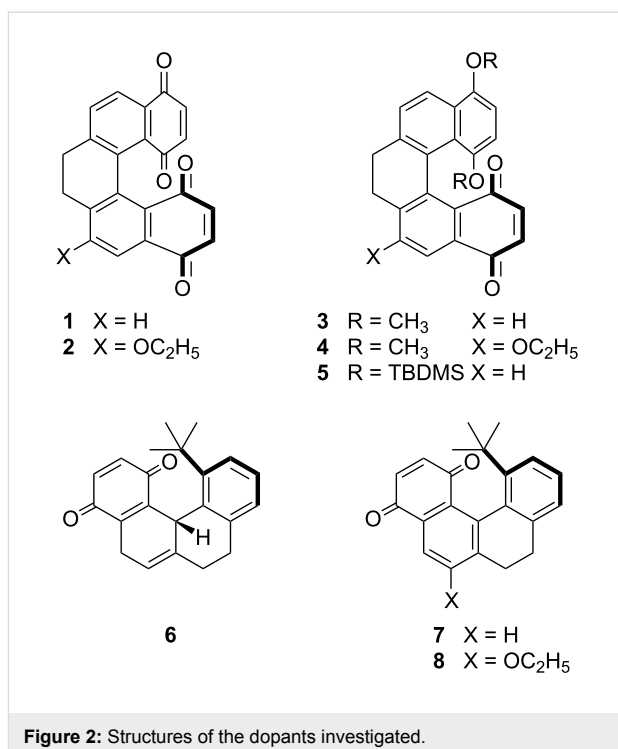

Figure 2: Structures of the dopants investigated.

Table 1: Helical twisting power (HTP) measured in the nematic host E7 and chirality parameter *Q* calculated by the SC method.

Compound	HTP (µm⁻¹)	Q (Å³)
1	+68	+14.8
2	+45	+20.6
3	+31	+8.3
4	+29	+9.3
5	+2.4	−0.1 (**I**) [0.44][b]
		−4.4 (**II**) [0.37]
		+6.2 (**III**) [0.19]
6	+4.3[a]	−0.2
7	+9.2	+2.4
8	+5.6	+8.0

[a]HTP was measured for the enantiomer of **6**; therefore, the opposite of the measured value is reported in the table.
[b]Values refer to the three conformers of **5**, whose statistical weights are reported in brackets (see Figure 3).

cenes [51]. (*P*)-7,8-Dihydro[5]helicene quinones or bisquinones **1–4** show moderate to high HTPs; despite the presence of the same tetracyclic core, derivative **5**, with the tert-butyldimethyl-silyl (TBDMS) blocking group, exhibits the lowest measured HTP. This is a confirmation of the fact that bulky substituents, though lacking centres of chirality (or other stereogenic elements), can strongly affect the molecule-to-phase chirality transfer. The data in Table 1 also show that, unlike derivatives **1–4**, the [4]helicene quinones **6–8** have low twisting ability.
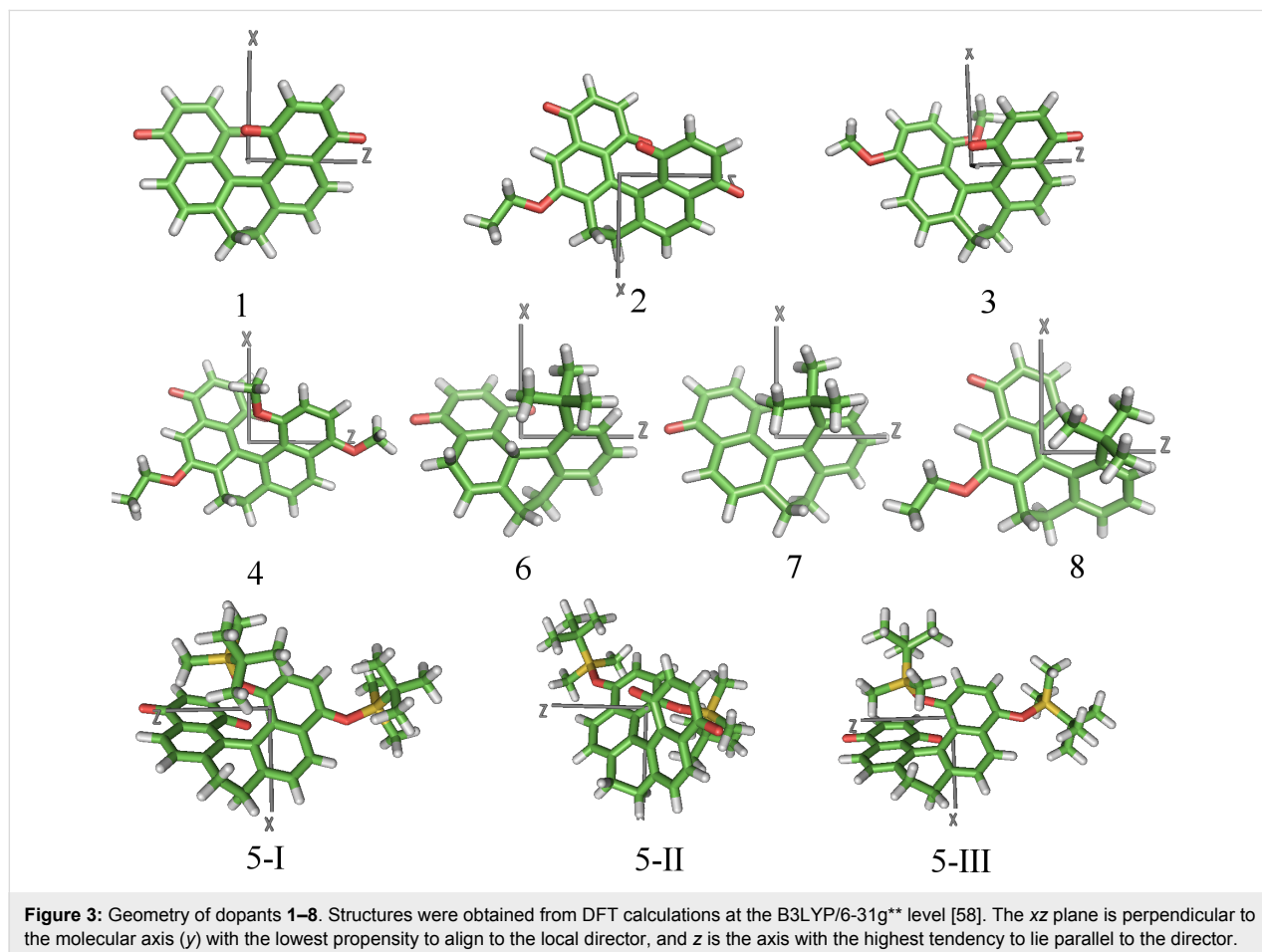
The structure of the dopants under investigation was determined by DFT calculations at the B3LYP/6-31g** level [58]; the optimized geometries are shown in Figure 3. In the dihydro[5]-helicene quinones and bisquinones **1–5**, the naphthoquinone rings are approximately planar, with twist angles ranging between 42° and 43° for **1–4** and a slightly lower angle, around 40°, for **5**. A larger twist angle of 50.1° is found in dihydro[4]helicene quinones **7** and **8**, whereas a wider value, 81.7°, is allowed in tetrahydro[4]helicene quinone **6**, because of the higher flexibility arising from the presence of an additional dihydro ring. In all derivatives, the core of the fused rings is conformationally constrained, and for most of them, even the introduced substituents do not provide high conformational freedom. The O–C$_{Alkyl}$ bond of alkoxy groups lies in the plane of the adjacent aromatic ring; for steric reasons, only the conformations shown in Figure 3 are allowed when a methoxy substituent is present. For **2**, **4**, and **8**, other structures, differing in the conformation of the ethoxy side chain, are also possible, but in view of their high energy, they have a negligible weight at room temperature. A different behavior is exhibited by derivative **5**, which has bulkier TBDMS substituents; one of them is constrained by the proximity of the quinone ring, whereas the

other is pointing towards the molecular periphery and is more free. Three structures with similar energy were obtained, differing essentially in the value of the torsional angle for the O–Si bond of the less hindered *tert*-butyl-silyl group. These structures are also displayed in Figure 3.

The twisting ability of derivatives **1–8** was analysed according to the SC method [31,32]; molecular surfaces generated on the basis of the optimized geometries [59] were used. Within this approach, the HTP of a chiral dopant in a nematic solvent is proportional to the so-called *chirality parameter Q*, which holds the coupling of the chirality and orientational order and is proper of each dopant; the *chirality parameter Q* is defined as:

$$Q = -\sqrt{(2/3)}(Q_{xx}S_{xx} + Q_{yy}S_{yy} + Q_{zz}S_{zz}) \qquad (2)$$

where S_{ii} is the ith cartesian component of the Saupe ordering matrix, which specifies the degree of alignment to the local director of the ith molecular axis, and Q_{ii} quantifies the helicity of the molecular surface, as viewed along the same axis. The proportionality factor A between HTP and Q depends on the

Figure 3: Geometry of dopants **1–8**. Structures were obtained from DFT calculations at the B3LYP/6-31g** level [58]. The *xz* plane is perpendicular to the molecular axis (*y*) with the lowest propensity to align to the local director, and *z* is the axis with the highest tendency to lie parallel to the director.

macroscopic properties of the host, being defined as $A = RT\,\xi/2\pi\,K_{22}\,v_m$, where T is the absolute temperature, R is the gas constant, K_{22} and v_m are the twist elastic constant and the molar volume of the liquid crystal host, respectively, and the parameter ξ is the orienting strength of the medium (and is related to the degree of order of the host).

The principal elements of the ordering matrix **S** calculated for derivatives **1–8** are reported in Table 2. The x, y, z labels denote the principal alignment axes in the molecule; in particular, z and y identify the molecular directions with the strongest tendency to align parallel and perpendicular to the local director, respectively. These directions, which are univocally identified once the ordering matrix **S** is calculated, are shown by the axes superimposed on the chemical structures in Figure 3. We can see that in most of the cases y lies close to what can be considered as the 'molecular helix axis', whereas the xz plane corresponds to what can be approximately defined as the 'molecular plane'. The z axis, which is preferentially aligned to the director, lies in the direction of maximum molecular elongation, which for most derivatives is close to that of the aryl–aryl bond; for dopants

with twofold rotational symmetry, the x direction is parallel to the C_2 axis. To understand the orientational behavior of dopants, we must recall the relationship $-0.5 \le S_{ii} \le 1$, with $S_{ii} = 1$ and $S_{ii} = -0.5$ denoting perfect alignment of the ith molecular axis parallel and perpendicular to the director, respectively [31]. Thus, the S_{ii} values reported in Table 2 indicate that all the derivatives have a similar orientational behavior in the nematic host. The relatively low S_{zz} values say that these dopants are not strongly ordered in the liquid crystal host; more important for their twisting ability, they tend to keep the 'molecular helix axis' perpendicular to the director, whereas the latter preferentially lies on the 'molecular plane'. As a consequence, our dopants are expected to induce a cholesteric phase with the same helicity as that characterising the 'molecular helix axis' (y in Figure 4).

The Q_{ii} values reported in Table 2 quantify the magnitude and sign of the helicity of the molecular surface, as seen along the x, y, z axes. Since the relationship $Q_{xx} + Q_{yy} + Q_{zz} = 0$ holds [31], any molecule is characterized by the helicities of opposite signs, depending on the direction along which the molecular surface is

Table 2: Principal elements of the Saupe ordering matrix, **S**, and corresponding elements of the chirality tensor **Q**. Axis labels are shown in Figure 3.

Compound	S_{xx}	S_{yy}	S_{zz}	Q_{xx} (Å^3)	Q_{yy} (Å^3)	Q_{zz} (Å^3)
1	0.02	−0.29	0.27	−89.5	72.4	17.1
2	0	−0.32	0.32	−89.2	84.7	4.5
3	−0.05	−0.29	0.34	−83.3	67.1	16.2
4	−0.07	−0.31	0.37	−117.3	92.0	25.3
5-I[a]	−0.15	−0.19	0.34	−7.0	6.3	0.7
5-II	−0.16	−0.20	0.36	−62.5	48.1	14.4
5-III	−0.06	−0.26	0.32	−28.8	32.0	−3.2
6	−0.03	−0.18	0.21	−76.5	47.7	28.8
7	0.02	−0.22	0.20	−68.0	37.0	31.0
8	0.03	−0.26	0.23	−48.0	39.8	8.2

[a]Values refer to the three conformers of **5**, with different conformations around the O–Si bond of the less hindered TBDMS group (see text and Figure 3).
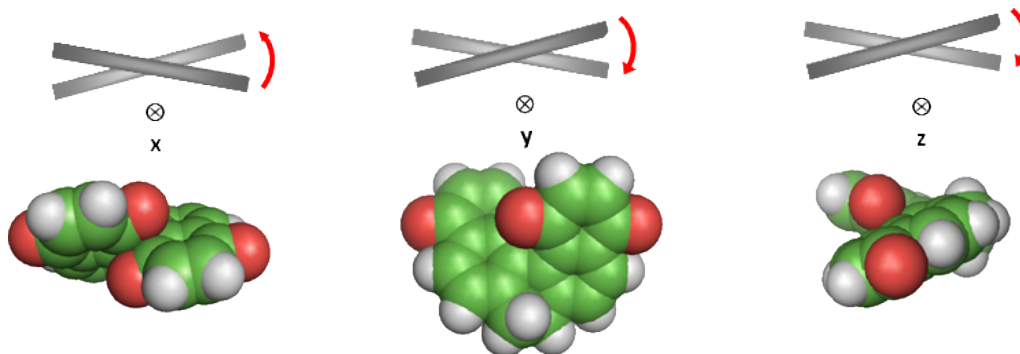

Figure 4: Helicity of the molecular surface of derivative **1** along its principal alignment axes in the liquid crystal environment.

viewed. This is not in contradiction with the presence of a well-defined stereochemical descriptor, because a given axis is chosen for such a definition by convention. We can see in Table 2 that for all dopants with the exception of one conformer of **5**, the molecular surface has negative helicity along the *x* axis, whereas the helicity is positive along the *y* and *z* axes. This is in agreement with the *P* helical stereochemical descriptor of the chiral dopants under investigation, which is defined with respect to the helix axis (*y*).

In the case of derivative **5**, order and chirality properties are not dictated by the central core, but seem to be significantly affected by the bulky substituents. Table 2 shows that different order parameters are predicted for the **I–III** conformers of **5**, which are also different from those of the other dopants under investigation. We can see even more substantial differences between Q_{ii} components, with particularly low values predicted for the **5-I** conformer.

As a result of the surface chirality and the orientational behavior, induction of right-handed cholesterics is predicted for our dopants. The trend of the chirality parameter *Q* reported in Table 1 mirrors that of the measured HTPs, with more discrepancy for the weaker cholesteric inducers. A negative *Q* is obtained for **6** and the *Q* value calculated for **5** as a weighted average over all conformers is also negative. However, these negative values are very small and we can see that they are obtained just for the two derivatives with the lowest measured HTPs. Indeed, the twisting ability of a given dopant results from a delicate balance of chirality and anisotropy of dopant–host interactions and predictions of small effects would require a very detailed modelling of all intermolecular interactions. The SC method is particularly suitable for dopants with relatively high HTP, whose behavior is dominated by short-range interactions with the host. In general, low *Q* values may not be in agreement with measured HTPs. Another possible reason for this discrepancy, besides the neglect of long-range intermolecular interactions, such as the electrostatic ones, might be the molecular geometry used for *Q* calculation: in the absence of a net prevailing term, even relatively small geometry changes can modify the balance between the positive and negative contributions.

According to our SC model results, the low HTP measured for **5** and **6** has a different explanation: in the latter case, it simply reflects the low twisting ability of the dopant, whereas in the former, it comes from the cancelling effect of conformers which individually would induce a left-handed (**5-II**) and a right-handed twist (**5-III**). Moreover, inspection of Table 2 suggests that the lower twisting ability, measured and predicted for all the [4]helicene quinones **6–8** can be ascribed to weaker orienta-

tional order and lower helicity along the *y* axis. Both effects can ultimately be traced back to the larger dimensions of the [4]helicene quinone derivatives, which possess a wider extension of aromatic rings, capable of establishing stronger dispersion interactions with the host molecules. As to the effect of substituents, we can compare the results obtained for the pairs **1–2**, **3–4**, and **7–8**, which differ by the replacement of a phenyl hydrogen by an ethoxy group. The measured HTPs are smaller for the derivatives with the ethoxy substituent, whereas the opposite change is predicted from the SC calculations; the discrepancy between calculations and experiments is especially evident in the case of derivative **8**. These differences might indicate a role of electrostatic solute–solvent interactions, which are neglected in our model. It was already observed that these can be considered as a generally small, but non-negligible, correction to the underlying short-range interactions; their relative contribution can become relevant in the case of dopants with otherwise small twisting ability [7].

Conclusion

Chirality is a peculiar molecular feature and its manifestations elude any trivial interpretation: different, often completely uncorrelated, responses depending on the experiment used are obtained in the attempt to quantify it.

The helical twisting power cannot simply be correlated with a global stereochemical descriptor of the molecule, as demonstrated for homochiral series of propeller-like heptalenes and oligonaphthalenes for which the handedness of the induced cholesteric depends critically on the substituents attached to the chiral core [49,50].

The investigation presented here confirms that, as already found for helicene derivatives [51], the simple relationship "molecular *P*-helicity" → "cholesteric *P*-handedness" exists for helicene-like compounds, in the absence of bulky and highly flexible substituents. Not surprisingly, taking into account molecular shape, the orientational behavior of **1–8** derivatives is analogous to that of bridged binaphthyls and also the helical twisting power can be interpreted in a similar way: the outcome is that pseudo-*P* dopants induce a right-handed (*P*)-cholesteric phase. The results obtained for the dopants investigated in the present work, with a clear molecular *P*-helicity and low conformational freedom, differing from each other in the presence of variously distributed substituents, confirm that short-range intermolecular interactions, parameterizable according to the molecular surface, are the main determinants of cholesteric induction in thermotropic liquid crystals. Other interactions, ascribable to the presence of electronegative groups, though present, are less relevant, and can have non-negligible effects in the case of dopants with low twisting ability.

Experimental

Helical twisting power measurements

Pitches and handedness of the cholesteric solutions in E7 have been obtained at room temperature using the lens version of the Grandjean-Cano method [60]. E7 from BDH is a commercial mixture of 4′-pentyl-, 4′-heptyl-, 4′-octyloxy-, and 4′-(4-pentyl-phenyl)-4-biphenylcarbonitrile in a 51:25:16:8 wt ratio (T_i 60 °C). The standard error of the pitch determination is ca. 10%. The technique is described in detail in ref [61].

Geometry optimization

Calculation of the chirality parameter Q requires the molecular surface, which is generated on the basis of atomic coordinates. Since the chirality of the molecular surface strongly depends on the molecular geometry, accurate structures are needed to obtain reliable estimates of the twisting ability. The geometry of the molecules listed in Table 2 was obtained by quantum mechanical optimization with DFT at the B3LYP/6-31g** level [59].

Chirality parameter and Saupe matrix calculation

The Saupe ordering matrix **S** and the chirality parameter Q of dopants were calculated as explained in refs [31,32]. Once the atomic coordinates were obtained, the molecular surface (the surface generated by rolling a spherical probe on the assembly of van der Waals spheres centred at the nuclear positions and approximated by a set of triangles, obtained with the algorithm developed by Sanner et al. [59]) was computed. The results reported in this work were obtained by setting the orienting strength ξ to 0.025 Å^{-2} and the rolling sphere radius to 3 Å [32]. The van der Waals radii $r_H = 1$ Å, $r_C = 1.85$ Å, $r_O = 1.5$ Å, and $r_{Si} = 2.1$ Å were used [62]. A density of points equal to 5 Å^{-2} was assumed for the molecular surface.

Acknowledgements

References

1. Friedel, G. *Ann. Phys.* **1922,** *18,* 273–474.
2. Pieraccini, S.; Ferrarini, A.; Spada, G. P. *Chirality* **2008,** *20,* 749–759. doi:10.1002/chir.20482
3. Solladié, G.; Zimmermann, R. G. *Angew. Chem., Int. Ed. Engl.* **1984,** *23,* 348–362. doi:10.1002/anie.198403481
4. Eelkema, R.; Feringa, B. L. *Org. Biomol. Chem.* **2006,** *4,* 3729–3745. doi:10.1039/b608749c
5. Irie, M., Ed. Photochromism: memories and switches. *Chem. Rev.* **2000,** *100,* 1683–1890.
6. Spada, G. P.; Proni, G. *Enantiomer* **1998,** *3,* 301–314.
7. di Matteo, A.; Todd, S. M.; Gottarelli, G.; Solladié, G.; Williams, V. E.; Lemieux, R. P.; Ferrarini, A.; Spada, G. P. *J. Am. Chem. Soc.* **2001,** *123,* 7842–7851. doi:10.1021/ja010406r
8. Pieraccini, S.; Donnoli, M. I.; Ferrarini, A.; Gottarelli, G.; Licini, G.; Rosini, C.; Superchi, S.; Spada, G. P. *J. Org. Chem.* **2003,** *68,* 519–526. doi:10.1021/jo020427j
9. Celebre, G.; De Luca, G.; Maiorino, M.; Iemma, F.; Ferrarini, A.; Pieraccini, S.; Spada, G. P. *J. Am. Chem. Soc.* **2005,** *127,* 11736–11744. doi:10.1021/ja051589a
10. Gottarelli, G.; Spada, G. P. *Top. Stereochem.* **2003,** *24,* 425–455. doi:10.1002/0471471895.ch7
11. Kuball, H.-G.; Weiss, B.; Beck, A. K.; Seebach, D. *Helv. Chim. Acta* **1997,** *80,* 2507–2514. doi:10.1002/hlca.19970800818
12. Park, J. J.; Sternhell, S.; Vonwiller, S. C. *J. Org. Chem.* **1998,** *63,* 6749–6751. doi:10.1021/jo980572q
13. Holzwarth, R.; Bartsch, R.; Cherkaoui, Z.; Solladié, G. *Chem.–Eur. J.* **2004,** *10,* 3931–3935. doi:10.1002/chem.200400035
14. Eelkema, R.; Feringa, B. L. *J. Am. Chem. Soc.* **2005,** *127,* 13480–13481. doi:10.1021/ja054352n
15. Yoshida, J.; Sato, H.; Yamagishi, A.; Hoshino, N. *J. Am. Chem. Soc.* **2005,** *127,* 8453–8456. doi:10.1021/ja042549u
16. Eelkema, R.; Pollard, M. M.; Katsonis, N.; Vicario, J.; Broer, D. J.; Feringa, B. L. *J. Am. Chem. Soc.* **2006,** *128,* 14397–14407. doi:10.1021/ja065334o
17. Eelkema, R.; Feringa, B. L. *Org. Lett.* **2006,** *8,* 1331–1334. doi:10.1021/ol060076l
18. Shitara, H.; Aruga, M.; Odagiri, E.; Taniguchi, K.; Yasutake, M.; Hirose, T. *Bull. Chem. Soc. Jpn.* **2007,** *80,* 589–593. doi:10.1246/bcsj.80.589
19. Thompson, M. P.; Lemieux, R. P. *J. Mater. Chem.* **2007,** *17,* 5068–5076. doi:10.1039/b712253e
20. Yoshida, J.; Sato, H.; Hoshino, N.; Yamagishi, A. *J. Phys. Chem. B* **2008,** *112,* 9677–9683. doi:10.1021/jp8011206
21. Schreivogel, A.; Dawin, U.; Baro, A.; Giesselmann, F.; Laschat, S. *J. Phys. Org. Chem.* **2009,** *22,* 484–494. doi:10.1002/poc.1506
22. Berova, N.; Di Bari, L.; Pescitelli, G. *Chem. Soc. Rev.* **2007,** *36,* 914–931. doi:10.1039/b515476f
23. *Circular Dichroism – Principles and Applications,* 2nd ed.; Berova, N.; Nakanishi, K.; Woody, R. W., Eds.; Wiley-VCH: New York, 2000.
24. de Gennes, P. G.; Prost, J. *The Physics of Liquid Crystals;* Oxford University Press: Oxford, 1994.
25. Gossens, W. J. A. *Mol. Cryst. Liq. Cryst.* **1971,** *12,* 237–244. doi:10.1080/15421407108082776
26. Osipov, M. A.; Kuball, H.-G. *Eur. Phys. J. E* **2001,** *5,* 589–598. doi:10.1007/s101890170042
27. Emelyanenko, A. V.; Osipov, M. A.; Dunmur, D. A. *Phys. Rev. E* **2000,** *62,* 2340–2352. doi:10.1103/PhysRevE.62.2340
28. Allen, M. P. *Phys. Rev. E* **1993,** *47,* 4611–4614. doi:10.1103/PhysRevE.47.4611
29. Berardi, R.; Kuball, H.-G.; Memmer, R.; Zannoni, C. *J. Chem. Soc., Faraday Trans.* **1998,** *94,* 1229–1234. doi:10.1039/a708446c
30. Cook, M. J.; Wilson, M. R. *J. Chem. Phys.* **2000,** *112,* 1560–1564. doi:10.1063/1.480703
31. Ferrarini, A.; Moro, G. J.; Nordio, P. L. *Phys. Rev. E* **1996,** *53,* 681–688. doi:10.1103/PhysRevE.53.681
32. Ferrarini, A.; Janssen, F.; Moro, G. J.; Nordio, P. L. *Liq. Cryst.* **1999,** *26,* 201–210. doi:10.1080/026782999205335

33. Gottarelli, G.; Hibert, M.; Samorì, B.; Solladié, G.; Spada, G. P.; Zimmermann, R. *J. Am. Chem. Soc.* **1983**, *105,* 7318–7321. doi:10.1021/ja00363a019

34. Gottarelli, G.; Spada, G. P.; Bartsch, R.; Solladié, G.; Zimmermann, R. *J. Org. Chem.* **1986**, *51,* 589–592. doi:10.1021/jo00355a003

35. Rosini, C.; Franzini, L.; Salvadori, P.; Spada, G. P. *J. Org. Chem.* **1992**, *57,* 6820–6824. doi:10.1021/jo00051a028

36. Rosini, C.; Rosati, I.; Spada, G. P. *Chirality* **1995**, *7,* 353–358. doi:10.1002/chir.530070508

37. Proni, G.; Spada, G. P.; Lustenberger, P.; Welti, R.; Diederich, F. *J. Org. Chem.* **2000**, *65,* 5522–5527. doi:10.1021/jo0001683

38. Pieraccini, S.; Masiero, S.; Spada, G. P.; Gottarelli, G. *Chem. Commun.* **2003**, 598–599. doi:10.1039/b211421f

39. Frank, B. B.; Camafort Blanco, B.; Jakob, S.; Ferroni, F.; Pieraccini, S.; Ferrarini, A.; Boudon, C.; Gisselbrecht, J.-P.; Seiler, P.; Spada, G. P.; Diederich, F. *Chem.–Eur. J.* **2009**, *15,* 9005–9016. doi:10.1002/chem.200900913

40. Deussen, H.-J.; Shibaev, P. V.; Vinokur, R.; Bjørnholm, T.; Schaumburg, K.; Bechgaard, K.; Shibaev, V. P. *Liq. Cryst.* **1996**, *21,* 327–340. doi:10.1080/02678299608032841

41. Li, Q.; Green, L.; Venkataraman, N.; Shiyanovskaya, I.; Khan, A.; Urbas, A.; Doane, J. W. *J. Am. Chem. Soc.* **2007**, *129,* 12908–12909. doi:10.1021/ja0747573

42. Yoshizawa, A.; Kobayashi, K.; Sato, M. *Chem. Commun.* **2007**, 257–259. doi:10.1039/b611538a

43. Kobayashi, K.; Yoshizawa, A. *Liq. Cryst.* **2007**, *34,* 1455–1462. doi:10.1080/02678290701727491

44. Mori, T.; Kyotani, M.; Akagi, K. *Macromolecules* **2008**, *41,* 607–613. doi:10.1021/ma702470t

45. Kawamoto, M.; Aoki, T.; Shiga, N.; Wada, T. *Chem. Mater.* **2009**, *21,* 564–572. doi:10.1021/cm8029032

46. Lemieux, R. P. *Chem. Soc. Rev.* **2007**, *36,* 2033–2045. doi:10.1039/b612122p

47. Gottarelli, G.; Osipov, M. A.; Spada, G. P. *J. Phys. Chem.* **1991**, *95,* 3879–3884. doi:10.1021/j100162a080

48. Moss, G. P. *Pure Appl. Chem.* **1996**, *68,* 2193–2222. doi:10.1351/pac199668122193

49. Gottarelli, G.; Hansen, H.-J.; Spada, G. P.; Weber, R. H. *Helv. Chim. Acta* **1987**, *70,* 430–435. doi:10.1002/hlca.19870700222

50. Pieraccini, S.; Ferrarini, A.; Fuji, K.; Gottarelli, G.; Lena, S.; Tsubaki, K.; Spada, G. P. *Chem.–Eur. J.* **2006**, *12,* 1121–1126. doi:10.1002/chem.200500683

51. Ferrarini, A.; Gottarelli, G.; Nordio, P. L.; Spada, G. P. *J. Chem. Soc., Perkin Trans. 2* **1999**, 411–417. doi:10.1039/a809593k

52. Carreño, M. C.; García-Cerrada, S.; Urbano, A. *J. Am. Chem. Soc.* **2001**, *123,* 7929–7930. doi:10.1021/ja010831k

53. Carreño, M. C.; García-Cerrada, S.; Urbano, A. *Chem.–Eur. J.* **2003**, *9,* 4118–4131. doi:10.1002/chem.200304835

54. Carreño, M. C.; García-Cerrada, S.; Urbano, A. *Chem. Commun.* **2002**, 1412–1413. doi:10.1039/b203509j

55. Carreño, M. C.; Enríquez, Á.; García-Cerrada, S.; Sanz-Cuesta, M. J.; Urbano, A.; Maseras, F.; Nonell-Canals, A. *Chem.–Eur. J.* **2008**, *14,* 603–620. doi:10.1002/chem.200700762

56. Carreño, M. C.; García-Cerrada, S.; Sanz-Cuesta, M. J.; Urbano, A. *Chem. Commun.* **2001**, 1452–1453. doi:10.1039/b103447m

57. Urbano, A. *Angew. Chem., Int. Ed.* **2003**, *42,* 3986–3989. doi:10.1002/anie.200301667

58. *Gaussian 03,* Revision C.02; Gaussian, Inc.: Wallingford, CT, 2004.

59. Sanner, M. F.; Olson, A. J.; Spehner, J.-C. *Biopolymers* **1996**, *38,* 305–320. doi:10.1002/(SICI)1097-0282(199603)38:3<305::AID-BIP4>3.0.CO;2-Y

60. Heppke, G.; Oesterreicher, F. *Z. Naturforsch., A: Phys. Sci.* **1977**, *32,* 899–901.

61. Gottarelli, G.; Samorì, B.; Stremmenos, C.; Torre, G. *Tetrahedron* **1981**, *37,* 395–399. doi:10.1016/S0040-4020(01)92027-7

62. Bondi, A. *J. Phys. Chem.* **1964**, *68,* 441–451. doi:10.1021/j100785a001

A convenient method for preparing rigid-core ionic liquid crystals

Julien Fouchet[1], Laurent Douce[*1], Benoît Heinrich[1], Richard Welter[2] and Alain Louati[3]

Full Research Paper

Address:
[1]Institut de Physique et Chimie des Matériaux de Strasbourg, UMR 7504, DMO, CNRS-Université de Strasbourg, BP 43, 23 rue du Loess, F-67034 Strasbourg Cedex 2, France, [2]Laboratoire DECOMET, UMR CNRS 7177-LC003, Université Louis Pasteur, 4 rue Blaise Pascal, 67000 Strasbourg, France and [3]Laboratoire d'Electrochimie Analytique, Ecole Nationale Superieure de Chimie de Mulhouse, 3 rue Alfred Werner, 68093 Mulhouse Cedex, France

Email:
Laurent Douce[*] - Laurent.Douce@ipcms.u-strasbg.fr

* Corresponding author

Abstract

An efficient, solvent free method for the N-arylation of imidazole by 1-(dodecyloxy)-4-iodobenzene using Cu(II)-NaY as catalyst and K_2CO_3 as base is reported. By this synthetic approach, mesomorphic 3-[4-(dodecyloxy)phenyl]-1-methyl-1*H*-imidazol-3-ium iodide was synthesized in a two-step procedure, and its mesomorphism has been fully investigated by polarised optical microscopy, differential scanning calorimetry and X-ray diffraction. In addition its lamellar crystal structure, electrochemical behaviour and UV (absorption and emission) properties are reported.

Introduction

Over the past decade extensive studies of ionic liquids (ILs) have revealed their many useful properties such as extremely low volatility, high thermal stability, non-flammability, high chemical and radiochemical stability, high ionic conductivity and wide electrochemical window [1-3]. In addition, the ILs have been used as reaction media increasing the yields of many syntheses and eliminating the hazards associated conventional solvents [4]. Thus are extremely versatile in that changes in both the cation and its counter anion can be used to finely tune their properties (for example: viscosity, melting point, polarity, hydrophilicity/hydrophobicity…). Important emerging applica-

tions include those in separation and extraction processes, and in various electrochemical devices, such as lithium ion batteries, fuel cells, and capacitors, as well as in synthesis and catalysis [1-5].

Liquid crystals are characterised by both mobility and self-organisation at the macroscopic level [6]. Almost all such meso-morphic materials are based on molecules combining two antagonistic units consisting of rigid (aromatic) and flexible (alkyl) or hydrophilic (polar heads) and hydrophobic (alkyl chains) parts. The subtle balance of their effects governs the

formation of a multitude of supramolecular architectures depending on the temperature (thermotropic liquid crystals) and/or of the solvent (lyotropic liquid crystals) [7,8]. In the case of the thermotropic liquid crystals the arrangements give rise to nematic phases (molecules are aligned along an orientational axis), smectic phases (orientational/positional order in the layers) and columnar phases (orientational/positional order in the columns). The lyotropic compounds display not only lamellar and columnar organization but also hierarchical self-assembly in spheres (micelles), ribbons and fibres. These unique properties lead to their applications ranging from display technology through templating media for synthesis to biological activity (targeting and transporting of drugs and gene materials) [9].

Full convergence of the ionic liquid and liquid crystal fields could provide a vast range of materials (Ionic liquid crystals, ILCs) with novel and tunable characteristics such as those of ordered and oriented hybrid compound semiconductors exhibiting both electronic and ionic conductivity [10]. For this, the imidazolium unit is an excellent platform that can be designed to promote liquid crystalline phases and easily be doped by a large diversity of anions [11-21]. Variation of the N-substituents by Ullman coupling to extend the aromatic part is a facile means of creating this range [22,23].

Herein, we wish to report a solvent-free, N-arylation of imidazole as a means of expanding the aromatic core and obtaining unsymmetrical imidazolium liquid crystals (Scheme 1). We also describe the influence of the counter anion on the mesomorphism, electrochemistry and the UV properties of these imidazolium salts.
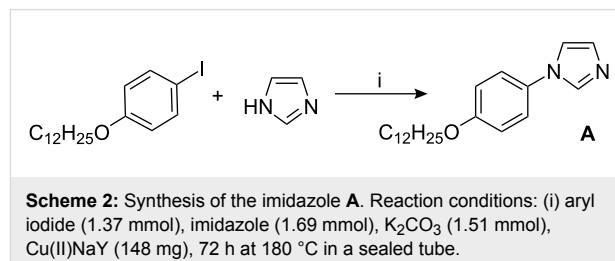

Scheme 1: 1-[4-(dodecyloxy)phenyl]-3-methyl-1*H*-imidazol-3-ium mesogenic salts.
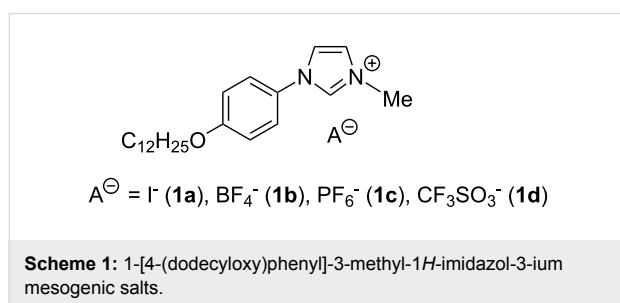
Results and Discussion
Synthesis and characterization

Compound **1a** was obtained in a two-step procedure. The first step was a coupling reaction between 1-(dodecyloxy)-4-iodobenzene and imidazole using Cu(II)-NaY as catalyst in the presence of potassium carbonate as base [23]. The reaction took place without solvent at 180 °C in a sealed tube over 72 h to afford 1-[4-(dodecyloxy)phenyl]-1*H*-imidazole (**A**) in a good

(<80%) and reproducible yield (Scheme 2). Swager has already published the synthesis of compound **A** under standard Ullman conditions (K_2CO_3, CuI, L-proline in DMSO, 16 h at 110 °C) [22].

Scheme 2: Synthesis of the imidazole **A**. Reaction conditions: (i) aryl iodide (1.37 mmol), imidazole (1.69 mmol), K_2CO_3 (1.51 mmol), Cu(II)NaY (148 mg), 72 h at 180 °C in a sealed tube.

The aryl-imidazole **A** was purified by column chromatography (ethyl acetate as eluent) on silica and characterized spectroscopically. The second step involved alkylation of **A** by iodomethane to give salt **1a** in 89% yield after purification (Scheme 3). Distinctive signals for the CH (1*H*-imidazolium) group appear in the ^1H and ^{13}C NMR spectra at 10.45 ppm and 134.97 ppm respectively.

Scheme 3: Synthesis of methyl imidazolium **1a**. Reaction conditions: (i) MeI in sealed tube, 54 h at RT.
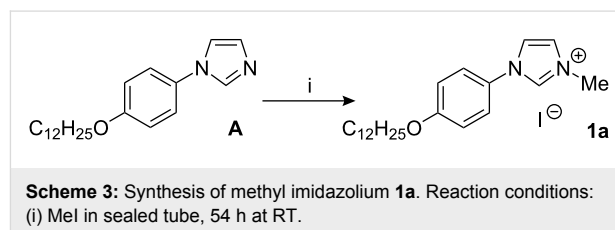
Single crystals of **1a** suitable for X-ray diffraction were obtained by slow diffusion of ether into a CH_2Cl_2 solution. The compound **1a** crystallizes in the triclinic space group *P*1. A partly labelled ORTEP view showing non-classical hydrogen bonds and C-H..π interactions is given in Figure 1 (the interactions also being listed in Table 1). The alkyloxy chains are quite parallel, as is clear from the crystal packing given in Figure 2, with segregation between the rigid part (including iodine atoms) and the alkyloxy chains ($\approx$20 Å, see Figure 2). The length of the molecule in the crystalline state is about 24 Å.

It should be emphasised that the lattice area (A = a·b·sin(γ) = $2V/d_{001}$ = 57.1 Å^2) is about three times the transverse area of an all-trans crystallised chain and that even so the alkyl tails organise in segregated double layers, without interdigitation but with a tilt angle of 71° with respect to the layer normal. This large tilt angle just compensates the discrepancy between areas, maintaining the compactness of the packing and the flatness of the segregated ionic and aliphatic double layers. Apart from the crystallised state of the tails, this structure is very close to a smectic type of organisation. The segregation between the alkyl
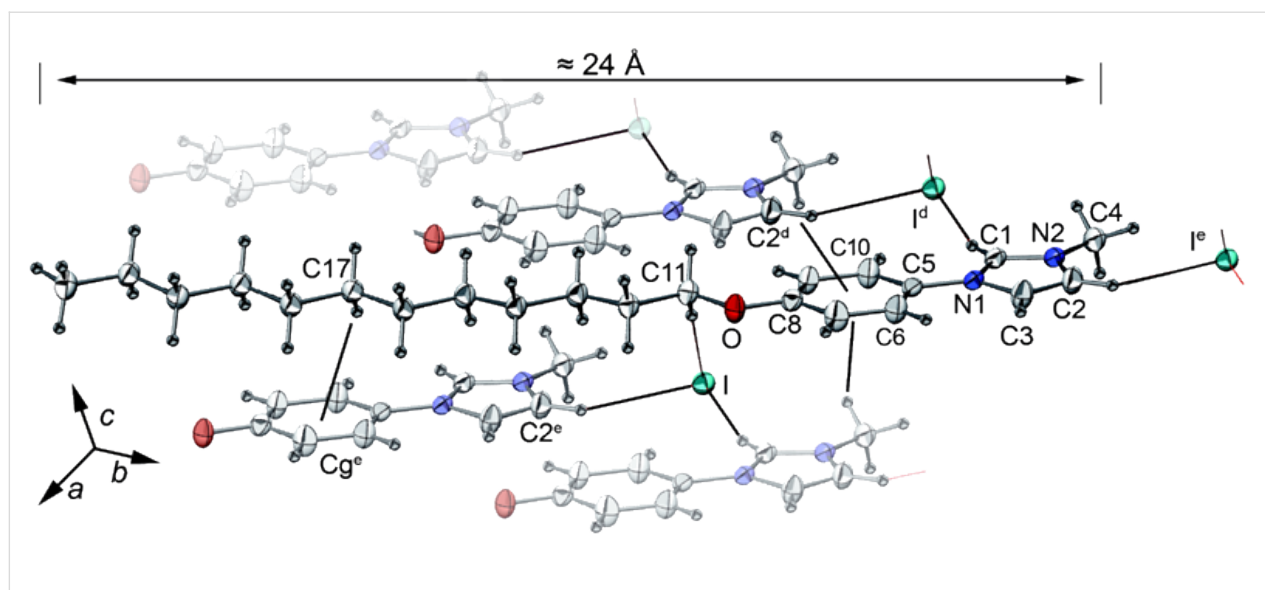
Figure 1: ORTEP view of compound **1a** with partial labelling. The closest molecules are represented (with lower opacity) when connected by CH-π and/or non classical H-bonds (black thin lines). The ellipsoids enclose 50% of the electronic density. Symmetry operators for equivalent positions: [d] = ±1+x, y, z; [e] = 1+x, 1+y, z.

Table 1: Non-classical hydrogen bonds and CH..π interactions[a] occurring in **1a**. **Cg** is the phenyl ring (C5 to C10). Symmetry operators for equivalent positions: [d] = ±1+x, y, z; [e] = 1+x, 1+y, z.

C-H..I	d_{C-H} (Å)	d_{H-I} (Å)	d_{C-I} (Å)	C-H-I (°)
C1-H1..I[d]	0.95	2.8270	3.746(5)	163.1
C2-H2..I[e]	0.95	2.9123	3.822(5)	160.6
C11-H11B..I	0.95	3.0026	3.992(5)	179.2
C-H..Cg	d_{C-H} (Å)	d_{H-Cg} (Å)	d_{C-I} (Å)	C-H-Cg (°)
C4-H4A..Cg[d]	0.95	3.109	3.502	105.6
C4-H4B..Cg[d]	0.95	3.309	3.502	93.1
C17-H17B..Cg[e]	0.95	3.310	4.207	151.5

[a]Platon software [24].

tails and the charged rigid parts indicates that by melting the chains they could show liquid crystal behaviour at a higher temperature. In order to understand the influence of the anion on the electrochemical, UV properties and mesomorphism, we prepared compounds with BF_4^- (**1b**), PF_6^- (**1c**), $CF_3SO_3^-$ (**1d**) and $(CF_3SO_2)_2N^-$ (**1e**) anions in excellent yield by anion metathesis in water/CH_2Cl_2 as solvent (Scheme 4).

All these compounds were fully characterized by ^{1}H NMR, ^{13}C NMR {[1]H}, FT-IR and UV spectroscopy, as well as elemental analysis. The IR spectra showed typical anion vibrations at 1024 cm^{-1} (**1b** BF_4^-), 826 cm^{-1} (**1c** PF_6^-), 1269 and 1028 cm^{-1} (**1d** $CF_3SO_3^-$), 1358 and 1183 cm^{-1} (**1e** $(CF_3SO_2)_2N^-$). ^{1}H NMR spectra were recorded in CDCl$_3$, in which the chemical shift for the CH (1*H*-imidazolium) is very

dependent upon the anion, with δ 10.45 (**1a**) 9.37 (**1b**), 9.10 (**1c**), 9.41 (**1d**) and 8.98 ppm (**1e**). This dependency is certainly due to the interactions though H-bonding and the charge localisation on the anion. The UV spectra displays typical charge transfer (π–π* or n–n*) transitions in CH_2Cl_2 at 240 nm (**1a** ε = 24000 M^{-1} cm^{-1}), 255 nm (**1b** ε = 10500 M^{-1} cm^{-1}), 249 nm (**1c** ε = 11700 M^{-1} cm^{-1}), 256 nm (**1d** ε = 10100 M^{-1} cm^{-1}) and 255 nm (**1e** ε = 11100 M^{-1} cm^{-1}). A blue emission was also observed at 384 nm (Figure 3).

Investigation of the Liquid Crystalline Behaviour

The thermogravimetric analysis of compounds **1a–e** showed the general stability order to be I[-]< BF_4^- ≈ PF_6^-< $CF_3SO_3^-$< $(CF_3SO_2)_2N^-$ (Figure 4).
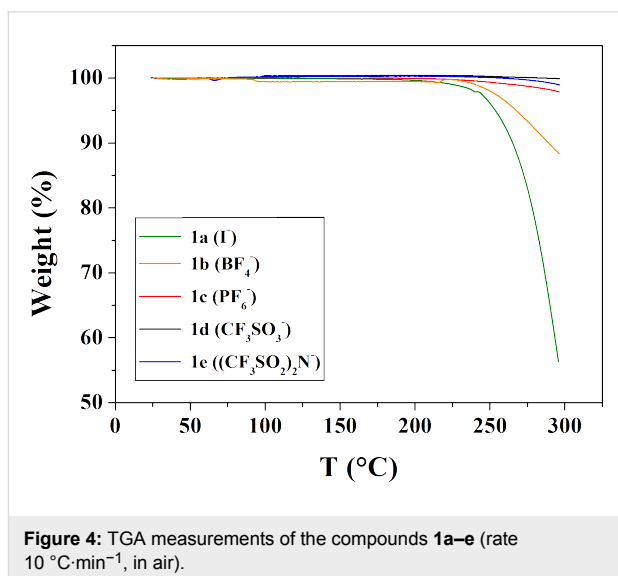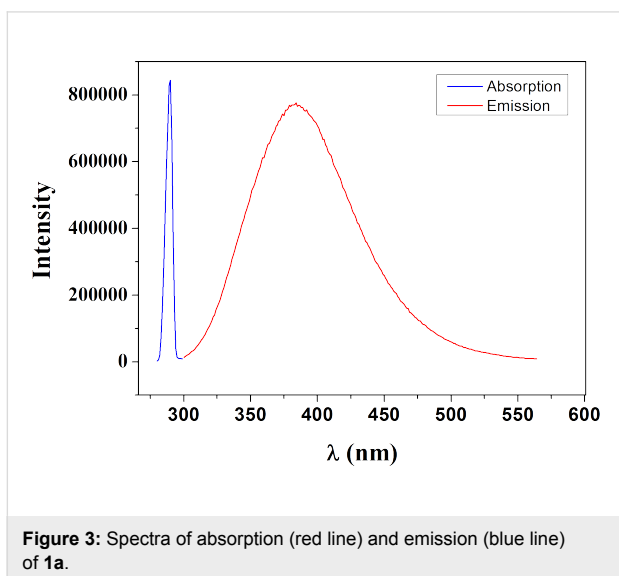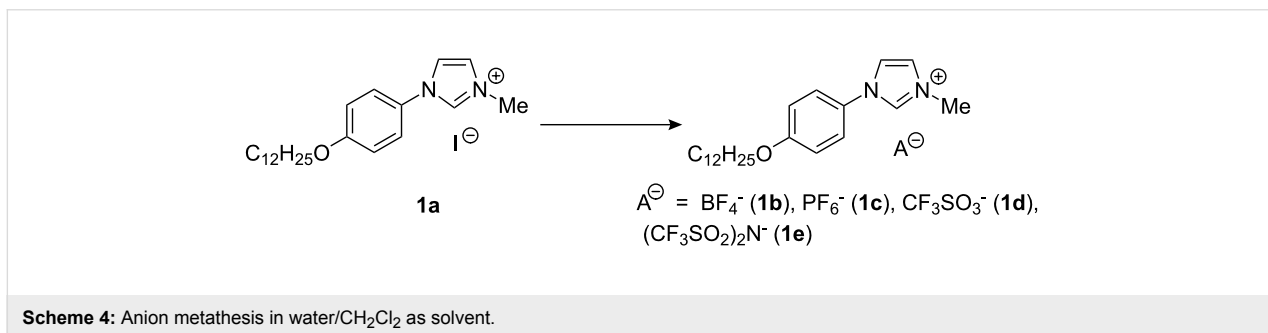
Figure 2: Packing diagram of compound **1a** in projection in the (b,c) lattice plane. Large spheres represent the iodine atoms.

Scheme 4: Anion metathesis in water/CH$_2$Cl$_2$ as solvent.

Figure 3: Spectra of absorption (red line) and emission (blue line) of **1a**.

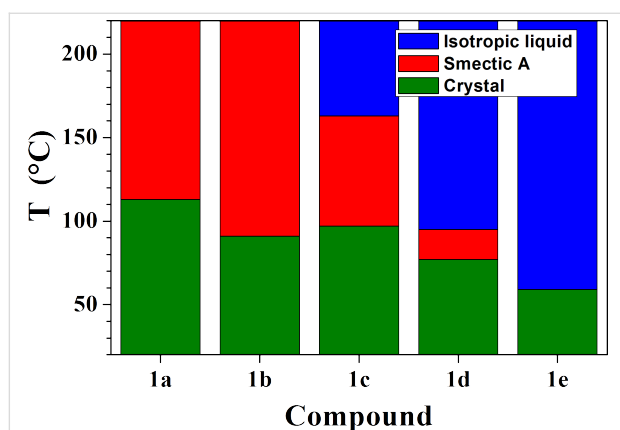**Figure 4:** TGA measurements of the compounds **1a–e** (rate 10 °C·min^{-1}, in air).
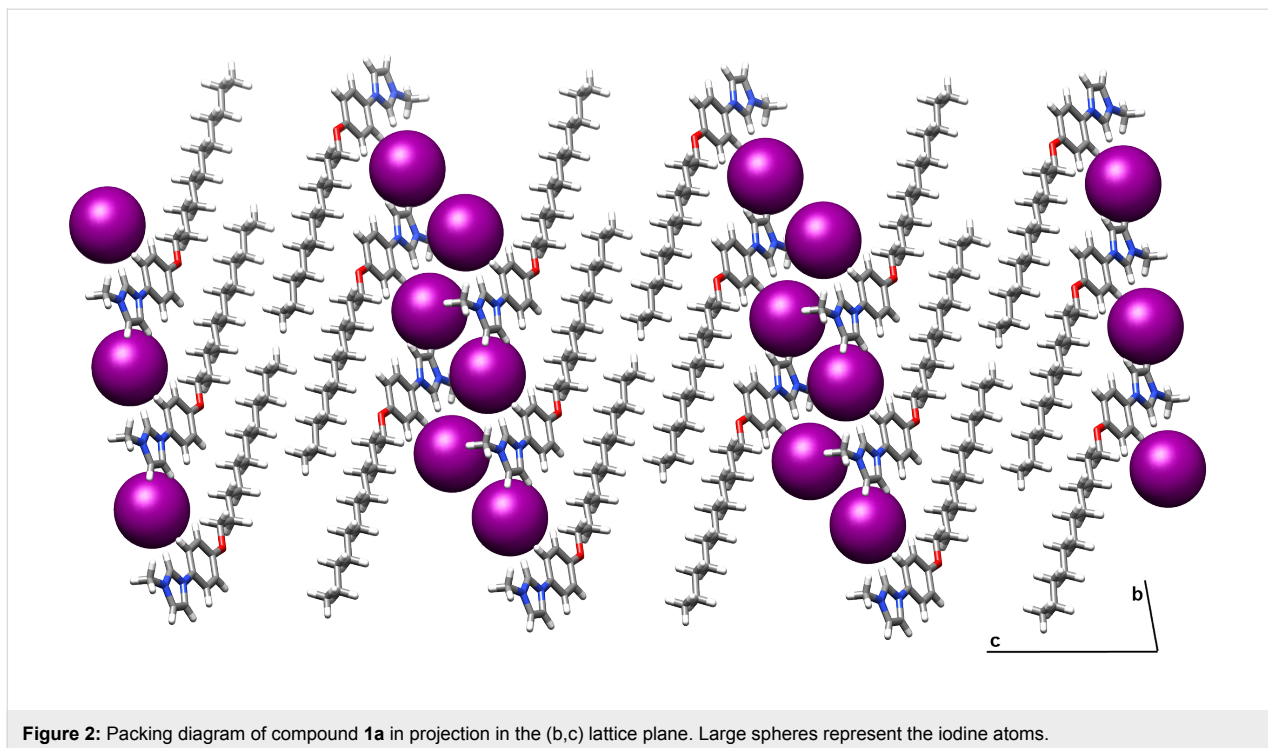
Table 2: Phase transition temperatures and corresponding enthalpies determined from the 2nd heating and cooling.

Anions	Phase	Cr → Temperature → LC	Phase	LC → Temperature → I	Phase
I$^-$	Crystal	113 °C (15.83 kJ/mol) / 81 °C (12.76 kJ/mol)	Smectic A	250 °C	Decomposition
BF$_4^-$	Crystal	91 °C (30.08 kJ/mol) / 60 °C (10.62 kJ/mol)	Smectic A	230 °C	Decomposition
PF$_6^-$	Crystal	97 °C (36.21 kJ/mol) / 68 °C (43.34 kJ/mol)	Smectic A	163 °C (1.12 kJ/mol) / 163 °C (1.76 kJ/mol)	Liquid
F$_3$CO$_3^-$	Crystal	77 °C (43.28 kJ/mol) / 49 °C (44.00 kJ/mol)	Smectic A	95 °C (0.79 kJ/mol) / 95 °C (1.04 kJ/mol)	Liquid
(F$_3$CSO$_2$)$_2$N$^-$	Crystal	59 °C (61.17 kJ/mol) / 39 °C (61.12 kJ/mol)	Liquid		

Legend: Cr: Crystal, LC: Liquid Crystal, I: Isotropic Liquid.

For all the compounds, the mesomorphic behaviour and phase transition temperatures were investigated by polarized optical microscopy (POM), differential scanning calorimetry (DSC), and powder X-ray diffractometry (XRD). To avoid possible effects of hydration of the materials, all were dried in vacuo before X-ray and DSC analyses. The phase transition temperatures and the corresponding enthalpy changes derived for compounds **1a–e** are compiled in Table 2, while typical results are displayed in Figure 5.

The high stability of the compounds was also demonstrated by the absence of significant perturbation of the DSC patterns following several heating–cooling cycles. Compounds **1e**, not unexpectedly, do not show thermotropic behaviour, while the data for **1a–d** give an order of anion stabilisation of liquid crystal behaviour of Br$^-$ > BF$_4^-$ > PF$_6^-$ > CF$_3$SO$_3^-$ (see Figure 5).

The optical textures observed during slow cooling from isotropic melt showed the emergence of a smectic A phase (appearance of Batônnet rods, turning into a wide, fan-like, focal-conic texture). The smectic structure of the liquid crystal phase was confirmed by XRD. The X-ray pattern (Figure 6) of the Smectic A form recorded at 120 °C contains a diffuse band at 4.6 Å (wide angle), which shows clearly that the alkyl chains have a liquid-like structure and are segregated from the aromatic cores.

The layer thickness in the Smectic A phase was determined from the position of the sharp reflection in the small angle region (d = 39.8 Å at 120 °C) and corresponds to the alternation between the sublayer formed by the molten chains and the sublayer formed by the ionic double layer and the mesogenic

Figure 5: Phase transition temperatures of compounds **1a–e**.
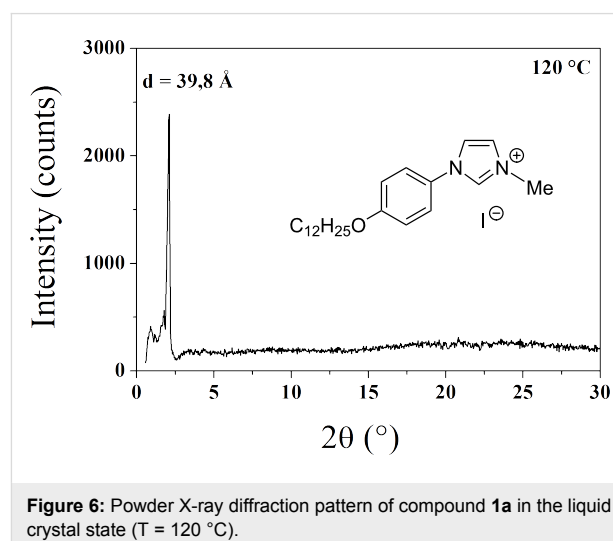
Figure 6: Powder X-ray diffraction pattern of compound **1a** in the liquid crystal state (T = 120 °C).
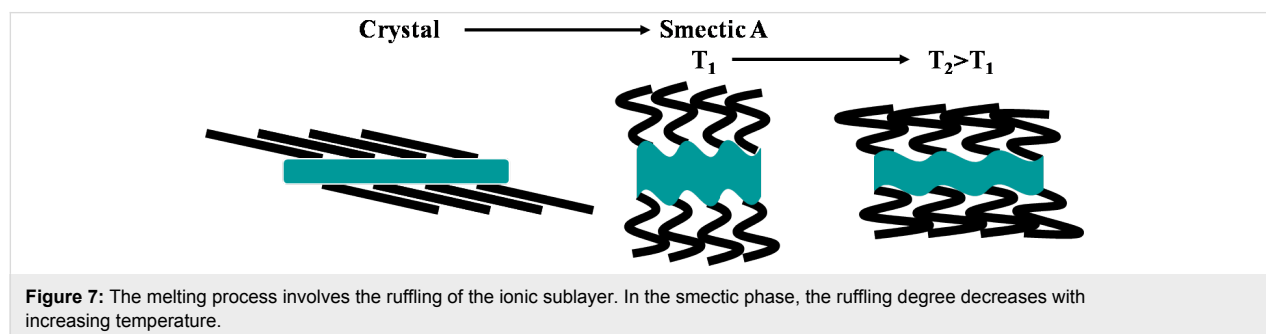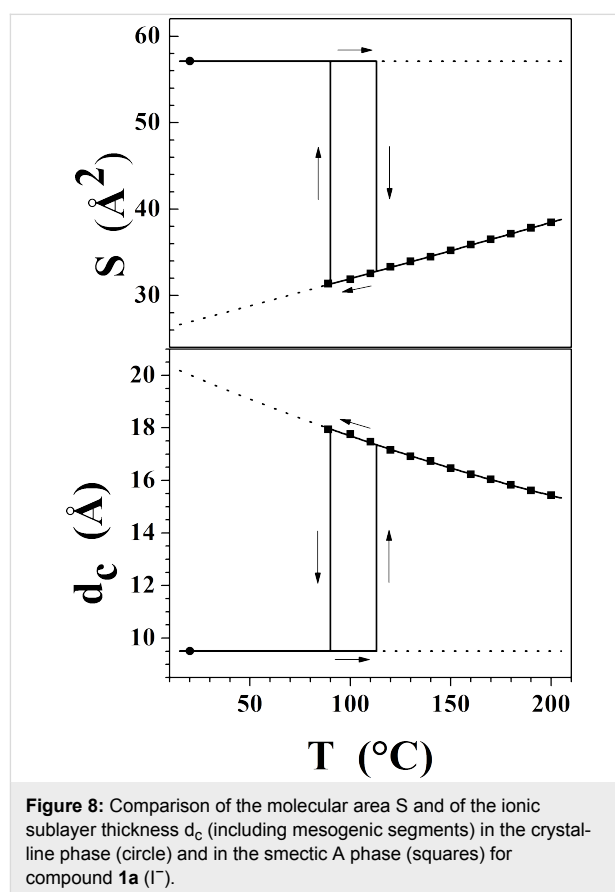
parts. The thickness of the corresponding sublayers' alternation in the crystalline phase is given by the location of the d_{001} reflection (d_{001} = 20.21 Å from single crystal pattern at room temperature). Despite the enormous difference in layer thicknesses between both phases (the extrapolation of the variation versus temperature gives d = 46.5 Å at 20 °C *i.e.* more than twice d_{001}), the difference in molecular volume (smectic phase: V_{mol} = 622 Å^3 at 20 °C; crystalline phase: V_{mol} = V/2 = 577 Å^3) just coincides with the contribution of the chain melting [25,26], indicating that the partial volume of the ionic sublayer does not change significantly between both phases. The observed layer thickness change is therefore the consequence of the different "molecular areas" S, i.e. the projection area of a mesogen counter-ion assembly within the mean smectic plane (S = $2V_{mol}$/d), which is identical to the lattice area in the crystalline phase (S = V/d_{001}). Thus, since no significant volume change is involved in the shrinking of S from 57.1 Å^2 in the crystalline phase to 27 Å^2 in the smectic A phase (value at 20 °C obtained from the extrapolation of the variation of S versus temperature), the ionic sublayer thickness d_c (determined as dc = 2[V_{mol}/−V_{ch}]/S, V_{ch} being the chain volume) simultaneously expands in proportion (from 9.5 Å in the crystalline phase to 20 Å in the smectic phase at 20 °C). These lateral shrinkage and longitudinal extension events are the result of a ruffling process of the ionic sublayers, starting from the completely flat state in the crystalline phase shown by the single crystal structure (see Figure 7).

The maximum degree of ruffling in the smectic A phase is reached just before crystallisation, since the experimental temperature dependence of S and d_c indicates that the sublayers continuously spread with increasing temperature (see Figure 8).

The counter-ion substitution within the series 1 involves large changes of S, but the temperature dependence and dc values are roughly the same for all terms (see Figure 9).

The influence of the substitution can therefore be considered as an anion size effect, since the lattice area expands with increasing counter-ion bulkiness without change of the degree of ruffling (the small discrepancies for compound **1d** ($CF_3SO_3^−$) being explained by the presence of the CF_3 lateral group, which contributes to d_c and perturbates slightly the interface with the aliphatic sublayer). It should be emphasised that the stability of the smectic A phase is not determined by the degree of ruffling of the ionic sublayer but by the folding degree of the tails and therefore the thickness of the aliphatic sublayers. Thus, depending upon the anion size, the isotropisation occurs at various temperatures, but for approximately the same maximum molecular area (S^{max} ≈ 41 Å^2) and therefore similar minimum aliphatic sublayer thicknesses (d_{ch}^{min} ≈ 19 Å).

Figure 8: Comparison of the molecular area S and of the ionic sublayer thickness d_c (including mesogenic segments) in the crystalline phase (circle) and in the smectic A phase (squares) for compound **1a** (I$^−$).

Figure 7: The melting process involves the ruffling of the ionic sublayer. In the smectic phase, the ruffling degree decreases with increasing temperature.
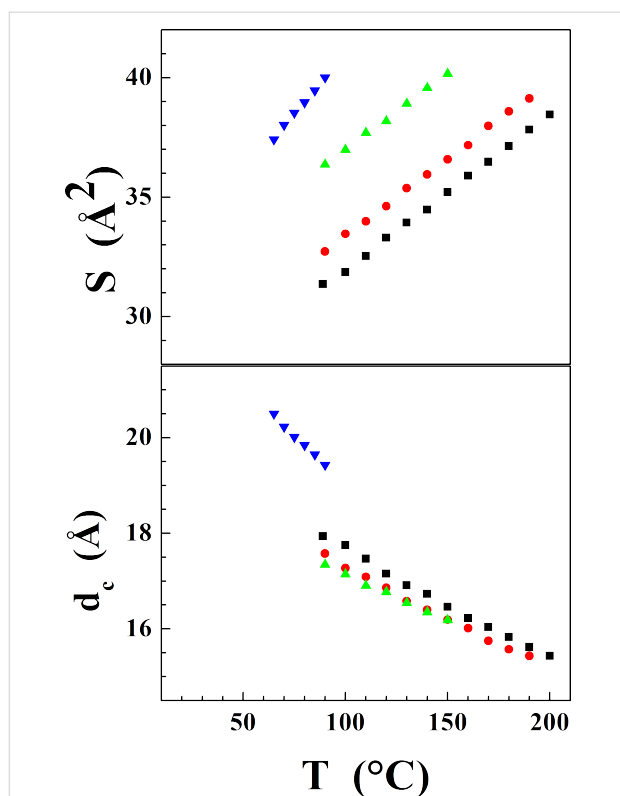
Figure 9: Variation with the counter-ion of the molecular area S and of the ionic sublayer thickness d_c (including mesogenic segments) in the smectic A phase for series 1: squares: **1a** (I^-); circles: **1b** (BF_4^-); up triangles: **1c** (PF_6^-); down triangles: **1d** ($CF_3SO_3^-$).

packing is reached. In the smectic phase, tail tilting is not favourable upon the amphipathic expelling at the interface with the ionic sublayer and the system adopts a compromise molecular area associating ruffled ionic sublayers and folded aliphatic tails. With increasing temperature, the aliphatic chains spread more easily and the organisation shifts toward flat sublayers. A more detailed investigation of the molecular area variation in series involving both, counter-ion substitution and tail-length variation, has been presented elsewhere for a very similar cationic structure [20,25,26].

Electrochemical behaviour

Cyclic voltammetry was used to determine the electrochemical behaviour of the compounds **1a**, **1b** and **1c**, the voltammograms being recorded in CH_3CN solutions containing 0.1 M NBu_4PF_6 as supporting electrolyte at a platinum working electrode. The peak potentials are given vs. a SCE. Representative cyclic voltammograms of **1a** are shown in Figure 10. The anodic portion of the voltage scan displays two oxidation steps having peak potentials of 0.42 V and 0.68 V, and likely involve the formation of I_2 and possibly then a higher-oxidation-state iodine (I_3^-) species. As seen for **1a** (Figure 9), for **1b** and **1c** the cathodic portion of the voltage scan displays only an irreversible reduction step at ca 1.58 V, which corresponds to the reduction of the cationic imidazolium species. Note that the peak at −0.8 V is probably due to the reduction of O_2 which is difficult to eliminate from the solution.

To summarise, the large discrepancy between the lattice area and the cross section of the aliphatic chains are taken into account differently in the crystalline and in the smectic molecular organisations. In the crystalline phase, the ionic sublayers just impose their area and the tails tilt until dense

Conclusion

In conclusion, we report synthetic methodology based on Ullman coupling to extend the imidazolium aromatic core. From this coupling product we have synthesized and fully characterized new mesomorphic compounds with different anions.
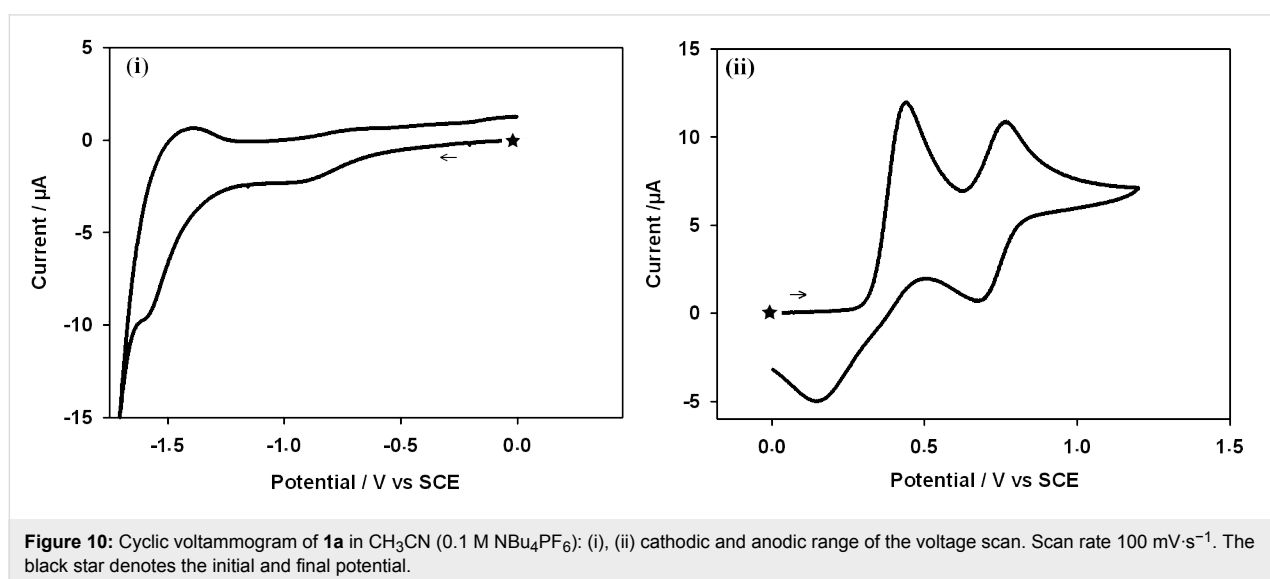

Figure 10: Cyclic voltammogram of **1a** in CH_3CN (0.1 M NBu_4PF_6): (i), (ii) cathodic and anodic range of the voltage scan. Scan rate 100 mV·s^{-1}. The black star denotes the initial and final potential.

We have also determined a structure by X-ray diffraction on a single crystal. The crystallisation shows the completely lamellar segregation between the flexible chains and the rigid part. The layers are linked to each other by the semi-interdigitation of alkyl tails. Despite an enormous difference between the cross-section of crystallised chains and the lattice area imposed by the organisation within the ionic sublayers, the latter just remain flat and the tails undergo a double layer dense packing with 71° tilting with respect to the layer normal. In the smectic phase, area matching is achieved by ruffling of the sublayers and folding of the molten aliphatic tails, the degree of ruffling decreasing with increasing temperature. The electrochemical windows have been measured and we are attempting to measure the carrier mobility in order to fully assess the prospects for using these molecules in molecular electronics. We intend also to introduce different length tails in order to obtain room temperature ionic liquid crystals, aswell as to explore use of the coupling reaction between imidazole and other aromatics and heterocycles to tune the electronic properties.

Experimental

X-ray diffraction pattern of powder samples in Lindeman capillaries or sealed cells were measured in transmission by using a focused $CuK_{\alpha 1}$ linear beam, temperature control being within 0.03 °C and acquisition being conducted with an Inel CS120 curved counter. The molecular volumes of all compounds were calculated with an accuracy of 0.5% from the measurements performed for an analogous compound [26] and from the methylene and counter ion partial volumes.

All reagents were purchased from commercial suppliers and used without further purification. Chromatography was carried out with Merck silica gel 60 (40–63 mm). Analytical TLC was performed with Merck silica gel 60 F254 aluminium sheets. ^{1}H NMR and ^{13}C NMR (300 MHz and 75 MHz respectively) spectra were recorded with a Bruker Avance 300 spectrometer at 25 °C. Chemical shifts, δ, are reported in ppm using TMS as internal standard, spin-spin coupling constants, *J*, are given in Hz and the abbreviations s, br, s, t, q, m were used to denote respectively the multiplicity of signals: singlet, broad singlet, triplet, quadruplet, multiplet. Infrared spectra were recorded (KBr pastille) with a spectrophotometer IR Digital FTS 3000. UV/Vis spectra were recorded with a spectrophotometer U-3000. Elemental analyses were performed by the analytical service at the Institut Charles Sadron and by the analytical service at the Université de Strasbourg (Strasbourg, France). The optical structures of mesophases were studied with a Leitz polarizing microscope equipped with a Mettler FP80 hot stage and an FP80 central processor. The TGA measurements were carried out on a SDTQ 600 apparatus at scanning rate of 10 °C·min^{-1}. The transition temperatures and enthalpies were measured by differential scanning calorimetry with a DSC Q1000 from TA Instruments at different temperature rates (5 °C·min^{-1}, 2 °C·min^{-1}) on heating and cooling.

1-[4-(Dodecyloxy)phenyl]-1*H*-imidazole (**A**)

1-Dodecyloxy-4-iodobenzene (0.533 g, 1.37 mmol), imidazole (0.115 g, 1.69 mmol), K_2CO_3 (0.288 g, 1.51 mmol) and Cu(II)-NaY (0.148 g) were heated in sealed tube to 180 °C for 72 h. The reaction mixture was filtered to remove the catalyst and the filtrate was purified by column chromatography (silica gel, ethyl acetate) to afford pure **A** (0.378 g, 84%).

^{1}H NMR (300 MHz, CDCl$_3$): δ = 0.88 (t, 3H, *J* = 6.5 Hz, CH$_3$ aliphatic chain), 1.27 (broad s, 16H, CH$_2$ aliphatic chain), 1.42–1.49 (m, 2H, O-CH$_2$-CH$_2$-CH$_2$), 1.75–1.84 (m, 2H, O-CH$_2$-CH$_2$), 3.98 (t, 2H, *J* = 6.6 Hz, O-CH$_2$), 6.96 and 7.27 (AA′ and BB′, 2 × 2H, *J* = 9.0 Hz, CH phenyl), 7.17–7.19 (m, 2H, N-CH-CH-N), 7.75 (broad s, 1H, N-CH-N). ^{13}C NMR (75 MHz, CDCl$_3$): δ = 14.03 (CH$_3$ aliphatic), 22.61, 25.94, 29.13, 29.27, 29.30, 29.50, 29.52, 29.57, 29.59, 31.84 (CH$_2$ aliphatic), 68.40 (O-CH$_2$), 115. 39 (CH phenyl), 118.67 (CH imidazolium), 123.09 (CH phenyl), 129.97 (CH imidazolium), 130.47 (N-C phenyl), 135.79 (CH imidazolium), 158.48 (C-O-CH$_2$ phenyl). v_{max}/cm^{-1} 3118 (C-H aromatic), 2921 and 2851 (C-H aliphatic), 1520 (C=C aromatic), 1243 (C-O aromatic). UV/Vis (CH$_2$Cl$_2$): λ$_{max}$ (ε, L·mol^{-1}·cm^{-1}) = 241 nm (15000). Elemental analysis for C$_{21}$H$_{32}$N$_2$O, Cacld: C, 76.78; H, 9.82; N, 8.53%. Found: C, 76.96; H, 10.58; N, 8.57%.

1-[4-(Dodecyloxy)phenyl]-3-methyl-1*H*-imidazol-3-ium iodide (**1a**)

A mixture of **A** (1.069 g, 3.25 mmol) and iodomethane (2 mL, 31.80 mmol) was stirred in a sealed tube for 54 h and was heated to 40 °C for 10 minutes. Diethyl ether was added and the reaction mixture was filtered and the solid was washed with diethyl ether. Crystallization with dichloromethane and diethyl ether gave de **1a** (1.318 g, 89%).

^{1}H NMR (300 MHz, CDCl$_3$): δ = 0.89 (t, 3H, *J* = 6.9 Hz, CH$_3$ aliphatic chain), 1.28 (broad s, 16H, CH$_2$ aliphatic chain), 1.41–1.48 (m, 2H, O-CH$_2$-CH$_2$-CH$_2$), 1.76–1.85 (m, 2H, O-CH$_2$-CH$_2$), 3.99 (t, 2H, *J* = 6.6 Hz, O-CH$_2$), 4.27 (s, 3H, N-CH$_3$), 7.04 and 7.66 (AA′ and BB′, 2 × 2H, *J* = 9.1 Hz, CH phenyl), 7.46–7.48 (m, 2H, N-CH-CH-N), 10.45 (broad s, 1H, N-CH-N). ^{13}C NMR (75 MHz, CDCl$_3$): δ = 14.01 (CH$_3$ aliphatic), 22.58, 25.89, 29.00, 29.25, 29.29, 29.48, 29.51, 29.54, 29.57, 31.82 (CH$_2$ aliphatic), 37.57 (N-CH$_3$), 68.65 (O-CH$_2$), 115. 99 (CH phenyl), 121.03 (CH imidazolium), 123.65 (CH phenyl), 124.42 (CH imidazolium), 127.05 (N-C phenyl), 135.49 (CH imidazolium), 160.47 (C-O-CH$_2$ phenyl). v_{max}/cm^{-1} 3131 (C-H aromatic), 2921 and 2851 (C-H

aliphatic), 1514 (C=C aromatic), 1251 (C-O aromatic). UV–vis (CH$_2$Cl$_2$): λ$_{max}$ (ε, L·mol^{-1}·cm^{-1}) = 240 nm (24000). Elemental analysis for C$_{22}$H$_{35}$IN$_2$O·1/4H$_2$O, Calcd: C, 55.64; H, 7.53; N, 5.90%. Found: C, 55.78; H, 7.48; N, 5.34%.

General procedure for metathesis in water–anion exchange

A mixture of **1a** dissolved in dichloromethane (4 mL) and a mixture of the corresponding salts dissolved in water (3 mL) were stirred together for 140 h. The organic layer was separated off, washed with water and dried over calcium chloride. Crystallization with dichloromethane and diethyl ether gave the corresponding imidazolium salt.

1-[4-(Dodecyloxy)phenyl]-3-methyl-1*H*-imidazol-3-ium tetrafluoroborate (**1b**)

Following the general procedure using **1a** (0.797 g, 1.69 mmol) and sodium tetrafluoroborate (0.511 g, 4.56 mmol) provided **1b** with a yield of 72% (0.525 g, 1.22 mmol).

^{1}H NMR (300 MHz, CDCl$_3$): δ = 0.86 (t, 3H, *J* = 6.3 Hz, C*H*$_3$ aliphatic chain), 1.28 (broad s, 16H, C*H*$_2$ aliphatic chain), 1.41–1.46 (m, 2H, O-CH$_2$-CH$_2$-C*H*$_2$), 1.75–1.84 (m, 2H, O-CH$_2$-C*H*$_2$), 3.98 (t, 2H, *J* = 6.3 Hz, O-C*H*$_2$), 4.11 (s, 3H, N-C*H*$_3$), 7.02 and 7.53 (AA′ and BB′, 2 × 2H, *J* = 9.0 Hz, C*H* phenyl), 7.48 (broad s, 2H, N-C*H*-C*H*-N), 9.37 (broad s, 1H, N-C*H*-N). ^{13}C NMR (75 MHz, CDCl$_3$): δ = 14.07 (*C*H$_3$ aliphatic), 22.65, 25.95, 29.08, 29.32, 29.37, 29.55, 29.59, 29.61, 29.64, 31.89 (*C*H$_2$ aliphatic), 36.81 (N-*C*H$_3$), 68.65 (O-*C*H$_2$), 115. 96 (*C*H phenyl), 121.34 (*C*H imidazolium), 123.59 (*C*H phenyl), 124.50 (*C*H imidazolium), 127.24 (N-*C* phenyl), 134.97 (*C*H imidazolium), 160.47 (*C*-O-CH$_2$ phenyl). ν$_{max}$/cm^{-1} 2917 and 2849 (C-H aliphatic), 1514 (C=C aromatic), 1249 (C-O aromatic), 1024 (BF$_4^-$). UV–vis (CH$_2$Cl$_2$): λ$_{max}$ (ε, L·mol^{-1}·cm^{-1}) = 255 nm (10500). Elemental analysis for C$_{22}$H$_{35}$BF$_4$N$_2$O·3/4H$_2$O, Calcd: C 59.53, H 8.29, N 6.31%. Found: C 59.74, H 8.02, N 6.20%.

1-[4-(Dodecyloxy)phenyl]-3-methyl-1*H*-imidazol-3-ium hexafluorophosphate (**1c**)

Following the general procedure using **1a** (0.695 g, 1.48 mmol) and potassium hexafluoroborate (0.518 g, 2.18 mmol) provided **1c** with a yield of 84% (0.607 g, 1.24 mmol).

^{1}H NMR (300 MHz, CDCl$_3$): δ = 0.89 (t, 3H, *J* = 6.8 Hz, C*H*$_3$ aliphatic chain), 1.28 (broad s, 16H, C*H*$_2$ aliphatic chain), 1.41–1.46 (m, 2H, O-CH$_2$-CH$_2$-C*H*$_2$), 1.76–1.85 (m, 2H, O-CH$_2$-C*H*$_2$), 3.98 (t, 2H, *J* = 6.6 Hz, O-C*H*$_2$), 4.07 (s, 3H, N-C*H*$_3$), 7.02 and 7.48 (AA′ and BB′, 2 × 2H, J = 8.8 Hz, C*H* phenyl), 7.45 (broad s, 2H, N-C*H*-C*H*-N), 9.10 (broad s, 1H, N-C*H*-N). ^{13}C NMR (75 MHz, CDCl$_3$): δ = 14.06 (*C*H$_3$

aliphatic), 22.65, 25.95, 29.08, 29.32, 29.37, 29.55, 29.59, 29.61, 29.64, 31.89 (*C*H$_2$ aliphatic), 36.81 (N-*C*H$_3$), 68.65 (O-*C*H$_2$), 115. 91 (*C*H phenyl), 121.60 (*C*H imidazolium), 123.70 (*C*H phenyl), 124.33 (*C*H imidazolium), 127.21 (N-*C* phenyl), 134.42 (*C*H imidazolium), 160.51 (*C*-O-CH$_2$ phenyl). ν$_{max}$/cm^{-1} 2921 and 2850 (C-H aliphatic), 1516 (C=C aromatic), 1255 (C-O aromatic), 826 cm^{-1} (PF$_6^-$). UV–vis (CH$_2$Cl$_2$): λ$_{max}$ (ε, L·mol^{-1}·cm^{-1}) = 249 nm (11700). Elemental analysis for C$_{22}$H$_{35}$F$_6$N$_2$OP·1/7H$_2$O, Calcd: C 53.81, H 7.24, N 5.70%. Found: C 53.77, H 7.31, N 5.51%.

1-[4-(Dodecyloxy)phenyl]-3-methyl-1*H*-imidazol-3-ium trifluoromethanesulfonate (**1d**)

Following the general procedure using **1a** (0.730 g, 1.55 mmol) and sodium trifluoromethanesulfonate (0.616 g, 3.51 mmol) provided **1d** with a yield of 46% (0.349 g, 0.71 mmol).

^{1}H NMR (300 MHz, CDCl$_3$): δ = 0.89 (t, 3H, *J* = 6.8Hz, C*H*$_3$ aliphatic chain), 1.28 (broad s, 16H, C*H*$_2$ aliphatic chain), 1.41–1.46 (m, 2H, O-CH$_2$-CH$_2$-C*H*$_2$), 1.76–1.83 (m, 2H, O-CH$_2$-C*H*$_2$), 3.99 (t, 2H, *J* = 6.6 Hz, O-C*H*$_2$), 4.10 (s, 3H, N-C*H*$_3$), 7.02 and 7.51 (AA′ and BB′, 2 × 2H, *J* = 8.8 Hz, C*H* phenyl), 7.49 (broad s, 2H, N-C*H*-C*H*-N), 9.41 (broad s, 1H, N-C*H*-N). ^{13}C NMR (75 MHz, CDCl$_3$): δ = 13.96 (*C*H$_3$ aliphatic), 22.54, 25.85, 28.97, 29.21, 29.26, 29.44, 29.48, 29.51, 29.53, 31.78 (*C*H$_2$ aliphatique), 36.52 (N-*C*H$_3$), 68.54 (O-*C*H$_2$), 115. 84 (*C*H phenyl), 120.49 (q, *J* = 318.18 Hz, *C*F$_3$SO$_3^-$), 121.36 (*C*H imidazolium), 123.33 (*C*H phenyl), 124.44 (*C*H imidazolium), 127.15 (N-*C* phenyl), 134.95 (*C*H imidazolium), 160.36 (*C*-O-CH$_2$ phenyl). ν$_{max}$/cm^{-1} 3119 (C-H aromatic), 2915 and 2849 (C-H aliphatic), 1520 (C=C aromatic), 1269 and 1028 (CF$_3$SO$_3^-$). UV–vis (CH$_2$Cl$_2$): λ$_{max}$ (ε, L·mol^{-1}·cm^{-1}) = 256 nm (10100). Elemental analysis for C$_{22}$H$_{35}$F$_3$N$_2$O$_4$S, Cacld: C 56.08, H 7.16, N 6.59%. Found: C 55.84, H 6.86, N 5.40%.

1-[4-(Dodecyloxy)phenyl]-3-methyl-1*H*-imidazol-3-ium bis(trifluoromethane) sulfon-amide (**1e**)

1a (0.101 g, 0.21 mmol) and lithium bis(trifluoromethane)-sulfonamide (0.145 g, 0.51 mmol) were dissolved in water (3 mL) and stirred for 140 h. The precipitate was filtred and washed. Crystallization (chloroform/cyclohexane) provided **1e** with a yield of 90% (0.121 g, 0.19 mmol).

^{1}H NMR (300 MHz, CDCl$_3$): δ = 0.89 (t, 3H, *J* = 6.8 Hz, C*H*$_3$ aliphatic chain), 1.28 (broad s, 16H, C*H*$_2$ aliphatic chain), 1.42–1.52 (m, 2H, O-CH$_2$-CH$_2$-C*H*$_2$), 1.77–1.86 (m, 2H, O-CH$_2$-C*H*$_2$), 4.01 (t, 2H, *J* = 6.6 Hz, O-C*H*$_2$), 4.07 (s, 3H, N-C*H*$_3$), 7.05 and 7.46 (AA′ and BB′, 2 × 2H, *J* = 8.8 Hz, C*H* phenyl), 7.43–7.49 (m, 2H, N-C*H*-C*H*-N), 8.98 (broad s, 1H,

N-C*H*-N). ^{13}C NMR (75 MHz, CDCl$_3$): δ = 14.06 (*CH$_3$* aliphatic), 22.65, 25.94, 29.05, 29.31, 29.34, 29.53, 29.57, 29.60, 29.63, 31.89 (*CH$_2$* aliphatic), 36.69 (N-*CH$_3$*), 68.70 (O-*CH$_2$*), 116.04 (*CH* phenyl), 119.77 (q, *J* = 319.29 Hz, *CF$_3$*SO$_3^-$), 121.89 (*CH* imidazolium), 123.77 (*CH* phenyl), 124.31 (*CH* imidazolium), 126.99 (N-*C* phenyl), 134.67 (*CH* imidazolium), 160.78 (*C*-O-CH$_2$ phenyl). ν$_{max}$/cm^{-1} 2918 and 2850 (C-H aliphatic), 1517 (C=C aromatic), 1358 cm^{-1} and 1183 ((CF$_3$SO$_2$)$_2$N$^-$). UV–vis (CH$_2$Cl$_2$): λ$_{max}$ (ε, L·mol^{-1}·cm^{-1}) = 255 nm (11100). Elemental analysis for C$_{24}$H$_{35}$F$_6$N$_3$O$_5$S$_2$·$_{1/2}$H$_2$O, Cacld: C 45.56, H 5.74, N 6.64%. Found: C 45.52, H 5.66, N 6.58%.

Acknowledgements

References

1. Wasserscheid, P.; Welton, T. *Ionic Liquid in Synthesis;* Wiley-VCH: Weinheim, Germany, 2003.
2. Rogers, R. B.; Seddon, K. R., Eds. *Ionic Liquids IIIA: Fundamentals, Progress, Challenges and Opportunities,* American Chemical Society, Symp. Ser.: Washington DC, 2005. doi:10.1021/bk-2005-0901
3. Rogers, R. B.; Seddon, K. R., Eds. *Ionic Liquids IIIB: Fundamentals, Progress, Challenges and Opportunities,* American Chemical Society, Symp. Ser.: Washington DC, 2005. doi:10.1021/bk-2005-0902
4. Dupont, J.; de Souza, R. F.; Suarez, P. A. *Chem. Rev.* **2002,** *102,* 3667–3692. doi:10.1021/cr010338r
5. Endres, F.; Abbott, A. P.; MacFarlane, D. R. *Electrodeposition from Ionic liquids;* Wiley-VCH: Weinheim, 2008. doi:10.1002/9783527622917
6. Handbook of Liquid Crystals, Vols. 1, 2a, 2b and 3. Demus, D.; Goodby, J. W.; Gray, G. W.; Spiess, H.-W.; Vill, V., Eds.; Wiley-VCH: Weinheim, 1998.
7. Guillon, D. *Struct. Bond.* **1999,** *95,* 41–82. doi:10.1007/3-540-68118-3_2
8. Goodby, J. W.; Saez, I. M.; Cowling, S. J.; Görtz, V.; Draper, M.; Hall, A. W.; Sia, S.; Cosquer, G.; Lee, S.-E.; Raynes, E. P. *Angew. Chem., Int. Ed.* **2008,** *47,* 2754–2787. doi:10.1002/anie.200701111
9. Dobbs, W.; Heinrich, B.; Bourgogne, C.; Donnio, B.; Terazzi, E.; Bonnet, M.-E.; Stock, F.; Erbacher, P.; Bolcato-Bellemin, A.-L.; Douce, L. *J. Am. Chem. Soc.* **2009,** *131,* 13338–13346. doi:10.1021/ja903028f
10. Ohno, H. *Electrochemical Aspect of Ionic Liquids;* John Wiley and Sons, 2005. doi:10.1002/0471762512
11. Binnemans, K. *Chem. Rev.* **2005,** *105,* 4148–4204. doi:10.1021/cr0400919
12. Bowlas, C. J.; Bruce, D. W.; Seddon, K. R. *Chem. Commun.* **1996,** 1625–1626. doi:10.1039/cc9960001625
13. Yoshio, M.; Mukai, T.; Ohno, H.; Kato, T. *J. Am. Chem. Soc.* **2004,** *126,* 994–995. doi:10.1021/ja0382516
14. Taubert, A. *Angew. Chem., Int. Ed.* **2004,** *43,* 5380–5382. doi:10.1002/anie.200460846
15. Suisse, J.-M.; Bellemin-Laponnaz, S.; Douce, L.; Maisse-François, A.; Welter, R. *Tetrahedron Lett.* **2005,** *46,* 4303–4305. doi:10.1016/j.tetlet.2005.04.114
16. Dobbs, W.; Suisse, J.-M.; Douce, L.; Welter, R. *Angew. Chem., Int. Ed.* **2006,** *45,* 4179–4182. doi:10.1002/anie.200600929
17. Dobbs, W.; Douce, L.; Allouche, L.; Louati, A.; Malbosc, F.; Welter, R. *New J. Chem.* **2006,** *30,* 528–532. doi:10.1039/b600279j
18. Suisse, J.-M.; Douce, L.; Bellemin-Laponnaz, S.; Maisse-François, A.; Welter, R.; Miyake, Y.; Shimizu, Y. *Eur. J. Inorg. Chem.* **2007,** 3899–3905. doi:10.1002/ejic.200700251
19. Yazaki, S.; Kamikawa, Y.; Yoshio, M.; Hamasaki, A.; Mukai, T.; Ohno, H.; Kato, T. *Chem. Lett.* **2008,** *37,* 538–539. doi:10.1246/cl.2008.538
20. Yoshio, M.; Ichikawa, T.; Shimura, H.; Kagata, T.; Hamasaki, A.; Mukai, T.; Ohno, H.; Kato, T. *Bull. Chem. Soc. Jpn.* **2007,** *80,* 1836–1841. doi:10.1246/bcsj.80.1836
21. Fanta, P. E. *Synthesis* **1974,** 9–21. doi:10.1055/s-1974-23219
22. Kouwer, P. H. J.; Swager, T. M. *J. Am. Chem. Soc.* **2007,** *129,* 14042–14052. doi:10.1021/ja075651a
23. Kantam, M. L.; Rao, B. P. C.; Choudary, B. M.; Reddy, R. S. *Synlett* **2006,** *14,* 2195–2198. doi:10.1055/s-2006-949615
24. Spek, A. L. *J. Appl. Crystallogr.* **2003,** *36,* 7–13. doi:10.1107/S0021889802022112
25. Cruz, C.; Heinrich, B.; Ribeiro, A. C.; Bruce, D. W.; Guillon, D. *Liq. Cryst.* **2000,** *27,* 1625–1631. doi:10.1080/026782900750037185
26. Dobbs, W.; Heinrich, B.; Douce, L. *Beilstein J. Org. Chem.* **2009,** *5,* No. 62. doi:10.3762/bjoc.5.62

Novel banana-discotic hybrid architectures

Hari Krishna Bisoyi, H. T. Srinivasa and Sandeep Kumar[*]

Abstract

Here we present the design and synthesis of novel banana-discotic dimers and banana-bridged discotic dimers. The chemical structures have been characterized by spectral techniques and elemental analysis. The thermal behaviors of the compounds have been investigated by polarizing optical microscopy and differential scanning calorimetry. None of these synthesized compounds exhibit any liquid crystalline property probably because of the incompatibility of the bent-core with the discotic core.

Introduction

Liquid crystals are unique functional self-organized soft materials which possess order and dynamics. Recently, banana liquid crystals or bent-shaped mesogens have attracted considerable research interest in the field of soft condensed matter. The mesomorphic properties of a variety of bent shaped molecules have been investigated quite extensively. The polar order of these molecules, due to their bent shape, display interesting properties such as ferroelectric or anti-ferroelectric switching [1-7]. The occurrence of superstructural chirality in the mesophase of bent-core compounds with no inherent chirality is not only of fundamental scientific interest but also of industrial application as this chirality can be switched in external electric fields. Various new applications of these materials include nonlinear optics, flexoelectricity, photoconductivity, molecular electronics and the design of biaxial nematic phases [8,9]. In

addition to various banana phases, these mesogens also display classical nematic, smectic and columnar phases.

On the other hand, the unique geometry of the columnar mesophase formed by discotic liquid crystals is of great importance not only as models for the study of one-dimensional charge and energy migration in organized systems but also as functional materials for device applications such as one-dimensional conductors, photoconductors, light emitting diodes, photovoltaic solar cells, gas sensors etc. [10-21]. The functional capabilities of these materials are due to their easier processibility, spontaneous alignment between electrodes and self-healing of defects owing to their dynamic nature. Furthermore, there has been considerable interest in the field of non-conventional low molar mass liquid crystals, especially in liquid crystal dimers
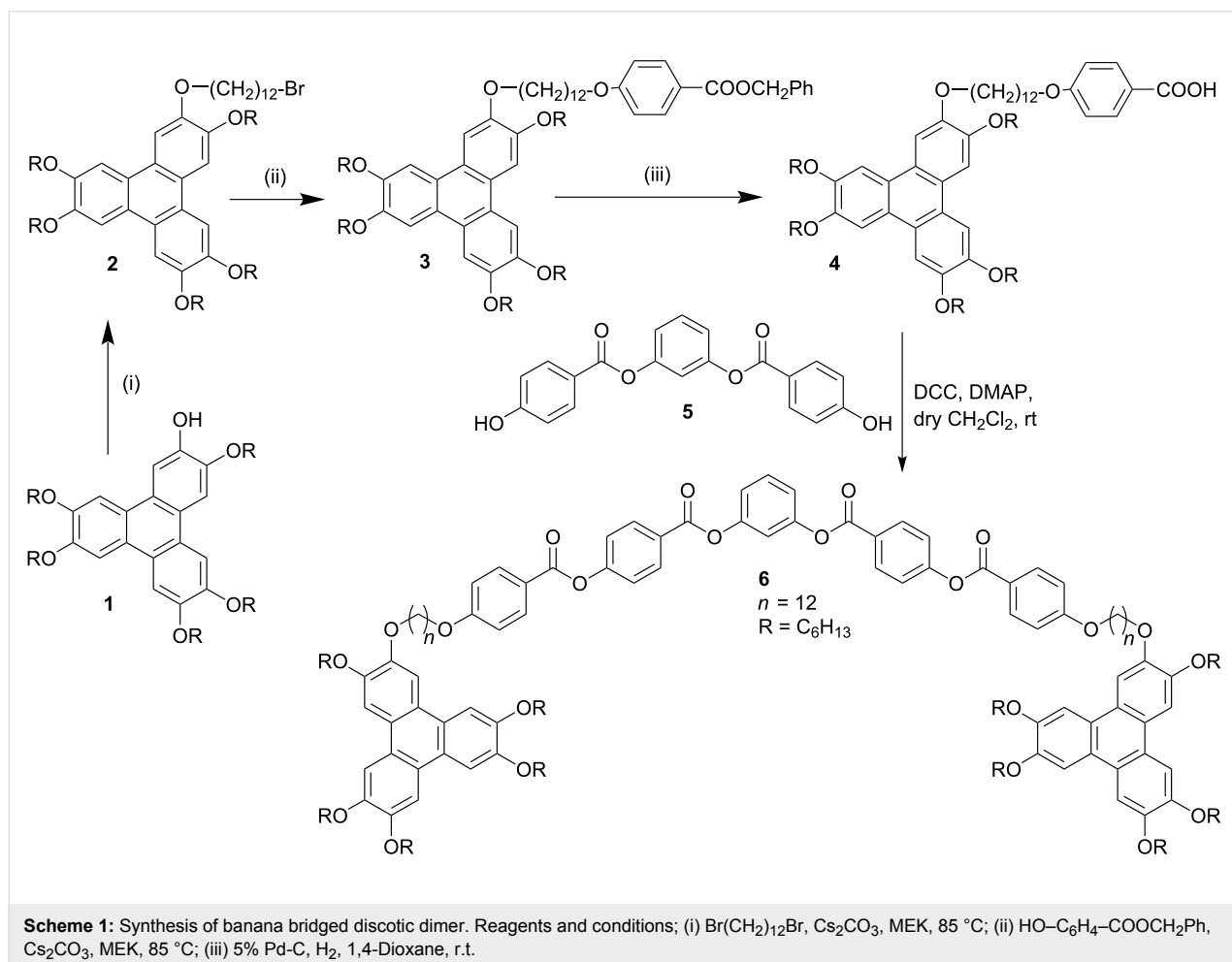
because of their interesting mesomorphic properties. Liquid crystal oligomers serve as ideal models for polymers and networks due to the striking similarity in their transitional behavior and like polymers, some oligomers form glassy mesophases [22-26]. Their purification and characterization are easy unlike polydisperse polymers. Owing to the restricted motion of the components, liquid crystal oligomers provide and stabilize a variety of fluid phases with fascinating functions and oligomeric approach provides a wide flexibility in the molecular design.
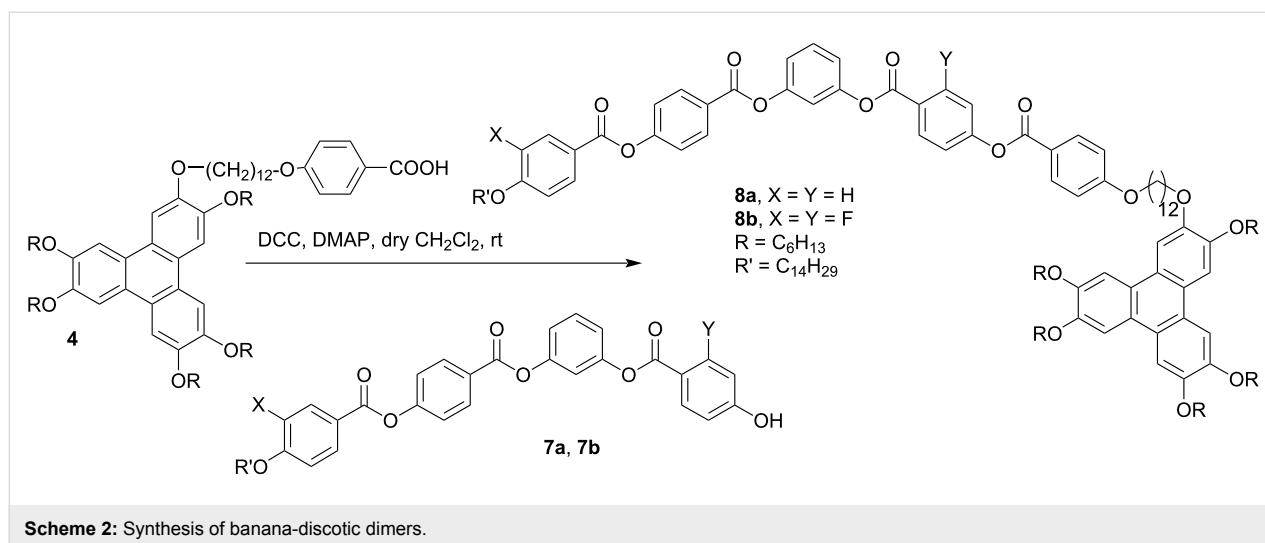
The hybridization of above mentioned two varieties of liquid crystals may lead to novel nanostructured materials with interesting physical properties important for device applications. If such architectures could provide columnar mesophases then the charge carrier mobilities are expected to increase owing to the presence of conducting aromatic bent-cores in the otherwise insulating alkyl chain mantle around the discotic cores. Hence these compounds are anticipated to display superior electronic and optoelectronic performance in organic semiconducting devices. Moreover, these hybrids may also display new types of

banana phases whose potential applications have been mentioned in the introductory paragraph. With this idea in mind, we have designed and synthesized novel banana-discotic dimers. A typical five-ring banana liquid crystal and triphenylene based discotic [27] liquid crystals were chosen to prepare these novel dimers. Here we report the synthesis, characterization and phase behavior of these novel dimers.

Results and Discussion

The bend in the rigid cores of the banana liquid crystal compounds leads to a reduction of the rotational disorder of the molecules around their long axes. If segregation of aromatic cores and aliphatic chains is sufficiently strong, the molecular structure facilitates an organization into layers. Since the molecules are closely packed within the smectic layers and additionally, the rotation about their long axes is strongly hindered, the bent directions align parallel in each layer. As a result of this directed organization, each layer develops a spontaneous polarization. On the other hand, most of the discotic liquid crystalline compounds form columnar phases because of the strong π-π interaction of poly aromatic cores. In the

Scheme 1: Synthesis of banana bridged discotic dimer. Reagents and conditions; (i) Br(CH₂)₁₂Br, Cs₂CO₃, MEK, 85 °C; (ii) HO–C₆H₄–COOCH₂Ph, Cs₂CO₃, MEK, 85 °C; (iii) 5% Pd-C, H₂, 1,4-Dioxane, r.t.

Scheme 2: Synthesis of banana-discotic dimers.

columnar mesophases, the discotic molecules stack one on top of the other to form columns and the columns so formed arrange themselves in various two dimensional lattices.

The synthesis of the target compounds, banana-bridged discotic dimer **6** and banana-discotic dimers **8a** and **8b** are shown in Scheme 1 and Scheme 2, respectively. In compound **6** a five-ring banana unit joins two triphenylene discotic cores via two flexible alkyl spacers whereas in compound **8a** and **8b** a five-ring banana unit joins to a triphenylene core via a flexible alkyl spacer.

The chemical structures of the final compounds have been characterized by spectral techniques and elemental analysis. The analytical data is in good agreement with their chemical structures. The phase behavior of the novel compounds have been observed by polarizing optical microscopy and differential scanning calorimetry. All the solvent crystallized compounds pass from crystalline state to isotropic liquid state on heating, and on cooling they crystallize into the solid state without any intervening mesophase. The transition temperatures and their associated enthalpies of the novel compounds are listed in Table 1.

Table 1: Transition temperatures (°C, peak temperature) and enthalpies (kJ/mol in parentheses) of the banana-discotic dimers both on heating and cooling at the scan rate of 5 °C/min.

Compound	Heating	Cooling
6	Cr[a] 51.1 (38.8) I[b]	I 38.7 (15.4) Cr
8a	Cr 92.6 (57.7) I	I 77.6 (43.6) Cr
8b	Cr 75.8 (40.9) I	I 54.9 (35.2) Cr

[a]Cr = Crystalline solid, [b]I = Isotropic liquid

The symmetric dimer **6** melts at 51.1 °C on heating and crystallizes at 38.7 °C on cooling. Under polarizing optical microscopy we do not see any other transition, which was confirmed by differential scanning calorimetry measurements. The absence of either B-phase or discotic columnar mesophase in compound **6** may be explained as follows: since the five-ring banana unit, which otherwise exhibits mesophase with two terminal alkyl chains, is now attached with two bulky triphenylene units at the ends, the packing of the bent-cores in layers will not be favored. In other words, the bent core-bent core interactions are too weak to produce any B-phase. On the other hand, the two triphenylene units in compound **6** when attached with flexible methylene spacers exhibit columnar mesomorphism. However, in compound **6** they are attached to each other with a intervening rigid bent core unit which is probably not allowing the two discs to lie in the same plane and hence hinders columnar mesomorphism in this architecture. So non-coplanarity of the discs and the rigid bent-core unit in the spacer seems to be the reason for absence of liquid crystallinity in compound **6**. The banana discotic hybrid **8a** melts at 92.6 °C to an isotropic liquid and on cooling it slowly crystallizes at 77.6 °C. Similarly, compound **8b** on heating melts to isotropic liquid at 75.8 °C and on cooling slowly crystallizes at 54.9 °C. These polarizing optical microscopy observations are confirmed by differential scanning calorimetry measurements. The absence of mesomorphism in this architecture may arise from two competing factors. First, the bent core units will try to pack in layers by microsegregation but in this kind of packing arrangement the attached discs have to lie side by side which is not a preferable option for discs. Moreover, the cross-sectional area of the disc is such that it will not allow efficient packing of the bent cores in layers. Secondly, when the discs try to stack one above the other to produce columnar phases, the bent core unit will disrupt it owing to its rigidity and high volume frac-

tion compared to the other alkyl chains surrounding the triphenylene disc which otherwise provide space filling effect for columnar mesomorphism. The difluoro compound **8b**, has a lower melting point than its hydrocarbon parent compound **8a** which is very common observation in bent-core compounds.

Conclusion

We have designed and synthesized banana-discotic dimers and a banana-bridged discotic dimer to investigate possible mesomorphism in such supermolecular architectures. The chemical structures have been characterized by spectral techniques and elemental analysis which establishes the identity and purity of the new compounds. The thermal behavior of the novel mesogenic oligomers has been investigated by differential scanning calorimetry and polarizing optical microscopy. These novel banana-discotic hybrid oligomers are unable to exhibit mesomorphism presumably because of the incompatibility of the bent-core with the discotic core and/or the volume fraction mismatch of the mesogenic rigid cores. Attempts to realize mesophase in such architectures with different molecular topologies are currently under way in our laboratory.

Experimental

All the reagents and solvents were used as received without any further purification except CH_2Cl_2 which was dried and distilled before the reactions. Column chromatographic separation was performed on silica gel (100–200 mesh). ^{1}H NMR spectra were recorded in $CDCl_3$ on a 400 MHz (Bruker AMX 400) spectrometer. All chemical shifts are reported in δ (ppm) units down field from tetramethylsilane (TMS) and *J* values are reported in Hz. FT-IR spectra were recorded as KBr discs on a Shimadzu FTIR-8400 spectrophotometer. Elemental analysis was performed on a Carlo-Erba Flash 1112 analyzer. Transition temperatures were observed using a Mettler FP82HT hot stage and FP90 central processor in conjunction with an Olympus BX51 polarizing microscope. Transition temperatures and associated enthalpies were measured by differential scanning calorimetry heating from room temperature to isotropic temperatures at the scan rate of 5 °C per minute (Perkin-Elmer Model Pyris 1D).

Synthesis

Compound **1**, compound **5** and Compound **7a–b** were prepared by following the literature procedures [28-31].

Preparation of 2-(12-bromododecyloxy)-3,6,7,10,11-pentakis(hexyloxy)triphenylene (2): A mixture of monohydroxy triphenylene (2.0 g, 2.7 mmol), 1,12-dibromododecane (4.4 g, 13.0 mmol), cesium carbonate (1.12 g, 8.8 mmol) and 50 ml of methyl ethyl ketone (MEK) was refluxed for 48 h at 85 °C. The resulting mixture was cooled and poured into 50 ml of water

and then extracted into chloroform. The organic layer was washed with water, dried over anhydrous sodium sulfate followed by removal of solvent. The crude product was purified by column chromatography over silica gel with eluent 2% ethyl acetate in hexane. Finally the product was precipitated as waxy solid from dichloromethane by adding hexane, yield 2.44 g.

Preparation of benzyl 4-{12-[3,6,7,10,11-pentakis(hexyloxy)-triphenylene-2-yloxy]dodecyloxy}benzoate (3): Triphenylene bromide **2** (2.34 g, 2.3 mmol), benzyl 4-hydroxy benzoate (0.45 g, 1.98 mmol) and cesium carbonate (2.0 g, 5.94 mmol) in 50 mL of MEK was refluxed for 48 h. The reaction mixture was poured into 50 mL of water and then extracted with chloroform, the chloroform layer was washed with 50 mL of water followed by drying over anhydrous sodium sulfate. The solvent was removed to yield a viscous oily residue **3** which was taken as such for hydrogenolysis.

Preparation of 4-{12-[3,6,7,10,11-pentakis(hexyloxy)triphenylene-2-yloxy]dodecyloxy}benzoic acid (4): A mixture of compound **3** (2.3 g) dissolved in 1,4-dioxane (20 ml) and 5% Pd-C catalyst (0.4 g) was stirred in an atmosphere of hydrogen until the required quantity of hydrogen was absorbed. The resulting mixture was filtered in hot and the solvent removed under reduced pressure. The solid material obtained was recrystallised using methanol. Yield 1.0 g. mp 68–70 °C.

Preparation of bent-core bridged discotic dimer 6: A mixture of compound **4** (0.5 g, 0.48 mmol), compound **5** (0.085 g, 0.24 mmol), DCC (0.22 g, 1.07 mmol) and catalytic quantity of DMAP was stirred in dry dichloromethane at room temperature for about 24 hours. The solvent was removed and the residue purified by column chromatography on silica gel using mixture of petroleum ether and ethyl acetate (2%) as eluent. Removal of solvent afforded a residue which was recrystallised from dichloromethane and hexane to afford **6**. Yield 0.2 g. IR (KBr), v_{max} (cm^{-1}): 2922, 2852, 1734, 1456, 1377, 1261, 1170, 721; ^{1}H NMR (400 MHz, $CDCl_3$, δ/ppm): 8.28 (d, 4H, *J* = 8.7 Hz, Ar-H), 8.16 (d, 4H, *J* = 8.0 Hz, Ar-H), 7.83 (s, 12H, Ar-H), 7.51 (t, 1H, *J* = 8.5 Hz, Ar-H), 7.36 (d, 4H, *J* = 8.7 Hz, Ar-H), 7.30 (t, 1H, *J* = 8.2 Hz, Ar-H), 7.26 (d, 2H, *J* = 8.1 Hz, Ar-H), 6.98 (d, 4H, *J* = 8.9 Hz, Ar-H), 4.24 (t, 24H, *J* = 6.4 Hz, -OCH$_2$), 4.03 (t, 4H, *J* = 6.2 Hz, -OCH$_2$), 1.97 (m, 28H, -CH$_2$-), 1.69–1.31 (m, 92H, -CH$_2$-), 0.94 (t, 30H, *J* = 6.1 Hz, -CH$_3$); Elemental analysis: Found: C, 76.34; H, 9.01. $C_{154}H_{210}O_{22}$ requires C, 76.64; H, 8.77.

Compounds **8a** and **8b** were prepared following the similar procedure for compound **6**. **8a**: IR (KBr), v_{max} (cm^{-1}): 2922, 2850, 1743, 1733, 1602, 1508, 1437, 1259, 1159, 1068, 721; [1]H

NMR (400 MHz, CDCl$_3$, δ/ppm): 8.31 (m, 4H, Ar-H), 8.16 (d, 4H, J = 8.8 Hz, Ar-H), 7.83 (s, 6H, Ar-H), 7.63 (t, 1H, J = 3.4 Hz, Ar-H), 7.40 (m, 4H, Ar-H), 7.13–6.95 (m, 7H, Ar-H), 4.24 (t, 12H, J = 6.4 Hz, -OCH$_2$-), 4.08 (t, 2H, J = 6.2 Hz, -OCH$_2$-), 3.98 (t, 2H, J = 6.1 Hz, -OCH$_2$-), 1.97–1.77 (m, 16H, -CH$_2$-), 1.51–1.19 (m, 68H, -CH$_2$-), 0.94 (t, 15H, J = 7 Hz, -CH$_3$), 0.87 (t, 3H, J = 6.7 Hz, -CH$_3$); Elemental analysis: **8a** Found: C, 75.91; H, 8.74. C$_{108}$H$_{144}$O$_{16}$ requires C, 76.38; H, 8.54. **8b**: IR (KBr), ν$_{max}$ (cm^{-1}): 2922, 2852, 1726, 1606, 1462, 1377, 1263, 1169, 721; ^{1}H NMR (400 MHz, CDCl$_3$, δ/ppm): 8.31 (m, 3H, Ar-H), 8.15 (m, 4H, Ar-H), 7.85 (s, 6H, Ar-H), 7.61 (t, 1H, J = 8 Hz, Ar-H), 7.39 (m, 3H, Ar-H), 7.28 (m, 3H, Ar-H), 6.98 (m, 4H, Ar-H), 4.25 (t, 12H, J = 6.5 Hz, -OCH$_2$-), 4.08 (m, 4H, -OCH$_2$-), 2.06–1.78 (m, 16H, -CH$_2$-), 1.62–1.23 (m, 68H, -CH$_2$-), 0.95 (t, 15H, J = 6.9 Hz, -CH$_3$), 0.88 (t, 3H, J = 6.5 Hz, -CH$_3$); Elemental analysis: **8b** Found: C, 74.3; H, 8.39. C$_{108}$H$_{142}$O$_{16}$F$_2$ requires C, 74.79; H, 8.25.

References

1. Niori, T.; Sekine, T.; Watanabe, J.; Furukawa, T.; Takezoe, H. *J. Mater. Chem.* **1996,** *6,* 1231–1233. doi:10.1039/jm9960601231
2. Pelzl, G.; Diele, S.; Weissflog, W. *Adv. Mater.* **1999,** *11,* 707–724. doi:10.1002/(SICI)1521-4095(199906)11:9<707::AID-ADMA707>3.0.CO;2-D
3. Tschierske, C.; Dantlgraber, G. *Pramana* **2003,** *61,* 455–481. doi:10.1007/BF02708325
4. Ros, M. B.; Serrano, J. L.; De la Fuente, M. R.; Folcia, C. L. *J. Mater. Chem.* **2005,** *15,* 5093–5098. doi:10.1039/b504384k
5. Reddy, A.; Tschierske, C. *J. Mater. Chem.* **2006,** *16,* 907–961. doi:10.1039/b504400f
6. Takezoe, H.; Takanishi, Y. *Jpn. J. Appl. Phys.* **2006,** *45,* 597–625. doi:10.1143/JJAP.45.597
7. Etxebarria, J.; Ros, M. B. *J. Mater. Chem.* **2008,** *18,* 2919–2926. doi:10.1039/b803507e
8. Madsen, L. A.; Dingemans, T. J.; Nakata, M.; Samulski, E. T. *Phys. Rev. Lett.* **2004,** *92,* 145505. doi:10.1103/PhysRevLett.92.145505
9. Acharya, B. R.; Primak, A.; Kumar, S. *Phys. Rev. Lett.* **2004,** *92,* 145506. doi:10.1103/PhysRevLett.92.145506
10. Kumar, S. *Chem. Soc. Rev.* **2006,** *35,* 83–109. doi:10.1039/b506619k
11. Laschat, S.; Baro, A.; Steinke, N.; Giesselmann, F.; Hägele, C.; Scalia, G.; Judele, R.; Kapatsina, E.; Sauer, S.; Schreivogel, A.; Tosoni, M. *Angew. Chem., Int. Ed.* **2007,** *46,* 4832–4887. doi:10.1002/anie.200604203
12. Sergeyev, S.; Pisula, W.; Geerts, Y. H. *Chem. Soc. Rev.* **2007,** *36,* 1902–1929. doi:10.1039/b417320c
13. Wu, J.; Pisula, W.; Müllen, K. *Chem. Rev.* **2007,** *107,* 718–747. doi:10.1021/cr068010r
14. Shimizu, Y.; Oikawa, K.; Nakayama, K.; Guillon, D. *J. Mater. Chem.* **2007,** *17,* 4223–4229. doi:10.1039/b705534j
15. Boden, N.; Bushby, R. J.; Clements, J.; Movaghar, B. *J. Mater. Chem.* **1999,** *9,* 2081–2086. doi:10.1039/a903005k
16. Bushby, R. J.; Lozman, O. R. *Curr. Opin. Solid State Mater. Sci.* **2002,** *6,* 569–578. doi:10.1016/S1359-0286(03)00007-X
17. Bushby, R. J.; Lozman, O. R. *Curr. Opin. Colloid Interface Sci.* **2002,** *7,* 343–354. doi:10.1016/S1359-0294(02)00085-7
18. Takezoe, H.; Kishikawa, K.; Gorecka, E. *J. Mater. Chem.* **2006,** *16,* 2412–2416. doi:10.1039/b603232j
19. Ohta, K.; Hatsusaka, K.; Sugibayashi, M.; Ariyoshi, M.; Ban, K.; Maeda, F.; Naito, R.; Nishizawa, K.; van de Craats, A. M.; Warman, J. M. *Mol. Cryst. Liq. Cryst.* **2003,** *397,* 25–45. doi:10.1080/714965592
20. Manickam, M.; Cooke, G.; Kumar, S.; Ashton, P. R.; Preece, J. A.; Spencer, N. *Mol. Cryst. Liq. Cryst.* **2003,** *397,* 99–116. doi:10.1080/714965597
21. Cammidge, A. N.; Bushby, R. J. In *Handbook of Liquid Crystals;* Demus, D.; Goodby, J.; Gray, G. W.; Spiess, H.-W.; Vill, V., Eds.; Wiley-VCH: Weinheim, 1998; Vol. 2B, Chapter VII, p 693.
22. Kumar, S. *Liq. Cryst.* **2005,** *32,* 1089–1113. doi:10.1080/02678290500117415
23. Imrie, C. T.; Henderson, P. A. *Chem. Soc. Rev.* **2007,** *36,* 2096–2124. doi:10.1039/b714102e
24. Imrie, C. T.; Henderson, P. A. *Curr. Opin. Colloid Interface Sci.* **2002,** *7,* 298–311. doi:10.1016/S1359-0294(02)00092-4
25. Imrie, C. T. *Struct. Bonding* **1999,** *95,* 149–191. doi:10.1007/3-540-68118-3_4
26. Imrie, C. T.; Luckhurst, G. R. In *Handbook of Liquid Crystals;* Demus, D.; Goodby, J.; Gray, G. W.; Spiess, H.-W.; Vill, V., Eds.; Wiley-VCH: Weinheim, 1998; Vol. 2B, Chapter X, p 801.
27. Kumar, S. *Liq. Cryst.* **2004,** *31,* 1037–1059. doi:10.1080/02678290410001724746
28. Kumar, S.; Manickam, M. *Synthesis* **1998,** 1119–1122. doi:10.1055/s-1998-2133
29. Kumar, S.; Naidu, J. J.; Varshney, S. K. *Mol. Cryst. Liq. Cryst.* **2004,** *411,* 355–362. doi:10.1080/15421400490435387
30. Reddy, A.; Sadashiva, B. K. *Liq. Cryst.* **2003,** *30,* 1031–1050. doi:10.1080/0267829031000152978
31. Murthy, H. N. S.; Sadashiva, B. K. *Liq. Cryst.* **2004,** *31,* 567–578. doi:10.1080/02678290410001666093

Functional properties of metallomesogens modulated by molecular and supramolecular exotic arrangements

Alessandra Crispini[1], Mauro Ghedini[2] and Daniela Pucci[*2]

Review

Address:
[1]Centro di Eccellenza CEMIF.CAL-LASCAMM, CR-INSTM Unità della Calabria, Dipartimento di Scienze Farmaceutiche, Università della Calabria, Edificio Polifunzionale, Arcavacata di Rende (CS), 87036, Italy and [2]Centro di Eccellenza CEMIF.CAL-LASCAMM, CR-INSTM Unità della Calabria, Dipartimento di Chimica, Università della Calabria, Via P. Bucci Cubo 14C, Arcavacata di Rende (CS), 87036, Italy

Email:
Daniela Pucci[*] - d.pucci@unical.it

* Corresponding author

Abstract

New concepts for the synthesis of metallomesogens have been recently developed in order to use the metal centre as a scaffold for grafting different functionalities and inducing non-conventional shapes and properties in the resulting complexes. Our strategy was based on the synthesis of mesogenic coordination complexes whose molecular architectures are controlled by the modulation of different and tunable molecular motifs: the nature of the metal ion and the surrounding ligands as central unit, the number of flexible chains at the periphery, and the nature of counter-ions in ionic complexes. The appropriate choice of molecular construction motifs allows control at global architectures and induces pre-selected properties from the level of single molecule to supramolecular network, confirming that metal coordination provides a helpful tool for obtaining multifunctional soft materials.

Introduction

Recent interest in designing novel soft and functional materials with more and more challenging requirements such as improved charge transport, luminescence, chirality and biological functions for high-tech applications has been directed towards the use of new mesomorphic systems [1-14]. Design principles based only on the shape and the symmetry of the mesogenic molecules is giving way to alternative concepts for achieving new molecular and supramolecular motifs able to give rise to dynamic functional properties and unusual topologies and families of mesophases. This goal has been reached through different strategies: the creation of hybrid molecular topologies [15-22]; the micro-segregation between incompatible units within molecules [15,23-25]; the development of self-organizing super and supramolecules able to generate complex hier-

archical structures through specific inter- or intramolecular interactions [25-30]. The high level of functionality integrated into molecular-based electronic systems obtained by incorporating metal centres into selected organic structures [31] supports the design of metal-containing liquid crystals (metallomesogens) as an effective and helpful way to expand of the traditional range of technological applications of liquid crystals [32-37].

We have been involved for long time in the field of metallomesogens with the synthesis of cyclopalladated rod-like complexes starting from mesogenic azo and azoxybenzenes, confirming that mesomorphism of the organic precursors is preserved after complexation [38]. More recently, our work has addressed the design of new, higher performing complexes, whose structures, inaccessible for organic liquid crystalline systems, are able both to induce very low transition temperatures and to modulate their optical, electronic and thermal properties [34,36,38]. A multi-motif approach based on the spontaneous association of single tectons such as the metal-ligand central unit, the number of flexible chains at the periphery, the type of complementary ligands occupying the coordination sphere of the metal ion and the counter-ion in ionic systems, has been followed. In this paper selected examples of recently synthesised multifunctional metallomesogens are highlighted, all obtained from classical and unusual nitrogen ligands and different metal centres from across the periodic table, going from the most common Pd(II) to the scarcely used Pt(II) and Zinc(II), until the never used Ga(III). Indeed, with the nature of the metal centre being the leading actor in the design of new metallomesogens, the choice of unexplored metal centres is an effective route to a new generation of dynamically multifunctional soft materials, with higher performance than classical liquid crystals. Our interest in the synthesis of metallomesogens and their wide use in the field of material science, coupled with the fact that transition metal complexes have potential antitumor activity, led us to believe that a great number of metal-containing liquid crystals, already synthesized and analysed with respect to their chemical and physical properties, can constitute a huge database for the design of new biologically relevant complexes.
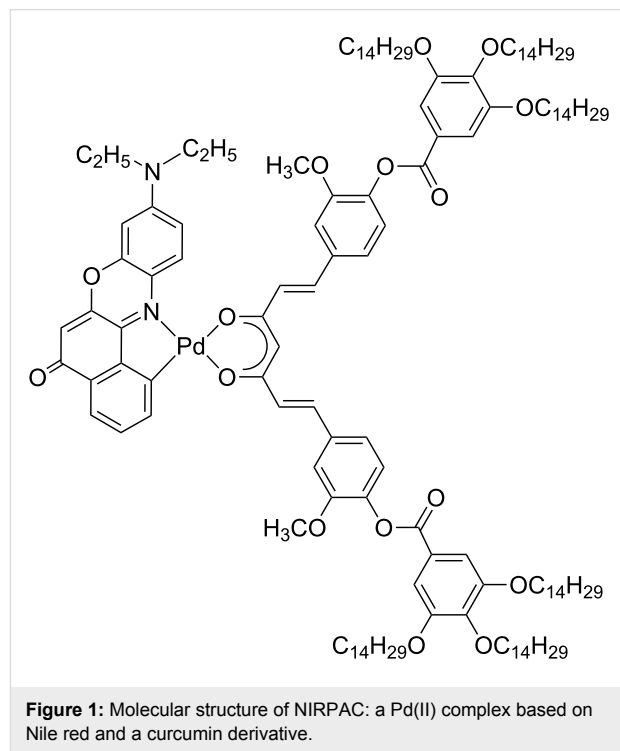
Review
Palladium(II) complexes

New mononuclear *ortho*-palladated complexes have been prepared in order to expand the applications of these systems towards new peculiar properties induced by innovative cyclometallating and ancillary ligands.

For example, an interesting red emitting mesomorphic complex has been prepared starting from the Nile red dye

(9-diethylamino-5*H*-benzo[*a*]phenoxazine-5-one) as a cyclometallating ligand and from the suitably functionalized curcumin β-diketonate as a complementary O,O chelating ligand (Figure 1).

Figure 1: Molecular structure of NIRPAC: a Pd(II) complex based on Nile red and a curcumin derivative.

The presence of the principal ligand [39-44] introduces interesting luminescence properties into the metallic system (which is luminescent in solution), in the red region of the Vis spectrum ($\lambda = 610$ nm), with emission quantum yields in the range of 6–23%, depending on the solvent. However, the 3,4,5-trialkoxy-substituted benzoato fragment of the curcumin ligand imposes an overall hemi-disc structure to the resulting palladium derivative [45] allowing the onset, even at room temperature, of a rectangular columnar mesophase which is stable over a very large temperature range (140 °C). The emission properties observed in the solution are preserved in the liquid crystalline state, therefore the flat disk-like molecular structure organized into columns, the broad thermal stability and the luminescence in the red region of the visible spectrum make this new Pd(II) complex a very intriguing candidate for applications in OLED devices.

A further class of *ortho*-palladated complexes has been obtained starting from the 2-phenylquinoline, a ligand extensively used in the synthesis of cyclometallated iridium(III) and platinum(II) derivatives [46,47] but whose reactivity towards Pd(II) centres is unexplored. This kind of ligand has been functionalised with a chiral group such as a cholesteryl ester unit, introduced as

terminal substituent in 4 position, and chosen for many different purposes, including its universal affinity for cell membranes and its ability to self order into liquid crystalline state [48]. The functionalised 2-phenylquinoline ligand has firstly been cyclo-palladated and then conjugated to a number of O,O chelating β-diketonate ligands, giving rise to a series of mononuclear complexes combining two chelating functional moieties in their structures (Figure 2) [49].

The coordination to the Pd(II) centre induces, in all the resulting compounds, thermotropic mesomorphism whose nature has been found to be strictly related to the ancillary ligand. Indeed a transition from a calamitic to a columnar mesophase is observed, through a calamitic/discotic cross-over point, due to the peculiar combination of two different molecular architectures. The mononuclear tropolonate derivative (A in Figure 2) shows a chiral nematic phase while the half-disc-shaped curcuminoids (B in Figure 2) self-assemble with the formation of columnar mesophases.

Moreover, the presence of biologicaly active fragments (the O,O chelating ligands) induces promising anticancer activity *in vitro* against two human prostatic cancer cell lines in all these complexes suggesting that, through the careful choice of the molecular building blocks, cyclopalladated mesogens represent multifunctional biomaterials. They bear at the same time the active principle and the membrane-compatible delivery component, and are becoming innovative tools in establishing new and effective anticancer therapies.

Finally, in order to investigate the unexplored cyclopalladating ability of 2,2′-pyridylpyrroles, a series of 3,5-disubstituted-2,2′-pyridylpyrroles and their mononuclear Pd(II) *ortho*-palladated

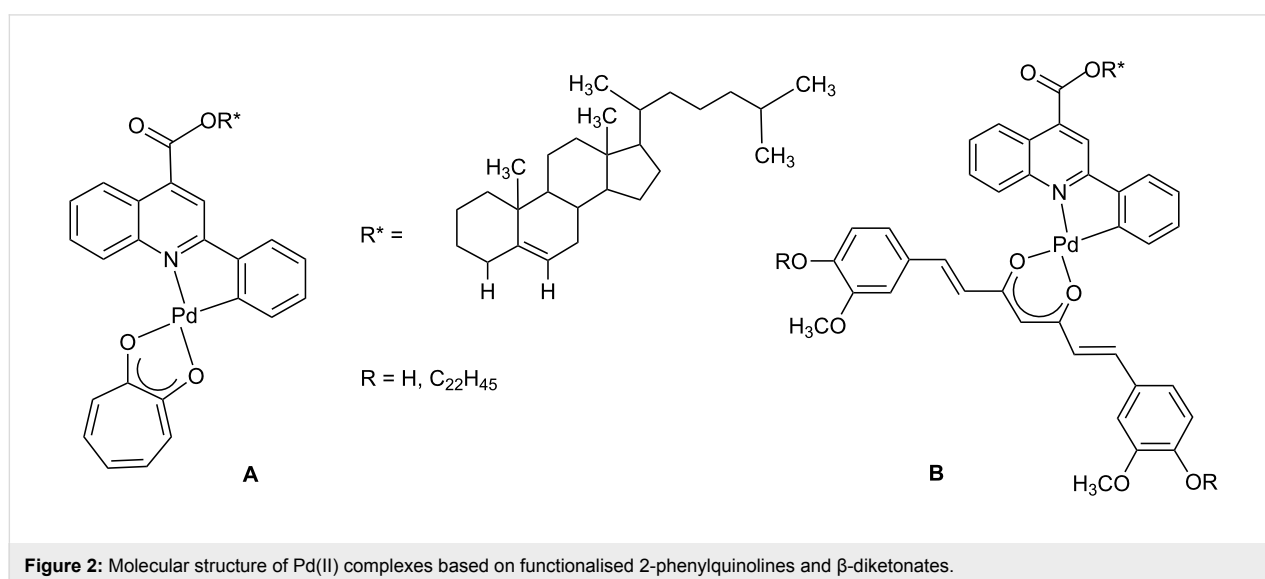**Figure 3:** Some unusual palladiomesogens based on 3,5-disubstituted-2,2′-pyridylpyrroles and β-diketonates.
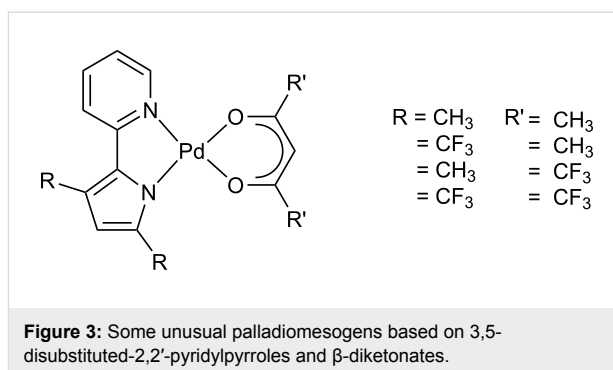
derivatives (Figure 3) have been prepared [50].

The resulting complexes, containing as ancillary ligands some acetylacetonates, are "non conventional" shaped palladiomesogens. Indeed, they completely lack terminal tails, usually necessary for inducing mesomorphism. In this case the presence of fluorinated groups on the complementary ligands promotes a delicate balance between incompatible parts of the molecules, generating phase segregated structures favourable for the appearance of mesomorphism through hexagonal columnar phases. The strategy adopted, building on the modulation of incompatible simple synthons on a metallomesogenic molecule, opens new possibilities for tailoring soft materials with non-conventional structures.

Platinum(II) and Zinc(II)

For the less explored Pt(II) and Zn(II) metal centres versatile 2,2′-bipyridines have been selected since they are well-known building blocks for the formation of inorganic functional nano-materials [51]. The complexation of non-mesogenic 4,4′-disub-ted 2,2′-bipyridine ligands with Pt(II) salts confirmed the role of

Figure 2: Molecular structure of Pd(II) complexes based on functionalised 2-phenylquinolines and β-diketonates.

coordination chemistry in the metal-mediated formation of liquid crystals. Indeed the induction of a dipole moment upon coordination with an MX_2 moiety, allowed most of the half-disc shaped complexes $[L^nPtX_2]$ (Figure 4) to self-assemble into full disc shaped dimers as described by the complementary shape approach [52].

The appearance of mesomorphism is related to the length of the alkyl chains: indeed the complexes based on the 2,2′-bi-pyridines with short tails melted directly into an isotropic liquid, while the higher homologues produce the global rod-like shape responsible for the liquid crystalline behaviour, namely of a lamello-columnar type. Changes of the ancillary ligands have been carried out in order to use dipole coupling as a tool for molecular architecture. Mesomorphic behaviour was found to depend on the size of the X group and on the dipole moment associated with the Pt-X bond, with the sequence, for the clearing points Cl<Br<I and the azide group which promoted a lowering of both transition temperatures. Moreover, these Pt(II) complexes revealed to be photoluminescent with a good degree of tunability, depending on the π-donor capacity of the X ligands.

Zinc(II) complexes are widely applied in OLED technology for their light emitting efficiency, high thermal and redox stability, and tunable electronic properties [53-55]. Hence the design of Zn(II) complexes showing at the same time, order, mobility, and changes in molecular organization in response to external stimuli could be a good strategy for developing new soft materials for innovative applications. In this context the same 2,2′-bi-pyridines have been coordinated to Zn(II) ions where the tetra-hedral geometry of the Zn(II) derivatives prevented the single molecules self-assembling in dimers. Moreover, strong inter-molecular contacts stabilized the crystalline state and no meso-morphic behaviour was observed below the melting point [52]. We decided to extend this work changing the substituents on the

bipyridine ligands by introducing of further aromatic rings equipped with several aliphatic tails each. Hence the synthesis of a series of *cis*-dichloro hexacatenar Zn(II) complexes has been performed (Figure 5) [56].
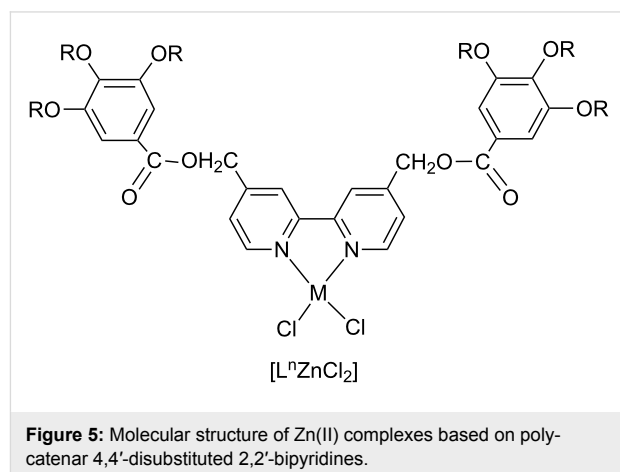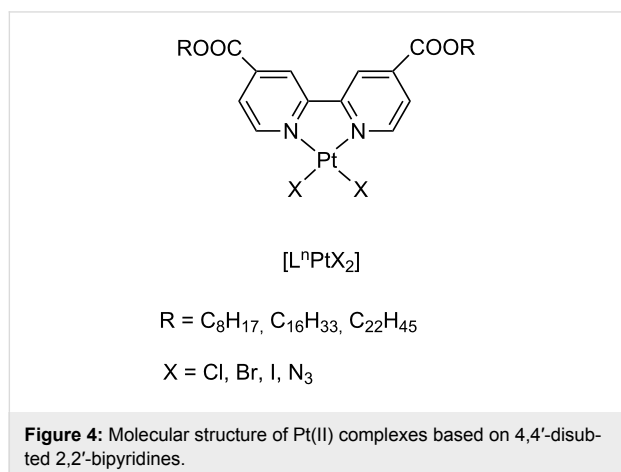
In this case the molecular organization in the mesophase, mainly driven by intermolecular attractive interactions (hydrogen bonds, C–H–π and π–π contacts) between the large flat aromatic cores rather than dipolar or metal-metal interactions, is able to produce supramolecular columnar meso-morphism, appearing for the first time in tetrahedral Zn(II) derivatives.

These results show more and more that, by careful choice of molecular building blocks, it is possible to modulate the interactions necessary for organization of single molecules in to supra-molecular architectures to give rise to the desired metallomeso-genic material. Moreover, preliminary measurements of photo-conductivity on these complexes doped with C_{60} to increase absorption in the visible region, have given excellent results and further experiments are still in progress.

Gallium (III)

Since the nature of the metal centre represents an important tool for tailoring specific molecular shapes and topologies, we have selected the Ga(III) ion, never used before in the design of metallomesogens, in order to explore the possibility of induc-ing mesomorphism in luminescent metal complexes [57].

In particular, we have explored the possibility of promoting mesomorphism in pentacoordinate bisquinolinate Ga(III) coordination compounds, well-known blue emitting species, whose properties derive from solid state interactions [58-60]. Hence we have introduced the mobility of a promesogenic poly-catenar group through the 3,4,5-tris(tetradecyloxy)-benzoyloxy monodentate ligand in the carboxylate unit, keeping the two
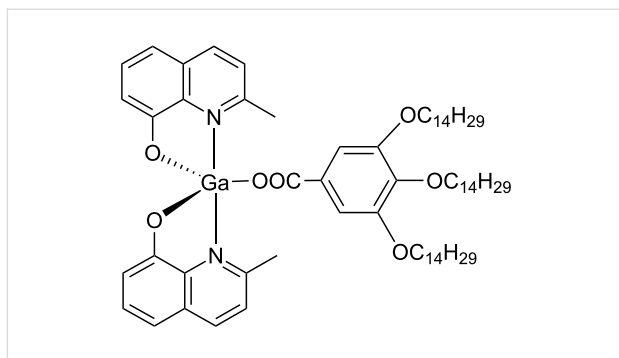
Figure 4: Molecular structure of Pt(II) complexes based on 4,4′-disub-ted 2,2′-bipyridines.

Figure 5: Molecular structure of Zn(II) complexes based on poly-catenar 4,4′-disubstituted 2,2′-bipyridines.

Figure 6: Molecular structure of a gallium(III) mesogen.

quinolinate groups responsible for intermolecular interactions in the crystalline organization grafted around the gallium(III) centre [61]. In this way a unconventional jellyfish shape molecule has been obtained and its molecular structure has been confirmed through single crystal X-ray diffraction (Figure 6).

Despite its unusual molecular shape, this complex shows thermotropic mesomorphism, with a lamello-columnar organization and, at the same time, a light-green emission with the typical high quantum yield of pentacoordinated Ga(III) complexes (40% in solution) [62], has been detected.

Conclusions
We have selected some examples of recent works on metallomesogens demonstrating that, moving across the periodic table, it is possible to expand the pool of metal ions able to induce mesomorphism in an appropriate framework. Hence it is possible to modulate single molecular geometries starting from the conventional square planar ion [Pd(II)], and going to the tetrahedral [Zn(II)] and pentacoordinate Ga(III) to obtain novel, non conventional structures. Moreover, by changing the nature of coordinating ligands and the kinds of substituents, further properties such as luminescence and bioactivity can be promoted at the same time, leading to smart multifunctional material. Finally, through the appropriate choice of crucial single synthons, it is possible to modulate the role of intermolecular interactions in the resulting architecture in order to create new supramolecular arrays with peculiar properties arising either from individual building blocks or from their synergy.

Acknowledgments

References

1. Bushby, R. J.; Lozman, O. R. *Curr. Opin. Solid State Mater. Sci.* **2002,** *6,* 569–578. doi:10.1016/S1359-0286(03)00007-X
2. Bushby, R. J.; Lozman, O. R. *Curr. Opin. Colloid Interface Sci.* **2002,** *7,* 343–354. doi:10.1016/S1359-0294(02)00085-7
3. O'Neill, M.; Kelly, S. M. *Adv. Mater.* **2003,** *15,* 1135–1146. doi:10.1002/adma.200300009
4. Hanna, J. *Opto-Electron. Rev.* **2005,** *13,* 259–267.
5. Iino, H.; Hanna, J. *Opto-Electron. Rev.* **2005,** *13,* 295–302.
6. Woliński, T. R.; Ertman, S.; Lesiak, P.; Domański, A. W.; Czapla, A.; Dąbrowski, R.; Nowinowski-Kruszelnicki, E.; Wójcik, J. *Opto-Electron. Rev.* **2006,** *14,* 329–334. doi:10.2478/s11772-006-0045-6
7. Palffy-Muhoray, P.; Cao, W.; Moreira, M.; Taheri, B.; Munoz, A. *Philos. Trans. R. Soc. London, Ser. A* **2006,** *364,* 2747–2761. doi:10.1098/rsta.2006.1851
8. Ford, A. D.; Morris, S. M.; Coles, H. J. *Mater. Today* **2006,** *9,* 36–42. doi:10.1016/S1369-7021(06)71574-7
9. Woltman, S. J.; Jay, G. D.; Crawford, G. P. *Nat. Mater.* **2007,** *6,* 929–938. doi:10.1038/nmat2010
10. Goodby, J. W.; Saez, I. M.; Cowling, S. J.; Görtz, V.; Draper, M.; Hall, A. W.; Sia, S.; Cosquer, G.; Lee, S.-E.; Raynes, E. P. *Angew. Chem., Int. Ed.* **2008,** *47,* 2754–2787. doi:10.1002/anie.200701111
11. Sergeyev, S.; Pisula, W.; Geerts, Y. H. *Chem. Soc. Rev.* **2007,** *36,* 1902–1929. doi:10.1039/b417320c
12. Laschat, S.; Baro, A.; Steinke, N.; Giesselmann, F.; Hägele, C.; Scalia, G.; Judele, R.; Kapatsina, E.; Sauer, S.; Schreivogel, A.; Tosoni, M. *Angew. Chem., Int. Ed.* **2007,** *46,* 4832–4887. doi:10.1002/anie.200604203
13. Shimizu, Y.; Oikawa, K.; Nakayama, K.-i.; Guillon, D. *J. Mater. Chem.* **2007,** *17,* 4223–4229. doi:10.1039/b705534j
14. Vera, F.; Serrano, J. L.; Sierra, T. *Chem. Soc. Rev.* **2009,** *38,* 781–796. doi:10.1039/b800408k
15. Tschierske, C. *J. Mater. Chem.* **2001,** *11,* 2647–2671. doi:10.1039/b102914m
16. Goodby, J. W.; Bruce, D. W.; Hird, M.; Imrie, C.; Neal, M. *J. Mater. Chem.* **2001,** *11,* 2631–2636. doi:10.1039/b108757f
17. Tschierske, C. *Nature* **2002,** *419,* 681–683. doi:10.1038/419681a
18. Amaranatha Reddy, R.; Tschierske, C. *J. Mater. Chem.* **2006,** *16,* 907–961. doi:10.1039/b504400f
19. Kato, T.; Hirai, Y.; Nakaso, S.; Moriyama, M. *Chem. Soc. Rev.* **2007,** *36,* 1857–1867. doi:10.1039/b612546h
20. Lehmann, M. *Chem.–Eur. J.* **2009,** *15,* 3638–3651. doi:10.1002/chem.200802625
21. Marcos, M.; Martín-Rapún, R.; Omenat, A.; Serrano, J. L. *Chem. Soc. Rev.* **2007,** *36,* 1889–1901. doi:10.1039/b611123h
22. Imrie, C. T.; Henderson, P. A. *Chem. Soc. Rev.* **2007,** *36,* 2096–2124. doi:10.1039/b714102e
23. Kato, T. *Science* **2002,** *295,* 2414–2418.
24. Kato, T.; Mizoshita, N. *Curr. Opin. Solid State Mater. Sci.* **2002,** *6,* 579–587. doi:10.1016/S1359-0286(03)00006-8
25. Saez, I. M.; Goodby, J. W. *J. Mater. Chem.* **2005,** *15,* 26–40. doi:10.1039/b413416h
26. Tschierske, C. *Chem. Soc. Rev.* **2007,** *36,* 1930–1970. doi:10.1039/b615517k
27. Hirai, Y.; Monobe, H.; Mizoshita, N.; Moriyama, M.; Hanabusa, K.; Shimizu, Y.; Kato, T. *Adv. Funct. Mater.* **2008,** *18,* 1668–1675. doi:10.1002/adfm.200701313

28. Kato, T.; Mizoshita, N.; Kishimoto, K. *Angew. Chem., Int. Ed.* **2006,** *45,* 38–68. doi:10.1002/anie.200501384

29. Kato, T.; Yasuda, T.; Kamikawa, Y.; Yoshio, M. *Chem. Commun.* **2009,** 729–739. doi:10.1039/b816624b

30. Tam-Chang, S.-W.; Huang, L. *Chem. Commun.* **2008,** 1957–1967. doi:10.1039/b714319b

31. Low, P. J. *Dalton Trans.* **2005,** 2821–2824. doi:10.1039/b506017f

32. Serrano, J. L. *Metallomesogens;* VCH: Weinheim, 1996.

33. Donnio, B.; Bruce, D. W. In *Liquid Crystals II Metallomesogens;* Mingos, D. M. P., Ed.; Structure and Bonding, Vol. 95; Springer: Berlin, 1999.

34. Donnio, B.; Guillon, D.; Deschenaux, R.; Bruce, D. W. Metallomesogens. In *Comprehensive Coordination Chemistry II;* McCleverty, J. A.; Meyer, T. J., Eds.; Elsevier: Oxford, 2003; Vol. 6.

35. Date, R. W.; Iglesias, E. F.; Rowe, K. E.; Elliott, J. M.; Bruce, D. W. *Dalton Trans.* **2003,** 1914–1931. doi:10.1039/b212610a

36. Bruce, D. W.; Deschenaux, R.; Donnio, B.; Guillon, D. Organometallic Metallomesogens. In *Comprehensive Organometallic Chemistry III;* Crabtree, R. H.; Mingos, D. M. P., Eds.; Elsevier: Oxford, U.K., 2006; Vol. 12, Chapter 12.05, pp 195–294.

37. Porta, B.; Khamsi, J.; Noveron, J. C. *Curr. Org. Chem.* **2008,** *12,* 1298–1321. doi:10.2174/138527208785909565

38. Ghedini, M.; Aiello, I.; Crispini, A.; Golemme, A.; La Deda, M.; Pucci, D. *Coord. Chem. Rev.* **2006,** *250,* 1373–1390. doi:10.1016/j.ccr.2005.12.011

39. Rotkiewicz, K.; Grellmann, K. H.; Grabowski, Z. R. *Chem. Phys. Lett.* **1973,** *19,* 315–318. doi:10.1016/0009-2614(73)80367-7

40. Bhattacharyya, K.; Chowdhury, M. *Chem. Rev.* **1993,** *93,* 507–535. doi:10.1021/cr00017a022

41. Hicks, J.; Vandersall, M.; Babarogic, Z.; Eisenthal, K. B. *Chem. Phys. Lett.* **1985,** *116,* 18–24. doi:10.1016/0009-2614(85)80117-2

42. Golini, C. M.; Williams, B. W.; Foresman, J. B. *J. Fluoresc.* **1998,** *8,* 395–404. doi:10.1023/A:1020584801600

43. Dutta, A. K.; Kamada, K.; Ohta, K. *J. Photochem. Photobiol., A: Chem.* **1996,** *93,* 57–64. doi:10.1016/1010-6030(95)04140-0

44. Hazra, P.; Chakrabarty, D.; Chakraborty, A.; Sarkar, N. *Chem. Phys. Lett.* **2004,** *388,* 150–157. doi:10.1016/j.cplett.2004.02.078

45. Ghedini, M.; Pucci, D.; Crispini, A.; Bellusci, A.; La Deda, M.; Aiello, I.; Pugliese, T. *Inorg. Chem. Commun.* **2007,** *10,* 243–246. doi:10.1016/j.inoche.2006.10.032

46. Lo, K. K.-W.; Chung, C.-K.; Lee, T. K.-M.; Lui, L.-H.; Tsang, K. H.-K.; Zhu, N. *Inorg. Chem.* **2003,** *42,* 6886–6897. doi:10.1021/ic0346984

47. DePriest, J.; Zheng, G. Y.; Goswami, N.; Eichhorn, D. M.; Woods, C.; Rillema, D. P. *Inorg. Chem.* **2000,** *39,* 1955–1963. doi:10.1021/ic991306d

48. Simões, S.; Moreira, J. N.; Fonseca, C.; Düzgüneş, N.; Pedroso de Lima, M. C. *Adv. Drug Delivery Rev.* **2004,** *56,* 947–965. doi:10.1016/j.addr.2003.10.038

49. Pucci, D.; Bloise, R.; Bellusci, A.; Bernardini, S.; Ghedini, M.; Valentini, A.; Crispini, A. *Mol. Cryst. Liq. Cryst.* **2008,** *481,* 14–25. doi:10.1080/15421400701833981

50. Pucci, D.; Aiello, I.; Aprea, A.; Bellusci, A.; Crispini, A.; Ghedini, M. *Chem. Commun.* **2009,** 1550–1552. doi:10.1039/b818603k

51. Newkome, G. R.; Patri, A. K.; Holder, E.; Schubert, U. S. *Eur. J. Org. Chem.* **2004,** 235–254. doi:10.1002/ejoc.200300399

52. Pucci, D.; Barberio, G.; Crispini, A.; Francescangeli, O.; Ghedini, M.; La Deda, M. *Eur. J. Inorg. Chem.* **2003,** 3649–3661. doi:10.1002/ejic.200300223

53. Evans, R. C.; Douglas, P.; Winscom, C. J. *Coord. Chem. Rev.* **2006,** *250,* 2093–2126. doi:10.1016/j.ccr.2006.02.007

54. Xu, X.; Liao, Y.; Yu, G.; You, H.; Di, C.; Su, Z.; Ma, D.; Wang, Q.; Li, S.; Wang, S.; Ye, J.; Liu, Y. *Chem. Mater.* **2007,** *19,* 1740–1748. doi:10.1021/cm062960b

55. Son, H.-J.; Han, W.-S.; Chun, J.-Y.; Kang, B.-K.; Kwon, S.-N.; Ko, J.; Han, S.-J.; Lee, C.; Kim, S. J.; Kang, S. O. *Inorg. Chem.* **2008,** *47,* 5666–5676. doi:10.1021/ic702491j

56. Barberio, G.; Bellusci, A.; Crispini, A.; Ghedini, M.; Golemme, A.; Prus, P.; Pucci, D. *Eur. J. Inorg. Chem.* **2005,** 181–188. doi:10.1002/ejic.200400528

57. Binnemans, K. *J. Mater. Chem.* **2009,** *19,* 448–453. doi:10.1039/b811373d

58. Sapochak, L. S.; Burrows, P. E.; Garbuzov, V.; Ho, D. M.; Forrest, S. R.; Thompson, M. E. *J. Phys. Chem.* **1996,** *100,* 17766–17771. doi:10.1021/jp961770t

59. Tan, S.; Zhao, B.; Zou, Y.; Xiao, Z.; Wang, X.; Yu, G.; Liu, Y.; Zhu, D. *J. Mater. Sci.* **2004,** *39,* 1405–1406. doi:10.1023/B:JMSC.0000013904.51380.d7

60. Sapochak, L. S.; Padmaperuma, A.; Washton, N.; Endrino, F.; Schmett, G. T.; Marshall, J.; Fogarty, D.; Burrows, P. E.; Forrest, S. R. *J. Am. Chem. Soc.* **2001,** *123,* 6300–6307. doi:10.1021/ja010120m

61. Pucci, D.; Aiello, I.; Bellusci, A.; Crispini, A.; De Franco, I.; Ghedini, M.; La Deda, M. *Chem. Commun.* **2008,** 2254–2256. doi:10.1039/b800030a

62. Crispini, A.; Aiello, I.; La Deda, M.; De Franco, I.; Amati, M.; Lelj, F.; Ghedini, M. *Dalton Trans.* **2006,** 5124–5134. doi:10.1039/b606895b

Saddle-shaped tetraphenylenes with peripheral gallic esters displaying columnar mesophases

Eugen Wuckert[1], Constanze Hägele[2], Frank Giesselmann[2], Angelika Baro[1] and Sabine Laschat[*1]

Abstract

Tetraphenylenes **2** with eight peripheral gallic esters were prepared in two steps from octamethoxytetraphenylene **1** in 19–72% yield. Investigation of the mesomorphic properties of **2** by DSC, POM and X-ray diffraction revealed that derivatives **2a–d** with short alkoxy chain lengths (C_5–C_8) did not show any mesomorphic properties, whereas compounds **2e–i** with C_9–C_{13} chains displayed rectangular columnar mesophases and compounds **2j–l** with C_{14}–C_{16} chains displayed hexagonal columnar mesophases. Furthermore an anomalous odd-even effect of the clearing points of compounds **2e–l** versus chain length was detected.

Introduction

Columnar liquid crystals have received increasing interest during the last decade due to their 1D charge transport and self-healing properties, which make them particularly promising candidates for organic field effect transistors, organic photovoltaic devices and light emitting diodes [1-3]. Tetraphenylenes, whose saddle-shaped conformation is caused by the antiaromatic character of the corresponding central flat 8-membered ring [4-6], are suitable building blocks for supramolecular chemistry, asymmetric catalysis and formation of inclusion complexes [3-28]. We have shown that tetraphenylenes with eight peripheral alkoxy or alkanoate chains display thermo-

tropic columnar and smectic mesophases [29,30]. Furthermore, anomalous odd-even effects were discovered for these discotic tetraphenylenes, i.e. the ascending and descending transition temperatures with increasing numbers of methylene groups in the side chain exhibit an inversion of this alternation between $n = 12$ and $n = 14$ homologues [31]. In order to explore whether this anomalous odd-even effect is a more general phenomenon, the corresponding gallic ester-substituted tetraphenylenes were prepared and their liquid crystalline properties were investigated. In addition, we were curious about the mesophase types, because tetraphenylenes with peripheral alkoxy or alkanoate

chains displayed smectic mesophases in addition to columnar phases, whereas the corresponding tetraphenylenes with *p*-alkoxybenzoate substituents displayed only columnar mesophases even with long chain lengths [29-31]. Thus, we anticipated that the presence of the sterically demanding gallic esters in the periphery of the tetraphenylene can be accommodated much better by columnar packing as compared to a smectic layer structure. The results are discussed below.
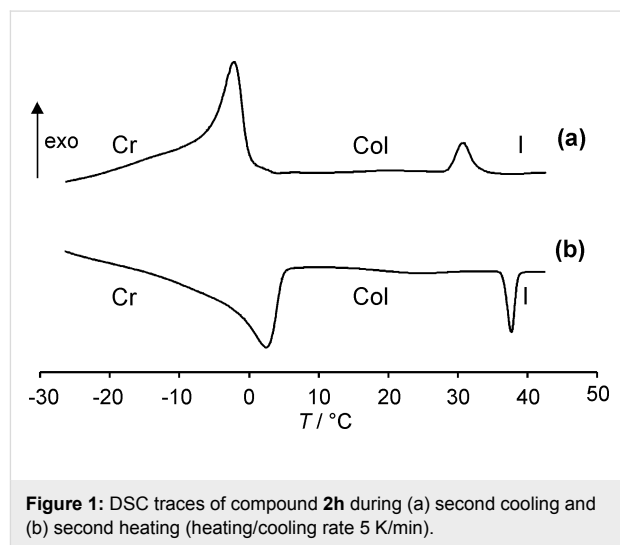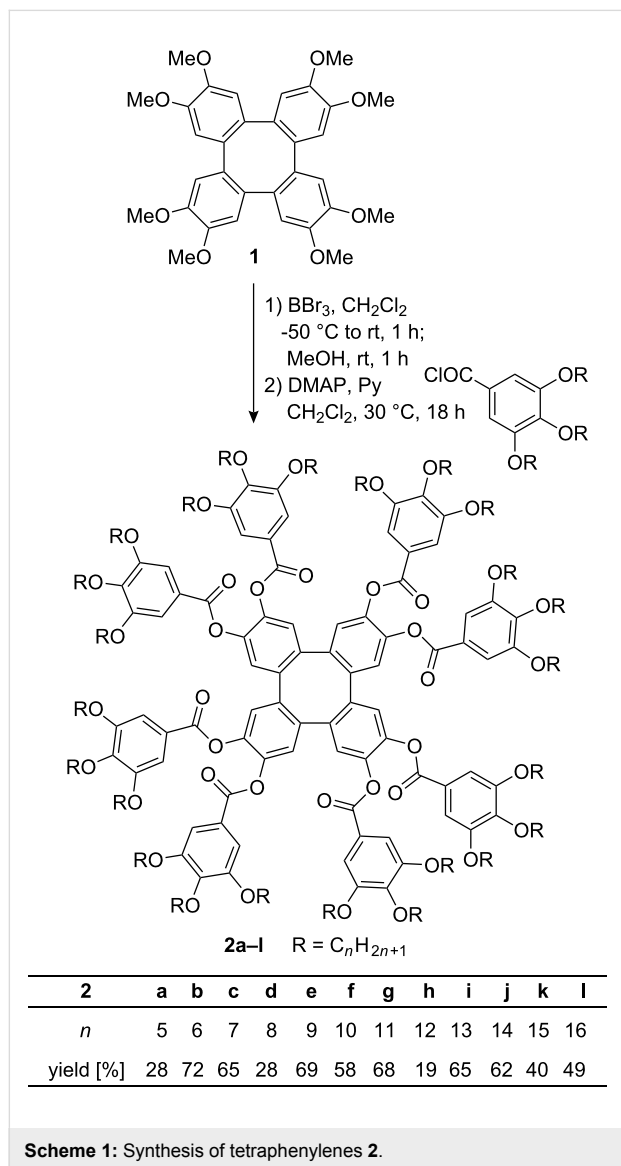
Results and Discussion

The synthesis started from the known octamethoxytetraphenylene **1** [4,19,20,29-31], which was demethylated with boron tribromide in CH_2Cl_2 at −50 °C to room temp. followed by hydrolysis with MeOH (Scheme 1). Subsequent treatment with gallic acid chlorides in the presence of catalytic amounts of DMAP in pyridine/CH_2Cl_2 yielded after aqueous workup and

chromatographic purification the desired gallic ester-substituted tetraphenylenes **2a–l** in 19–72%. In some cases purification turned out to be rather tedious resulting in decreased yields.

Mesomorphic properties of compounds **2** were studied by differential scanning calorimetry (DSC), polarizing optical microscopy (POM) and X-ray diffraction (WAXS, SAXS). The DSC results are summarized in Table 1.

While compounds **2a–d** with chain lengths up to C_8 showed only crystal to crystal transitions and isotropic melting, tetraphenylenes **2e–l** with chain lengths between C_9 and C_{16} displayed enantiotropic mesomorphism. For compounds **2e,f** additional crystal to crystal transitions were detected. A typical DSC curve is shown in Figure 1. Thus tetraphenylene **2h** with dodecyl chains displays a melting transition at 3 °C and a clearing transition at 36 °C upon second heating. Upon cooling an isotropic to mesophase transition at 33 °C and a crystallization peak at 0 °C were detected. The hysteresis phenomena observed for some compounds are probably due to supercooling, which is common for such highly viscous materials.

Figure 1: DSC traces of compound **2h** during (a) second cooling and (b) second heating (heating/cooling rate 5 K/min).

POM investigations revealed focal conic and fan-shaped textures typical for columnar mesophases (Figure 2).

However, clear evidence was possible only by XRD data, which are summarized in Table 2. While rectangular columnar mesophases were observed for tetraphenylenes **2e–i** with shorter chains (*n* = 9–13) (shown for **2f** in Figure S1 in the Supporting Information), hexagonal columnar mesophases were found for the long chain derivatives **2j–l** (*n* = 14–16) (shown for **2j** in Figure S2 in the Supporting Information). Indeed, as expected the columnar mesophase seems to accommodate the eight bulky gallic esters much better than the smectic layer structure.

2	a	b	c	d	e	f	g	h	i	j	k	l
n	5	6	7	8	9	10	11	12	13	14	15	16
yield [%]	28	72	65	28	69	58	68	19	65	62	40	49

Scheme 1: Synthesis of tetraphenylenes **2**.

Table 1: Phase transition temperatures [°C] and (enthalpies [kJ/mol])[a].

2	n	Cr$_1$	Cr$_2$		Cr$_3$		Col		I	
a	5	•	51 (10.1)	•	79 (4.4)	•	191 (15.3)	--	•	2. heating
b	6	•	46 (8.3)	•	69 (7.4)	•	142 (11.2)	--	•	2. heating
c	7	•	10 (1.7)	•	41 (0.6)	•	55 (0.6)	--	•	2. heating
d	8	•	4 (15.0)	•	41 (27.7)	•	62 (7.2)	--	•	2. heating
e	9	•	−6 (11.6)	•	35 (4.2)	--		•	37 (3.8)	•	2. heating
e	9	•	1 (−2.7)	•	11 (−0.8)	--		•	26 (−5.3)	•	2. cooling
f	10	•	7 (4.1)	•	40 (12.5)	--		•	46 (5.6)	•	2. heating
f	10	•	24 (−7.9)	--		--		•	39 (−5.7)	•	2. cooling
g	11	•	29 (7.4)	--		--		•	43 (1.0)	•	2. heating
g	11	•	20 (−7.6)	--		--		•	40 (−1.1)	•	2. cooling
h	12	•	3 (19.4)	--		--		•	36 (10.3)	•	2. heating
h	12	•	0 (−18.6)	--		--		•	33 (−9.7)	•	2. cooling
i	13	•	16 (18.5)	--		--		•	33 (11.9)	•	2. heating
i	13	•	13 (−18.9)	--		--		•	28 (−13.4)	•	2. cooling
j	14	•	16 (9.6)	--		--		•	41 (2.5)	•	2. heating
j	14	•	16 (−5.8)	--		--		•	29 (−1.8)	•	2. cooling
k	15	•	25 (8.0)	--		--		•	36 (20.1)	•	2. heating
k	15	•	20 (−10.3)	--		--		•	32 (−16.2)	•	2. cooling
l	16	--		--		--		•	41 (36.2)	•	2. heating
l	16	•	22 (−5.2)	--		--		•	36 (−17.3)	•	2. cooling

[a]Cr crystalline, Col columnar, I isotropic; • phase was observed, -- phase was not observed; heating/cooling rate 10 K/min for **2a–e,i,j**, 5 K/min for **2f–h,k,l**.

The crossover from rectangular columnar to hexagonal columnar mesophases with increasing chain lengths has been also observed in other columnar systems [32,33] and has been attributed to the enhanced core–core interaction necessary for the formation of the Col$_r$ phases [34]. According to molecular modelling [35] and comparison with the XRD data each disk within the hexagonal and rectangular columnar pattern is occu-pied by one tetraphenylene molecule. For better visibility only the modelled tetraphenylene (octakis)acyl core unit is shown in Figure 3, which reveals the saddle shape.

Next, the clearing points of mesogenic compounds **2e–l** were plotted against the chain lengths *n* (Figure 4). An anomalous odd-even effect can be seen, which inverts at *n* = 11.
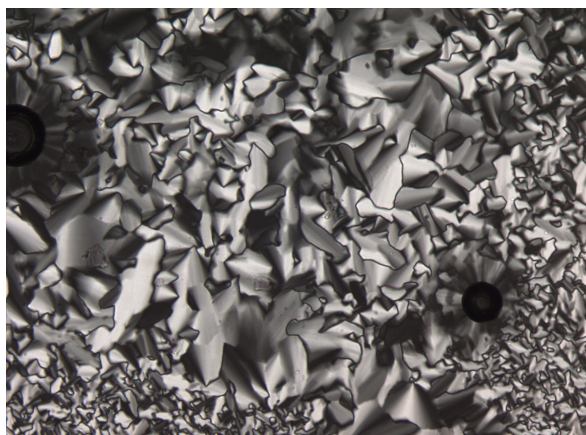

Figure 2: Texture of **2h** under the POM at 25 °C upon cooling from the isotropic liquid (heating/cooling rate 5 K/min; magnification 100×).
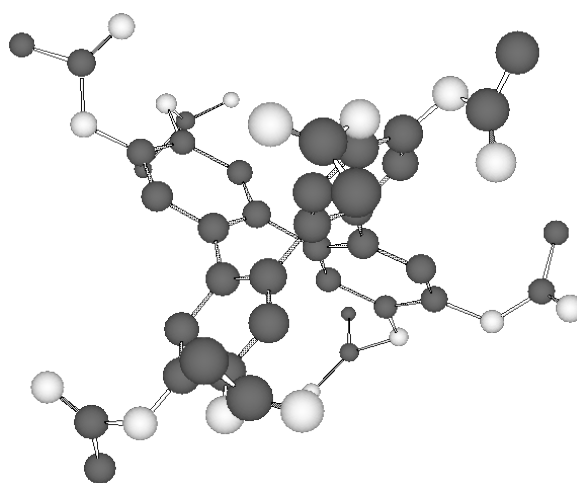

Figure 3: Molecular modelling of the saddle-shaped tetraphenylene (octakis)acyl core unit of **2** [35].

Table 2: X-Ray diffraction data for compounds **2e–l**[a].

2	T [°C]	θ [°]	d_{obs} [Å]	hk	d_{calc} [Å]	Mesophase parameters
2e	20	1.71	25.9	(20)	25.9	Col$_r$
		2.93	15.1	(11)	15.1	a = 51.8 Å
		3.33	13.3	(21)	13.5	b = 15.8 Å
2f	32	1.73	25.6	(20)	18.4	Col$_r$
		2.32	19.0	(11)	19.0	a = 51.2 Å
		3.34	13.2	(31)	13.1	b = 20.5 Å
2g	15	1.60	27.7	(20)	27.7	Col$_r$
		2.17	20.4	(11)	20.4	a = 55.4 Å
		3.14	14.1	(31)	14.1	b = 21.9 Å
2h	20	1.51	29.3	(20)	29.3	Col$_r$
		2.25	19.6	(11)	19.6	a = 58.6 Å
						b = 20.8 Å
2i	25	1.47	30.1	(20)	30.1	Col$_r$
		2.28	19.4	(11)	19.4	a = 60.3 Å
						b = 20.5 Å
2j	30	1.46	30.3	(10)	30.6	Col$_h$
		2.47	17.9	(11)	17.7	a = 35.3 Å
2k	20	1.40	31.6	(10)	31.9	Col$_h$
		2.39	18.5	(11)	18.4	a = 36.9 Å
		2.75	16.1	(20)	16.0	
		3.65	12.1	(21)	12.1	
2l	20	1.35	32.8	(10)	33.1	Col$_h$
		2.32	19.0	(11)	19.1	a = 38.2 Å
		3.50	12.6	(21)	12.5	

[a]Diffraction angle θ; observed and calculated diffraction spacings d_{obs} and d_{calc}; Miller indices hk.

For the previously studied tetraphenylene derivatives with alkoxy, alkanoate and *p*-alkoxybenzoate chains the inversion was observed at *n* = 12–13 [31]. Although in all four cases an anomalous odd-even effect is present, the chain length dependence of the clearing temperatures differs somewhat. For derivatives with alkoxy or alkanoate chains directly attached to the tetraphenylene unit, the oxygen atom is part of the chain and thus odd carbon chains are actually even-numbered. They
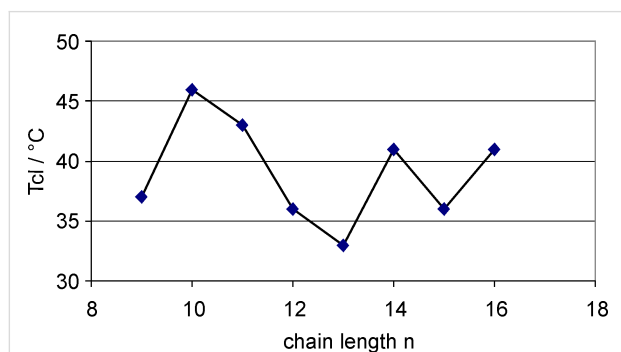

Figure 4: Clearing temperatures T_{cl} [°C] of tetraphenylenes **2e–l** as a function of the chain lengths *n*.

should thus have an elongated shape which should lead to a higher degree of orientational order and hence a higher clearing temperature than the odd-numbered chains (including oxygen), i.e. those with an even-number of carbon atoms. The data in Figure 4 suggest that for 3,4,5-trialkoxygallic esters **2** this argument does not hold and the orientational order and hence the clearing temperature is determined both by the alkoxy chain lengths as well as the rigid gallic acid moiety. In order to eliminate the influence of the alkyl side chain on the odd-even effect of the tetraphenylenes the melting temperatures T_m^{alk} of *n*-alkanes were subtracted from the clearing points T_{cl} of the respective tetraphenylenes **2** (Figure 5). An almost regular effect could be seen. Thus it seems that transition temperatures are also governed by the influence of the gallic ester moiety on the dynamic properties of the alkyl tails.

Conclusion

In conclusion, only columnar mesophases have been found for gallic ester-substituted tetraphenylenes **2e–l** with a minimum chain length of *n* = 9. An anomalous odd-even effect was detected, in which the alternation of the melting transition inverses at *n* = 11. The results agree with previous findings, and
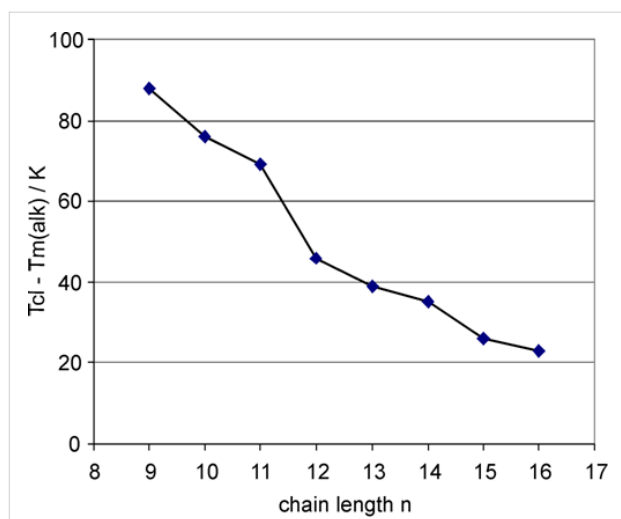
Figure 5: The differences between the clearing temperatures T_{cl} [°C] of tetraphenylenes **2** and the melting points T_m^{alk} of the *n*-alkanes exhibit an almost normal odd-even effect without any inversion of the alteration.

suggest that the anomalous odd-even effect is a more general phenomenon than previously thought. Investigations to extend this concept to other classes of liquid crystals are currently in progress.

Experimental
General

Melting points were measured on a Mettler Toledo DSC822 and are uncorrected. NMR spectra were recorded on a Bruker Avance 300 and Avance 500 spectrometer. FT-IR spectra were recorded on a Bruker Vektor22 spectrometer with MKII Golden Gate Single Reflection Diamant ATR system. Mass spectra were recorded on a Finnigan MAT 95 and a Varian MAT 711 apparatus. Small-angle scattering data from unaligned samples (filled into Mark capillary tubes of 0.7 mm diameter) were obtained using a Kratky compact camera (A. Paar) provided with a temperature controller (A. Paar) and a one-dimensional electronic detector (M. Braun). Aligned samples were exposed in a home-made flat-film camera and the 2D diffraction patterns recorded with an imaging plate detector (Fuji BAS SR). In the flat-film camera, the sample was placed in a small hole of a brass block, the temperature of which was controlled by a Lakeshore controller and kept in a 1.5 T magnetic field for alignment.

Differential scanning calorimetry (DSC) was performed using a Mettler Toledo DSC822, and polarizing optical microscopy (POM) using an Olympus BX50 polarizing microscope combined with a Linkam LTS350 hot stage and a Linkam TP93 central processor. Flash chromatography was performed using Kieselgel 60, 40–63 μm (Fluka). All solvents were dried, and

reactions were performed in dried glassware. The used petroleum ether (PE) had a boiling range of 30–75 °C. Octamethoxytetraphenylene **1** was prepared as described in ref. [31].

General procedure for the preparation of heptakis[(3,4,5-trialkoxybenzoyl)oxy]tetraphenylen-2-yl 3,4,5-trialkoxybenzoates (**2**)

To a solution of octamethoxytetraphenylene **1** (0.14 g, 0.25 mmol) in CH_2Cl_2 (2 mL) were added BBr_3 (2.2 mL, 2.2 mmol, 1 M solution in CH_2Cl_2) at −50 °C and the mixture was stirred for 1 h at room temp. The solvent was removed in vacuo and the residue was dissolved in degassed MeOH (5 mL) for 1 h and evaporated. The residue was dissolved in CH_2Cl_2 (2 mL), treated with DMAP (4 mg, 0.03 mmol) and pyridine (1 mL) and gallic acid chloride (5 mmol) were added dropwise. After stirring overnight at 30 °C, the mixture was diluted with CH_2Cl_2 (10 mL), hydrolyzed with 2 M HCl and the layers separated. The aqueous layer was extracted with CH_2Cl_2 (2 × 10 mL), the organic layers were washed with sat. $NaHCO_3$ (10 mL), H_2O (10 mL), dried over $MgSO_4$ and concentrated in vacuo. The crude product was purified by column chromatography on SiO_2 (hexanes/ethyl acetate 20 : 1) to yield colorless waxy solids.

3,6,7,10,11,14,15-Heptakis[(3,4,5-dodecyloxybenzoyl)oxy]tetraphenylen-2-yl 3,4,5-tridodecyloxybenzoate (**2h**)

270 mg (19%) of a colorless solid. ^{1}H NMR (500 MHz, $CDCl_3$): δ = 0.85–0.89 (m, 72H), 1.25–1.49 (m, 432H), 1.70–1.75 (m, 48H), 3.79–3.86 (m, 32H), 3.98 (t, *J* = 6.5 Hz, 16H), 7.24 (s, 16H), 7.39 (s, 8H) ppm. ^{13}C NMR (125 MHz, $CDCl_3$): δ = 14.1, 22.7, 26.1, 26.2, 29.4, 29.4, 29.5, 29.6, 29.7, 29.7, 29.8, 29.8, 30.4, 32.0, 69.0, 73.5, 108.3, 123.0, 124.5, 138.1, 142.0, 143.0, 152.9, 163.8 ppm. FT-IR (ATR): ν = 2921 (vs), 2852 (s), 1976 (w), 1743 (m), 1585 (m), 1499 (w), 1466 (w), 1430 (m), 1390 (w), 1335 (s), 1291 (w), 1240 (w), 1190 (s), 1114 (s), 947 (w), 802 (w), 748 (w), 623 (m), 546 (w) cm^{-1}. UV/VIS (*n*-hexane): λ_{max} (lg ε_{max}) = 275 (5.15), 214 (5.60) nm. $C_{368}H_{624}O_{40}$ (5688.9) calcd. C 77.69, H 11.06; found: C 77.74, H 10.95.

Supporting Information

Supporting information includes experimental and spectroscopic data for compounds **2a–f**, **2g–l**, and X-ray diffraction measurements of derivatives **2f,j**.

Supporting Information File 1
Analytical data of compounds **2a–f**, **2g–l**.
[http://www.beilstein-journals.org/bjoc/content/supplementary/1860-5397-5-57-S1.pdf]

Acknowledgments

References

1. Laschat, S.; Baro, A.; Steinke, N.; Giesselmann, F.; Hägele, C.; Scalia, G.; Judele, R.; Kapatsina, E.; Sauer, S.; Schreivogel, A.; Tosoni, M. *Angew. Chem.* **2007,** *119,* 4916–4973. doi:10.1002/ange.200604203
   Angew. Chem., Int. Ed. **2007,** *46,* 4832–4887. doi:10.1002/anie.200604203 (Review).

2. Sergeyev, S.; Pisula, W.; Geerts, Y. H. *Chem. Soc. Rev.* **2007,** *36,* 1902–1929. doi:10.1039/b417320c
   (Review).

3. Tschierske, C. *Annu. Rep. Prog. Chem., Sect. C: Phys. Chem.* **2001,** *97,* 191–267. doi:10.1039/b101114f
   (Review).

4. Rathore, R.; Le Magueres, P.; Lindeman, S. V.; Kochi, J. K. *Angew. Chem.* **2000,** *112,* 818–821. doi:10.1002/(SICI)1521-3757(20000218)112:4<818::AID-ANGE818>3.0.CO;2-#
   Angew. Chem., Int. Ed. **2000,** *39,* 809–812. doi:10.1002/(SICI)1521-3773(20000218)39:4<809::AID-ANIE809>3.0.CO;2-6

5. Iyoda, M.; Kabir, S. M. H.; Vorasingha, A.; Kuwatani, Y.; Yoshida, M. *Tetrahedron Lett.* **1998,** *39,* 5393–5396. doi:10.1016/S0040-4039(98)01082-X

6. Irngartinger, H.; Reibel, W. R. K. *Acta Crystallogr., Sect. B* **1981,** *37,* 1724–1728. doi:10.1107/S0567740881006985

7. Huang, H.; Hau, C.-K.; Law, C. C. M.; Wong, H. N. C. *Org. Biomol. Chem.* **2009,** *7,* 1249–1257. doi:10.1039/b818029f

8. Rajca, A.; Rajca, S.; Pink, M.; Miyasaka, M. *Synlett* **2007,** 1799–1822. doi:10.1055/s-2007-984538
   (Review).

9. Hou, X.-L.; Huang, H.; Wong, H. N. C. *Synlett* **2005,** 1073–1089. doi:10.1055/s-2005-865213
   (Review).

10. Mak, T. C. W.; Wong, H. N. C. In *Comprehensive Supramolecular Chemistry;* MacNicol, D. D.; Toda, F.; Bishop, R., Eds.; Elsevier: Oxford, U.K., 1996; Vol. 6, pp 351–369.
    (Review).

11. Mak, T. C. W.; Wong, H. N. C. *Top. Curr. Chem.* **1987,** *140,* 141–164. doi:10.1007/BFb0003839
    (Review).

12. Huang, H.; Stewart, T.; Gutmann, M.; Ohhara, T.; Niimura, N.; Li, Y.-X.; Wen, J.-F.; Bau, R.; Wong, H. N. C. *J. Org. Chem.* **2009,** *74,* 359–369. doi:10.1021/jo802061p

13. Wu, A.-H.; Hau, C.-K.; Wong, H. N. C. *Adv. Synth. Catal.* **2007,** *349,* 601–608. doi:10.1002/adsc.200600499

14. Peng, H.-Y.; Lam, C.-K.; Mak, T. C. W.; Cai, Z.; Ma, W.-T.; Li, Y.-X.; Wong, H. N. C. *J. Am. Chem. Soc.* **2005,** *127,* 9603–9611. doi:10.1021/ja051013l

15. Hui, C. W.; Mak, T. C. W.; Wong, H. N. C. *Tetrahedron* **2004,** *60,* 3523–3531. doi:10.1016/j.tet.2004.02.022

16. Wen, J.-F.; Hong, W.; Yuan, K.; Mak, T. C. W.; Wong, H. N. C. *J. Org. Chem.* **2003,** *68,* 8918–8931. doi:10.1021/jo0302408

17. Lai, C. W.; Lam, C. K.; Lee, H. K.; Mak, T. C. W.; Wong, H. N. C. *Org. Lett.* **2003,** *5,* 823–826. doi:10.1021/ol020253s

18. Rajca, A.; Wang, H.; Bolshov, P.; Rajca, S. *Tetrahedron* **2001,** *57,* 3725–3735. doi:10.1016/S0040-4020(01)00241-1

19. Kabir, S. M. H.; Hasegawa, M.; Kuwatani, Y.; Yoshida, M.; Matsuyama, H.; Iyoda, M. *J. Chem. Soc., Perkin Trans. 1* **2001,** 159–165. doi:10.1039/b006375o

20. Kabir, S. M. H.; Iyoda, M. *Synthesis* **2000,** 1839–1842. doi:10.1055/s-2000-8239

21. Yang, X.-P.; Du, D.-M.; Li, Q.; Mak, T. C. W.; Wong, H. N. C. *Chem. Commun.* **1999,** 1607–1608. doi:10.1039/a904144c

22. Rajca, A.; Safronov, A.; Rajca, S.; Shoemaker, R. *Angew. Chem.* **1997,** *109,* 504–507. doi:10.1002/ange.19971090510
    Angew. Chem., Int. Ed. Engl. **1997,** *36,* 488–491. doi:10.1002/anie.199704881

23. Wang, X. M.; Hou, X.; Zhou, Z.; Mak, T. C. W.; Wong, H. N. C. *J. Org. Chem.* **1993,** *58,* 7498–7506. doi:10.1021/jo00078a031

24. Man, Y. M.; Mak, T. C. W.; Wong, H. N. C. *J. Org. Chem.* **1990,** *55,* 3214–3221. doi:10.1021/jo00297a043

25. Rashidi-Ranjbar, P.; Man, Y. M.; Sandstroem, J.; Wong, H. N. C. *J. Org. Chem.* **1989,** *54,* 4888–4892. doi:10.1021/jo00281a034

26. Wong, H. N. C.; Man, Y.-M.; Mak, T. C. W. *Tetrahedron Lett.* **1987,** *28,* 6359–6362. doi:10.1016/S0040-4039(01)91373-5

27. Wong, H. N. C.; Luh, T. Y.; Mak, T. C. W. *Acta Crystallogr., Sect. C* **1984,** *40,* 1721–1723. doi:10.1107/S0108270184009288

28. Wong, H. N. C.; Sondheimer, F. *Tetrahedron* **1981,** *37,* 99–109. doi:10.1016/0040-4020(81)85045-4

29. Wuckert, E.; Laschat, S.; Baro, A.; Hägele, C.; Giesselmann, F.; Luftmann, H. *Liq. Cryst.* **2006,** *33,* 103–107. doi:10.1080/02678290500277953

30. Wuckert, E.; Dix, M.; Laschat, S.; Baro, A.; Schulte, J. L.; Hägele, C.; Giesselmann, F. *Liq. Cryst.* **2004,** *31,* 1305–1309. doi:10.1080/02678290412331312051

31. Hägele, C.; Wuckert, E.; Laschat, S.; Giesselmann, F. *ChemPhysChem* **2009,** *10,* 1291–1298. doi:10.1002/cphc.200900090

32. Lai, C. K.; Tsai, C.-H.; Pang, Y.-S. *J. Mater. Chem.* **1998,** *8,* 1355–1360. doi:10.1039/a800657a

33. Zheng, H.; Lai, C. K.; Swager, T. M. *Chem. Mater.* **1995,** *7,* 2067–2077. doi:10.1021/cm00059a013

34. Tinh, N. H.; Levelut, A. M.; Malthête, J. *Mol. Cryst. Liq. Cryst.* **1984,** *106,* 121–146. doi:10.1080/00268948408080183

35. Chem3D Pro 7.0 Software was used for molecular modelling.

License and Terms

Coaxial electrospinning of liquid crystal-containing poly(vinylpyrrolidone) microfibres

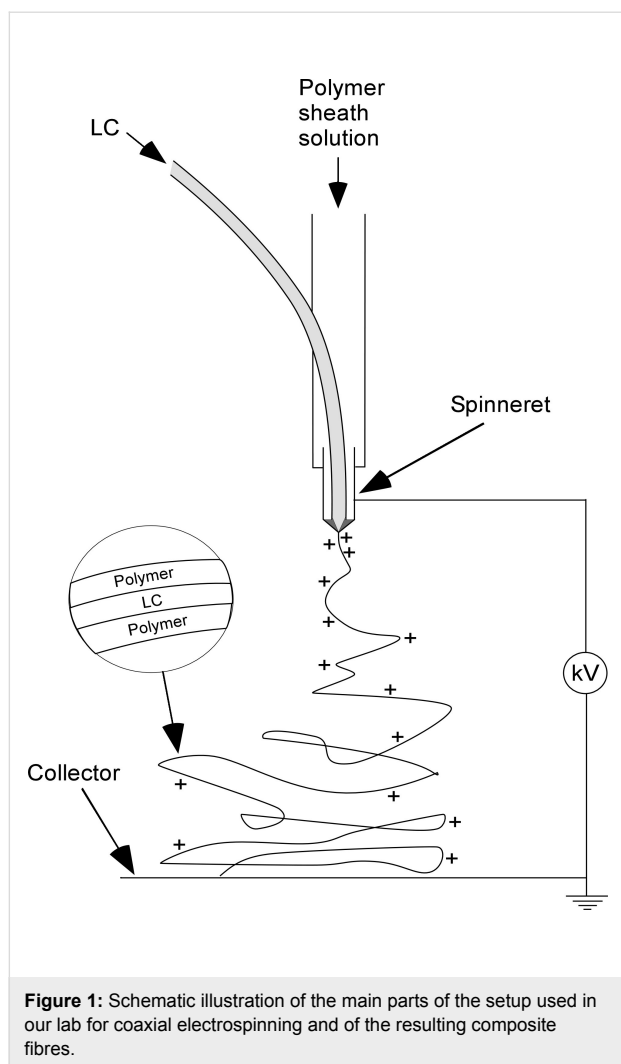Eva Enz, Ute Baumeister and Jan Lagerwall[*]

Abstract

With the relatively new technique of coaxial electrospinning, composite fibres of poly(vinylpyrrolidone) with the liquid crystal 4-cyano-4′-octylbiphenyl in its smectic phase as core material could be produced. The encapsulation leads to remarkable confinement effects on the liquid crystal, inducing changes in its phase sequence. We conducted a series of experiments to determine the effect of varying the relative flow rates of inner and outer fluid as well as of the applied voltage during electrospinning on these composite fibres. From X-ray diffraction patterns of oriented fibres we could also establish the orientation of the liquid crystal molecules to be parallel to the fibre axis, a result unexpected when considering the viscosity anisotropy of the liquid crystal kept in its smectic phase during electrospinning.

Introduction

Electrospinning is a versatile process for producing nano- and microfibrous materials through electrostatic means. Even though the basic principles have been known for a long time and the first patents on electrospinning go back to 1902 [1,2], there has been a revival of interest since the beginning of the 1990s [3-6]. For laboratory scale purposes the simplest setup for electrospinning consists of three main components: a chargeable spinneret (e.g. a metallic needle) through which a polymer solution or melt is pumped, a grounded collector (e.g. an aluminium foil) and a high voltage power supply connecting spinneret and collector (see Figure 1).

The mechanism behind the electrospinning process is driven by an interplay of electrostatic forces and the surface tension of the polymer solution [5,7]. By applying a high DC voltage (several kV) between the spinneret and ground, surface charges are induced in a droplet of polymer solution protruding from the end of the spinneret, which then deforms into a so-called Taylor cone. When the electrostatic repulsion between the induced charges together with the coulomb force of the applied field become strong enough to overcome the surface tension, a liquid jet is ejected from the cone. This highly charged liquid jet experiences an electrostatic self-repulsion leading to a whip-

Figure 1: Schematic illustration of the main parts of the setup used in our lab for coaxial electrospinning and of the resulting composite fibres.

ping motion and stretching process on its way to the collector, the latter leading to a dramatic reduction of fibre diameter. During this process most of the solvent must be evaporated, so that a stable, essentially dry fibre (the length of which in the ideal case is determined only by the time spinning is continued) is collected on a target substrate. This collection can be made on glass slides placed on the collector during electrospinning, resulting in a randomly oriented, nonwoven mat. Beside this, oriented fibres can also be achieved by modification of the target, e.g. by using two parallel electrodes as collector [8]. A recent review on different electrospinning setup designs is given in [9].

The morphology and final diameter of the resulting fibres can be influenced by several parameters, which can be divided into two categories: intrinsic properties of the polymer solution, and operational conditions. The most important are: type of polymer and its concentration; viscosity, electrical conductivity, polarity and surface tension of the solvent; applied electric field,

distance between spinneret and collector, flow rate of the polymer solution and also the humidity and temperature of the surroundings, since they influence the evaporation of the solvent.

An interesting variation of electrospinning is the use of a spinneret comprising two coaxial capillaries, allowing two different liquids to be spun, one inside the other, leading to a composite fibre with core–sheath structure [10-12]. Recently it could be shown that also a room temperature nematic liquid crystal (LC) can be coaxially spun with a composite sheath of TiO_2 and poly(vinylpyrrolidone) (PVP) [13]. Such composite fibres with a core exhibiting the responsiveness and special properties (in particular optical) that result from the unique combination of fluidity and long-range order of liquid crystals are interesting from different points of view. On the one hand, the LC can give the fibre new functionality, in particular sensitivity to temperature variations or to the application of electric and/or magnetic fields, on the other the strong confinement that can be achieved by the process can affect the LC phase sequence [14]. Electrospinning offers a cheap and simple way of studying such confinement effects systematically.

In this work we present our results on composites of PVP as sheath and the liquid crystal 4-cyano-4′-octylbiphenyl (8CB) as core produced by coaxial electrospinning. The latter LC exhibits a smectic phase (phase sequence: cryst. 20.5 SmA 32.0 N 39.2 iso.) in contrast to the LC used in our previous work, which formed only a nematic liquid crystal phase. After some general remarks on the properties of these composites, we show in the first part a systematic study on fibres with different content of LC core. Secondly we studied the influence of the magnitude of the applied voltage on the fibres. Finally we show X-ray investigations on these materials and discuss the orientation of the LC based on these results.

Results and Discussion

All fibres were spun at room temperature, i.e. with the LC in its smectic phase. In the resulting fibres the PVP sheaths were transparent and isotropic so that one could directly observe the birefringent liquid crystal core through a polarising optical microscope (POM) and follow the phase sequence (Figure 2). The fibres are thermally stable enough to allow repeated heating into the isotropic phase of the contained liquid crystal and cooling to room temperature again without any change in appearance. In differential scanning calorimetry (DSC) investigations only the transitions of the liquid crystal are found up to about 100 °C, where decomposition of the PVP sheath starts to take place. When fully dried the fibres also show good mechanical stability so that they can be pulled from the glass slide and folded or rolled together.
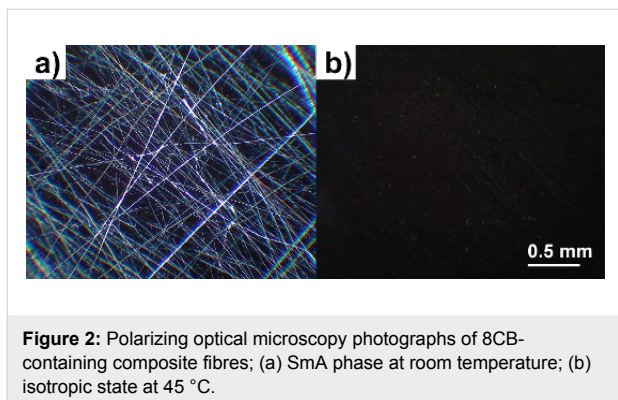
Figure 2: Polarizing optical microscopy photographs of 8CB-containing composite fibres; (a) SmA phase at room temperature; (b) isotropic state at 45 °C.

Variation of the extent of LC filling

In this part we will discuss characteristic examples of a series of composite fibres in which the flow rate of the polymer solution was kept constant at $\dot{V}_{out}$ = 125 µl h^{-1}, while the flow rate of the LC was increased stepwise: $\dot{V}_{in}$ = 5, 20, 45, 70, 115, 145, 190 and 215 µl h^{-1}. In the upper row of Figure 3 non-polarising microscopy pictures of these samples are shown, while the lower row displays the corresponding POM pictures.

At the smallest flow rate presented here no liquid crystal is visible inside the resulting fibres (Figure 3a). At 20 µl h^{-1} droplets of LC appear in many of the fibres, the thicker ones being visible also in the non-POM photos as darker spots inside the fibres (Figure 3b). In the next sample (45 µl h^{-1}, Figure 3c) the droplets have transformed into elongated segments. Such a transformation upon increasing flow rate of the inner fluid has been predicted by numerical modelling of the coaxial electrospinning process [15]. Depending on the exact spinning conditions either a bubbly slug or annular flow pattern may result. On the other hand there are still many parts of the fibre samples where no LC seems to be present at all.

When increasing the LC flow rate to 145 µl h^{-1} almost all fibres, besides some very thin ones, are (partially) filled with the liquid crystal while the diameter of the deposited fibres grows substantially (Figure 3d). At points where many fibres meet they fuse. This tendency is further increased in the last sample in Figure 3e. The smeared-out morphology in this last texture strongly suggests that the fibre still contained substantial amounts of solvent upon collection. The liquid state of such a deposited material then allowed a post-collection morphology change, ruining the desired coaxial fibre structure.

Measuring the exact outer and inner fibre diameter by optical microscopy is quite difficult for such small structures, but we can give reasonably accurate estimates at least for the outer diameter. We determined the mean, minimal and maximal outer diameter of the filled fibres by measuring the diameter at 50 points of each sample. The resulting values are plotted in Figure 4, taking unfilled pure PVP fibres as reference. As one can see, up to the sample with $\dot{V}_{in}$ = 70 µl h^{-1} all three determined kinds of diameter are unchanged compared to the sample without liquid crystal, within the accuracy of this kind of measurement. With further increasing content of LC core, the smallest found diameters are still in the same range as before, but the mean diameter and especially the largest found diameter increase strongly. In the last samples this may be partly because of the smearing out of the fibres as described at the end of the previous paragraph. But at least for the two highest flow rates the LC core visible in the non-POM photographs is as thick as the whole fibres in the first samples (see for Figure 3d1 and Figure 3e1).

DSC thermograms of these fibres are presented in Figure 5, as well as the thermogram of bulk 8CB for comparison. The effect of confinement on the LC phase sequence can be clearly seen.
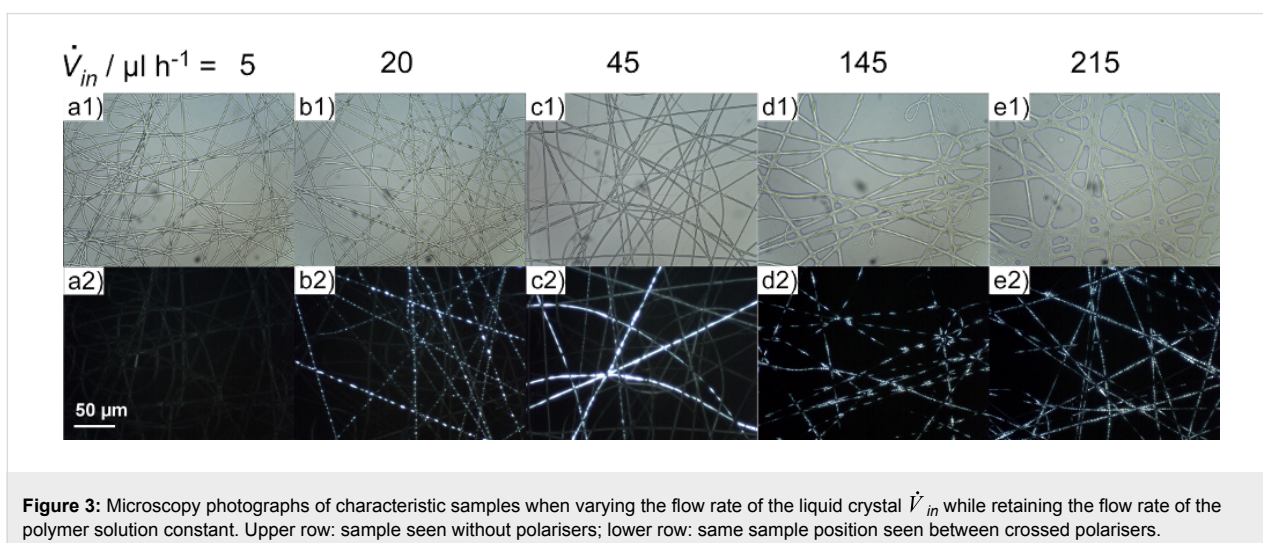

Figure 3: Microscopy photographs of characteristic samples when varying the flow rate of the liquid crystal $\dot{V}_{in}$ while retaining the flow rate of the polymer solution constant. Upper row: sample seen without polarisers; lower row: same sample position seen between crossed polarisers.
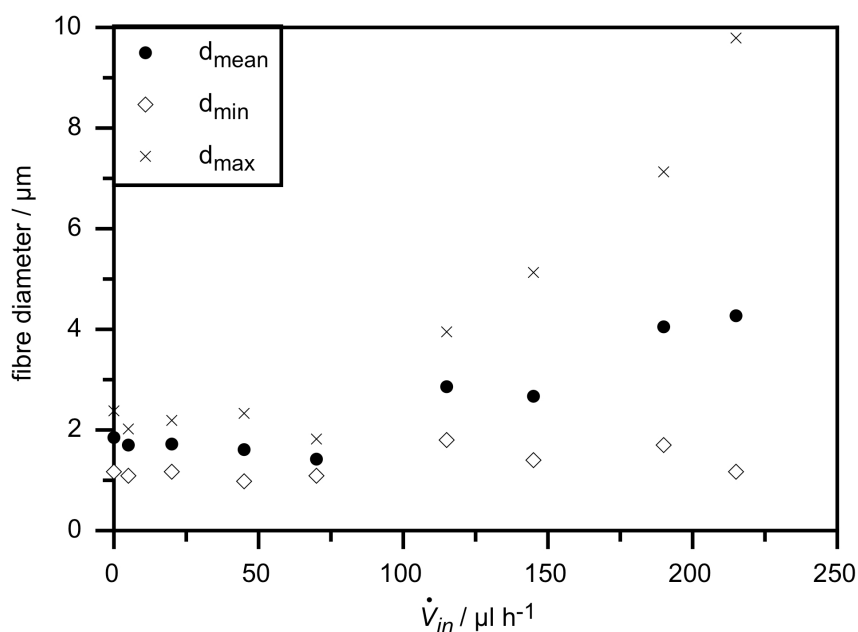
Figure 4: Outer fibre diameters as a function of LC flow rate as determined from 50 measurements by optical microscopy on each sample.
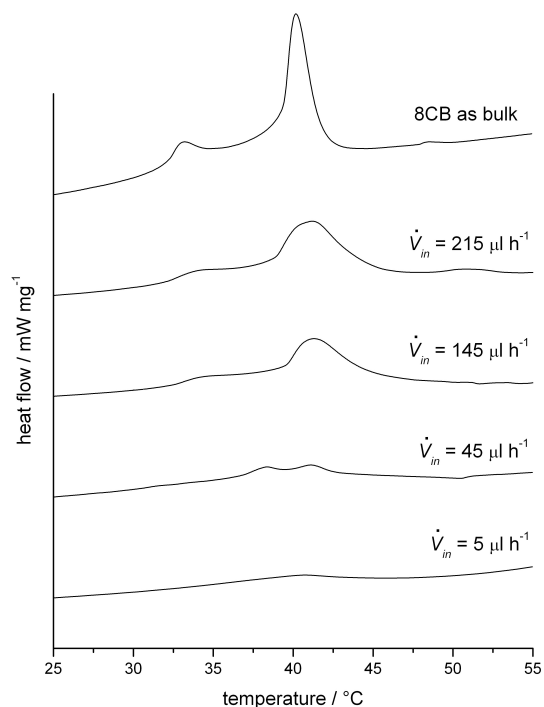

Figure 5: DSC thermograms on heating of 8CB as bulk and as inclusion compound in PVP fibres produced with different flow rates of the LC ($\dot{V}_{in}$).

In the fibres the clearing peak is broadened and shifted towards higher temperatures compared to the bulk LC, but between the different fibres the clearing point variations are small. The smectic to nematic transition, on the other hand, is shifted to higher temperatures with decreasing LC content of the fibres until it finally disappears in the last shown sample ($\dot{V}_{in} = 5$ μl h^{-1}). During this process the shape of this transition in the thermogram transforms continuously from a peak in the bulk to a step, signifying a change from (weakly) first- to second-order character of the transition.

Another remarkable effect is that in the thermograms obtained for $\dot{V}_{in} = 20$ μl h^{-1} and 45 μl h^{-1} during a first heating experiment the SmA-N as well as the clearing transition were visible, but in the cooling run and in a subsequent second heating experiment only the N-iso. transition was found and it was shifted towards lower temperatures. This change in the effective phase sequence could be verified by textural observations during a similar experiment in the microscope. When repeating the DSC heating scan after having kept the sample at room temperature for several weeks, again two peaks were found, just like at the very beginning. We interpret these findings as a strong supercooling effect on the smectic phase, meaning that transformation from the nematic to smectic phase is kinetically hindered in the encapsulated liquid crystal, most likely due to mesogen anchoring without positional order at the inner surface of the polymer sheath. So, after heating into the isotropic phase,

on subsequent cooling the smectic phase cannot be formed immediately even though it is the thermodynamically stable phase at room temperature.

Conversely, the same phenomenon explains the increase of the SmA-N transition on initial heating as the fibre diameter is made thinner (Figure 5): if the smectic phase is present in the fibre the layer geometry will be retained even when the temperature is raised somewhat above that where a bulk sample becomes nematic, because the mesogens at the inner sheath surface are anchored in the smectic configuration, with 1D positional order, and the extreme surface-to-volume ratio in a thin fibre gives these surface molecules a much stronger than usual influence on the whole sample behaviour. This reasoning presumes a planar anchoring of the mesogens at the sheath surface, a geometry that was confirmed by X-ray scattering experiments, as described at the end of this article. This finding also correlates with the previously described result that the outer fibre diameter is not changed for a small content of LC core, meaning that only a small fraction of the LC molecules are not affected directly by the polymer surface, so that a strong effect on the LC phase sequence could be expected in this case.
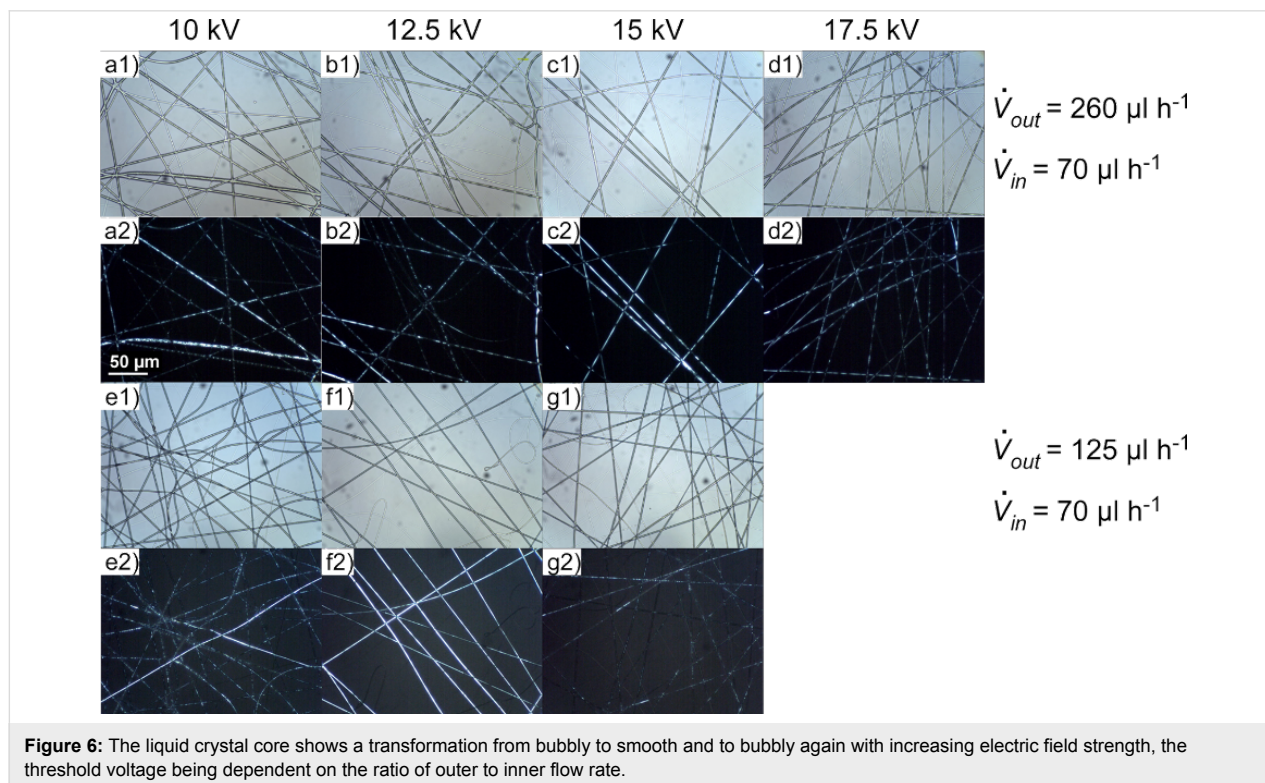
Influence of applied voltage

According to the numerical study on flow patterns in coaxial electrospinning [15] annular flows with smooth core-sheath interfaces appear only if the electrical field strength is above a certain threshold level. It is also known from another study [12] that the reduction of outer fibre diameter that is generally seen upon increasing field strength is not coupled to any substantial decrease in wall thickness, i.e. the reduction of total fibre diameter is almost completely given by a reduction of core thickness.

Examples of our fibres produced at different field strengths are shown in Figure 6. As one can see, at a combination of outer and inner flow rates of 125 and 70 µl h^{-1}, respectively, a smooth inner core is achieved at a voltage of 12.5 kV, while an increase of the outer flow rate to 260 µl h^{-1} (without changing the inner flow rate) requires a voltage of 15 kV. At even higher voltages the filling gets non-uniform again and it becomes more and more difficult to achieve a homogenous fibre mat.

In Figure 7 a plot of the dependence on applied voltage of mean fibre diameters measured by optical microscopy of these samples is shown. It is clear from the diagram that the diameters are reduced with increasing field strength and increase with higher flow rate of the polymer outer solution, as is to be expected. But when comparing this reduction of outer fibre diameters to the diameter range found in the previous described experiment with different flow rates of LC (see Figure 4), the variation is rather small. This observation suggests that the effect of the electric field strength variations on the inner diameter is in fact almost negligible, which would explain that
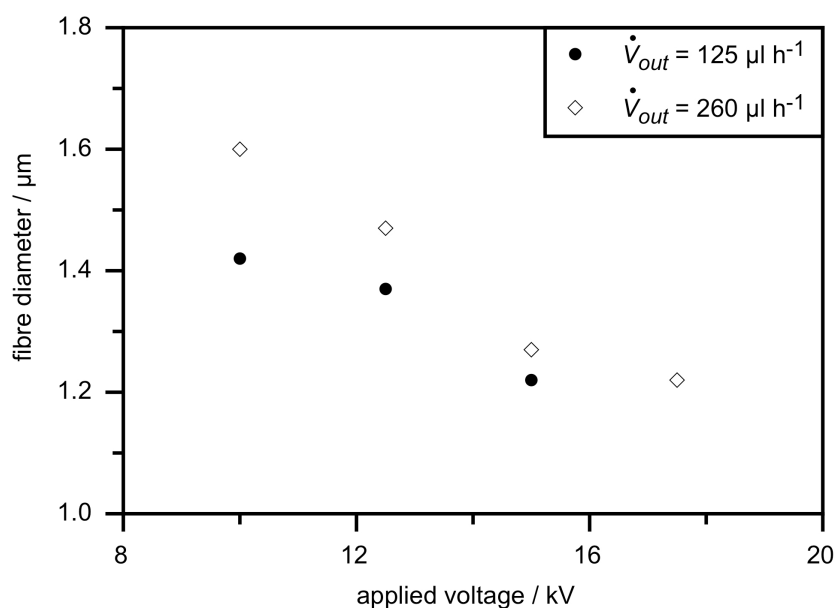

Figure 6: The liquid crystal core shows a transformation from bubbly to smooth and to bubbly again with increasing electric field strength, the threshold voltage being dependent on the ratio of outer to inner flow rate.

Figure 7: Influence of the applied voltage and the flow rate of the polymer solution on the mean fibre diameter.

we found no influence on the phase transition temperatures, which are the same for all samples shown and whose values fit to the results shown in Figure 5 with corresponding LC flow rate.

Since our observations of the inner diameter are only indirect and would have to be corroborated with direct measurement (practically very difficult to achieve with these particular fibres) our experiments can not be yet fully compared to the results of the above mentioned reference [12] on composites of TiO_2/PVP sheath with mineral oil as core. We hope to be able to modify our procedures and/or material combinations such that in the future we will be able to investigate the fibres by electron microscopy with respect to the diameter of the LC core.

X-Ray investigations on fibres

To gain information about the orientation of the liquid crystal molecules (and the layers of the SmA phase) inside the fibres, 2D X-ray diffraction patterns were recorded. For this purpose two samples of uniformly aligned fibres with maximum LC content were spun between bars of aluminium foil and were then rolled up in two perpendicular directions. A schematic sketch of the fibre directions before and after rolling is given in Figure 8c and Figure 8d, respectively. The corresponding diffraction patterns can be seen in Figure 8a and Figure 8b, the orientation being more clearly distinguishable in the first pattern than in the second one. This is mainly due to the facts that the roll-up direction can be better controlled in this case and that in
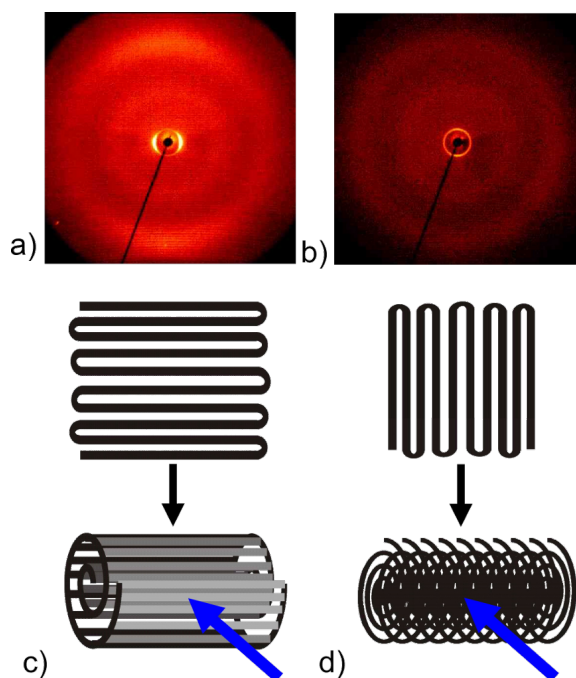

Figure 8: a), b): 2D X-ray diffraction pattern of oriented fibres at two perpendicular roll-up directions schematically sketched in c) and d), respectively. The incident X-ray beam is represented by the blue arrow. These scattering patterns from the composite fibres should be compared to those from unfilled PVP fibres and bulk 8CB, respectively, shown in Figure 9.
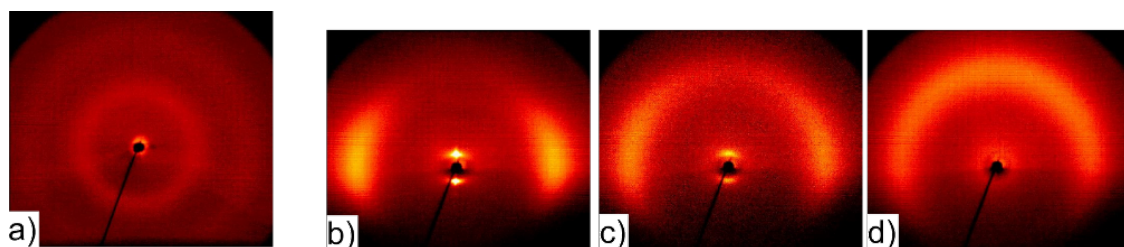
Figure 9: X-ray diffraction patterns of PVP fibres without LC (a) and of surface-aligned samples of bulk 8CB in the SmA, nematic and isotropic phase, respectively (b to d).

the second case the X-ray beam is directed along rather than across the fibres in a large part of the sample, thereby not producing any significant scattering response. So in the following we will discuss Figure 8c in more detail.

The layer reflections of the SmA phase can be seen on the equator in the small angle region. The corresponding layer spacing $d_A = 3.08$ nm can be very well compared to the value of 3.14 nm measured for bulk 8CB (Figure 9b) and to literature values (see for example [16,17]). In the middle and wide angle regions of the diffractogram two diffuse rings can be seen, caused by the polymer sheath (compare to Figure 9a). The outer diffuse ring is on the meridian overlayed by diffuse scattering due to the liquid-like distributed lateral distance between the LC molecules.

When considering the orientation of the fibres with respect to the incident X-ray beam the finding of layer reflections on the equator and of transverse spacing peaks on the meridian leads to a model in which the smectic layers are arranged perpendicular to the fibre formation axis (cf. Figure 10). This is somewhat unexpected, since the fibres are spun at a temperature at which the liquid crystal is in its smectic phase, in which the lowest viscosity is along the layers and not perpendicular to them. Considering only the flow geometry [18,19] one would thus expect concentric layers extended along the fibre axis in contrast to our experimental results. Possible explanations of
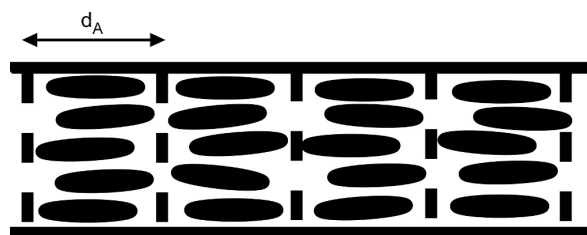

Figure 10: Schematic sketch of the arrangement of LC molecules and the smectic layers in an electrospun fibre.

this discrepancy might be either that the significant stretching during the electrospinning process leads to a shear induced phase transition to the nematic phase, causing a rearrangement of the molecules, or that the molecules are rearranged after electrospinning as a result of the interaction with the inner PVP sheath surface.

Conclusion

We show in this work that a liquid crystal in its smectic phase can be embedded as core in a PVP microfibre via coaxial electrospinning resulting in a new composite material with interesting properties. In our system the behaviour of the LC could be investigated by calorimetry measurements, X-ray diffraction experiments and by polarized optical microscopy, the latter one being possible only because the polymer we used as sheath material is transparent and isotropic, which is an improvement to previous work with PVP/TiO_2 as sheath [13]. From the X-ray diffraction patterns determined on oriented fibres we can conclude that in our fibres at room temperature the smectic phase still exists with the smectic layers being oriented perpendicular to the fibre formation axis, an unexpected result when considering the flow geometry of a smectic phase.

By varying the relation between the flow rate of the outer polymer solution and the flow rate of the LC the morphology of the core could be changed stepwise from discontinuous to very thin but continuous with overall fibre thicknesses comparable to unfilled fibres. In this regime complex phase behaviour dictated by strong surface effects was found. At higher LC flow rates a continuous bulk-like core and thick fibres were found. On the other hand, by increasing the voltage applied during electrospinning over a certain threshold value (dependent on the outer flow rate) a discontinuous core could be transformed into a continuous one while reducing the fibre diameter only slightly so that the phase behaviour was not influenced by this parameter. So by combining these two variables, maybe also with others relevant for electrospinning like the concentration of the polymer solution, composite fibres with the desired properties can be produced.

Experimental

The fibres were spun from a solution of 12.5 wt % PVP (Acros, MW 1,300,000 g/mol) and 0.5 wt % NaCl in ethanol through an outer tube of 0.7 mm inner diameter. The core liquid crystal 8CB (Synthon Chemicals GmbH) was pumped at room temperature through an inner capillary of 320 μm inner and 450 μm outer diameter (fused silica tubing, BGB Analytik AG). The spinneret–collector distance was kept constant at 10 cm. With a high voltage power supply (Gamma High Voltage Research) a voltage of 10 kV was applied, unless otherwise stated. All fluids were pumped at a controlled rate using a Fluigent MFCS4C microfluidics controller. The resulting samples were kept at room temperature for several days prior to conducting DSC or X-ray studies to ensure that all solvent was evaporated so that the fibres were mechanically stable. Oriented fibres for X-ray investigations were spun across parallel bars of aluminium foil placed on the collector.

Calorimetry investigations were carried out on a Perkin Elmer Pyris 1 DSC at a heating rate of 10 K min^{-1}. Samples of about 5 to 15 mg fibres were used for the measurements. X-ray investigations of fibres were performed on oriented fibres, rolled up to achieve a compact sample (see Figure 8c and Figure 8d). The sample of the bulk liquid crystal was aligned at the sample–air interface while cooling slowly on a glass plate, the temperature-controlled heating stage partially shadowing the patterns below the equator. The diffraction patterns were recorded with a 2D detector (HI-STAR, Siemens) using Ni-filtered CuK$_\alpha$ radiation.

Acknowledgments

References

1. Cooley, J. F. US Patent 692631, 1902.
2. Morton, W. J. US Patent 705691, 1902.
3. Li, D.; Xia, Y. N. *Adv. Mater.* **2004,** *16,* 1151–1170. doi:10.1002/adma.200400719
4. Burger, C.; Hsiao, B. S.; Chu, B. *Annu. Rev. Mater. Res.* **2006,** *36,* 333–368. doi:10.1146/annurev.matsci.36.011205.123537
5. Reneker, D. H.; Yarin, A. L. *Polymer* **2008,** *49,* 2387–2425. doi:10.1016/j.polymer.2008.02.002
6. Greiner, A.; Wendorff, J. H. *Adv. Polym. Sci.* **2008,** *219,* 107–171. doi:10.1007/12_2008_146
7. Rutledge, G. C.; Fridrikh, S. V. *Adv. Drug Delivery Rev.* **2007,** *59,* 1384–1391. doi:10.1016/j.addr.2007.04.020
8. Li, D.; Wang, Y.; Xia, Y. *Nano Lett.* **2003,** *3,* 1167–1171. doi:10.1021/nl0344256
9. Teo, W. E.; Ramakrishna, S. *Nanotechnology* **2006,** *17,* R89–R106. doi:10.1088/0957-4484/17/14/R01
10. Sun, Z.; Zussman, E.; Yarin, A. L.; Wendorff, J. H.; Greiner, A. *Adv. Mater.* **2003,** *15,* 1929–1932. doi:10.1002/adma.200305136
11. Loscertales, I. G.; Barrero, A.; Márquez, M.; Spretz, R.; Velarde-Ortiz, R.; Larsen, G. *J. Am. Chem. Soc.* **2004,** *126,* 5376–5377. doi:10.1021/ja049443j
12. Li, D.; Xia, Y. *Nano Lett.* **2004,** *4,* 933–938. doi:10.1021/nl049590f
13. Lagerwall, J. P. F.; McCann, J. T.; Formo, E.; Scalia, G.; Xia, Y. *Chem. Commun.* **2008,** 5420–5422. doi:10.1039/b810450f
14. Cordoyiannis, G.; Zidansek, A.; Lahajnar, G.; Kutnjak, Z.; Amenitsch, H.; Nounesis, G.; Kralj, S. *Phys. Rev. E* **2009,** *79,* No. 051703. doi:10.1103/PhysRevE.79.051703
15. Hu, Y.; Huang, Z. M. *J. Appl. Phys.* **2007,** *101,* No. 084307. doi:10.1063/1.2717605
16. Gray, G. W.; Lydon, J. E. *Nature* **1974,** *252,* 221–222. doi:10.1038/252221a0
17. Urban, S.; Przedmojski, J.; Czub, J. *Liq. Cryst.* **2005,** *32,* 619–624. doi:10.1080/02678290500116920
18. Safinya, C. R.; Sirota, E. B.; Plano, R. J. *Phys. Rev. Lett.* **1991,** *66,* 1986–1989. doi:10.1103/PhysRevLett.66.1986
19. Hamley, I. W.; Castelletto, V.; Parras, P. *Phys. Rev. E* **2006,** *74,* No. 020701. doi:10.1103/PhysRevE.74.020701

1-(4-Alkyloxybenzyl)-3-methyl-*1H*-imidazol-3-ium organic backbone: A versatile smectogenic moiety

William Dobbs[*], Laurent Douce[*] and Benoît Heinrich

Abstract

The merger of ionic liquid and liquid crystal fields, obtained by using the imidazolium ring as a common element, has allowed us to tailor a new set of materials which associate specific functionalities. These functionalities are consequences of the original properties of the component, ionic liquids, liquid crystals and their association in a single compound. The study of this interesting association led us to elaborate environment-flexible cationic architectures from which mesomorphic properties emerge. Moreover, we have also explored the influence of different anions on the mesomorphic properties.

Introduction

Uniting the properties of ionic derivatives with those of liquid crystals, with their many forms of labile macroscopic ordering, raises interesting prospects [1]. By themselves ionic liquids are organic salts (i.e. totally composed of cations and anions) that are – unlike traditional salts – liquid at or near ambient temperatures. The combination of properties is truly unique: ionic liquids are non-volatile and non-flammable, have high chemical and radiochemical stabilities, tunable electric conductivities, exceptional dissolution properties [2-4]. By varying the cations and anions the physico-chemical properties of ionic liquids can be tuned and specifically optimised for a wide range of applications [5-11]. Although many organic cations (e.g. phosphonium, ammonium, pyridinium, imidazolium) can be used for the design of ionic liquids, none of these cations are as popular as the imidazolium ion.

In particular, the modification of the N,N′ substituents in imidazolium systems is a facile mean of creating various amphotropic liquid crystals. Such imidazolium liquid crystals have especially great potential as ordered reaction media that can impart selectivity in reactions by organising reactants, as scaffolds for the synthesis of nanostructured particles [12-14], in dye-sensitized solar cells [15,16] or also in bio-related science [17,18].

In conclusion, this combination represents a fascinating class of new multifunctional materials [19] in which the organic modifications afforded to the imidazolium central part and the ions' environment (e.g. ion assemblies) closely govern their melting points and their use [20].
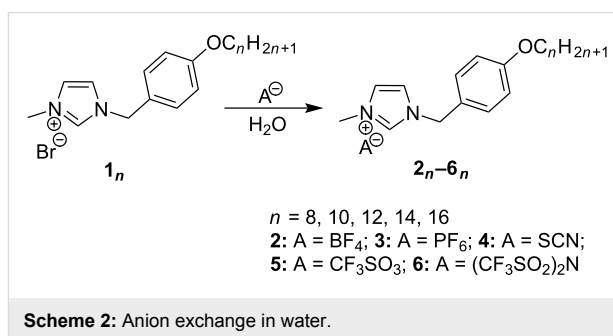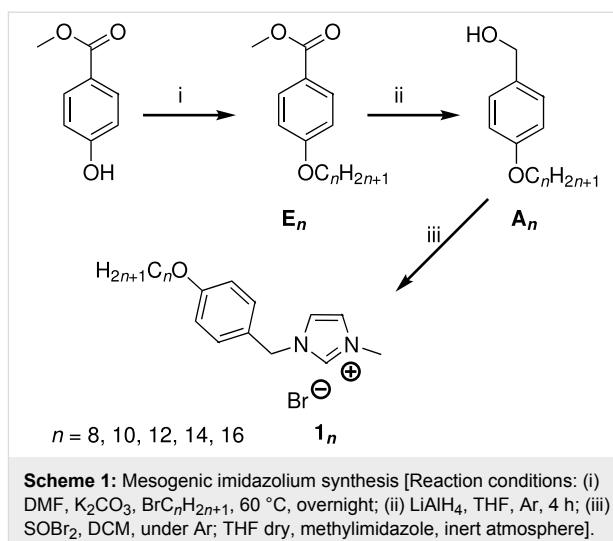
The present article concerns a synthetic route to imidazolium salts, which have been modified to present thermotropic liquid crystal behaviour. In association with different anions and in relation to the chain length incorporated in the methylimidazolium cations, we were able to tune the different transition temperatures and thus obtain stable smectic A phase from ambient temperature to 250 °C (decomposition temperature). The mesomorphic properties were studied by polarizing optical microscopy, differential scanning calorimetry and X-ray diffraction. With the support of dilatometry, models for the lamellar supramolecular arrangement of the salts are proposed and its evolution is discussed as a function of the counter ions' morphology.

Results and Discussion
Synthesis and characterization
Our molecules are based on an organic calamitic structure in which a polar rigid group (methylimidazolium head) is associated to a flexible aliphatic chain with 8 to 16 carbons. The syntheses of all the compounds presented in this study began with the preparation of the bromide imidazolium salts followed by an anionic exchange step. Bromide derivatives 1_n of 1-(4-alkyloxybenzyl)-3-methyl-*1H*-imidazol-3-ium with n = 8, 10, 12, 14, 16 have been synthesized in good yield (>82%) and on the gram scale. These compounds were obtained in three steps, following slightly modified literature procedures. Methyl 4-hydroxybenzoate was etherified with various 1-bromoalkanes ($C_nH_{2n+1}Br$, n = 8, 10, 12, 14, 16) in the presence of K_2CO_3 in DMF (yield > 96%), and the resulting amphipathic esters E_n reduced by $LiAlH_4$ to the corresponding benzyl alcohols A_n. The different resulting alcohols were converted quantitatively into the intermediate 4-(alkoxy)benzyl bromides with thionyl bromide. The final compounds 1_n were then obtained by quaternization of 1-methylimidazole with the bromides in refluxing THF under inert atmosphere (Scheme 1).

To obtain the desired set of compounds, we performed as a final step an anionic metathesis in water from 1_n in order to give 2_n, 3_n, 4_n, 5_n and 6_n respectively with BF_4^-, PF_6^-, SCN^-, $CF_3SO_3^-$ and $(CF_3SO_2)_2N^-$ anions (Scheme 2) in good yield, easily scaled up to gram quantities. In this part, we used the good solubility of the bromide derivatives 1_n in water to perform the anionic exchange. By a simple addition in water solution of the corresponding lithium, potassium or sodium salts of the desired products, our targeted compounds were dearly obtained by

Scheme 1: Mesogenic imidazolium synthesis [Reaction conditions: (i) DMF, K_2CO_3, BrC_nH_{2n+1}, 60 °C, overnight; (ii) $LiAlH_4$, THF, Ar, 4 h; (iii) $SOBr_2$, DCM, under Ar; THF dry, methylimidazole, inert atmosphere].

Scheme 2: Anion exchange in water.

phase separation ($n \leq 10$) or precipitation ($n > 10$) according to the chain length.

All imidazolium compounds (1_8–6_8, 1_{10}–6_{10}, 1_{12}–6_{12}, 1_{14}–6_{14}, 1_{16}–6_{16}) were purified by flash chromatography or crystallization. Their structural characterizations and their purities were established by ^1H NMR, ^{13}C NMR{^1H}, FT-IR spectroscopy and elemental analysis.

Due to their close chemical structures, similar behaviour was observed during NMR characterization for all 1_n samples as a function of concentration. A significant chemical shift related to the proton of the imidazolium head (H_{im}), and in particular a $\Delta\delta$ = 0.43 ppm (from low to high concentration) for the H_{im} carried by the carbon atom between the two nitrogen atoms, was observed for 1_{12}. As already mentioned in a previous article [21], these spectroscopic results clearly indicate the formation of aggregates in solution and underline the high sensitivity of these protons to their environment.

This second point was definitively demonstrated by a NMR study performed as a function of the anionic species (constant concentration [c] = $3.1 \cdot 10^{-2}$ mol·L^{-1}) (Figure 1).
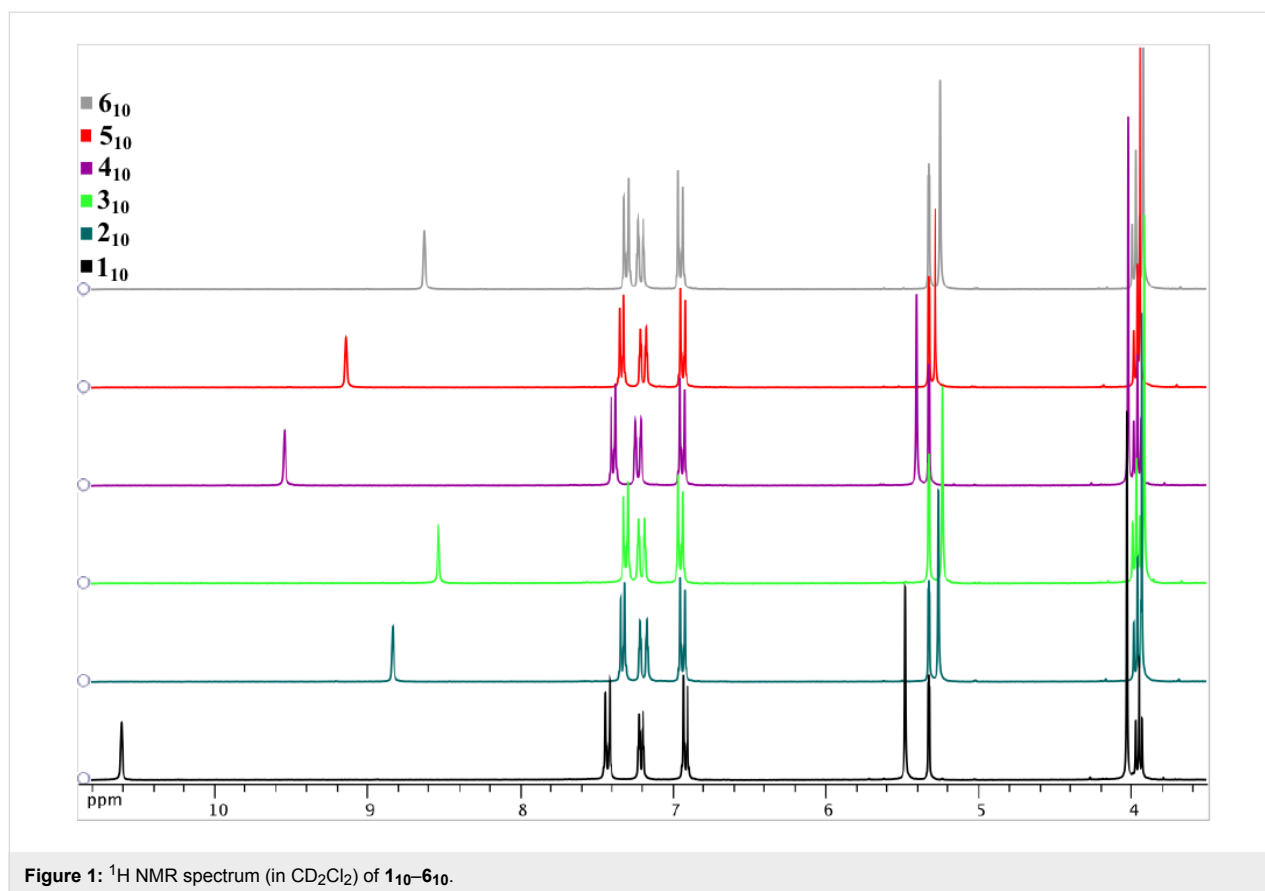
Figure 1: ^{1}H NMR spectrum (in CD_2Cl_2) of 1_{10}–6_{10}.

Related to their morphologies and to their abilities to interact with the imidazolium moiety, we observed significant variation of the chemical shift of the H_{im} between the two nitrogen atoms: $\delta = 10.61$ ppm (Br^-); 8.83 ppm (BF_4^-); 8.53 ppm (PF_6^-); 9.54 ppm (SCN^-); 9.14 ppm ($CF_3SO_3^-$); 8.63 ppm ($[CF_3SO_2]_2N^-$). We could also observe some modifications of the spectrum for the protons of the first substituent group of the imidazolium core ($N–CH_3$ and $N–CH_2$) localized respectively around 4 ppm and 5.3 ppm.

Correlated to the crystal structure of compound 1_{12} these observations were made on all the protons used for the organization of the polar part by multiple anion-cation and cation-cation interactions [21]. These NMR studies carried out as a function of the nature of the anion are a reflection of the modifications that occur in the polar layer in function of the anion source in solution.

Investigation of the liquid crystalline behaviour

As expected most of the ionic compounds showed liquid crystalline properties [19,22-30]. Their characterization was the result of the combination and interpretation of thermal studies (Thermogravimetry Analysis or TGA, Differential Scanning Calorimetry or DSC), direct polarized optical microscopy (POM) observation and small angle X-ray diffraction studies (SAXS).

Thermic behaviour

Due to their amphipathic structures, all imidazolium salts interact more or less rapidly with the water contained in air. This property explains the presence of different amounts of water in the elemental analyses. Otherwise, water-free samples can be obtained and used for the investigation of liquid crystalline behaviour, if we conserved them under vacuum at 50 °C during the night preceding the analysis (Figure 2).

The TGA realized on all samples indicated their good stability; no degradation occurred below 220 °C (Figure 3). The analysis showed a degree of stability as a function of the anion but no real tendency can be extracted as a function of chain length. In all series the general order of stability order is $SCN^- \approx Br^- < BF_4^- \approx PF_6^- < CF_3SO_3^- < (CF_3SO_2)_2N^-$.

To avoid any phenomenon related to the sample preparation (purification, crystallisation, hydration) our reported DSC results are obtained from the second thermic cycle (2nd heating and cooling) and all phase transitions described occurred in the
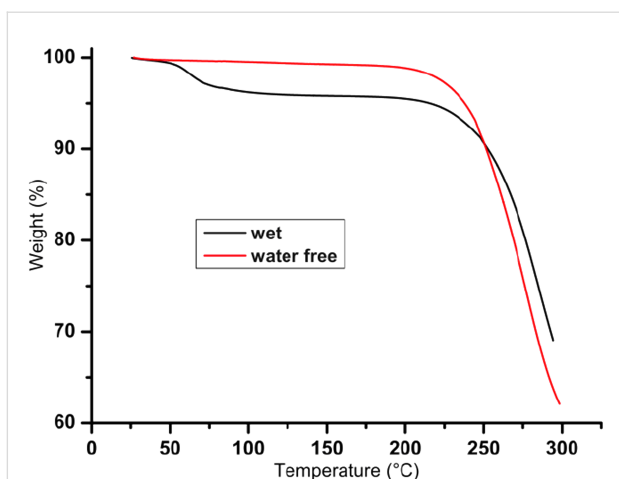
Figure 2: TGA measurements of wet and water free **1_{12}** imidazolium salt.

Figure 3: TGA measurements of the two entire series **1_{10}–6_{10}** and **1_{14}–6_{14}** (rate 10° C·min⁻¹, in air).

ionic liquids between −80 °C to 200 °C (ESI). The DSC graphs for the compounds with short aliphatic chains exhibit a glass transition during the cooling process rather than a crystallization peak. In contrast, increasing the chain length ($n > 10$) we have almost detected a crystalline transition. During the following heating process, most of these compounds ($n > 10$) show crystalline polymorphism with some rearrangement between different solid organizations (cold crystallization, transition crystal to crystal) (Table 1).

The transitions between crystal and mesomorphic state and also the clearing point increase with the chain length, allowing liquid
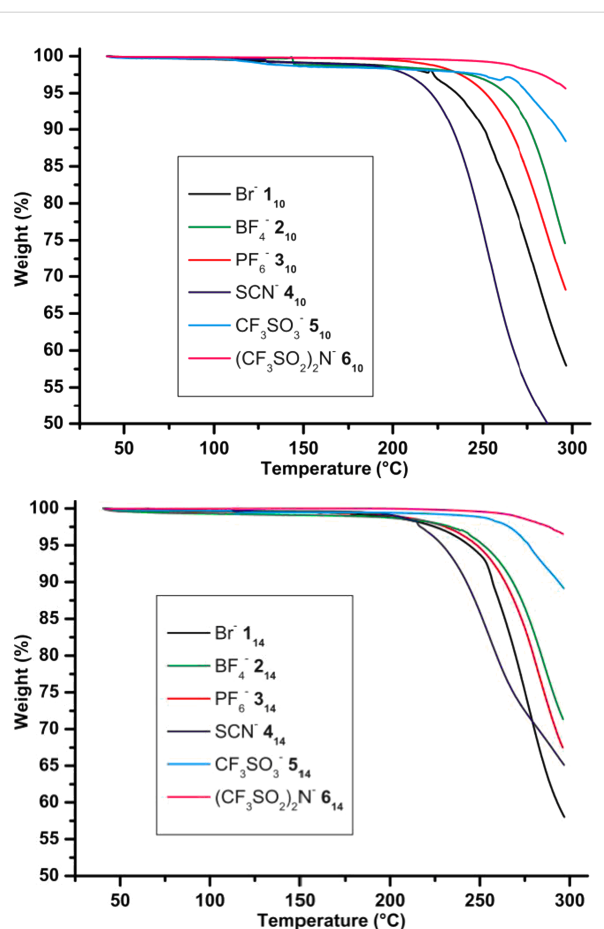
Table 1: Temperatures and enthalpy changes of the phase transitions for **$1_{8–10}$** to **$6_{8–10}$**. G: Glass; Cr: solid; SmA: Smectic A phase; I: isotropic liquid; Dec: decomposition.

1_n–5_n	Phase sequences °C (kJ·mol⁻¹)	2_n–6_n	Phase sequences °C (kJ·mol⁻¹)
1_8	G −15.6(–) SmA 155.1(0.4) I I 155(0.45) SmA −30.7(–) G	2_8	G −29.1(–) SmA 71(0.3) I I 69.9(0.4) SmA −36.1(–) G
3_8	G −26.1(–) Cr 34.8(0.15) I I 33.6(0.2) Cr −31.9(–) G	4_8	Cr 33.7(24.3) SmA 50.9(0.35) I I 50.2(0.28) SmA 7.1(25.6) Cr
5_8	G −44.3(–) I I −51.9(–) G	6_8	G −59.4(–) Cr$_1$ −14.5(29.9)[a] Cr$_2$ 26.7(36.3) I I (–) G
1_{10}	G −14.5 (–) SmA 227(–)[b] I I 227(–)[b] SmA −23.2(–) G	2_{10}	G −29.1 (–) Cr$_1$ −0.1(17.9)[a] Cr$_2$ 30(18.0) SmA 143.4(0.47) I I 142.5(0.88) SmA −29.7(–) G
3_{10}	G −26.2 (–) Cr$_1$ 7.1(24.2)[a] Cr$_2$ 66.3 (31.5) SmA 93.3(0.4) I I 92.1(1.1) SmA −33.2(–) G	4_{10}	Cr 32.3(23.8) SmA 116.6(0.7) I I 115.6(1.0) SmA 8(28.0) Cr
5_{10}	Cr$_1$ −13.1 (5.6)[a] Cr$_2$ 5.31(1.4)[a] Cr$_3$ 13.5 (5.9)[a] Cr$_4$ 45.66 (4.9) Cr$_5$ 56.37 (30.8) I I −16.7(–) Cr$_1$	6_{10}	Cr$_1$ −24.1 (8.7)[a] Cr$_2$ 36.8(51.3) I I −30.7(17.4) Cr$_1$

[a]Cold crystallisation, [b]Transition observed by POM.

crystalline properties to exist from sub-ambient temperature (1_8, 2_8, 4_8) to very high temperature avoiding any isotropization before decomposition of the material (molecules with long alkyl chain $n \geq 12$). In parallel, the nature of the anion (shape, size) played an important role in the evolution of the clearing point. In the same family (from 1_n to 6_n) the stability of the liquid crystalline phase dramatically decreases, finally disappearing completely (Figure 4).

This evolution will be more discussed later in regard to the results obtained with the dilatometry study. In summary, only 9 of the compounds did not show liquid crystal characteristics; 6_n, which are constituted by the larger anion (bis[(trifluoromethyl)-sulfonyl]amide), are ionic liquid compounds without any supra-molecular organization into mesophase. This is also the case in

the series of compounds 5_n with $n < 12$ (only a monotropic mesophase was observed for 5_{12}), and finally for 3_8.

Supramolecular arrangement

Despite the significant tendency of these molecules to form spontaneously a single homeotropic monodomain (Figure 5a) the nature of the mesophases could be quite easily assigned on the basis of their optical textures if separated microscope slides (100 μm spacer) were used.

The utilization of a spacer allows the formation of large oriented monodomains to be avoided and thus furtive forma-tion of birefringent batonnets upon slow cooling from the isotropic melt, followed by developed focal conic texture (Figure 5b) can be clearly observed. These observations exem-
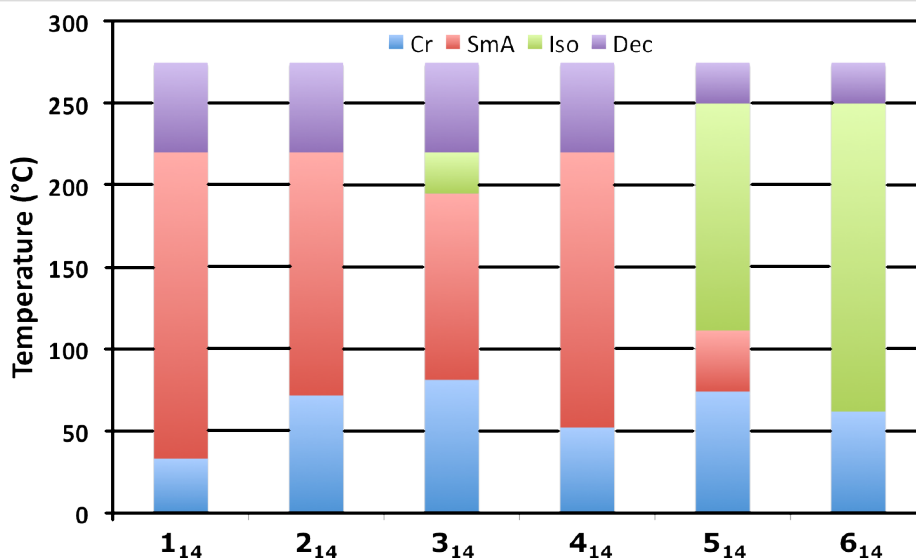

Figure 4: Transition temperatures of 1_{14}–6_{14} as a function of the anion (Cr = crystal; SmA: smectic A phase; Iso: Isotropic Liquid; Dec: decomposi-tion).
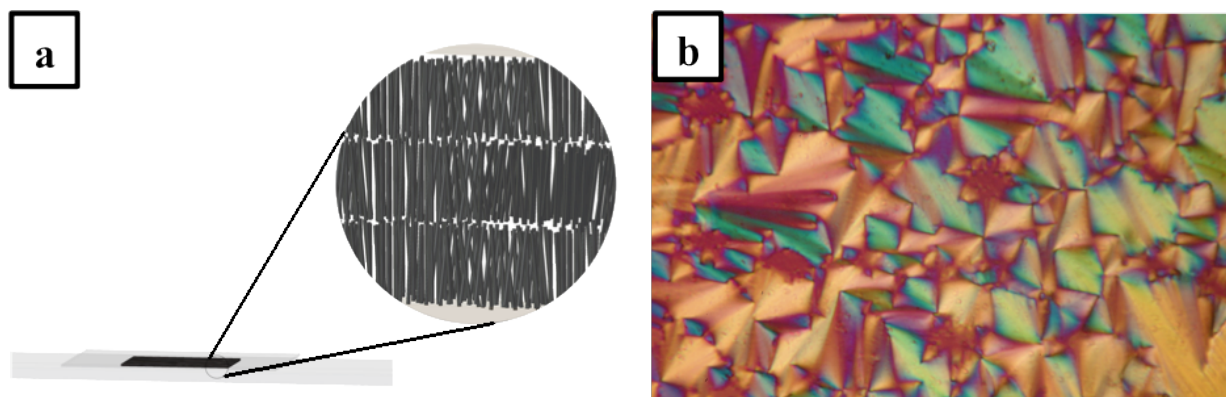

Figure 5: (a) Illustration of a single homeotropic monodomain, which is observed as a black isotropic texture under POM, (b) focal conic texture observed at 80 °C with 1_8 (spacer Mylar foil 100 μm).

plified the existence of a smectic-A phase for all ionic meso-morphic compounds.

The identification of all mesophases was supported by small-angle X-ray diffraction. SAXS patterns were collected for the mesomorphic salts as a function of temperature (Figure 6). Typically, in all cases, in the large angle region, i.e. at ca. 4.5–4.6 Å, a very intense and diffuse scattering halo was observed, corresponding to the molten alkyl chain in liquid-like order (A), whilst in the low-angle part of the diffractogram one to three equidistant sharp and intense peaks were observed, characteristic of the layered organization.

Figure 6: Diffraction small-angle X-ray pattern of the smectic phase of **2₁₂** recorded at T = 100 °C.
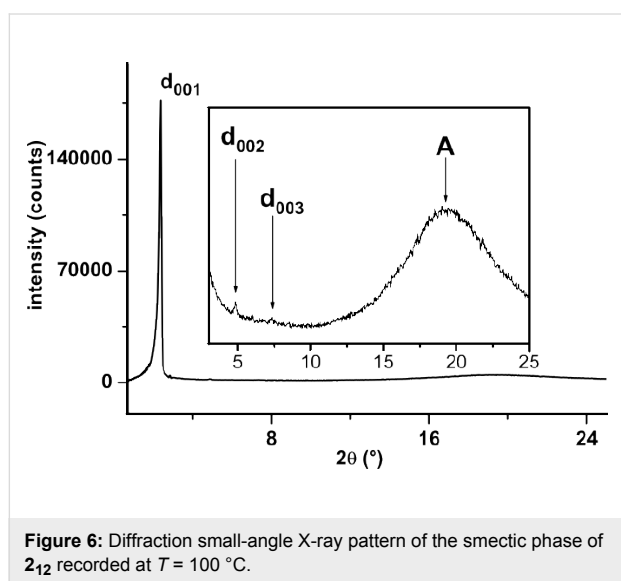
The very intense first sharp peak was directly correlated to the periodicity value. In each system, the smectic periodicity increases with the chain length and decreases with increasing temperature, reflecting the higher thermal mobility of the alkyl chains, concomitant with the compression of the smectic layers. Interestingly also, the periodicity of the salts is closely correl-ated to the anion species and the general order is $Br^- > BF_4^- \approx SCN^- > PF_6^- > CF_3SO_3^-$.

Dilatometric studies

Prior to the analysis of the molecular packing of the various compounds in the smectic mesophase, the molecular volume (V_{mol}) of one salt, **1₁₂**, was measured by using a home built high precision apparatus, incorporating temperature control within 0.03 °C, relative density measurement within 0.01% and absolute density measurement within 0.1%. The molecular volumes of the other homologues and of the analogues with the other counter ions were calculated with an accuracy of 0.5% from the molecular volume measured before and from the methylene and counter ion partial volumes.

Despite the untilted smectic layering and the tiny thermal expansion of the molecular volume mainly due to the contribu-tion of the alkyl tails, all compounds exhibited a very strong dependence upon temperature of the layer spacing. This evid-ence is the consequence of the evolution of the projection area of a mesogen counter-ion assembly within the mean smectic plane, the thickness of the aliphatic sublayer variating in proportion since the spreading of the liquid alkyl chains occurs without volume variation [31]. This projection area, called "molecular area" S, is equal to the ratio $N \cdot V_{mol}/d$, in which d is the layer spacing, V_{mol} the molecular volume and N the number of superposed mesogen counter-ion assemblies in the ionic sublayer. Thus, the alkyl tails expelled from each side of the sublayer containing the ions and the mesogens impose a bilayer ($N = 2$) type of organisation on these sublayers, consisting of two head-to-head facing ionic monolayers.

The resulting variations of S versus temperature T within the analogous series of various anions but constant chain length (see Figure 7) consist of steep increases, approximately linear
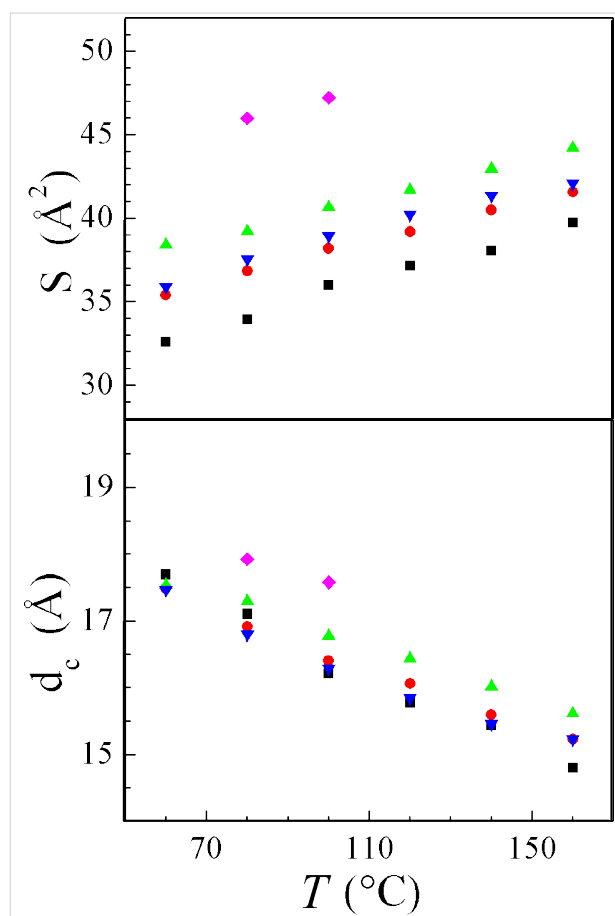

Figure 7: Variation with the counter-ion of the molecular area S and of the ionic sublayer thickness d_c (including mesogenic segments) in the smectic A phase for series: squares: **1₁₄**; circles: **2₁₄**; up triangles: **3₁₄**; down triangles: **4₁₄**; diamonds: **5₁₄**.

with very similar slopes and with lateral shifts following the different bulk of the anions. Anion substitution actually leads to large variations of S, but very small variations of the ionic sublayer thickness d_c (obtained by subtracting the aliphatic sublayer contribution, see Figure 7), the residual discrepancies being explicable by the different shapes of the anions. This indicates that polymorphic evolution in the series is almost exclusively due an anion size effect with no significant influence on the segregation in sublayers. As a clear confirmation, close to the isotropization temperatures, the values reached by S depend on the chain length but are almost independent of the anion (between 43 and 44 $Å^2$ and around 47 $Å^2$, for the C_{12} and the C_{14} analogous series respectively, see Table SI-7 in Supporting Information File 1).

So far the results are nearly identical to the ones already discussed for a series with the same counter ions, C_{12} alkyl tails but a small change in the mesogenic part [32]: from S and d_c in the smectic A phase and also from comparison with the crystalline organization it was deduced that the enormous difference between the cross-section of the tails and the ionic lattice area is compensated by the gathering of the ionic sublayer and by the folding of the tails. As in the present case, the dependences upon *T* of S and d_c indicated the decrease of gathering degree and therefore the increase of folding with increasing *T*. Thus the compromise molecular areas are still 1.5 to 1.9 times larger than the cross-sectional area of a molten but stretched aliphatic chain (between 21 and 24 $Å^2$, depending on *T*), from which a high degree of folding geometrically equivalent to 50° random tilting is deduced. Indeed, this significant folding of the tails is directly observed in oriented X-ray patterns (see Figure 8): despite the very good alignment of the smectic layers deduced from the narrow first and second order spots on the meridian, the diffuse band in the wide angle region occurring from the lateral packing does not lie on the equator but spreads over the whole azimuthal range.
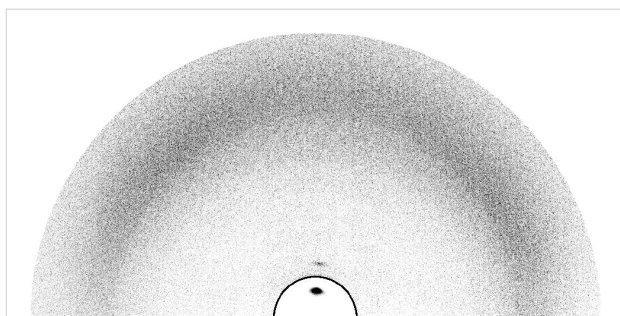

Figure 8: Grazing incidence X-ray pattern at 100 °C on the top of a **3₁₂** droplet, slowly cooled down from isotropic phase; for image contrast compatibility with the surrounding zone, intensities inside the zone, delimited by the black line and containing the first order reflection of the lamellar stacking, are divided by one hundred.

Unlike temperature and counter ion size, a chain length increase induces only minor changes of S, the main effect being the evolution toward steeper variations versus *T* (Figure SI-2 in Supporting Information File 1). When plotting together the area isotherms S^T and the area close to isotropization S^{max}, differences in steepness and gaps clearly set the lower limit for the smectic packing (Figure 9).
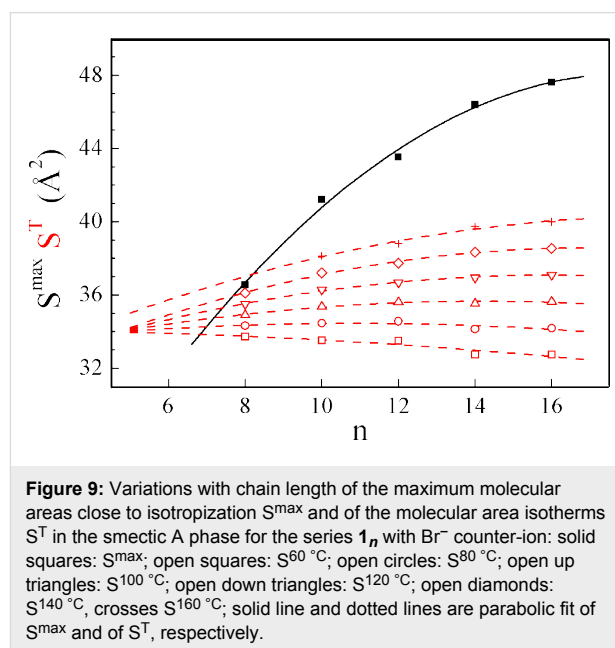

Figure 9: Variations with chain length of the maximum molecular areas close to isotropization S^{max} and of the molecular area isotherms S^T in the smectic A phase for the series **1**$_n$ with Br⁻ counter-ion: solid squares: S^{max}; open squares: $S^{60\,°C}$; open circles: $S^{80\,°C}$; open up triangles: $S^{100\,°C}$; open down triangles: $S^{120\,°C}$; open diamonds: $S^{140\,°C}$, crosses $S^{160\,°C}$; solid line and dotted lines are parabolic fit of S^{max} and of S^T, respectively.

Remarkably, the gaps between the extrapolated isotherms seem to vanish close to this low limit, for a chain length corresponding roughly to the segments incorporated in the interface layer, because of the gathering of the ionic sublayers. (On the basis of previous results [32], the calculated molecular area S^0 and ionic sublayer thickness d_c^0 for flat layers are estimated to be 54 $Å^2$ and 10 Å, respectively. S and d_c values close to the low limit are of about 33 $Å^2$ and 17 Å. With the hypothesis that the interface layer goes from d_c^0 to $(2d_c - d_c^0)$, the calculation results in chain segments incorporated in the interface layer that contain on average about 7 methylene groups). Thus, this would logically mean that smectic packing is only possible if the tails are long enough to jut out of the diffuse interface with the ionic sublayers and that the tail segments incorporated in the interface do not contribute significantly to the weak dependence of S upon chain length. Beyond the short chain limit, the major influence of chain length concerns the stability of the smectic packing revealed by the variation of S^{max}. Thus, increasing chain length causes an important stabilization in the whole explored domain, probably because of the better defined sublayer alternation, extending the smectic packing to larger molecular areas and to more disorganized chains. Nevertheless, increasing chain length also dilutes the ionic sublayers, redu-

cing the correlations between them, and a higher limit should therefore exist for the system, but for much longer tails than the longest grafted here ($n = 16$).

Conclusion

We have synthesised different series of thermotropic ionic liquid crystals based on the imidazolium cation and containing anions varying with regard to their shapes, sizes and charge localization. As expected, most of the imidazolium compounds show stable mesomorphism, which can be observed at sub-ambient to very high temperature. Both the alkyl chain length and the anion type have a strong influence on the mesomorphic behaviour.

In regard to the different studies realized and more precisely to the dilatometry analysis, the most interesting feature of this imidazolium architecture is its flexibility. This is highlighted, in the smectic A organization, by the ability of the system to compensate the difference between the cross-section of the tails and the ionic lattice area by the gathering of the ionic sublayer and by folding of the tails. This environment-flexible cationic organic backbone offers us, even in presence of large counterions, the opportunity to elaborate ionic liquid crystals. The 1-(4-alkoxybenzyl)-3-methyl-1*H*-imidazol-3-ium cationic moiety is a versatile smectogenic part which could in the near future organise into supramolecular arrangements involving numerous anions with specific functionalities.

Experimental
General procedure for imidazolium syntheses

The reactions were performed under Argon atmosphere. 4-(Alkyloxyphenyl)methanol (**A**$_n$) and thionyl bromide were dissolved in dry DCM. TLC monitored the progress of reaction until no more alcohol was observed. The solvent was removed under vacuum and the intermediate 1-bromomethyl-4-alkyloxy-benzene was used directly without further purification. This bromo derivative and freshly distilled 1-methylimidazole were stirred in THF during two days. After evaporation to dryness, the residue was purified by flash chromatography on silica gel column (elution DCM/MeOH, MeOH 0% to 9%) followed by flash chromatography on alumina gel column (elution DCM/MeOH, MeOH 3% to 8%) or by a recrystallisation from DCM/Et$_2$O.

General procedure for anion metathesis in water
C$_n$H$_{2n+1}$ with $n \leq 10$

The lithium, sodium or potassium salt of our desired anion was dissolved in water and added to an aqueous solution of a 1-(4-alkyloxybenzyl)-3-methyl-1*H*-imidazol-3-ium bromide. A slight precipitation of the desired imidazolium occurred imme-

diately. The reaction was stirred for a couple of hours, and dichloromethane was added. The organic layer was washed three times with water, dried on MgSO$_4$ and evaporated under reduced pressure.

C$_n$H$_{2n+1}$ with $n > 10$

The lithium, sodium or potassium salt of our desired anion was dissolved in water and added to an aqueous solution of a 1-(4-alkyloxybenzyl)-3-methyl-1*H*-imidazol-3-ium bromide. A precipitation of the desired imidazolium salt occurred immediately. The reaction was stirred for a couple of hours. After centrifugation, the solvent was removed and the crude product was washed twice with water. The product was finally obtained pure by crystallization on a mixture from dichloromethane and diethyl ether.

Supporting Information

Supporting Information File 1
Product characterization (spectroscopic and analytical data), complementary information about the characterization of the liquid crystalline properties (DSC, X-Ray, dilatometry).
[http://www.beilstein-journals.org/bjoc/content/supplementary/1860-5397-5-62-S1.doc]

Acknowledgments

References

1. Binnemans, K. *Chem. Rev.* **2005,** *105,* 4148–4204. doi:10.1021/cr0400919
2. Ohno, H., Ed. *Electrochemical Aspects of Ionic Liquids;* Wiley-Interscience, 2005.
3. Endres, F.; Abbott, A. P.; MacFarlane, D. R., Eds. *Electrodeposition from Ionic Liquids;* Wiley-VCH: Weinheim, 2008.
4. Wasserscheid, P.; Welton, T., Eds. *Ionic Liquids in Synthesis;* Wiley-VCH: Weinheim, 2003.
5. Song, C. E.; Roh, E. J. *Chem. Commun.* **2000,** 837–838. doi:10.1039/b001403f
6. Song, C. E.; Shim, W. H.; Roh, E. J.; Choi, J. H. *Chem. Commun.* **2000,** 1695–1696. doi:10.1039/b005335j
7. Dupont, J.; de Souza, R. F.; Suarez, P. A. Z. *Chem. Rev.* **2002,** *102,* 3667–3692. doi:10.1021/cr010338r
8. Taubert, A. *Acta Chim. Slov.* **2005,** *52,* 183–186.
9. Mazille, F.; Fei, Z.; Kuang, D.; Zhao, D.; Zakeeruddin, S. M.; Grätzel, M.; Dyson, P. J. *Inorg. Chem.* **2006,** *45,* 1585–1590. doi:10.1021/ic051751a
10. van Rantwijk, F.; Sheldon, R. A. *Chem. Rev.* **2007,** *107,* 2757–2785. doi:10.1021/cr050946x
11. Parvulescu, V. I.; Hardacre, C. *Chem. Rev.* **2007,** *107,* 2615–2665. doi:10.1021/cr050948h

12. Taubert, A. *Angew. Chem., Int. Ed.* **2004,** *43,* 5380–5382.
    doi:10.1002/anie.200460846
13. Taubert, A.; Steiner, P.; Mantion, A. *J. Phys. Chem. B* **2005,** *109,*
    15542–15547. doi:10.1021/jp051262w
14. Dobbs, W.; Suisse, J.-M.; Douce, L.; Welter, R. *Angew. Chem., Int. Ed.*
    2006, *45,* 4179–4182. doi:10.1002/anie.200600929
15. Yamanaka, N.; Kawano, R.; Kubo, W.; Masaki, N.; Kitamura, T.;
    Wada, Y.; Watanabe, M.; Yanagida, S. *J. Phys. Chem. B* **2007,** *111,*
    4763–4769. doi:10.1021/jp0671446
16. Yamanaka, N.; Kawano, R.; Kubo, W.; Kitamura, T.; Wada, Y.;
    Watanabe, M.; Yanagida, S. *Chem. Commun.* **2005,** 740–742.
    doi:10.1039/b417610c
17. Desigaux, L.; Sainlos, M.; Lambert, O.; Chevre, R.;
    Letrou-Bonneval, E.; Vigneron, J.-P.; Lehn, P.; Lehn, J.-M.; Pitard, B.
    Proc. Natl. Acad. Sci. U. S. A. **2007,** *104,* 16534–16539.
    doi:10.1073/pnas.0707431104
18. Dobbs, W.; Heinrich, B.; Bourgogne, C.; Donnio, B.; Terazzi, E.;
    Bonnet, M.-E.; Stock, F.; Erbacher, P.; Bolcato-Bellemin, A.-L.;
    Douce, L. *J. Am. Chem. Soc.* **2009,** *131,* 13338–13346.
    doi:10.1021/ja903028f
19. Kato, T.; Mizoshita, N.; Kishimoto, K. *Angew. Chem., Int. Ed.* **2006,** *45,*
    38–68. doi:10.1002/anie.200501384
20. Yoshio, M.; Ichikawa, T.; Shimura, H.; Kagata, T.; Hamasaki, A.;
    Mukai, T.; Ohno, H.; Kato, T. *Bull. Chem. Soc. Jpn.* **2007,** *80,*
    1836–1841. doi:10.1246/bcsj.80.1836
21. Dobbs, W.; Douce, L.; Allouche, L.; Louati, A.; Malbosc, F.; Welter, R.
    New J. Chem. **2006,** *30,* 528–532. doi:10.1039/b600279j
22. Bowlas, C. J.; Bruce, D. W.; Seddon, K. R. *Chem. Commun.* **1996,**
    1625–1626. doi:10.1039/cc9960001625
23. Yoshio, M.; Mukai, T.; Kanie, K.; Yoshizawa, M.; Ohno, H.; Kato, T.
    Adv. Mater. **2002,** *14,* 351–354.
    doi:10.1002/1521-4095(20020304)14:5<351::AID-ADMA351>3.0.CO;2
    -D
24. De Roche, J.; Gordon, C. M.; Imrie, C. T.; Ingram, M. D.; Ingram, A. R.;
    Kennedy, A. R.; Lo Celso, F.; Triolo, A. *Chem. Mater.* **2003,** *15,*
    3089–3097. doi:10.1021/cm021378u
25. Lee, K.-M.; Lee, Y.-T.; Lin, I. J. B. *J. Mater. Chem.* **2003,** *13,*
    1079–1084. doi:10.1039/b210562d
26. Yoshio, M.; Mukai, T.; Ohno, H.; Kato, T. *J. Am. Chem. Soc.* **2004,** *126,*
    994–995. doi:10.1021/ja0382516
27. Suisse, J.-M.; Bellemin-Laponnaz, S.; Douce, L.; Maisse-François, A.;
    Welter, R. *Tetrahedron Lett.* **2005,** *46,* 4303–4305.
    doi:10.1016/j.tetlet.2005.04.114
28. Chiou, J. Y. Z.; Chen, J. N.; Lei, J. S.; Lin, I. J. B. *J. Mater. Chem.*
    2006, *16,* 2972–2977. doi:10.1039/b600045b
29. Suisse, J.-M.; Douce, L.; Bellemin-Laponnaz, S.; Maisse-François, A.;
    Welter, R.; Miyake, Y.; Shimizu, Y. *Eur. J. Inorg. Chem.* **2007,**
    3899–3905. doi:10.1002/ejic.200700251
30. Yazaki, S.; Kamikawa, Y.; Yoshio, M.; Hamasaki, A.; Mukai, T.;
    Ohno, H.; Kato, T. *Chem. Lett.* **2008,** *37,* 538–539.
    doi:10.1246/cl.2008.538
31. Cruz, C.; Heinrich, B.; Ribeiro, A. C.; Bruce, D. W.; Guillon, D.
    Liq. Cryst. **2000,** *27,* 1625–1631. doi:10.1080/026782900750037185
32. Fouchet, J.; Douce, L.; Heinrich, B.; Welter, R.; Louati, A.
    Beilstein J. Org. Chem. **2009,** *5,* No. 51. doi:10.3762/bjoc.5.51

Influence of spacer chain lengths and polar terminal groups on the mesomorphic properties of tethered 5-phenylpyrimidines

Gundula F. Starkulla[1], Elisabeth Kapatsina[1], Angelika Baro[1], Frank Giesselmann[2], Stefan Tussetschläger[1], Martin Kaller[1] and Sabine Laschat[*1]

Full Research Paper

Address:
[1]Institut für Organische Chemie, Universität Stuttgart, Pfaffenwaldring 55, 70569 Stuttgart, Germany and [2]Institut für Physikalische Chemie, Universität Stuttgart, Pfaffenwaldring 55, 70569 Stuttgart, Germany

Email:
Sabine Laschat[*] - sabine.laschat@oc.uni-stuttgart.de

* Corresponding author

Abstract

Based on 5-(4-hydroxyphenyl)-2-octylpyrimidine **8**, 5-phenylpyrimidine derivatives **3–7**, **9** with different spacer chain lengths (C_2 up to C_6) and different terminal polar groups (Br, Cl, N_3, OH, CN) were synthesized by etherification and nucleophilic substitution. The mesomorphic behaviour of these compounds was investigated by differential scanning calorimetry (DSC), polarizing optical microscopy (POM) and X-ray diffraction (WAXS and SAXS) and revealed smectic A mesophases for bromides, chlorides and azides **3**, **4** and **6**. For these compounds a maximum phase width was observed for the C_5 spacer regardless of the terminal group, whereas the hydroxy- and cyano-substituted derivatives **5** and **7**, respectively, were non mesomorphic and showed only melting transitions.

Introduction

A tremendous amount of work has been done on calamitic liquid crystals, which has led to applications in the field of LC displays [1]. Among the large family of various calamitic mesogens 2-alkoxy-5-phenylpyrimidines **1** are prominent members due to the fact that the two nitrogen atoms increase the polarity of the rigid rod core structure (Scheme 1) as exemplified by the derivative **1a** which displays a SmA phase between 45 °C and
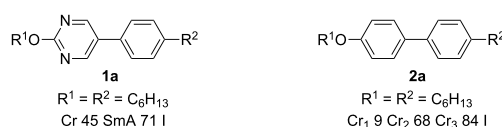
Scheme 1: Comparison of mesomorphic properties of **1a** and **2a**.

71 °C, while the corresponding biphenyl derivative **2a** with the same terminal alkyl chains does not have any liquid crystallinity [1].

Whereas three regioisomeric phenylpyrimidines are possible, i.e. 4-, 5-, and 2-phenylpyrimidine, only the latter two are suitable for liquid crystals. Furthermore 5- and 2-phenyl-pyrimidines differ in their overall conformation. According to ab initio calculation by Barone [2], 2-phenylpyrimidine is almost planar, whereas 5-phenylpyrimidine has a twisted conformation with a dihedral angle of 43.1° [3]. The different conformations together with differences of the polarisation and dipole moment between 2- and 5-phenylpyrimidines also lead to different mesomorphic properties as was shown by Lemieux for phenylpyrimidines tethered to terminal trisiloxanes [4,5] and by Tschierske for dimeric phenylpyrimidines tethered to oligoethyleneglycol units [6].

We recently reported the synthesis of 1,1′-biisoquinolines tethered to calamitic subunits [7]. During these studies we discovered that the 5-phenylpyrimidine building block **3e** already displayed a SmA mesophase. We thus wondered whether variation of the spacer chain lengths and terminal group X (Scheme 2) might have significant influence on the mesomorphism. The results of this study are discussed below.

Results and Discussion

Syntheses: In order to obtain different series **3–7** the known 5-(4-hydroxyphenyl)-2-octylpyrimidine **8** [7-12] was used as starting material (Scheme 3).

Compound **8** was deprotonated with KOH in DMSO at room temperature for 10 min followed by addition of 1,ω-dibromo-alkane. After 4 h, the reaction mixtures were purified and the desired bromides **3b–e** were isolated in 23 up to 60% yield. When 1,3-dibromopropane was used, 27% of the elimination product **9** was isolated as byproduct. For comparison the corresponding 4-allyloxy-4′-octylbiphenyl **11** was prepared in 49% yield by allylation of 4-hydroxy-4′-octylbiphenyl. Compound **3a** was obtained by etherification of 5-(4-hydroxyphenyl)-2-
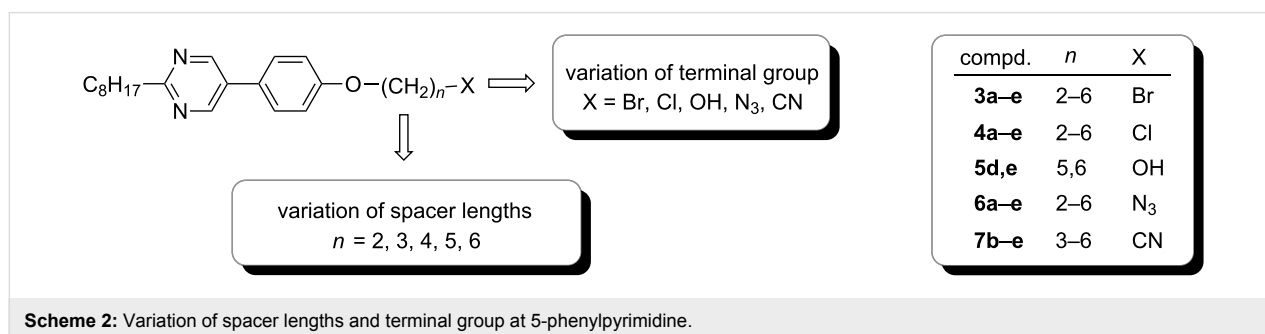
octylpyrimidine **8** using K_2CO_3 in MeCN under reflux for 12 h to yield 39%. The synthesis of series **4** with chloride as terminal group proceeded in a similar way by using 1,ω-dichloroalkanes giving **4a–e** in 31–70% yield. Upon deprotonation of **8** under the conditions described above, followed by treatment with 5-bromopentanol or 6-bromohexanol, the hydroxy compounds **5d** and **5e** were isolated in 76% and 80% yield, respectively. To obtain the azides **6**, bromides **3a–e** were treated with NaN_3 in DMF at 100 °C for 24 h and the products **6a–e** were isolated in 74% up to quantitative yield (Scheme 4). In a similar manner, the cyanides **7** were prepared from the bromides **3**. Treatment of the bromides **3c–e** with KCN in EtOH/H_2O at 110 °C for 12 h leads to the cyanides **7c–e** in 72 to 97% yield.
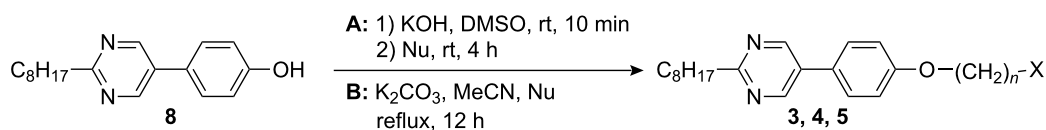
Since the yields of **3b** were limited due to side reactions like elimination, the respective cyanide **7b** was prepared by deprotonation of hydroxy derivative **8** with NaH in DMF for 40 min at 0 °C followed by addition of 1-bromo-3-propionitrile at room temperature. After 12 h, the cyanide **7b** was obtained in 33% yield.

Mesomorphic properties: Mesomorphic properties of compounds **3–10** were investigated by differential scanning calorimetry (DSC), polarizing optical microscopy (POM) and X-ray diffraction (WAXS and SAXS). The DSC results for bromides **3** are summarized in Table 1.

Whereas compounds **3a,c,e** with even chain lengths of the spacer displayed monotropic SmA phases, compounds **3b,d** with odd chain lengths displayed enantiotropic SmA phases. A typical DSC curve of derivative **3d** with a pentyloxy spacer is shown in Figure 1.

On the third heating a melting transition at 40 °C into the SmA phase and a clearing transition at 57 °C could be observed. Subsequent cooling revealed an isotropic to SmA transition at 60 °C and a crystallization peak at 24 °C. The SmA to crystalline transition tends to strong supercooling in the order of 10–30 K (Table 1, Figure 1).

Scheme 2: Variation of spacer lengths and terminal group at 5-phenylpyrimidine.

compd.	*n*	X
3a–e	2–6	Br
4a–e	2–6	Cl
5d,e	5,6	OH
6a–e	2–6	N_3
7b–e	3–6	CN

Scheme 3: Synthesis of compounds **3–5**, **9** and **11**.

POM observation of **3a–e** revealed fan-shaped textures typical of SmA phases. An illustrative example is depicted in Figure 2. The assignment of the SmA mesophases was further confirmed by XRD experiments (see the Supporting Information).

It should be noted that the allyloxy-substituted byproduct **9** showed a smectic mesophase between 50 °C and 67 °C as well. In contrast, the corresponding 4-allyloxy-4′-octylbiphenyl **11** showed only isotropic melting at 92 °C. The DSC results of chlorides **4** are summarized in Table 2.

All members **4a–e** showed enantiotropic SmA phases. For compounds **4a,c,e** with even numbered spacer lengths smaller mesophase widths were observed as compared to compounds **4b,d** with odd numbered spacer lengths. Furthermore an *odd–even* effect of both melting and clearing points was found. A typical DSC curve which is shown in Figure 3 for chloride **4e** with hexyloxy spacer, revealed a melting transition at 59 °C to the

smectic A phase and a clearing transition at 66 °C upon a second heating. Upon the second cooling run an isotropic to SmA transition at 64 °C and a crystallization peak at 42 °C were observed.

POM investigation displayed fan-shaped and focal conic textures, as exemplified in Figure 4. XRD experiments proved the smectic phase.

In contrast to the bromides **3** and chlorides **4**, the hydroxy and azide derivatives **5a,b** and **7b–e** were non mesomorphic and showed only melting transitions at 76 °C and 75 °C for compounds **5a,b** and at 77 °C, 86 °C, 67 °C and 68 °C for the azides **7b–e**, respectively (upon heating or cooling) in the DSC curve. Presumably, the higher polarity of the terminal hydroxy group with respect to the azido group, together with hydrogen bonding, inhibits mesophase formation. Next the azides **6** were investigated by DSC (Table 3).
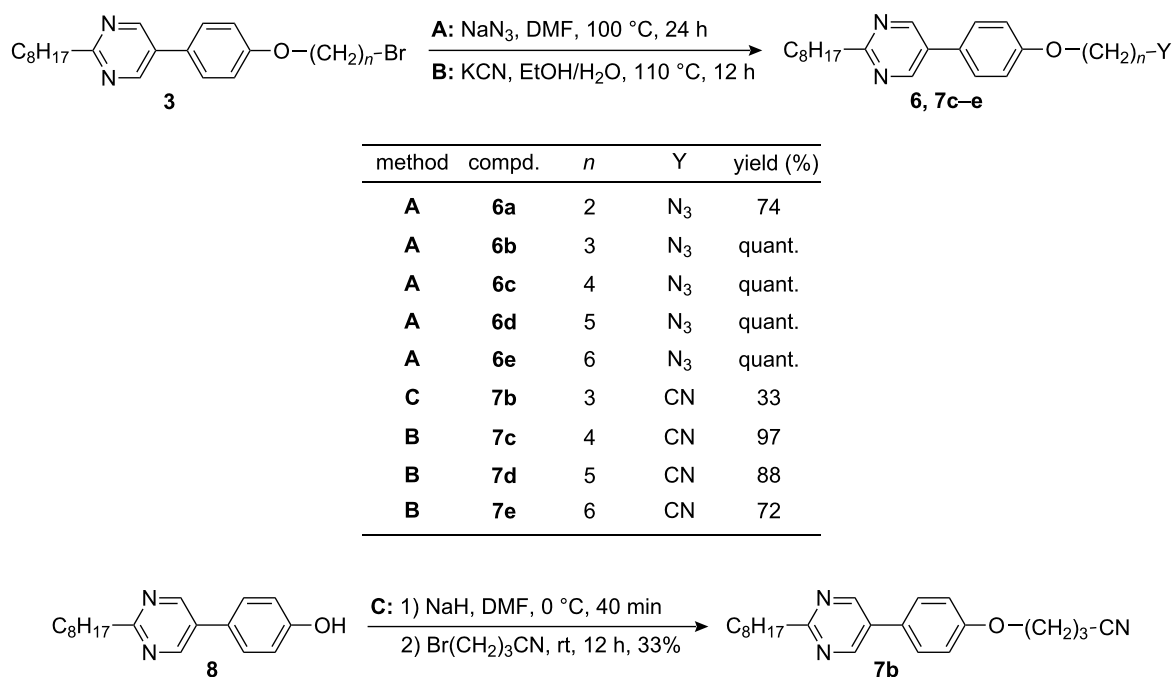
Scheme 4: Synthesis of compounds **6** and **7**.

method	compd.	n	Y	yield (%)
A	**6a**	2	N_3	74
A	**6b**	3	N_3	quant.
A	**6c**	4	N_3	quant.
A	**6d**	5	N_3	quant.
A	**6e**	6	N_3	quant.
C	**7b**	3	CN	33
B	**7c**	4	CN	97
B	**7d**	5	CN	88
B	**7e**	6	CN	72

Table 1: Phase transition temperatures [°C] and enthalpies [kJ/mol] of compounds **3**.[a]

3	n	Cr_1	T	ΔH	Cr_2	T	ΔH	SmA	T	ΔH	I	
a	2	•	52	3.9	•	63	32.2	-	-	-	•	2. heating
		•	29	−25.8	-	-	-	•	56	−5.6	•	2. cooling
b	3	•	46	13.0	-	-	-	•	52	1.9	•	2. heating
		•	35	−13.9	-	-	-	•	52	−3.2	•	2. cooling
c	4	•	66	31.1	-	-	-	-	-	-	•	2. heating
		•	49	−24.1	-	-	-	•	63	−5.0	•	2. cooling
d	5	•	40	17.6	-	-	-	•	57	5.1	•	2. heating
		•	24	−16.7	-	-	-	•	60	−5.3	•	2. cooling
e	6	•	64	36.3	-	-	-	-	-	-	•	2. heating
		•	35	−23.9	-	-	-	•	58	−5.5	•	2. cooling

[a]Cr crystalline; SmA smectic A; I isotropic; • phase was observed; - phase was not observed. Heating and cooling rate: 10 K/min.

Whereas compound **6a** with an ethoxy spacer was non mesomorphic, enantiotropic SmA phases were detected for all other chain lengths **6b–e**. Compound **6d** showed an additional crystal to crystal transition. A typical DSC curve of derivative **6c** is shown in Figure 5. POM revealed fan-shaped and focal conic texture, see for example Figure 6. Figure 7 and Figure 8 reveal that due to substantial supercooling for all spacer chain lengths and terminal groups the mesophases are smaller during the heating cycle as compared to the cooling cycle. The broadest mesophase was observed for the azide derivative **6d** with $\Delta T = 27$ °C upon heating and $\Delta T = 45$ °C upon cooling. In comparison to the compounds with an azide as terminal group the

halides ($n = 2, 5, 6$) have a lower tendency to supercooling. Whereas for azides **6** the broadest mesophase was observed for C_5 spacer (**6d**), for chlorides **4** derivatives **4b** and **4d** with C_3 and C_5 spacer displayed similar mesophase width. For bromides **3** again the derivative **3d** with C_5 spacer showed the broadest mesophase.

From the X-ray data, the following model (Figure 9) of the layer structure is proposed. The d values obtained from the X-ray experiments fit with the molecular lengths derived from simple molecular modelling (Chem3D) [13]. For example, the XRD pattern of the azide derivative **6c** results in a layer dis-

Figure 1: DSC curve of compound **3d** (heating/cooling rate 10 K/min).

Figure 2: Fan-shaped texture of **3e** under crossed polarizers upon cooling from the isotropic liquid (magnification 200×): at 55 °C (cooling rate 5 K/min): smectic A phase.
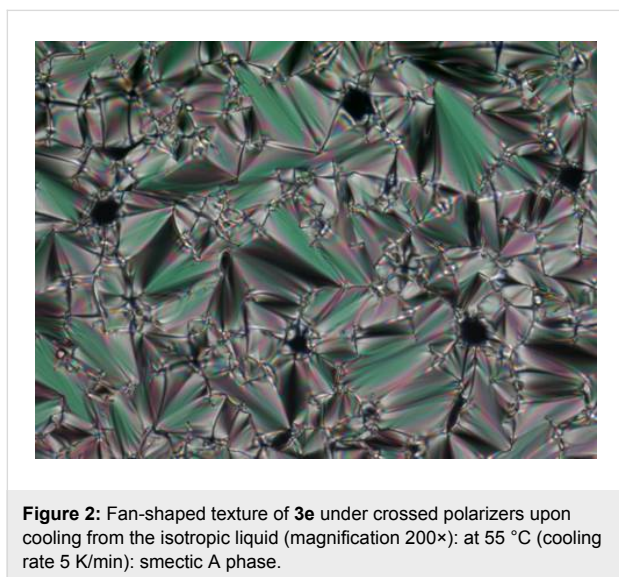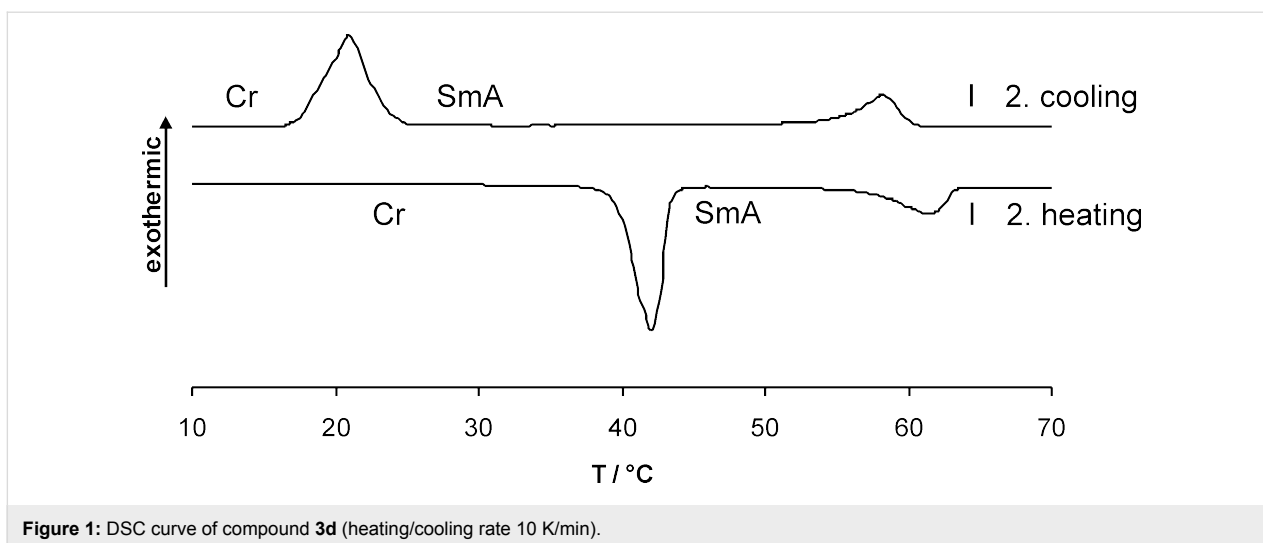
tance of 25.5 Å, whereas the calculated length of the molecule for the most elongated conformation is 26 Å, which is clear evidence for the presence of monolayers. This leads to the assumption that the molecules might be aligned antiparallel within each smectic layer (Figure 9). Packing the molecules in this array prevents close contacts between the polar regions of the rigid core and the terminal groups. The observed maximum phase width for the C_5 spacer regardless of the terminal group suggests that for this chain length space filling is optimal and the terminal group X can be accommodated well between the alkyl chains. This model might also explain why the mesophase is lost with strongly polar or hydrogen bonding terminal groups such as cyanides and hydroxy derivatives.

Conclusion

It has been shown that 5-phenylpyrimidine derivatives with terminal chloro-, bromo-, azido-, hydroxy- and cyano groups

Table 2: Phase transition temperatures [°C] and enthalpies [kJ/mol] of compounds **4**.[a]

4	n	Cr	T	ΔH	SmA	T	ΔH	I	
a	2	•	50	21.6	•	55	1.4	•	2. heating
		•	25	−18.7	•	53	−1.5	•	2. cooling
b	3	•	37	11.9	•	53	3.9	•	2. heating
		•	23	−11.8	•	58	−4.2	•	2. cooling
c	4	•	63	21.9	•	67	2.7	•	2. heating
		•	46	−23.5	•	70	−4.9	•	2. cooling
d	5	•	42	15.7	•	56	5.0	•	2. heating
		•	27	−17.0	•	62	−4.8	•	2. cooling
e	6	•	55	20.8	•	59	4.7	•	2. heating
		•	42	−25.3	•	64	−4.5	•	2. cooling

[a]Cr crystalline; SmA smectic A; I isotropic; • phase was observed; - phase was not observed. Heating and cooling rate: 10 K/min for **4a–d**, 5 K/min for **4e**.
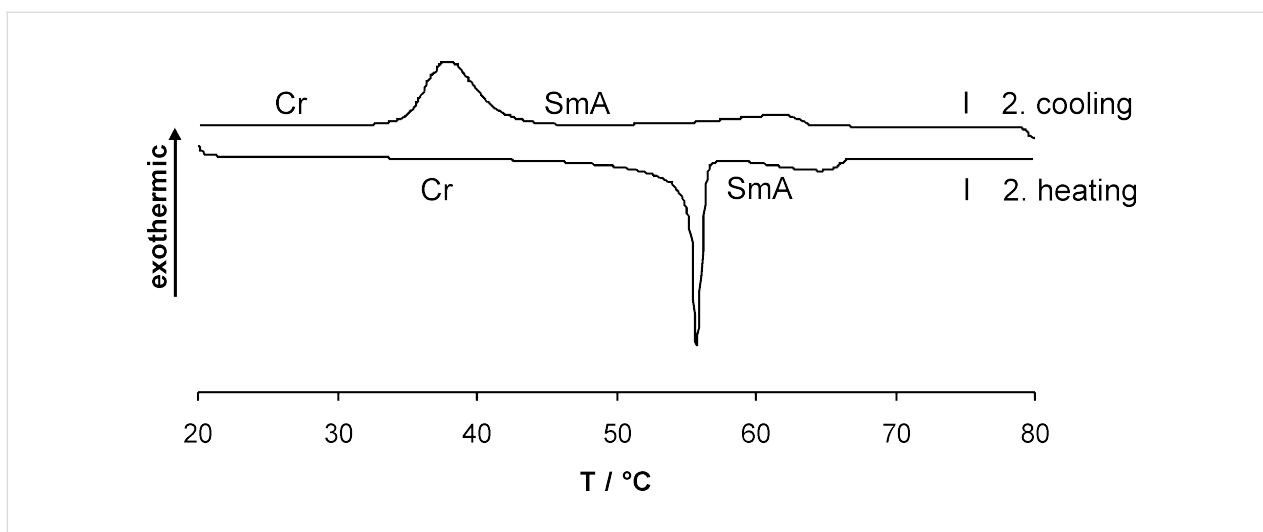
Figure 3: DSC curve of compound **4e** (heating/cooling rate 5 K/min).
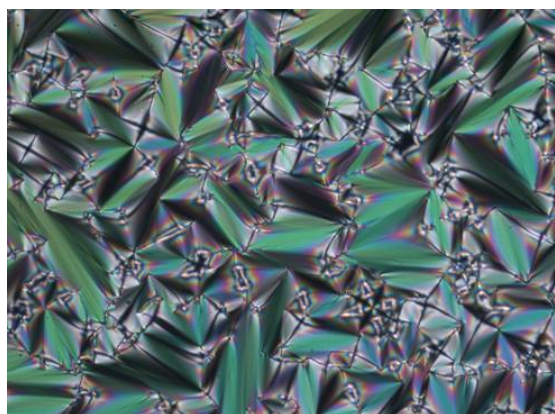

Figure 4: Fan-shaped texture of compound **4d** at 45 °C upon cooling from the isotropic liquid (cooling rate 1 K/min) (magnification 200×).

separated by an alkoxy spacer chain from the aromatic core were easily synthesised by nucleophilic substitution. Depending on the terminal group and the tether lengths the formation of smectic A mesophases was observed for the chloro-, bromo- and azido derivatives. Surprisingly, the strong latent dipole moment of hydroxy and cyano derivatives and the ability of hydroxy derivatives to form hydrogen bonds seems to completely suppress the formation of mesophases. Furthermore, the polar pyrimidine ring seems to play an important role in promoting liquid crystalline properties.

Experimental
General

Melting points were measured on a Mettler Toledo DSC822 and are uncorrected. NMR spectra were recorded on a Bruker Avance 300 and Avance 500 spectrometer. FT-IR spectra were recorded on a Bruker Vektor22 spectrometer with MKII Golden

Table 3: Phase transition temperatures [°C] and enthalpies [kJ/mol] of compounds **6**.[a]

6	*n*	Cr$_1$	*T*	Δ*H*	Cr$_2$	*T*	Δ*H*	SmA	*T*	Δ*H*	I	
a	2	•	48	30.6	-	-	-	-	-	-	•	2. heating
		•	44	−31.4	-	-	-	-	-	-	•	2. cooling
b	3	•	45	11.9	-	-	-	•	49	1.1	•	2. heating
		•	34	−13.7	-	-	-	•	47	−2.9	•	2. cooling
c	4	•	42	25.3	-	-	-	•	60	5.0	•	2. heating
		•	28	−17.8	-	-	-	•	63	−5.3	•	2. cooling
d	5	•	7	0.9	•	28	17.2	•	55	3.4	•	2. heating
		•	1	−0.6	•	11	−16.0	•	57	−4.7	•	2. cooling
e	6	•	41	26.5	-	-	-	•	53	6.1	•	2. heating
		•	20	−22.2	•	25	−0.5	•	58	−5.9	•	2. cooling

[a]Cr crystalline; SmA smectic A; I isotropic; • phase was observed; - phase was not observed. Heating and cooling rate: 10 K/min.
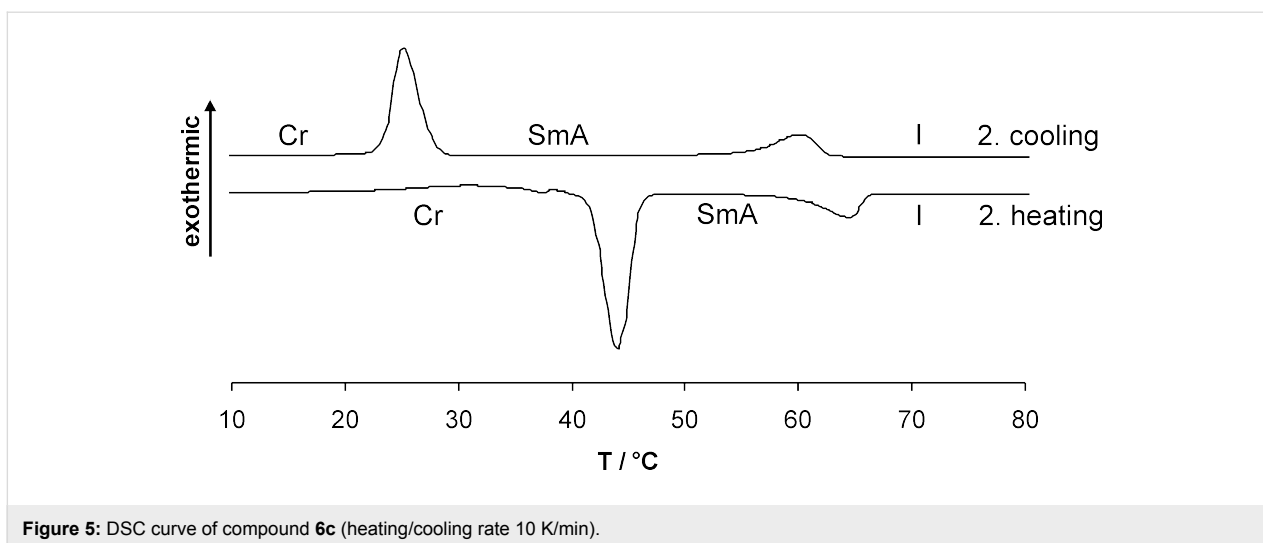
Figure 5: DSC curve of compound **6c** (heating/cooling rate 10 K/min).

Figure 6: Fan-shaped texture of compound **6e** at 45 °C upon cooling from the isotropic liquid (cooling rate 10 K/min) (magnification 200×).

Gate Single Reflection Diamant ATR system. Mass spectra were recorded on a Finnigan MAT 95 and a Varian MAT 711 apparatus. X-Ray powder experiments were performed on a Bruker Nanostar; software: SAXS 4.1.26. The samples were kept in Hilgenberg glass capillaries of 0.7 mm outside diameter in a temperature-controlled heating stage (±1 °C). A monochromatic Cu-K$_\alpha$1 beam (λ = 1.5405 Å) was obtained using a ceramic tube generator (1500 W) with cross-coupled Göbel-mirrors as the monochromator. The diffraction patterns were recorded on a real-time 2D-detector (HI-STAR, Bruker). The calibration of the patterns occurred with the powder pattern of Ag-Behenate. Differential scanning calorimetry (DSC) was performed using a Mettler Toledo DSC822, and polarizing optical microscopy (POM) using an Olympus BX50 polarizing microscope combined with a Linkam LTS350 hot stage and a Linkam TP93 central processor. Flash chromatography was
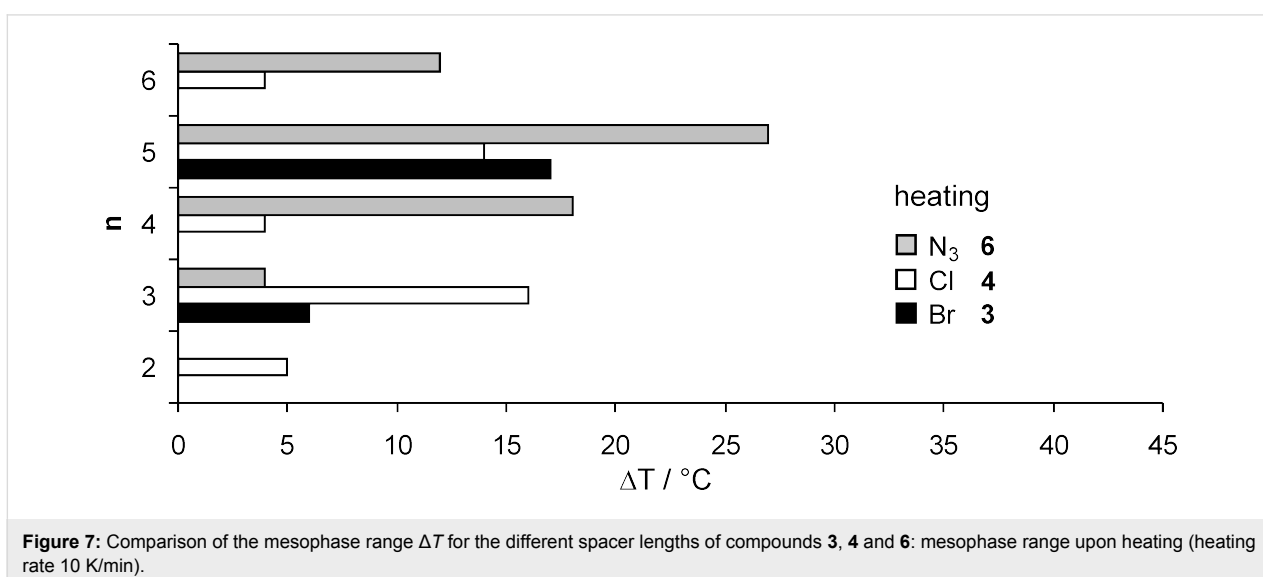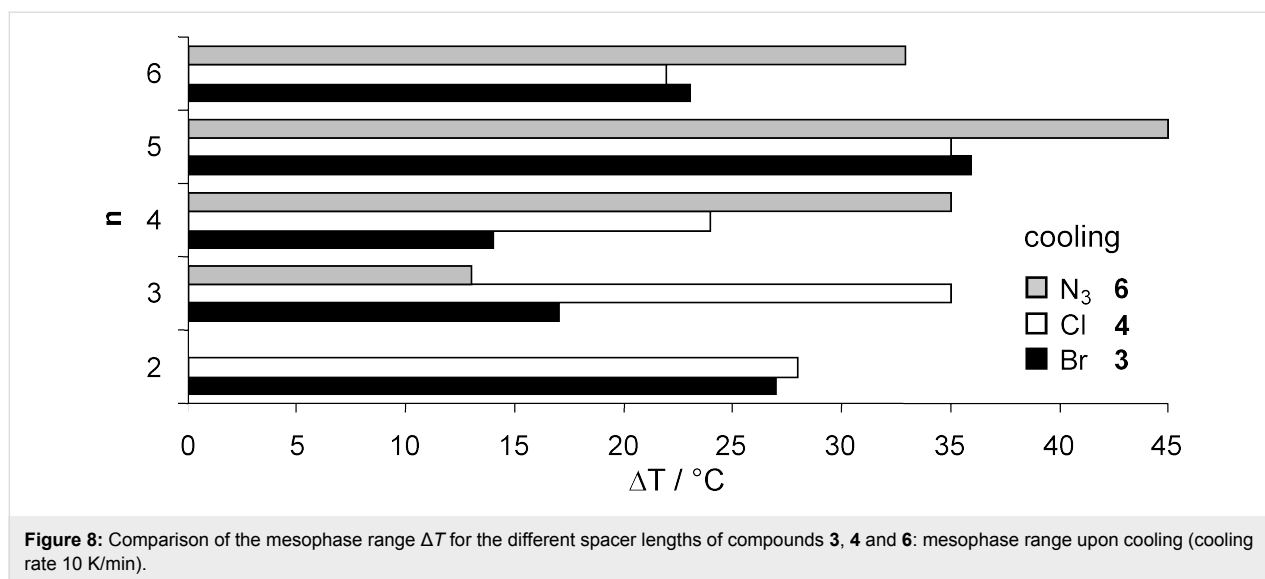

Figure 7: Comparison of the mesophase range ΔT for the different spacer lengths of compounds **3**, **4** and **6**: mesophase range upon heating (heating rate 10 K/min).

Figure 8: Comparison of the mesophase range Δ*T* for the different spacer lengths of compounds **3**, **4** and **6**: mesophase range upon cooling (cooling rate 10 K/min).

performed using Kieselgel 60, 40–63 μm (Fluka). All solvents were dried, and reactions were performed in dried glassware. The used petroleum ether (PE) had a boiling range of 30–75 °C.
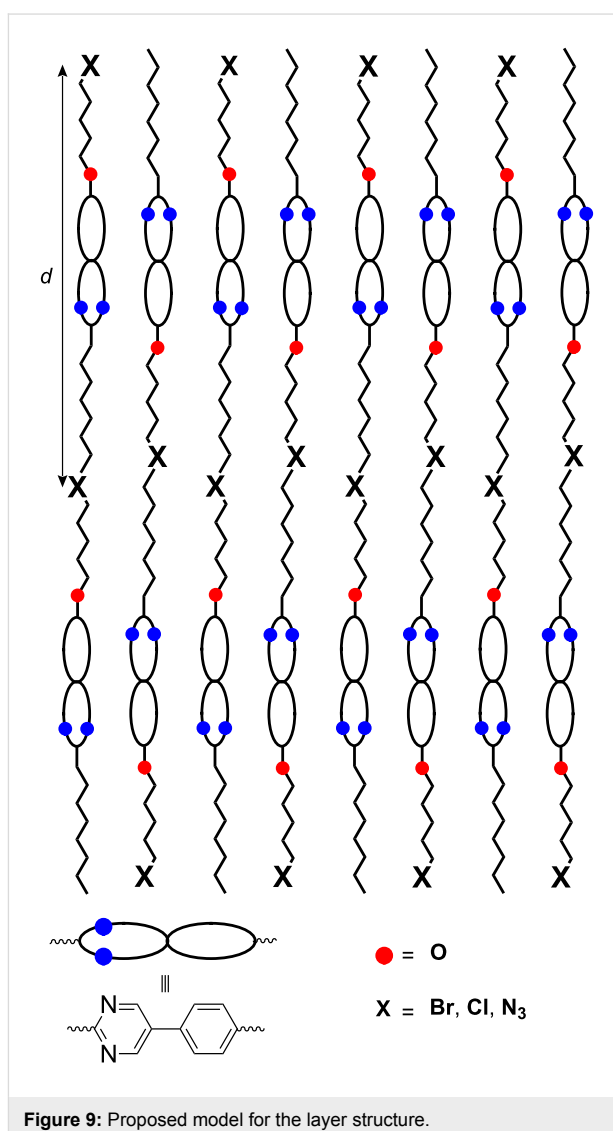
General procedure 1

To a solution of 5-(4-hydroxyphenyl)-2-octylpyrimidine **8** (852 mg, 3.00 mmol) in 4 mL DMSO was added powdered KOH (504 mg, 9.00 mmol). After stirring for 10 min at room temperature, the α,ω-dihaloalkane (or α-bromo-ω-alkanol respectively) (3.00 mmol) was added. Stirring was continued for 4 h followed by quenching with 20 mL H_2O and 100 mL CH_2Cl_2. The organic layer was dried (Na_2SO_4) and the solvents were evaporated. Finally the crude product was purified by flash chromatography.

General procedure 2

A solution of bromide **3** (0.50 mmol) and NaN_3 (81.0 mg, 1.25 mmol) in 15 mL DMF was stirred at 100 °C for 24 h. After cooling to room temperature, the reaction mixture was treated with 20 mL H_2O and extracted with CH_2Cl_2 (3 × 30 mL). The combined organic layers were dried (Na_2SO_4), the solvent was evaporated and the crude product purified by flash chromatography.

General procedure 3

A solution of bromide **3** (0.50 mmol) and KCN (35.8 mg, 0.55 mmol) in 4 mL $EtOH/H_2O$ (3:1, v/v) was stirred at 110 °C for 12 h. After cooling to room temperature, 10 mL CH_2Cl_2 were added and the aqueous layer was extracted with CH_2Cl_2 (3 × 10 mL). The combined organic layers were washed with 1 N NaOH (1 × 10 mL) and dried (Na_2SO_4). Finally the solvent was evaporated and the crude product purified by flash chromatography.

Figure 9: Proposed model for the layer structure.

5-[4-(6-Bromohexyloxy)phenyl]-2-octylpyrimidine (3e)

Prepared according to general procedure (1). Experiment: 284 mg (1.00 mmol) 5-(4-hydroxyphenyl)-2-octylpyrimidine **8**, 160 µL (245 mg, 1.00 mmol) 1,6-dibromohexane, 168 mg (3.00 mmol) KOH. Flash chromatography (PE/EtOAc, 4:1, v/v; R_f = 0.86: PE/EtOAc, 1:1, v/v) gave 268 mg (0.60 mmol, 60%) of **3e** as a colourless crystalline solid. DSC: Cr 35 °C [−23.9 kJ/ mol] (SmA 58 °C [−5.5 kJ/mol]) I. ^{1}H NMR (300 MHz, CDCl$_3$): δ = 0.88 (t, 3H J = 6.9 Hz, CH$_3$), 1.21–1.45 (m, 10H, CH$_2$), 1.49–1.58 (m, 4H, CH$_2$), 1.79–1.98 (m, 6H, CH$_2$), 2.96–3.01 (m, 2H, 2-CH$_2$), 3.44 (t, 2H, J = 6.6 Hz, CH$_2$Br), 4.02 (t, 2H, J = 6.4 Hz, OCH$_2$), 6.99–7.03 (m, 2H, 3′-H, 5′-H), 7.46–7.50 (m, 2H, 2′-H, 6′-H), 8.83 (s, 2H, 4-H, 6-H) ppm. ^{13}C NMR (125 MHz, CDCl$_3$): δ = 14.1 (CH$_3$), 22.7, 25.3, 27.9, 28.9, 29.0, 29.2, 29.4, 31.9, 32.7, 33.8 (CH$_2$), 39.2 (2-CH$_2$), 67.9 (OCH$_2$), 115.2 (C-3′, C-5′), 128.0 (C-2′, C-6′), 126.7, 130.8 (C-1′, C-5), 154.8 (C-4, C-6), 159.9 (C-4′), 169.5 (C-2) ppm. FT-IR (ATR): $\widetilde{ν}$ = 2916 (m), 2848 (m), 1586 (m), 1536 (m), 1515 (m), 1445 (s), 1247 (s), 1180 (m), 1116 (m), 1011 (m), 994 (m), 838 (s), 651 (m), 608 (m) cm^{-1}. MS (EI, 70eV): m/z (%) = 446.1 (100) [M]$^+$, 361.0 (20) [M−C$_6$H$_{13}$]$^+$, 348.0 (78) [M + H−C$_7$H$_{15}$]$^+$, 199.0 (10) 186.0 (28). C$_{24}$H$_{35}$BrN$_2$O (447.45): calcd. C 64.42, H 7.88, N 6.26, Br 17.86; found C 64.46, H 7.88, N 6.14, Br 17.61.

5-[4-(6-Chlorohexyloxy)phenyl]-2-octylpyrimidine (4e)

Prepared according to general procedure (1). Experiment: 85.0 mg (0.30 mmol) 5-(4-hydroxyphenyl)-2-octylpyrimidine **8**, 45.0 µL (47.0 mg, 0.30 mmol) 1,6-dichlorohexane, 50.0 mg (0.90 mmol) KOH. Flash chromatography (PE/EtOAc, 5:1, v/v; R_f = 0.40: PE/EtOAc, 3:1, v/v) gave 74.0 mg (0.18 mmol, 60%) of **4e** as a colourless crystalline solid. DSC: Cr 42 °C [−25.3 kJ/ mol] SmA 64 °C [−4.5 kJ/mol] I. ^{1}H NMR (300 MHz, CDCl$_3$): δ = 0.85–0.90 (m, 3H, CH$_3$), 1.23–1.44 (m, 10H, CH$_2$), 1.50–1.55 (m, 4H, CH$_2$), 1.78–1.90 (m, 6H, CH$_2$), 2.96–3.01 (m, 2H, 2-CH$_2$), 3.56 (t, 2H, J = 6.7 Hz, CH$_2$Cl), 4.01 (t, 2H, J = 6.4 Hz, OCH$_2$), 6.99–7.04 (m, 2H, 3′-H, 5′-H), 7.46–7.51 (m, 2H, 2′-H, 6′-H), 8.83 (s, 2H, 4-H, 6-H) ppm. ^{13}C NMR (75 MHz, CDCl$_3$): δ = 14.1 (CH$_3$), 22.7, 25.4, 26.6, 28.8, 29.1, 29.2, 29.4, 31.9, 32.5 (CH$_2$), 39.2 (2-CH$_2$), 45.0 (CH$_2$Cl), 67.9 (OCH$_2$), 115.3 (C-3′, C-5′), 127.9 (C-2′, C-6′), 126.7, 130.8 (C-1′, C-5), 154.5 (C-4, C-6), 159.6 (C-4′), 169.6 (C-2) ppm. FT-IR (ATR): $\widetilde{ν}$ = 2917 (m), 2849 (m), 1587 (m), 1516 (m), 1446 (s), 1392 (m), 1287 (m), 1246 (s), 1181 (m), 1116 (m), 1029 (m), 994 (m), 941 (m), 838 (m), 721 (m) cm^{-1}. MS (ESI): m/z = 403.3 [M + H]$^+$, 367.3 [M–Cl]$^+$. C$_{24}$H$_{35}$ClN$_2$O (403.00): calcd. C 71.53, H 8.75, N 6.95, Cl 8.80; found C 71.38, H 8.63, N 6.81, Cl 8.93.

5-[4-(6-Hydroxyhexyloxy)phenyl]-2-octylpyrimidine (5e)

Prepared according to general procedure (1). Experiment: 568 mg (2.00 mmol) 5-(4-hydroxyphenyl)-2-octylpyrimidine **8**, 270 µL (362 mg, 2.00 mmol) 6-bromohexane-1-ol, 336 mg (6.00 mmol) KOH. Flash chromatography (PE/EtOAc, 1:1, v/v; R_f = 0.29) gave 615 mg (1.60 mmol, 80%) of **5e** as a colourless crystalline solid. Mp: 75 °C. ^{1}H NMR (300 MHz, CDCl$_3$): δ = 0.85–0.90 (m, 3H, CH$_3$), 1.24–1.68 (m, 16H, CH$_2$), 1.79–1.90 (m, 4H, CH$_2$), 2.96–3.01 (m, 2H, 2-CH$_2$), 3.68 (t, 2H, J = 6.5 Hz, CH$_2$OH), 4.01 (t, 2H, J = 6.5 Hz, OCH$_2$), 6.99–7.04 (m, 2H, 3′-H, 5′-H), 7.46–7.51 (m, 2H, 2′-H, 6′-H), 8.83 (s, 2H, 4-H, 6-H) ppm. ^{13}C NMR (75 MHz, CDCl$_3$): δ = 14.1 (CH$_3$), 22.7, 25.6, 25.9, 28.9, 29.2, 29.5, 31.9, 32.7 (CH$_2$), 39.2 (2-CH$_2$), 62.8 (CH$_2$OH), 68.0 (OCH$_2$), 115.3 (C-3′, C-5′), 127.9 (C-2′, C-6′), 126.6, 130.8 (C-1′, C-5), 154.5 (C-4, C-6), 159.7 (C-4′), 169.6 (C-2) ppm. FT-IR (ATR): $\widetilde{ν}$ = 3303 (m, br), 2917 (s), 2848 (m), 1606 (m), 1586 (m), 1536 (m), 1516 (m), 1466 (m), 1445 (s), 1377 (m), 1291 (m), 1288 (m), 1248 (s), 1181 (m), 1118 (m), 1060 (m), 1007 (m), 994 (m), 918 (m), 838 (s), 707 (m), 652 (m) cm^{-1}. MS (EI, 70eV): m/z (%) = 384.3 (100) [M]$^+$, 299.2 (36), 286.2 (94). HRMS (ESI): m/z [M+H]$^+$ calcd. for C$_{24}$H$_{37}$N$_2$O$_2$: 385.2850; found: 385.2856. C$_{24}$H$_{36}$N$_2$O$_2$ (384.55): calcd. C 74.96, H 9.44, N 7.28; found C 75.05, H 9.27, N 7.26.

5-[4-(6-Azidohexyloxy)phenyl]-2-octylpyrimidine (6e)

Prepared according to general procedure (2). Experiment: 224 mg (0.50 mmol)) bromide **3e**, 81.0 mg (1.25 mmol) NaN$_3$. Flash chromatography (PE/EtOAc, 2:1, v/v; R_f = 0.56) gave 205 mg (0.50 mmol, quant.) of **6e** as a colourless crystalline solid. DSC: Cr$_1$ 20 °C [−22.2 kJ/mol] Cr$_2$ 25 °C [−0.5 kJ/mol] SmA 58 °C [−5.9 kJ/mol] I. ^{1}H NMR (300 MHz, CDCl$_3$): δ = 0.85–0.90 (m, 3H, CH$_3$), 1.24–1.58 (m, 14H, CH$_2$), 1.60–1.71 (m, 2 H, CH$_2$), 1.78–1.91 (m, 4H, CH$_2$), 2.97–3.01 (m, 2H, 2-CH$_2$), 3.30 (t, 2H, J = 6.8 Hz, CH$_2$N$_3$), 4.02 (t, 2H, J = 6.4 Hz, OCH$_2$), 7.00–7.04 (m, 2H, 3′-H, 5′-H), 7.47–7.51 (m, 2H, 2′-H, 6′-H), 8.83 (s, 2H, 4-H, 6-H) ppm. ^{13}C NMR (75 MHz, CDCl$_3$): δ = 14.1 (CH$_3$), 22.7, 25.7, 26.5, 28.8, 28.9, 29.1, 29.2, 29.5, 31.9 (CH$_2$), 39.2 (2-CH$_2$), 51.4 (CH$_2$N$_3$), 67.9 (OCH$_2$), 115.3 (C-3′, C-5′), 127.9 (C-2′, C-6′), 126.7, 130.8 (C-1′, C-5), 154.5 (C-4, C-6), 159.6 (C-4′), 169.6 (C-2) ppm. FT-IR (ATR): $\widetilde{ν}$ = 2921 (s), 2847 (m), 2091 (s), 1605 (m), 1587 (m), 1467 (m), 1446 (s), 1287 (m), 1246 (s), 1182 (m), 1032 (m), 993 (m), 836 (s), 654 (m) cm^{-1}. MS (ESI): m/z = 432.3 [M + Na]$^+$, 410.3 [M + H]$^+$. C$_{24}$H$_{35}$N$_5$O (409.58): calcd. C 70.38, H 8.61, N 17.10; found C 70.51, H 8.55, N 17.05.

5-[4-(6-Cyanohexyloxy)phenyl]-2-octylpyrimidine (**7e**)

Prepared according to general procedure (3). Experiment: 224 mg (0.50 mmol) bromide **3e**, 36.0 mg (0.55 mmol) KCN. Flash chromatography (PE/EtOAc, 4:1, v/v; R_f = 0.23) gave 142 mg (0.36 mmol, 72%) of **7e** as a colourless crystalline solid. Mp: 68 °C. ^{1}H NMR (500 MHz, CDCl$_3$): δ = 0.88 (t, 3H J = 6.9 Hz, CH$_3$), 1.20–1.45 (m, 10H, CH$_2$), 1.51–1.60 (m, 4H, CH$_2$), 1.68–1.90 (m, 6H, CH$_2$), 2.37 (t, 2H, J = 7.3 Hz, CH$_2$CN), 2.96–3.01 (m, 2H, 2-CH$_2$), 4.02 (t, 2H, J = 6.3 Hz, OCH$_2$), 6.99–7.03 (m, 2H, 3′-H, 5′-H), 7.46–7.51 (m, 2H, 2′-H, 6′-H), 8.81 (s, 2H, 4-H, 6-H) ppm. ^{13}C NMR (125 MHz, CDCl$_3$): δ = 14.1 (CH$_3$), 17.1, 22.7, 25.3, 25.4, 28.4, 28.9, 29.2, 29.5, 31.9 (CH$_2$), 39.2 (2-CH$_2$), 67.9 (OCH$_2$), 115.4 (C-3′, C-5′), 119.7 (CN), 128.0 (C-2′, C-6′), 126.9, 130.8 (C-1′, C-5), 154.5 (C-4, C-6), 159.6 (C-4′), 169.7 (C-2) ppm. FT-IR (ATR): $\widetilde{\nu}$ = 3035 (w), 2950 (m), 2920 (m), 2852 (m), 1608 (m) 1588 (m), 1541 (m), 1518 (m), 1440 (s), 1397 (m), 1245 (s), 1188 (s), 1048 (m), 996 (m), 836 (s), 738 (m), 706 (m), 652 (m), 556 (m) cm^{-1}. MS (EI, 70eV): *m/z* (%) = 393.2 (72) [M]$^+$, 350.2 (8), 308.2 (28), 395.2 (100), 185.1 (11). HRMS (ESI): *m/z* [M+H]$^+$ calcd. for C$_{25}$H$_{36}$N$_3$O: 394.2853; found: 394.2854. C$_{25}$H$_{35}$N$_3$O (393.56): calcd. C 76.29, H 8.96, N 10.68; found C 76.15, H 8.93, N 10.51.

Supporting Information

Supporting information includes experimental and spectroscopic data for compounds **4a–d**, **5d**, **6a–d**, **7a–d**, **9**, **11** and X-ray diffraction data.

Supporting Information File 1
Analytical data of compounds **4a–d**, **5d**, **6a–d**, **7a–d**, **9**, **11**. [http://www.beilstein-journals.org/bjoc/content/supplementary/1860-5397-5-63-S1.pdf]

Acknowledgments

References

1. Goodby, J. W. In *Handbook of Liquid Crystals;* Demus, D.; Goodby, J. W.; Gray, G. W.; Spiess, H.-W.; Vill, V., Eds.; Wiley-VCH: Weinheim, Germany, 1998; Vol. 2A, pp 411–440.
2. Adamo, C.; Barone, V. *J. Chem. Phys.* **1998,** *108,* 664–675. doi:10.1063/1.475428
3. Barone, V.; Commisso, L.; Lelj, F.; Russo, N. *Tetrahedron* **1985,** *41,* 1915–1918. doi:10.1016/S0040-4020(01)96554-8
4. Li, L.; Jones, C. D.; Magolan, J.; Lemieux, R. P. *J. Mater. Chem.* **2007,** *17,* 2313–2318. doi:10.1039/b700972k
5. Roberts, J. C.; Kapernaum, N.; Giesselmann, F.; Lemieux, R. P. *J. Am. Chem. Soc.* **2008,** *130,* 13842–13843. doi:10.1021/ja805672q
6. Neumann, B.; Hegmann, T.; Wagner, C.; Ashton, P. R.; Wolf, R.; Tschierske, C. *J. Mater. Chem.* **2003,** *13,* 778–784. doi:10.1039/b210271d
7. Kapatsina, E.; Lordon, M.; Baro, A.; Laschat, S. *Synthesis* **2008,** 2551–2560. doi:10.1055/s-2008-1067184
8. Lloyd, D.; Reichardt, C.; Struthers, M. *Liebigs Ann. Chem.* **1986,** 1368–1379. doi:10.1002/jlac.198619860807
9. Dox, A. W. *Org. Synth.* **1941,** *1,* 5–6.
10. Hooley, R. J.; Rebek, J. *Org. Lett.* **2007,** *9,* 1179–1182. doi:10.1021/ol062782s
11. Sugita, S.-I.; Toda, S.; Yoshiyasu, T.; Teraji, T.; Murayama, A. *Mol. Cryst. Liq. Cryst.* **1994,** *239,* 113–122. doi:10.1080/10587259408047176
12. Sugita, S.-I.; Takeno, H.; Teraji, T. *Mol. Cryst. Liq. Cryst.* **1991,** *206,* 139–146. doi:10.1080/00268949108037726
13. Chem3D Pro 2008 software was used for molecular modelling.

License and Terms

Molecular length distribution and the formation of smectic phases

Nadia Kapernaum[1], C. Scott Hartley[2], Jeffrey C. Roberts[2], Robert P. Lemieux[2] and Frank Giesselmann[*1]

Abstract

The phase diagrams of two mixtures of chemically similar smectogenic mesogens strongly differing in molecular length were investigated. In these mixtures the nematic phase present in the pure short mesogen disappeared rapidly on the addition of the longer mesogen, while the smectic state was preserved. In the smectic state the smectic A phase was the much more stable phase as the smectic C phase disappeared quite rapidly as well. In these compounds the loss of the smectic C phase is accompanied by a decrease in smectic translational order and very small tilt angles. This leads to a concentration induced smectic C to smectic A transition. Thus smectic A seems to be the most stable phase to accommodate mesogenic molecules of substantially different length. These surprising results are of general interest for the understanding of the structure and dynamics of smectic phases, as the structure of these bidisperse smectics is signified by extensive out-of-layer fluctuations.

Introduction

The classical (and highly successful) approach to systematically tailor liquid crystal materials for specific applications is the formulation of optimised mixtures consisting of several mesogenic compounds and non-mesogenic additives such as chiral dopants or UV-stabilizers. While the design of nematic mixtures is highly developed and widely applied, far less is known about the mixing of smectics and the particular effects thereof. In principle the mixing of different kind of mesogens can lead to a phase behaviour that differs completely from that

of the pure compounds. This effect is even amplified in mixtures of mesogens with strongly differing molecular structure. In this paper we report a systematic study with mesogens strongly differing in molecular length.

We recently discovered that the electroclinic effect of a chiral smectic A* (SmA*) material (consisting of a phenylpyrimidine host and 4 mol % of a chiral atropisomeric dopant) was amplified by a factor of three after adding only 5% of another homo-

logous phenylpyrimidine, the molecular length of which was about twice the length of the host molecule [1]. This remarkable electroclinic effect amplification stimulated a more general investigation of how the mixing of smectogenic homologues differing only in molecular lengths (and thus making the distribution of molecular length extremely bimodal) changes the structure and properties of the nematic and the SmA phases and the (possible) tilting transition to smectic C (SmC).

As a general first approximation calamitic mesogens are considered as rigid rods. This means they are treated as long and thin hard spherocylinders [2]. The justification for this rather crude approximation, which neglects the flexibility of the alkyl side chains, is the general observation that the thickness of e.g. a smectic A layer (as observed in X-ray diffraction) is only slightly smaller than the fully extended length of the constituting mesogenic molecules. In a naive model we now consider the liq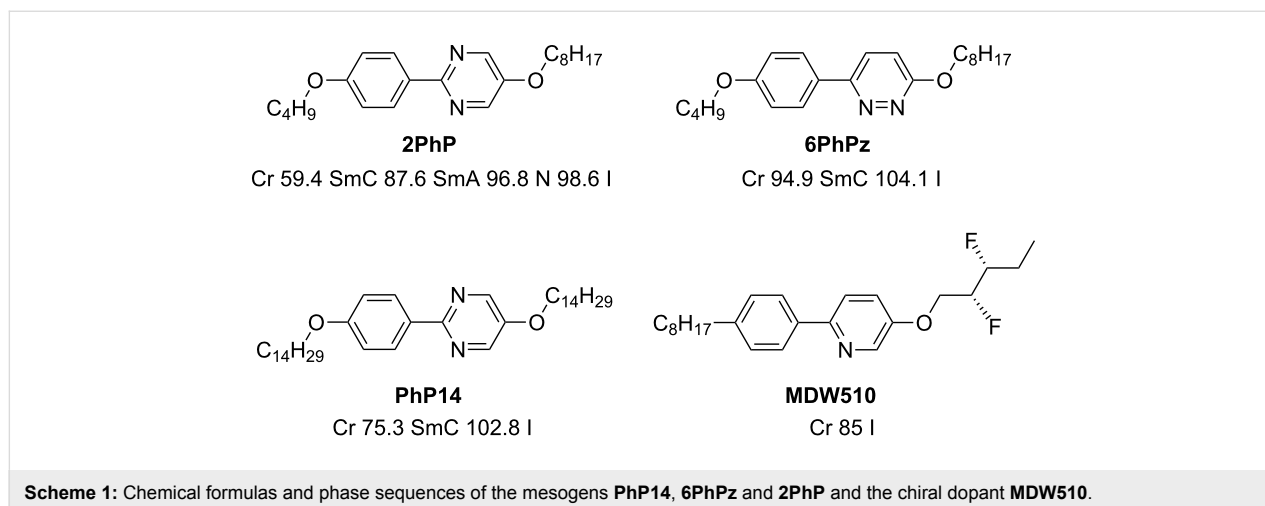uid crystalline phase behaviour of mixtures of two types of these hard spherocylinders, which exhibit the same diameter but their lengths are differing by a factor of two. In this naive model, the nematic phase is expected – due to the absence of translational order – to be the ideal liquid crystalline (LC) phase for accommodating molecules of substantially different lengths. On the other hand the smectic phases – due to their layer structure – seem to be unsuited to accommodate molecules of different lengths. Comparing SmC and SmA, the SmC phase might be better since it allows different tilt angles to fit different molecular lengths into a smectic layer with fixed spacing (Figure 1).

The actual results received in this study are indeed completely reverse to the naive picture drawn above. The bimodal length distribution of smectogenic molecules favours the formation of non-tilted SmA phases at the expense of nematic or tilted SmC phases.

Figure 1: Structure of different liquid crystalline phases build with two kinds of hard spherocylinders with strongly differing lengths.
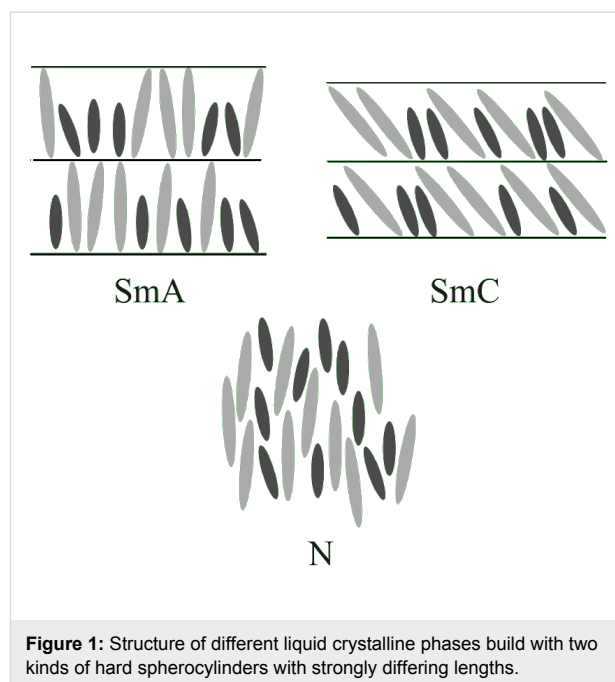
Results and Discussion

Scheme 1 and Figure 2 show the liquid crystalline materials we used in this experimental study. As the long component we chose the phenylpyrimidine **PhP14** (2-[4-(tetradecyloxy)-phenyl]-5-(tetradecyloxy)pyrimidine) [1], where the aromatic core is substituted symmetrically with two alkoxy chains each with 14 methylene units. It exhibits a molecular length of 45.5 Å. For the short compound we used either the phenylpyrimidine **2PhP** (2-[4-(butyloxy)phenyl]-5-(octyloxy)pyrimidine) [1] or the phenylpyridazine **6PhPz** (6-[4-(butyloxy)phenyl]-3-(octyloxy)pyridazine) [3,4]. Both were asymmetrically substituted with two alkoxy chains with four and eight methylene units, respectively. Their molecular length is 25.6 Å. This leads to a difference in lengths of a factor of the order of two.

2PhP
Cr 59.4 SmC 87.6 SmA 96.8 N 98.6 I

6PhPz
Cr 94.9 SmC 104.1 I

PhP14
Cr 75.3 SmC 102.8 I

MDW510
Cr 85 I

Scheme 1: Chemical formulas and phase sequences of the mesogens **PhP14**, **6PhPz** and **2PhP** and the chiral dopant **MDW510**.

Figure 2: Molecular structure of the mesogens **PhP14**, **6PhPz** and **2PhP** differing in molecular lengths by a factor of approximately two. The molecular lengths were determined from the most extended conformers, after optimizing their energy using molecular modelling with MOPAC/AM1.
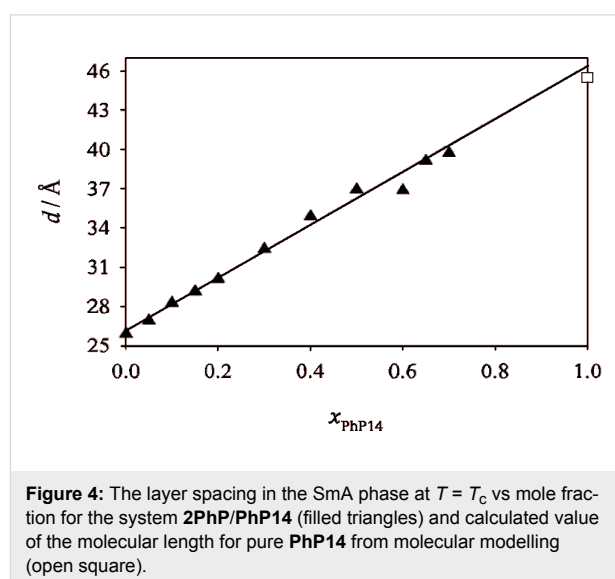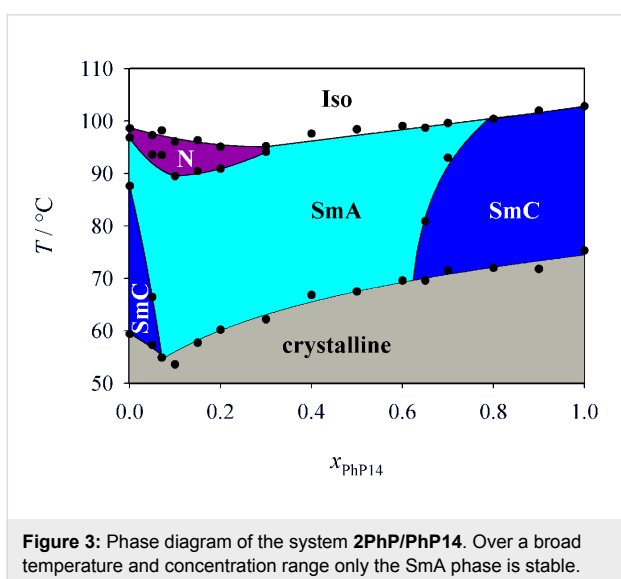
First we investigated the phase diagram of the system **2PhP/ PhP14** which is shown in Figure 3. This phase diagram shows completely different behaviour from that expected from the naive model. In particular we observed no indication of destabilization of the smectic state. We could even observe a eutectic point at $x_{PhP14} = 0.075$, where the temperature range of the smectic state is broadened. The nematic state on the other hand disappears rapidly with increasing mole fraction x_{PhP14} and is already lost at a mole fraction x_{PhP14} of 0.3. In the smectic state SmA turns out to be the much more stable phase. SmC disappears quite rapidly and SmA is the dominating phase in the phase diagram even though SmC is the dominating LC phase of **2PhP** and the only LC phase of **PhP14**. Taking into account that the average alkyl chain length increases with

increasing x_{PhP14}, this behaviour is to some extent analogous to the well known mesomorphism in homologous series where nematic is the dominating mesophase for short-length homologues, SmA for medium-length homologues and SmC for longer homologues (see e.g. [1]).

For all mixtures small angle X-ray scattering (SAXS) measurements were performed. Figure 4 shows the layer spacing in the SmA phase at $T = T_c$ in dependence on the mole fraction. A linear correlation between the layer spacing and the mole fraction is found. This linear dependence shows that the system **2PhP**/**PhP14** follows the Diele additivity rule [5]. It says that the layer spacing of a mixture can be calculated as: $d_{Mix} = d_A x_A + d_B x_B$, where d_{Mix}, d_A and d_B denote the layer spacings of

Figure 3: Phase diagram of the system **2PhP/PhP14**. Over a broad temperature and concentration range only the SmA phase is stable.

Figure 4: The layer spacing in the SmA phase at $T = T_c$ vs mole fraction for the system **2PhP/PhP14** (filled triangles) and calculated value of the molecular length for pure **PhP14** from molecular modelling (open square).

the mixture, the pure compound A and the pure compound B, respectively and x_A and x_B the mole fractions of compound A and B, respectively. From this equation the layer spacing of a hypothetical SmA phase of pure **PhP14** can be estimated. The extrapolated value of 46.4 Å corresponds quite well to the value of 45.5 Å we obtained for the extended length of the **PhP14** molecule from molecular modelling studies (see Figure 2). For **2PhP** the experimental *d*-value from SAXS (25.9 Å) also agrees very well with the extended length of the molecule (25.6 Å). This agreement between the experimental *d*-values and the extended molecular lengths for both pure compounds justifies to a certain extent the application of the spherocylinder model in these cases.

Figure 5 gives an overview of the layer spacings of pure **2PhP** and of the mixtures with 5%, 65% and 70% **PhP14** in **2PhP**, respectively. The reduced layer spacing (calculated from the measured layer spacing divided by the layer spacing of the SmA phase) is plotted vs the temperature difference $T-T_c$ relative to the phase transition temperature from SmA to SmC. The pure compound **2PhP** shows a 'common' behaviour of the layer spacing with significant layer shrinkage due to the molecular tilt in SmC of about 7% at $T-T_c = 20$ K. In the mixture with 5% **PhP14** the layer shrinkage in the SmC phase is reduced to only 5%. Very small layer shrinkage of only 1% was found for the mixture with 70% **PhP14**. And for the mixture with 65% **PhP14** no layer shrinkage at all could be found, although by polarizing microscopy the broken fan-shaped texture of a SmC phase was clearly observed (see Figure 6).
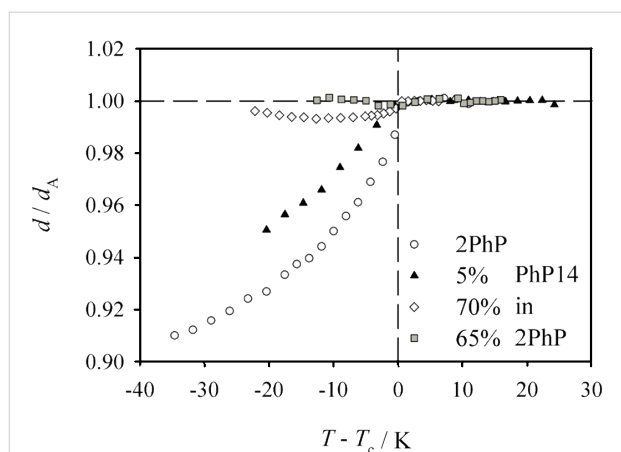

Figure 5: Reduced layer spacing for the mixtures which exhibit SmA and SmC phases in the system **2PhP/PhP14**. Pure **2PhP** shows quite normal layer shrinkage of 7% at $T-T_c = -20$ K (open circles). The addition of 5% of **PhP14** reduces the layer shrinkage to only 5% at $T-T_c = -20$ K (filled triangles). For the mixtures with excess of the long homologue **PhP14** the layer shrinkage is dramatically reduced. The 70%-mixture exhibits a layer shrinkage of only 1% at $T-T_c = -20$ K and for the mixture with 65% no layer shrinkage below the SmA to SmC phase transition could be observed at all.

To gain a deeper understanding of these smectic phases the optical tilt angle of the mixtures was measured in the corresponding ferroelectric SmC* state [6] (see Figure 7) after addition of 4 mol % of the chiral dopant **MDW510** ((*R,R*)-2-[4-(octyloxy)phenyl]-5-(2,3-difluorohexyloxy)pyridine) [7,8]. The pure compound **PhP14** exhibits the highest tilt angles, with a quite regular value of about 27°. The addition of more and more of the longer molecules reduces the SmC-tilt stepwise until only a SmA phase is left. This system thus shows a concentration induced SmC to SmA phase transition and therefore opens the possibility to design SmC phases with very small tilt angles [9]. These tilt angles are in good agreement with the tilt angles calculated from the X-ray layer shrinkage after: $\theta = \cos^{-1}(d_C/d_A)$. This correlation between the optical and X-ray tilt angles shows that, even if the layer shrinkage is very small, the mixtures do not necessarily exhibit the so-called 'de Vries-type' behaviour [10].

For a deeper insight into the quality of molecular ordering inside the smectic layer structure the translational order para-
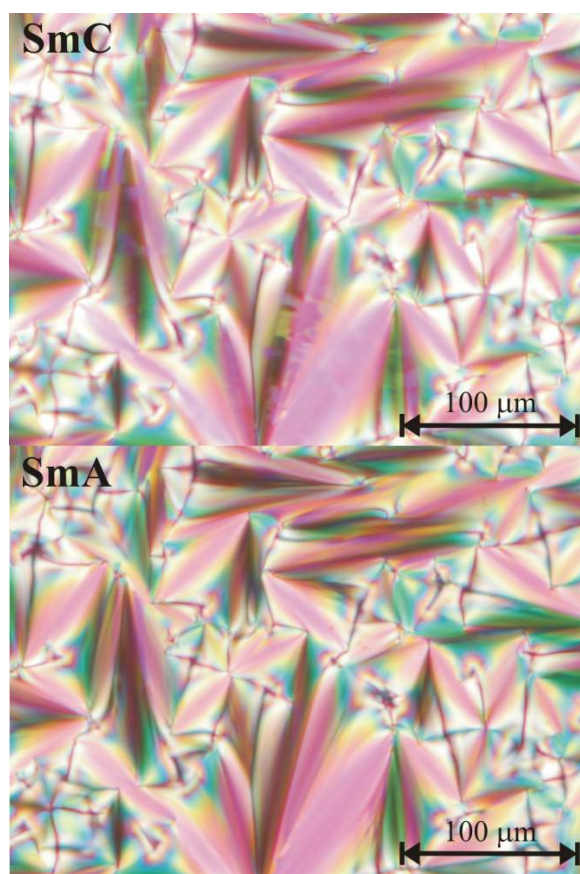

Figure 6: Textures of the mixture with 65% **PhP14** in **2PhP** as observed in the polarizing microscope. The upper part shows the broken fan-shaped texture of the SmC phase at *T* = 75 °C. In the lower part the fan-shaped texture of SmA is observed at *T* = 86 °C.
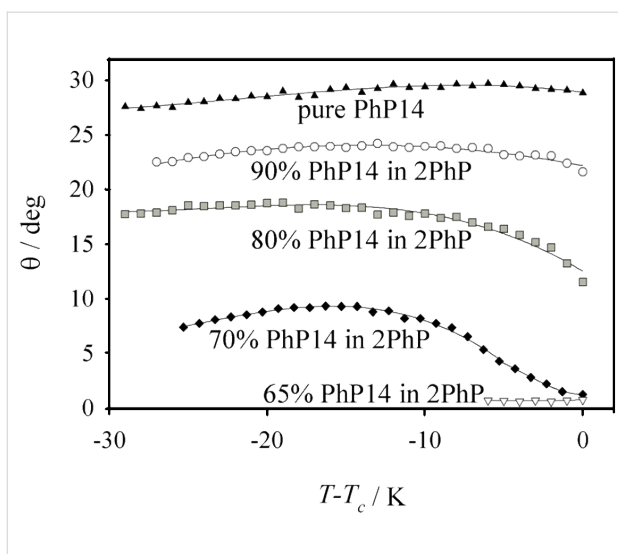
Figure 7: Tilt angle vs temperature difference to the phase transition temperature for pure **PhP14** (filled triangles), 90% (open circles), 80% (gray filled squares), 70% (filled diamonds) and 65% (open triangles) **PhP14** in **2PhP**. The tilt angle is reduced successively with increasing mole fraction of the short component **2PhP**. In this system a concentration-induced phase transition from SmC to SmA occurs.
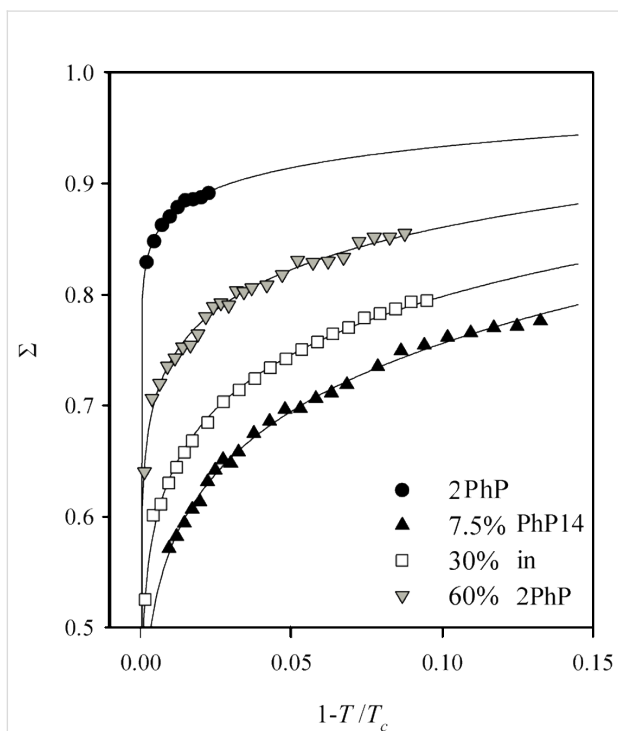

Figure 8: The translational order parameter Σ in the SmA phase is plotted vs the reduced temperature $1 - T/T_c$ for the pure component **2PhP** and the mixtures with 7.5%, 30% and 60% **PhP14** in **2PhP**, respectively. The pure **2PhP** shows the highest order parameters of about 0.9. The value of Σ is reduced after the addition of 7.5% of **PhP14** to about 0.7 and increases again slowly by the addition of more **PhP14** for the mixture with 30% **PhP14** until it reaches a value of 0.8 for the 60% mixture.

meter Σ [11] of the SmA phases was determined by a method previously described in [12]. The translational order parameter Σ gives a measure for the quality of smectic layering. It is defined as the amplitude of the density wave arising from the 1D-periodic smectic layer structure.

Figure 8 shows the smectic order parameters Σ of the SmA phase for the pure component **2PhP** and for the mixtures with 7.5%, 30% and 60% **PhP14** in **2PhP**, respectively. Pure **2PhP** forms a SmA phase with a high degree of smectic order. It exhibits a smectic order parameter of about 0.9. By adding a small amount of the other component the translational order is considerably reduced. For the mixture with 7.5% **PhP14** (the eutectic mixture, see Figure 3) Σ is in the range of about 0.7 and further increases on the addition of more of **PhP14**. It shows a value of about 0.75 for the 30% mixture and finally reaches a value of about 0.8 in the 60% mixture. The smallest value for Σ was observed at that point in the phase diagram where the SmC phase is lost. And the re-entering of the SmC phase into the phase diagram is preceded by a recovery of the smectic order.

To check whether these findings can be generalized, we investigated another phase diagram of two strict SmC mesogens with a length ratio of 1:2. The mixing of two strict SmC mesogens should lead to a phase diagram where only SmC phases emerge.

Figure 9 shows the phase diagram of the system **6PhPz/PhP14**. This phase diagram is very similar to the one of the system **2PhP/PhP14**. Although the two pure compounds show just SmC phases, the SmC phases disappear rapidly with increasing x_{PhP14} and SmA replaces SmC. However, the stability of the smectic state is preserved again.
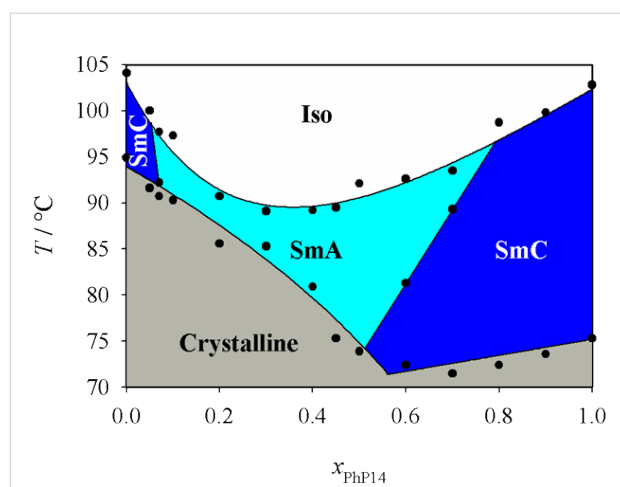

Figure 9: Phase diagram of the system **6PhPz/PhP14**. Over a broad temperature region only the SmA phase is stable, although the two pure compounds exhibit only SmC phases.

The reduced layer spacing of the mixtures with 60% and 70% **PhP14** in **6PhPz** can be seen in Figure 10. Both mixtures show small layer shrinkage of only 2% for the 70% mixture and 0.7% for the 60% mixture, respectively. This small layer shrinkage might also be related to small tilt angles in the corresponding SmC phases. The smectic order parameters Σ of the mixtures could not be compared with those of the pure compounds, as the method described in [12] only applies to SmA phases whereas the pure components exhibit SmC phases only.

Figure 10: Reduced layer spacing vs temperature difference to the phase transition temperature for the mixtures with 60% and 70% **PhP14** in **6PhPz**. The layer shrinkage is only 2% for the 70% mixture and 0.7% for the 60% mixture, respectively.
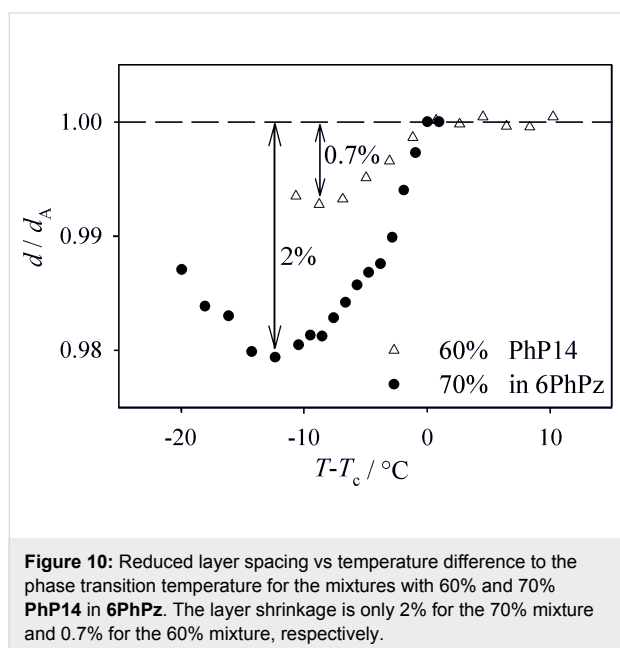
Conclusions

Our investigations on two different phase diagrams of mesogenic molecules with chemically similar cores but with length ratios in the order of 2:1 led us to the following general results:

- When the short-length compound exhibits a nematic phase, the nematic phase disappears quickly with increasing mole fraction of the compound with greater molecular length.
- Surprisingly, the temperature range of the smectic states is preserved. It even becomes broader in some cases. Nevertheless the quality of smectic layering is lowered.
- We observed that over a broad temperature range the SmC phase is completely lost even though SmC is the dominating phase in the pure compounds. Instead of SmC, now the non-tilted SmA phase temperature range is broadened.
- In the regimes before SmC phases disappear, the mixtures show exceptionally small tilt angles (maximum tilt < 10° over about 20 K).
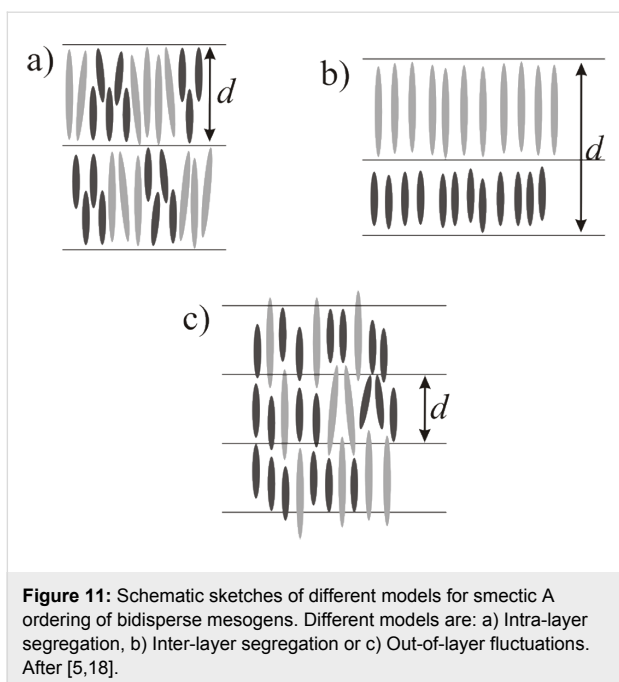
These results open pathways to a systematic design of interesting new low-tilt SmC materials.

To learn more about the ordering in smectic phases we compared our results with the work of Koden et al. [13]. They investigated several bidisperse mixtures of molecules with strongly differing molecular cores, but the same molecular length. In their mixtures they observed the same behaviour as in our mixtures. The nematic phases disappeared rapidly, as well as the smectic C phase, while the smectic A phase was the only stable phase over the whole phase diagram. They also found a dramatic decrease of the tilt angle in the remaining SmC phases, until the SmC phases disappeared at a concentration-induced phase transition to SmA.

These quite counterintuitive results are of general interest for the understanding of the structure and dynamics of smectic phases. Several theoretical approaches have been made to predict the behaviour of bidisperse mixtures [14-18]. They analyzed the stability of smectic A, nematic and isotropic phases by theoretical models of the Onsager-type in dependence on the composition of mesogens with different length and aspect ratios. They indeed predicted the occurrence of smectic phases in bidisperse mixtures for certain length and aspect ratios. In all these theoretical works however a stabilization of the nematic state at the expense of the smectic state was found. This is contradictory to the experimental findings, as our findings showed a stabilization of the smectic state while the nematic phase disappeared completely. The existing theories thus do not describe these results correctly. Furthermore there is no theoretical work on the influence of bidispersity on the balance between SmA and SmC.

In the existing theoretical approaches different models for the ordering in smectic A phases of molecules of substantially differing lengths are presented (Figure 11).

One possibility is to fill the space by nanosegregation of long and short mesogens. This segregation can be of the intra-layer (Figure 11a) or inter-layer (Figure 11b) type. Both options however are entropically unfavourable. In the intra-layer type all molecules are organized within one layer. Demixing of the two kinds of mesogens occurs locally inside the layers. Furthermore the layer spacing of such a smectic phase would – for all mole fractions – correspond to the length of the longer molecule (Figure 11a). However, in our SAXS-measurements we observed a layer spacing which varied linearly with the mole fraction and it was always smaller than the length of the long molecule. In the second kind of nanosegregation – the inter-layer type – the two kinds of molecules demix and each of them forms their own layers. The 'layer spacing' observed by SAXS

Figure 11: Schematic sketches of different models for smectic A ordering of bidisperse mesogens. Different models are: a) Intra-layer segregation, b) Inter-layer segregation or c) Out-of-layer fluctuations. After [5,18].

(cf. repeating unit) for this kind of smectic phase would correspond to the added lengths of the two molecules (Figure 11b). As the experimentally found layer spacing is always smaller than the long molecule, this also cannot be the correct explanation.

The last possibility is a more dynamic picture, where the space is filled by out-of-layer fluctuations (Figure 11c). The long molecules organize themselves in the layers formed by the short molecules by out-of-layer fluctuations. The layer spacing of this kind of smectic A phases would be in between the lengths of the two molecules, while the quality of smectic ordering, e.g. the smectic order parameter Σ, would be essentially lowered in comparison to the pure compounds. The experimental findings for both the layer spacing and the smectic ordering are in complete agreement with this model (see Figure 4 and Figure 8).

With all this results we thus believe that out-of-layer fluctuations are the most realistic model to describe the structure of bidisperse smectics. This also explains the strong influence of bidispersity on the balance between SmA and SmC. Since SmA phases might tolerate out-of-layer fluctuations much more easily, a stabilization of SmA at the expense of the SmC phase might occur. Therefore, the structure of bidisperse smectics is signified by extensive out-of-layer fluctuations.

Experimental

Compounds 2-[4-(tetradecyloxy)phenyl]-5-(tetradecyloxy)-pyrimidine (**PhP14**) [1], 6-[4-(butyloxy)phenyl]-3-(octyloxy)-pyridazine (**6PhPz**) [3] and (*R,R*)-2-[4-(octyloxy)phenyl]-5-

(2,3-difluorohexyloxy)pyridine (**MDW510**) [7] were synthesized according to published procedures and shown to have the expected physical and spectral properties. The liquid crystal 2-[4-(butoxy)phenyl]-5-(octyloxy)pyrimidine (**2PhP**) was obtained from a commercial source. X-Ray scattering experiments were performed with Ni-filtered CuK$_\alpha$ radiation (wavelength 1.5418 Å). Small angle scattering data from unaligned samples (filled into Mark capillary tubes of 0.7 mm diameter) were obtained using a Kratky compact camera (A. Paar) equipped with a temperature controller (A. Paar) and a one-dimensional electronic detector (M. Braun). For polarized optical microscopy a Leica DM-LP polarizing microscope with an Instec HS1-i hot stage was used. The optical tilt angles θ were determined by polarizing microscopy on samples aligned in rubbed nylon/ITO coated glass cells with a spacing of 1.6 μm (AWAT PPW, Poland). To enable ferroelectric switching of the tilt direction [19,20] in the achiral mixtures, 4 mol % of the chiral dopant **MDW510** was added to receive chiral SmC* phases. The measurements of θ were taken at a field strength *E* of 12.5 V μm^{-1} as half the rotation between the two optical extinction positions corresponding to opposite signs of *E*. A Netzsch DSC-204 Phoenix instrument was used for differential scanning calorimetry analyses at a scan rate of 5 K min^{-1}.

Acknowledgments

References

1. Hartley, C. S.; Kapernaum, N.; Roberts, J. C.; Giesselmann, F.; Lemieux, R. P. *J. Mater. Chem.* **2006,** *16,* 2329–2337. doi:10.1039/b515313a
2. Onsager, L. *Ann. N. Y. Acad. Sci.* **1949,** *51,* 627–659. doi:10.1111/j.1749-6632.1949.tb27296.x
3. Zaschke, H.; Hyna, C.; Schubert, H. *Z. Chem.* **1977,** *17,* 333–334.
4. Hegmann, T.; Meadows, M. R.; Wand, M. D.; Lemieux, R. P. *J. Mater. Chem.* **2004,** *14,* 185–190. doi:10.1039/b307673c
5. Diele, S. *Ber. Bunsen-Ges. Phys. Chem.* **1993,** *97,* 1326–1336.
6. The optical tilt angle is measured with a polarizing microscope in chiral SmC* phases by ferroelectric switching of the tilt direction [19,20].
7. Thurmes, W. N.; Wand, M. D.; Vohra, R. T.; Walba, D. M. *Mol. Cryst. Liq. Cryst.* **1991,** *204,* 1–7. doi:10.1080/00268949108046588
8. Thurmes, W. N.; Wand, M. D.; Vohra, R. T.; More, K. M.; Walba, D. M. *Liq. Cryst.* **1993,** *14,* 1061–1068. doi:10.1080/02678299308027814
9. These mixtures show a tilt angle which is smaller than 10° over a temperature range of about 20 K. This is quite unusual, as usual tilt angles of ferroelectric liquid crystals with second order SmA* to SmC* phase transitions are in the range of θ = 20° to 25°. Materials with first order phase transitions show tilt angles up to θ = 45°.
10. Lagerwall, J. P. F.; Giesselmann, F. *ChemPhysChem* **2006,** *7,* 20–45. doi:10.1002/cphc.200500472

11. The translational order parameter Σ gives a measure for the quality of smectic layering. It is defined as the amplitude of the density wave arising from the periodic one-dimensional smectic layer structure [21, 22].

12. Kapernaum, N.; Giesselmann, F. *Phys. Rev. E* **2008,** *78,* No. 062701. doi:10.1103/PhysRevE.78.062701

13. Koden, M.; Anabuki, T.; Nakagawa, K.; Awane, K. *Jpn. J. Appl. Phys., Part 2* **1991,** *30,* L1129–L1131. doi:10.1143/JJAP.30.L1129

14. Stroobants, A. *Phys. Rev. Lett.* **1992,** *69,* 2388–2391. doi:10.1103/PhysRevLett.69.2388

15. Stroobants, A. *J. Phys.: Condens. Matter* **1994,** *6,* A285–A288. doi:10.1088/0953-8984/6/23A/045

16. Koda, T.; Kimura, H. *J. Phys. Soc. Jpn.* **1994,** *63,* 984–994. doi:10.1143/JPSJ.63.984

17. Bemrose, R. A.; Care, C. M.; Cleaver, D. J.; Neal, M. P. *Mol. Phys.* **1997,** *90,* 625–635. doi:10.1080/00268979709482645

18. Cinacchi, G.; Mederos, L.; Velasco, E. *J. Chem. Phys.* **2004,** *121,* 3854–3863. doi:10.1063/1.1774153

19. Bahr, C.; Heppke, G. *Ber. Bunsen-Ges. Phys. Chem.* **1987,** *91,* 925–929.

20. Giesselmann, F.; Heimann, A.; Zugenmaier, P. *Ferroelectrics* **1997,** *200,* 237–256. doi:10.1080/00150199708008609

21. McMillan, W. L. *Phys. Rev. A* **1971,** *4,* 1238–1246. doi:10.1103/PhysRevA.4.1238

22. McMillan, W. L. *Phys. Rev. A* **1972,** *6,* 936–947. doi:10.1103/PhysRevA.6.936

Low temperature enantiotropic nematic phases from V-shaped, shape-persistent molecules

Matthias Lehmann[*] and Jens Seltmann

Abstract

A series of V-shaped, shape-persistent thiadiazole nematogens, based on an oligo(phenylene ethynylene) scaffold with ester groups connected via alkyloxy spacers, was efficiently prepared by a two-step procedure. Phase engineering results in an optimum of the mesophase range and low melting temperature when the nematogens are desymmetrised with a butoxy and a heptyloxy spacer. The mesophases are enantiotropic and over the whole temperature range nematic. For the optimised mesogen structure, optical investigations by conoscopy monitored a uniaxial nematic phase upon cooling from the isotropic phase to room temperature ($\Delta T = 150$ °C). X-ray studies on magnetic-field-aligned samples of this mesogen family revealed a general pattern, indicating the alignment of two molecular axes along individual directors in the magnetic field. These observations may be rationalised with larger assemblies of V-shaped molecules isotropically distributed around the direction of the magnetic field.

Introduction

Most molecules forming nematic liquid crystals, the nematogens, are based on rod-shaped (calamitic), anisometric cores with peripheral flexible chains along the molecular long axis [1]. Nematic phases are the simplest liquid crystalline mesophases, in which phase anisotropy of crystals is combined with fluid properties of liquids. In the nematic phases of calamitic mesogens only the molecular long axes are oriented along a so called director [2] and the molecular centres of gravity are distributed like in a liquid. In models, the molecules are thought to turn rapidly about their long axis and therefore the shape of

nematogens in theoretical studies has been simplified to a spherocylinder [3]. These phases are called uniaxial. Almost 40 years ago, M. J. Freiser predicted that real nematogens possess a non-cylindrical shape and thus should be able to form biaxial nematic phases at an appropriate low temperature [4]. What is a biaxial nematic phase and why is it so interesting? Uniaxial and biaxial phases can be best understood by the property from which this classification originates: the behaviour when light propagates in the material. The optical property of a uniaxial phase in a monodomain can be described by two refractive

indices spanning a rotationally symmetric ellipsoid, also called indicatrix (Figure 1, left side). There is one particular direction, perpendicular to the circular cross section of this special ellipsoid, along which the propagating linear polarised light does not change its polarisation. This direction is called the optical axis. In a uniaxial phase there is only one optical axis. However, if the monodomains of materials have to be optically described with three different refractive indices, the indicatrix is an ellipsoid spanned by three different semi-principal axes, possessing two different circular cross sections and consequently two optical axes (Figure 1, right side).

In a biaxial nematic phase three molecular axes align along individual directors resulting in a material with three different refractive indices. However, at the same time this material has a liquid-like distribution of the molecular centres of gravity. In spite of the high molec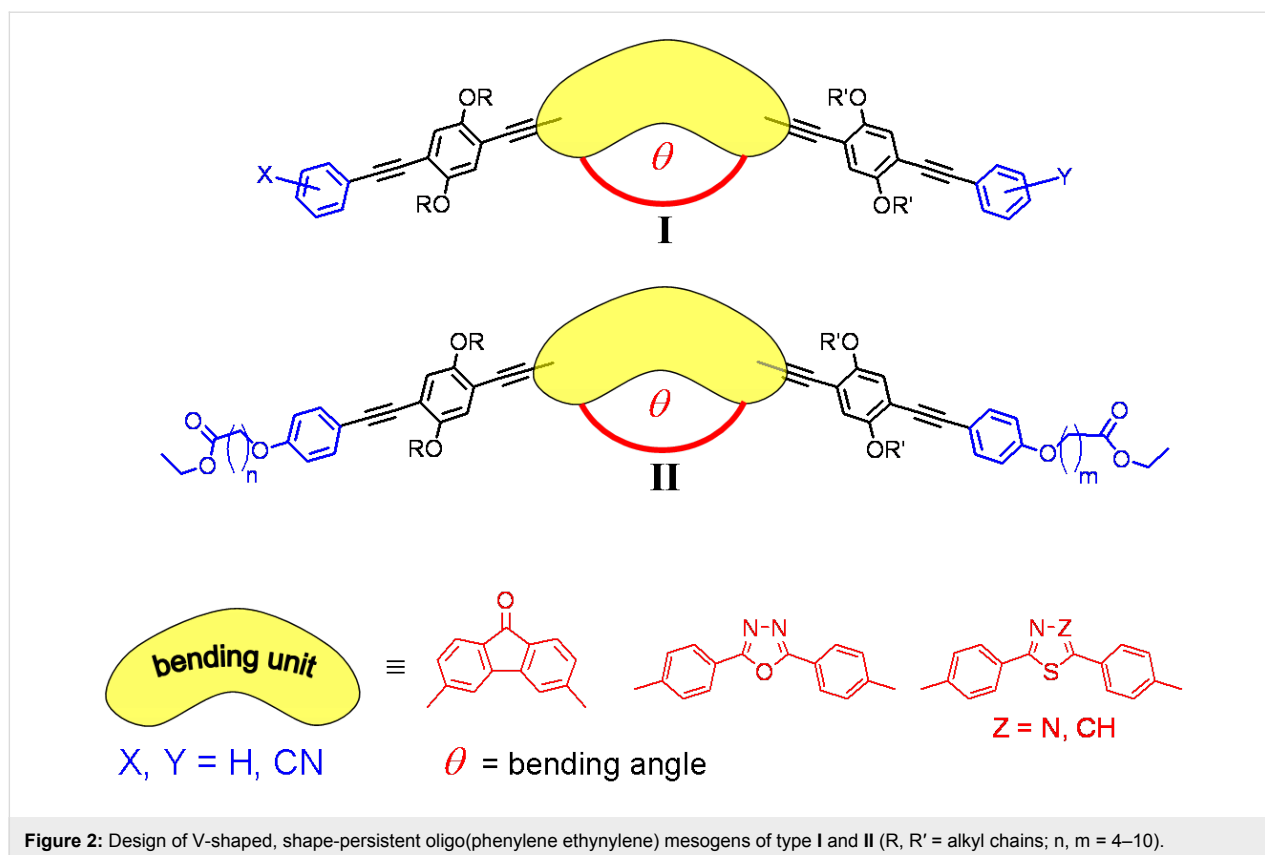ular mobility the high order should be maintained. These two parameters have to be balanced extremely precise in order to obtain a thermotropic biaxial nematic with molecules of low molar mass [5].

Historically, a biaxial nematic phase was found first in lyotropic mixtures, where the micellar shape can be gradually tuned [6]. A thermotropic biaxial nematic phase of molecules of low molar mass is in high demand because of its potential application in display technology. After the discovery of the biaxial nematic phase in lyotropic materials, many claims of biaxial thermotropic nematic phases were published without being accepted [5]. During this period also banana-shaped molecules were discovered and theoreticians highlighted the possibility to use bent-shaped molecules with rigorously defined shape (bending angle) for the formation of the desired phase [5,7]. But it was not until 2004 that sufficient evidence was presented for biaxiality of nematic phases in the series of V-shaped oxadiazoles by X-ray diffraction and solid-state ^{2}H NMR spec-

troscopy [8-10]. This has been recently confirmed by various other methods [11-14]. Since then several new materials have been designed and reported to be biaxial, among others tetrapodes [15-17] and banana-shaped oligoesters [18,19]. However, there is still a controversial discussion about the phase biaxiality of these materials and their switching behaviour [20-22]. All these latter molecular structures are, however, flexible and can change their conformation and thus their shape. Since theoretically biaxial nematic phases were predicted for a molecule with a defined shape and angle, we aimed to design a shape-persistent molecular scaffold of type **I** (Figure 2) based on oligo(phenylene ethynylene) building blocks. These molecules show liquid crystal behaviour only with a flat bending unit possessing a dipole along the apex of the mesogen, sufficiently long aliphatic chains R and at least one pyridyl or acceptor substituted aromatic unit at the periphery of the molecule [23, 24]. Fluorenone [25], oxadiazole [26], thiazole and thiadiazole [24] derivatives have been synthesised and evidence for biaxiality in their monotropic nematic phases has been presented. Monotropic phases are metastable and crystallise, thus making detailed studies of these phases extremely difficult. Therefore, low temperature stable (enantiotropic) phases are urgently demanded. In an earlier theoretical work, weak hydrogen bonds were suggested to possibly induce and stabilise biaxial nematic phases [27]. Therefore, we modified our design concept and attached ester groups to the peripheral aromatic unit via an alkyloxy spacer to obtain the general structures of type **II**. The esters may be subsequently cleaved, in order to generate carboxylic acids and thus hydrogen bonded dimers and oligomers. In this article, the synthesis of a series of thiadiazoles of general structure **II** is presented and the successful approach to low temperature, enantiotropic nematic liquid crystals in the family of bent-shaped oligo(phenylene ethynylenes) will be discussed.

Figure 1: Uniaxial nematic (left) and biaxial nematic (right) phases and their corresponding indicatrices.

Figure 2: Design of V-shaped, shape-persistent oligo(phenylene ethynylene) mesogens of type **I** and **II** (R, R′ = alkyl chains; n, m = 4–10).
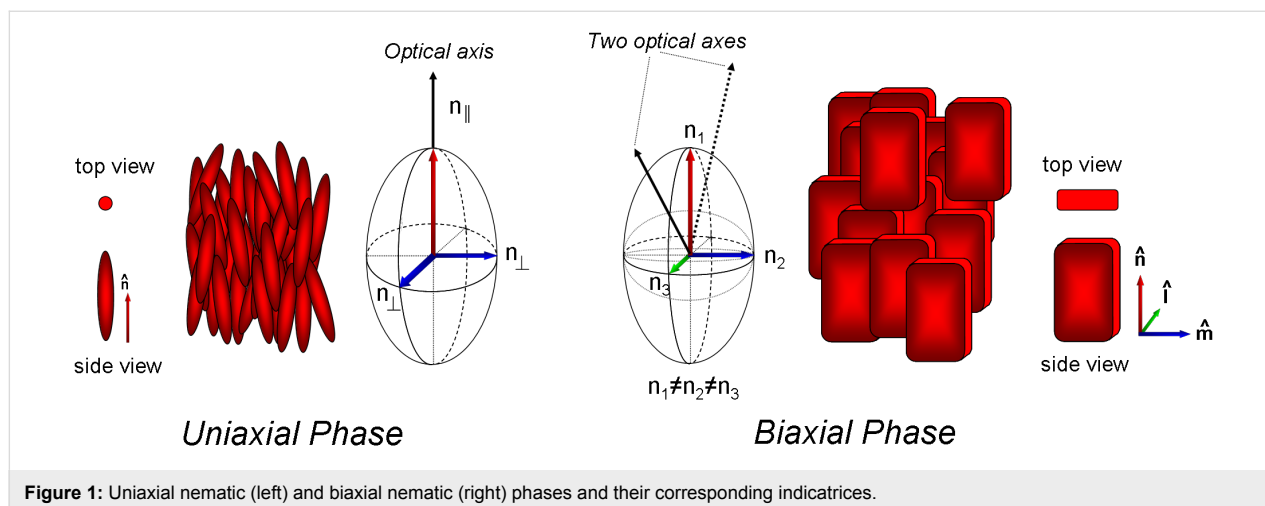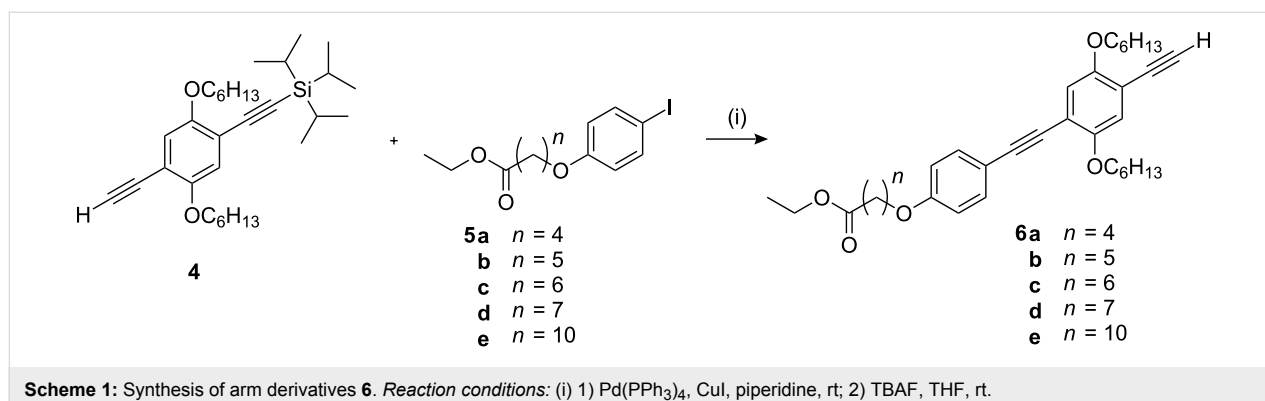
Results and Discussion
Synthesis

The shape-persistent arms of the new nematogens were prepared following the recent optimised procedure [25], using the mono-protected diethynylbenzene derivative **4** as a key compound (Scheme 1). The peripheral aromatic units **5** were obtained by etherification of 4-iodophenol with the corresponding ethyl ω-bromoalkanoate [28]. Cross-coupling of iodobenzene **5** with ethynyl compound **4** and subsequent cleavage of the silyl protecting group afforded the arm derivatives **6**. As in the previously published two-step synthesis, the arms **6** were linked successively to the non-symmetric thiadiazole bending unit **7**

(Scheme 2) [24]. All compounds were carefully purified and characterised by ^{1}H, ^{13}C NMR, mass spectrometry and elemental analysis (see experimental section).

Thermotropic Properties

The thermotropic behaviour of all materials was investigated by differential scanning calorimetry (DSC) and polarised optical microscopy (POM). The results are collected in Table 1. Interestingly, all phenylene ethynylene oligomers show exclusively enantiotropic nematic liquid crystal phases, even for the hockey stick shaped intermediates **3**. However, the temperature intervals for the latter are small, approaching a maximum of 43 °C

Scheme 1: Synthesis of arm derivatives **6**. *Reaction conditions:* (i) 1) Pd(PPh$_3$)$_4$, CuI, piperidine, rt; 2) TBAF, THF, rt.

Scheme 2: Two-step synthesis of V-shaped nematogens: symmetric (**1**) and non-*C*₂-symmetric (**2**) thiadiazoles. *Reaction conditions:* (i) Pd(PPh$_3$)$_4$, CuI, piperidine, rt; (ii) Pd(PPh$_3$)$_4$, CuI, piperidine, 65 °C.
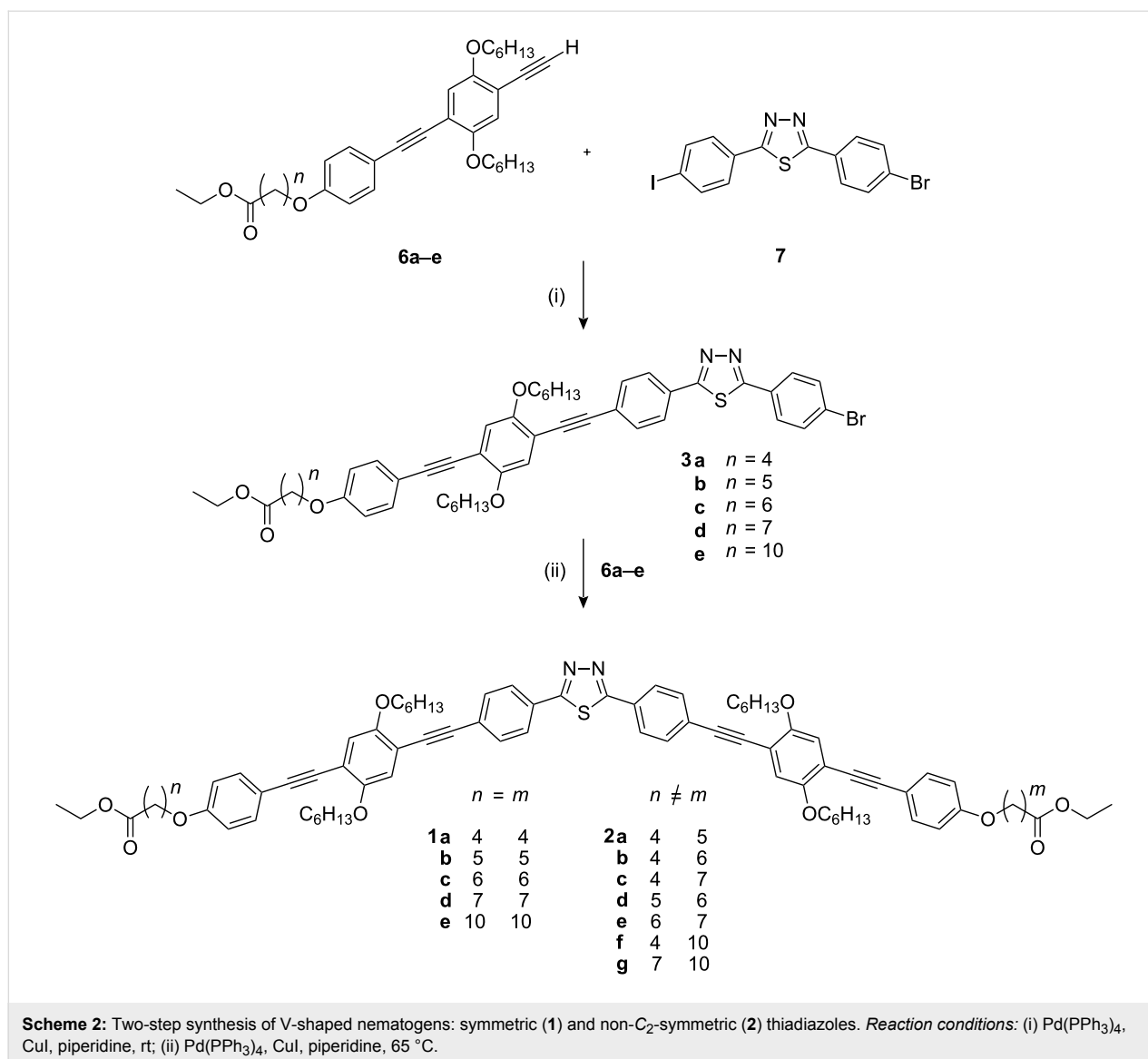
for compound **3c** and melting in all cases occurs only above 100 °C (Figure 3). In this series, an odd-even behaviour becomes apparent for the Cr–N, as well as for the N–I transition with increasing chain length (n = 4–7) [1,29]. It is important to note that for the first three members (**3a–c**) there is only a small impact of the chain length on the phase transition temperatures. Only with the heptyl chains do the transition temperatures decrease significantly. A closer look at transition enthalpies and entropies reveal very small values for **3a** and **3b** (ΔH = 0.1 kJ·mol^{-1}; ΔS = 0.2 J·K^{-1}·mol^{-1}). Entropy values approaching zero, i.e. second order transitions, are predited for direct transitions from the isotropic liquid to the biaxial nematic phase for biaxial molecules [30]. Thus, these hockey stick shaped derivatives may be good candidates for the investigation of the presence of phase biaxiality. POM studies reveal for derivatives **3a–e** Schlieren textures with two and four brushed
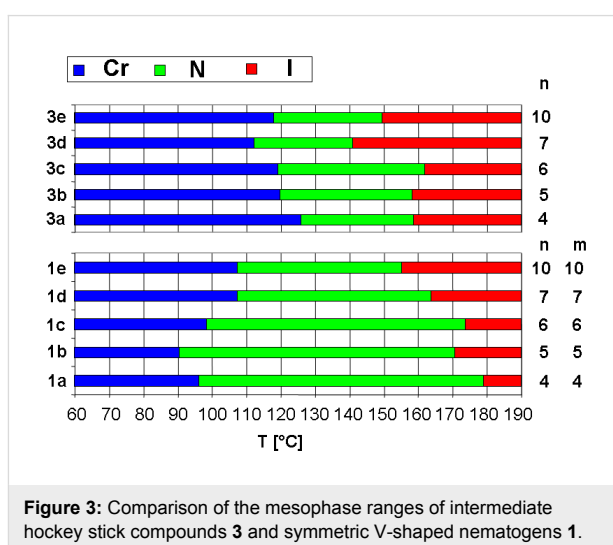

Figure 3: Comparison of the mesophase ranges of intermediate hockey stick compounds **3** and symmetric V-shaped nematogens **1**.

Table 1: Thermotropic behaviour of hockey stick compounds **3** and V-shaped molecules **1** and **2**.

Compound	Rate 10 °C/min (Onset [°C] / ΔH [kJ/mol])[a]	ΔS_N [J·mol^{-1}·K^{-1}]
3a	**Cr** 126 / *35.1* **N** 159 / *0.1* **I**	0.2
3b	**Cr** 120 / *44.0* **N** 158 / *0.1* **I**	0.2
3c	**Cr** 119 / *47.0* **N** 162 / 0.9 **I**	2.1
3d	**Cr** 112 / 42.6 **N** 141 / 1.4 **I**	3.4
3e	**Cr** 118 / *58.0* **N** 150 / *0.9* **I**	2.1
1a	**Cr** 96 / *65.9* **N** 179 / *1.8* **I**	4.0
1b	**Cr** 91 / *55.6* **N** 171 / *1.6* **I**	3.6
1c	**Cr** 99 / *56.5* **N** 174 / *1.8* **I**	4.0
1d	**Cr** 108 / *57.6* **N** 164 / *1.9* **I**	4.4
1e	**Cr** 108 / *117.7* **N** 155 / *1.8* **I**	4.2
2a	**Cr** 88 / *102.3* **N** 179 / *1.9* **I**	4.2
2b	**Cr** 68 / *38.5*[b] **N** 178 / *1.9* **I**	4.2
2c	**Cr** 67 / *37.0*[b] **N** 175 / *1.8* **I**	4.0
2d	**Cr** 89 / *48.3* **N** 175 / *1.7* **I**	3.8
2e	**Cr** 96 / *55.5* **N** 171 / *1.8* **I**	4.1
2f	**Cr** 70 / *37.3*[b] **N** 168 / *1.7* **I**	3.9
2g	**Cr** 77 / *53.6*[b] **N** 162 / *1.7* **I**	3.9

[a]Data are given for the second heating.
[b]Data for the first heating.

disclinations. Homeotropic alignment to study possible biaxiality of the samples was not obtained. Only for a sample of compound **3a** could planar aligned thin LC films be prepared. Upon rotation of the sample the film became alternately dark at 0° and birefringent at 45°.
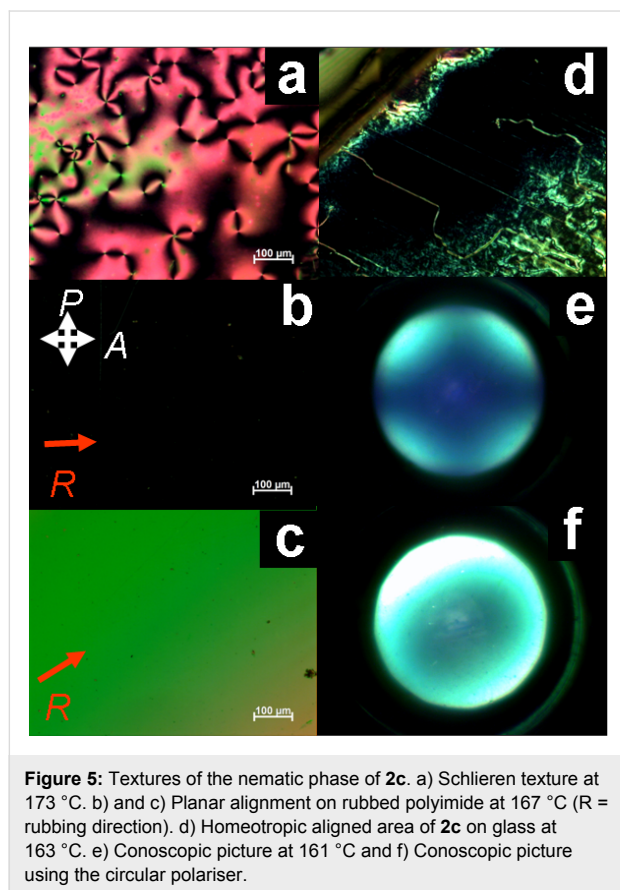
Figure 3 compares the transitions of symmetric V-shaped compounds **1a**–**e**. The transition temperatures I–N decrease from compounds with a short peripheral spacer between the aromatic and the ester group to long spacer derivatives. A clear odd-even effect is revealed. The transition enthalpies and entropies are relatively high (ΔH = 1.6–1.9 kJ·mol^{-1}; ΔS = 3.6–4.2 J·K^{-1}·mol^{-1}) pointing to first order transitions. Melting temperatures and melting enthalpies follow a different progression; they decrease from **1a** to **1b** and increase again from **1b** to **1e**. All melting temperatures are relatively high (above 90 °C). In order to lower the latter, non-symmetric V-shaped mesogens **2** with two arms consisting of different peripheral building blocks have been prepared. The series of molecules **2a**–**c**, **2f** with a pentanoic acid ethyl ester group on one side shows a decrease in melting and clearing temperatures with increasing spacer lengths on the other arm. The decrease of melting temperature dominates and reaches a minimum for molecule **2c** with an octanoic acid ethyl ester as a peripheral group. In this series of molecules no apparent odd-even effect can be monitored. The thermotropic properties in comparison with the increasing lengths of the peripheral alkanoic acid ethyl ester spacers are

illustrated in Figure 4. Apparently, the clearing temperature decreases with the total number of peripheral methylene groups (from 179.1 °C for **1a** to 155.2 °C for **1e**). Note that non-symmetric compounds always possess lower melting and higher clearing temperatures compared to their symmetric counterparts with the same number of methylene groups (compare **1b**/ **2b** and **1d**/**2f**). It appears that a large difference in chain lengths results in higher stability of the mesophase, i.e. a low crystallisation tendency (see **2f**, **2g**, **2b** and **2c** and compare to **2d** and **2a**). Maximum LC temperature intervals for enantiotropic liquid crystalline phases of 109 °C and 108 °C were found for **2b** and **2c**, showing the success of the strategy for this series of compounds. Note, as indicated in Table 1, that some of the samples can be supercooled without crystallisation. Some materials can be stored for more than 1 h at 25 °C without visible formation of crystal grains.
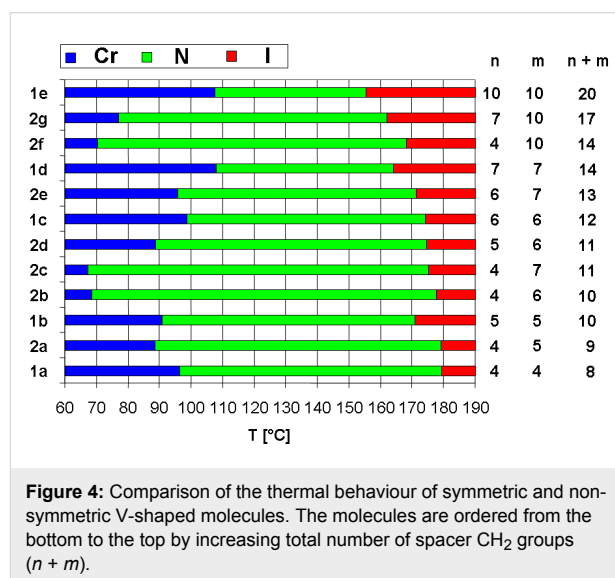
Figure 4: Comparison of the thermal behaviour of symmetric and non-symmetric V-shaped molecules. The molecules are ordered from the bottom to the top by increasing total number of spacer CH$_2$ groups (*n* + *m*).

Microscopy studies were performed to examine the nature of the mesophases. POM revealed for all samples Schlieren textures with two and four brushed disclinations (Figure 5) typically observed for nematic phases. The high mobility of the phases, combined with a blaze of colours upon external pressure and the absence of homeotropic alignment after shearing, is also a sign of their nematic nature. The nematic materials aligned preferentially planar on conventional glass substrates and between glass coated with antiparallel rubbed polyimide alignment layers. Rotation of the samples exhibited alternately birefringent and dark textures. Conoscopy switched between a blurry conoscopic cross and birefringent photographs. However, the circular polariser could not reveal any optical axes. These results would be expected for uniaxial as well as biaxial nematic phases with planar alignment. Only homeotropic aligned samples allow distinction between uniaxial and biaxial phases.

In the case of **2c** small homeotropically aligned areas could be obtained on glass substrates. Conoscopy revealed positive optical anisotropy, thus the molecules' long axes are aligned perpendicular to the glass substrate. The black texture between the crossed polarisers at all rotation angles of the sample indicates the uniaxial nature right after the phase transition, further confirmed by the conoscopic cross. Upon cooling, the sample becomes slightly birefringent in some areas. This process yielded an inhomogenous texture pointing to the formation of multiple small domains. The domains which remained dark revealed a conoscopic cross at all temperatures. The symmetry of the cross changed only slightly upon rotation of the sample. These observations are in good agreement with the uniaxial nature of the nematic phase of nematogen **2c** even at room temperature.

Figure 5: Textures of the nematic phase of **2c**. a) Schlieren texture at 173 °C. b) and c) Planar alignment on rubbed polyimide at 167 °C (R = rubbing direction). d) Homeotropic aligned area of **2c** on glass at 163 °C. e) Conoscopic picture at 161 °C and f) Conoscopic picture using the circular polariser.
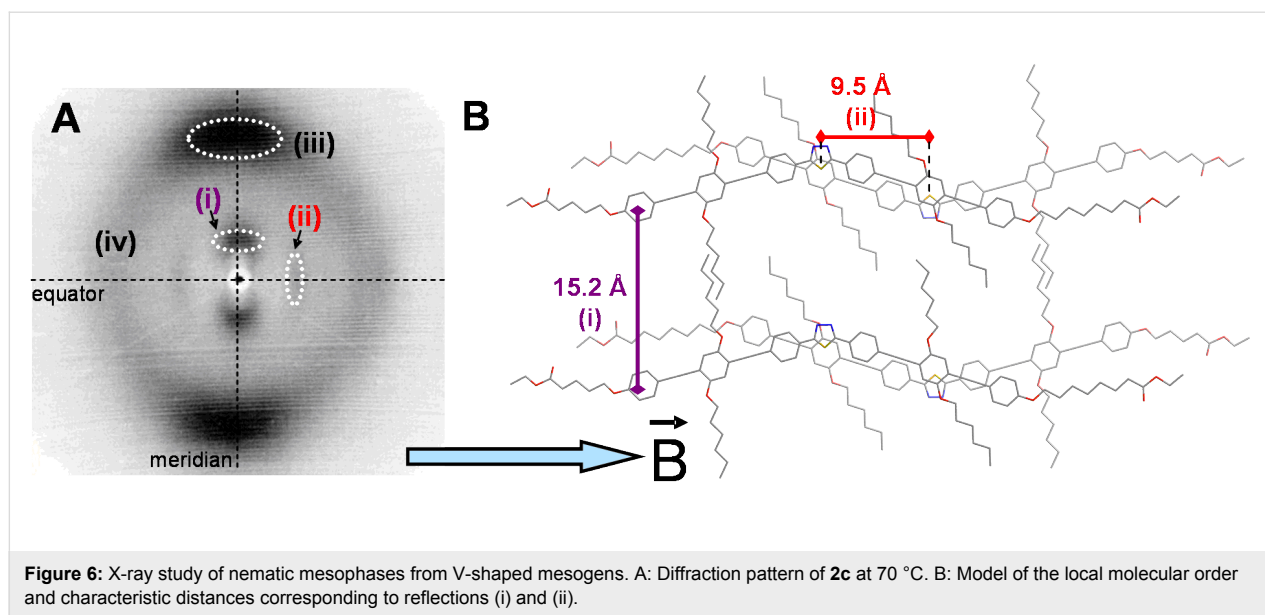
X-ray Diffraction

X-ray studies were performed on magnetic-field-aligned samples with the X-ray beam perpendicular to the alignment direction. Figure 6A shows a typical X-ray pattern found for all investigated derivatives with three diffuse pairs of reflections (i–iii) and a halo (iv) corresponding to the average separation of the liquid-like chains. As shown in Figure 6B, reflections (i) are assigned to the separation of the molecules along the bisector.

Reflections (ii) correspond to a distance which can be rationalised by the separation of two antiparallel thiadiazole rings along the molecular long axis. Reflections (iii) are typical for the π–π distance between conjugated molecules. Note that for reflections (i) and (iii) the reflection conditions cannot be simultaneously fulfilled. This points to the fact that at least two distinct domains are observed by the experiment [31,32].

Table 2 summarises the Bragg distances d together with the correlation lengths ξ/d obtained by the Scherrer formula [33, 34]. It reveals that the values d(i–iv) are not a function of the spacer lengths between peripheral aromatic units and the ester groups. For example d(i) distances are almost constant in the range of 15–16 Å although the molecular length increases by 12 CH_2 units from compound **1a** to **1e**. Even the distances d(ii), attributed to the molecular long axis, on which the different spacer length should have the largest impact, remain constant between 9 and 10 Å. The latter can be rationalised when the electron-poor thiadiazole units interact with the electron-rich 2,5-dialkyloxybenzenes of an antiparallel aligned mesogen. As illustrated in Figure 6B, the sulfur atoms are then separated throughout the sample on average by 9–10 Å. The fact that with small angle X-ray scattering no reflection corresponding to the overall molecular length could be found is not fully understood. The correlation lengths ξ/d are all in the range of 3–5 repeating units indicating the absence of any long range positional order and thus confirming the nematic nature of the mesophases. The π–π-distances are relatively large and only marginally smaller than the average separation of alkyl chains. However, at this temperature range similar values have been obtained previously in the series of fluorenone derivatives, in which the π–π interaction increased with decreasing temperature and moderated the uniaxial to biaxial transition [25].

X-ray diffraction shows the orientation of two molecular axes in this mesogen family, which may be an indication for phase biaxiality. In contrast, the optical experiments of compound **2c** point to the uniaxial nature of its nematic phase. In order to rationalise these two different results, it can be assumed on the bases of the correlation lengths that the thiadiazoles form small aggregates. These aggregates are responsible for the observed diffuse X-ray pattern, however, they either rotate about their long axis or the two different axes of the aggregates are isotropically distributed around the direction of the magnetic field, eventually resulting in a uniaxial phase even at room temperature. The latter model has been recently suggested by a theoretical work from Vanakaras [35], in which three different uniaxial and biaxial nematic phases based on aggregates or clusters have been proposed. The model is further supported by results obtained from a bent-shaped oxazole derivative, which forms polar clusters in the nematic phase [36]. However, further

Figure 6: X-ray study of nematic mesophases from V-shaped mesogens. A: Diffraction pattern of **2c** at 70 °C. B: Model of the local molecular order and characteristic distances corresponding to reflections (i) and (ii).

work is in progress in order to draw a more detailed picture of the supramolecular organisation of thiadiazole derivatives **1** and **2** in their nematic phase.

Conclusion

Thiadiazole nematogens with ester groups connected via alkyloxy spacers could be efficiently prepared by a previously reported two-step procedure. These mesogens are capable of hydrogen bonding if the esters are cleaved. The mesophase range and the melting temperature reach an optimum when the nematogens are desymmetrised with a butoxy and a heptyloxy spacer. For this molecule, optical observations by conoscopy monitored a uniaxial nematic phase over the whole temperature range of 150 °C upon cooling from the isotropic phase to room temperature. X-ray diffraction points to the alignment of two axes in the magnetic field in this family of mesogens. Both features may be rationalised if larger assemblies of V-shaped molecules are isotropically distributed around the direction of

the magnetic field, thus leading only to uniaxial nematic phases. Work is in progress to synthesise molecules with a smaller bending angle in order to induce possibly a biaxial order at high temperature.

Experimental

Chemicals were obtained from Fisher Scientific and Sigma-Aldrich and used as received. The synthesis of compounds **4** [23,25] and **7** [24] was described previously. Column chromatography was carried out on silica 60 (Merck, mesh 70–230). PFT ^{1}H and ^{13}C NMR spectra were recorded in CDCl$_3$ with a Varian Oxford 400 MHz spectrometer with the residual solvent signal at 7.26 ppm as a reference. Mass spectra were obtained on a Finnigan MAT95 (FD MS). Elemental analysis was carried out in the microanalytical laboratory at the University of Mainz. POM observations were made with a Zeiss Axioscop 40 equipped with a Linkam THMS600 hot stage. DSC was performed using a Perkin Elmer Pyris 1.

Table 2: X-ray diffraction data. The correlation length ξ was estimated from the half width of the reflections by using the Scherrer formula [33,34].

Compound	T [°C]	d (i) [Å](ξ/d)	d (ii) [Å](ξ/d)	d (iii) [Å](ξ/d)	d (iv) [Å](ξ/d)
1a	105	15.1 (4.0)	10.2 (4.2)	4.3 (5.2)	4.6 (4.3)
2a	80	14.9 (4.1)	9.8 (4.4)	4.2 (5.3)	4.4 (4.7)
1c	100	15.7 (3.4)	9.3 (4.3)	4.4 (5.4)	4.6 (4.1)
2c	70	15.2 (2.4)	9.5 (6.3)	4.0 (6.1)	4.7 (3.7)
1e	105	16.4 (2.8)	9.5 (4.3)	4.4 (5.4)	4.6 (3.9)

X-ray diffraction measurements were carried out on powder samples in glass capillaries of 1.5 mm diameter. The nematic phases were aligned in a magnetic field (1T) upon cooling from the isotropic to the nematic phase. The WAXS measurements were performed by using a standard copper anode (2.2 kW) source with pinhole collimation equipped with a X-ray mirror (Osmic typ CMF15-sCu6) and a Bruker detector (High-star) with 1024 × 1024 pixels. The diffraction data were calibrated by using silver behenate as a calibration standard [37]. The X-ray patterns were evaluated using the datasqueeze software (http://www.datasqueezesoftware.com/).

General method for preparation of intermediate products 3a–e

The mixture of 1.0 equiv of thiadiazole **7**, 1.0 equiv of the corresponding terminal alkyne **6a–e**, 0.1 equiv of Pd(PPh₃)₄ and 0.05 equiv of CuI in piperidine is stirred for 2 h at room temperature. Subsequently, the solvent is removed *in vacuo* and the products are isolated by column chromatography using a mixture of EtOAc/hexane.

2-{4-[4-{4-[4-(Ethoxycarbonyl)butoxy]phenylethynyl}-2,5-bis(hexyloxy)phenyl]ethynylphenyl}-5-(4-bromophenyl)-1,3,4-thiadiazole (3a) Hexane/EtOAc = 6/1 (R_f = 0.25), yellow solid; yield 0.12 g (78%). ^{1}H NMR (400 MHz, CDCl₃): δ = 7.99 (2H, AA′BB′), 7.89 (2H, AA′BB′), 7.64 (4H, AA′BB′), 7.46 (2H, AA′BB′), 7.02 (s, 1H), 7.01 (s, 1H), 6.86 (2H, AA′BB′), 4.14 (q, 2H, COOCH₂CH₃, J = 7.2), 4.05 (t, 2H, OCH₂, J = 6.4), 4.04 (t, 2H, OCH₂, J = 6.4), 3.99 (m, 2H, OCH₂), 2.39 (t, 2H, CH₂COOEt, J = 7.2), 1.85 (m, 8H, CH₂); 1.55 (m, 4H, CH₂); 1.36 (m, 8H, CH₂); 1.26 (t, 3H, CH₃, J = 7.2); 0.91 (t, 3H, CH₃, J = 7.2), 0.90 (t, 3H, CH₃, J = 7.2); ^{13}C NMR (100 MHz, CDCl₃): δ = 173.8 (C$_q$, C=O), 167.9, 167.2 (C$_q$, N=C–S); 159.3 (C$_q$, C–OCH₂), 154.0, 153.3 (C$_q$, C–OC₆H₁₃), 133.2, 132.6, 132.4 (C$_t$), 129.4 (C$_t$), 129.1 (C$_q$), 127.9 (C$_t$), 126.8, 125.8 (C$_q$), 117.0, 116.8 (C$_t$); 115.4, 115.2 (C$_q$), 114.6 (C$_t$), 112.9 (C$_q$), 95.6, 94.0, 89.2, 84.7 (C≡C), 69.8, 69.7, 67.8 (OCH₂), 60.4 (COOCH₂CH₃), 34.4 (CH₂COOEt), 31.7, 29.5, 29.4, 29.0, 25.9, 25.8, 24.8, 22.8 (CH₂), 14.4, 14.2 (CH₃); EA: Calc. for C₅₉H₅₃BrN₂O₅S: C 68.28, H 6.20, N 3.25, S 3.72; Found: C 68.38, H 6.31, N 3.33, S 3.70; FD MS: *m/z* [%]:861.7 (87, [M+2]$^+$); 859.7 (100, M$^+$).

General method for preparation of V-shaped molecules 1a–e and 2a–g

The mixture of 1.0 equiv of thiadiazole derivatives **3a–e**, 1.0 equiv of the corresponding terminal alkine **6a–e**, 0.2 equiv of Pd(PPh₃)₄ and 0.1 equiv of CuI in piperidine is stirred for 2 h at 65 °C. The solvent is then removed *in vacuo* and the products are isolated by means of column chromatography using a mixture of EtOAc/hexane.

2,5-Bis-{4-[4-{4-[4-(ethoxycarbonyl)butoxy]phenylethynyl}-2,5-bis(hexyloxy)phenyl]ethynylphenyl}-1,3,4-thiadiazole (1a) Hexane/EtOAc = 6/1 (R_f = 0.1), yellow solid; yield 120 mg (74%). ^{1}H NMR (400 MHz, CDCl₃): δ = 8.00 (4H, AA′BB′), 7.64 (4H, AA′BB′), 7.46 (4H, AA′BB′), 7.02 (s, 2H), 7.01 (s, 2H), 6.86 (4H, AA′BB′), 4.13 (q, 4H, COOCH₂CH₃, J = 7.2), 4.04 (t, 4H, OCH₂, J = 6.4), 4.03 (t, 4H, OCH₂, J = 6.4), 3.98 (t, 4H, OCH₂, J = 6.4), 2.34 (t, 4H, CH₂COOEt, J = 7.2), 1.85 (m, 16H, CH₂), 1.55 (m, 8H, CH₂), 1.37 (m, 16H, CH₂), 1.26 (t, 6H, CH₃, J = 7.2), 0.91 (t, 6H, CH₃, J = 7.2), 0.90 (t, 6H, CH₃, J = 7.2); ^{13}C NMR (100 MHz, CDCl₃): δ = 173.6 (C$_q$, C=O), 167.8 (C$_q$, N=C–S), 159.2 (C$_q$, C–OCH₂), 154.0, 153.5 (C$_q$, C–OC₆H₁₃), 133.2, 132.3 (C$_t$), 129.6 (C$_q$), 127.9 (C$_t$), 126.7 (C$_q$), 117.0, 116.8 (C$_t$), 115.5, 115.2 (C$_q$), 114.6 (C$_t$), 112.9 (C$_q$), 95.5, 94.1, 89.2, 84.7 (C≡C), 69.8, 69.7, 67.6 (OCH₂), 60.5 (COOCH₂CH₃), 34.1 (CH₂COOEt), 31.8, 29.4, 28.7, 25.9, 22.81, 22.79, 21.7 (CH₂), 14.4, 14.2 (CH₃); EA: Calc. for C₈₄H₉₈N₂O₁₀S: C 75.99, H 7.44, N 2.11, S 2.41; Found: C 75.94, H 7.47, N 2.05, S 2.42; FD MS: *m/z* [%]: 1325.9 (100, M$^+$); 663.1 (70, M^{2+}).

Supporting Information

Supporting Information File 1
Synthetic procedures and analytical results for compounds **1b–e**, **2a–g**, **3b–e**, **5a–e** and **6a–e**.
[http://www.beilstein-journals.org/bjoc/content/supplementary/1860-5397-5-73-S1.doc]

References

1. Demus, D. In *Handbook of Liquid Crystals;* Demus, D.; Goodby, J. W.; Gray, G. W.; Spiess, H.-W.; Vill, V., Eds.; Wiley-VCH: Weinheim, Germany, 1998; Vol. 1, pp 133 ff.
2. The director is a direction to which certain molecular axes point preferentially (in conventional nematic liquid crystals these are the molecular long axes).
3. Osipov, M. A. In *Handbook of Liquid Crystals;* Demus, D.; Goodby, J. W.; Gray, G. W.; Spiess, H.-W.; Vill, V., Eds.; Wiley-VCH: Weinheim, Germany, 1998; Vol. 1, pp 40 ff.

4. Freiser, M. J. *Phys. Rev. Lett.* **1970,** *24,* 1041–1043. doi:10.1103/PhysRevLett.24.1041
5. Luckhurst, G. R. *Thin Solid Films* **2001,** *393,* 40–52. doi:10.1016/S0040-6090(01)01091-4
6. Yu, L. J.; Saupe, A. *Phys. Rev. Lett.* **1980,** *45,* 1000–1003. doi:10.1103/PhysRevLett.45.1000
7. Teixeira, P. I. C.; Masters, A. J.; Mulder, B. M. *Mol. Cryst. Liq. Cryst.* **1998,** *323,* 167–189. doi:10.1080/10587259808048440
8. Acharya, B. R.; Primak, A.; Dingemans, T. J.; Samulski, E. T.; Kumar, S. *Pramana* **2003,** *61,* 231–237. doi:10.1007/BF02708305
9. Madsen, L. A.; Dingemans, T. J.; Nakata, M.; Samulski, E. T. *Phys. Rev. Lett.* **2004,** *92,* No. 145505. doi:10.1103/PhysRevLett.92.145505
10. Acharya, B. R.; Primak, A.; Kumar, S. *Phys. Rev. Lett.* **2004,** *92,* No. 145506. doi:10.1103/PhysRevLett.92.145506
11. Southern, C. D.; Brimicombe, P. D.; Siemianowski, S. D.; Jaradat, S.; Roberts, N. W.; Görtz, V.; Goodby, J. W.; Gleeson, H. F. *EPL* **2008,** *82,* No. 56001. doi:10.1209/0295-5075/82/56001
12. Southern, C. D.; Gleeson, H. F. *Eur. Phys. J. E* **2007,** *24,* 119–127. doi:10.1140/epje/i2007-10223-3
13. Xiang, Y.; Goodby, J. W.; Görtz, V.; Gleeson, H. F. *Appl. Phys. Lett.* **2009,** *94,* No. 193507. doi:10.1063/1.3138867
14. Lee, G. S.; Cho, J. S.; Kim, J. C.; Yoon, T.-H.; Shin, S. T. *J. Appl. Phys.* **2009,** *105,* No. 094509. doi:10.1063/1.3108486
15. Cordoyiannis, G.; Apreutesei, D.; Mehl, G. H.; Glorieux, C.; Thoen, J. *Phys. Rev. E* **2008,** *78,* No. 011708. doi:10.1103/PhysRevE.78.011708
16. Figueirinhas, J. L.; Cruz, C.; Filip, D.; Feio, G.; Ribeiro, A. C.; Frère, Y.; Meyer, T.; Mehl, G. H. *Phys. Rev. Lett.* **2005,** *94,* No. 107802. doi:10.1103/PhysRevLett.94.107802
17. Merkel, K.; Kocot, A.; Vij, J. K.; Korlacki, R.; Mehl, G. H.; Meyer, T. *Phys. Rev. Lett.* **2004,** *93,* No. 237801. doi:10.1103/PhysRevLett.93.237801
18. Prasad, V.; Kang, S.-W.; Suresh, K. A.; Joshi, L.; Wang, Q.; Kumar, S. *J. Am. Chem. Soc.* **2005,** *127,* 17224–17227. doi:10.1021/ja052769n
19. Dong, R. Y.; Kumar, S.; Prasad, V.; Zhang, J. *Chem. Phys. Lett.* **2007,** *448,* 54–60. doi:10.1016/j.cplett.2007.09.070
20. Le, K. V.; Mathews, M.; Chambers, M.; Harden, J.; Li, Q.; Takezoe, H.; Jákli, A. *Phys. Rev. E* **2009,** *79,* No. 030701(R). doi:10.1103/PhysRevE.79.030701
21. Lee, J.-H.; Lim, T.-K.; Kim, W.-T.; Jin, J.-I. *J. Appl. Phys.* **2007,** *101,* No. 034105. doi:10.1063/1.2433126
22. Stannarius, R. *J. Appl. Phys.* **2008,** *104,* No. 036104. doi:10.1063/1.2963702
23. Lehmann, M.; Levin, J. *Mol. Cryst. Liq. Cryst.* **2004,** *411,* 273–281. doi:10.1080/15421400490435260
24. Lehmann, M.; Seltmann, J.; Auer, A. A.; Prochnow, E.; Benedikt, U. *J. Mater. Chem.* **2009,** *19,* 1978–1988. doi:10.1039/b818240j
25. Lehmann, M.; Kang, S.-W.; Köhn, C.; Haseloh, S.; Kolb, U.; Schollmeyer, D.; Wang, Q.; Kumar, S. *J. Mater. Chem.* **2006,** *16,* 4326–4334. doi:10.1039/b605718g
26. Lehmann, M.; Köhn, C.; Kresse, H.; Vakhovskaya, Z. *Chem. Commun.* **2008,** 1768–1770. doi:10.1039/b718348h
27. Zannoni, C. *J. Mater. Chem.* **2001,** *11,* 2637–2646. doi:10.1039/b103923g
28. Sekine, C.; Iwakura, K.; Minai, M.; Fujisawa, K. *Liq. Cryst.* **2001,** *28,* 1505–1512. doi:10.1080/02678290110068947
29. Imrie, C. T.; Luckhurst, G. R. In *Handbook of Liquid Crystals;* Demus, D.; Goodby, J. W.; Gray, G. W.; Spiess, H.-W.; Vill, V., Eds.; Wiley-VCH: Weinheim, Germany, 1998; Vol. 2B, pp 801 ff.
30. Kouwer, P. H. J.; Mehl, G. H. *J. Am. Chem. Soc.* **2003,** *125,* 11172–11173. doi:10.1021/ja037075y And references therein.
31. In general, the molecular long axes are aligned with the magnetic field, however, domains may be isotropically distributed around the magnetic field vector. A similar X-ray diffraction pattern has been observed for cinnamic acid derivatives.
32. Praefcke, K.; Kohne, B.; Gündogan, B.; Singer, D.; Demus, D.; Diele, S.; Pelzl, G.; Bakowsky, U. *Mol. Cryst. Liq. Cryst.* **1991,** *198,* 393–405. doi:10.1080/00268949108033415
33. Jenkins, R.; Snyder, R. L. Chemical Analysis: A Series of Monographs on Analytical Chemistry and Its Applications. In *Introduction to X-ray Powder Diffractometry;* Winefordner, J. D., Ed.; Wiley: New York, 1996; Vol. 138.
34. Scherrer, P. *Nachr. Ges. Wiss. Goettingen, Math.-Phys. Kl.* **1918,** *2,* 98–100.
35. Vanakaras, A. G.; Photinos, D. J. *J. Chem. Phys.* **2008,** *128,* No. 154512. doi:10.1063/1.2897993
36. Francescangeli, O.; Stanic, V.; Torgova, S. I.; Strigazzi, A.; Scaramuzza, N.; Ferrero, C.; Dolbnya, I. P.; Weiss, T. M.; Berardi, R.; Muccioli, L.; Orlandi, S.; Zannoni, C. *Adv. Funct. Mater.* **2009,** *19,* 2592–2600. doi:10.1002/adfm.200801865
37. Huang, T. C.; Toraya, H.; Blanton, T. N.; Wu, Y. *J. Appl. Crystallogr.* **1993,** *26,* 180–184. doi:10.1107/S0021889892009762

Ring-alkyl connecting group effect on mesogenic properties of *p*-carborane derivatives and their hydrocarbon analogues

Aleksandra Jankowiak[1], Piotr Kaszynski[*1], William R. Tilford[1],
Kiminori Ohta[2], Adam Januszko[1], Takashi Nagamine[2] and Yasuyuki Endo[2]

Full Research Paper

Address:
[1]Organic Materials Research Group, Department of Chemistry, Vanderbilt University, Box 1822 Station B, Nashville, TN 37235, USA, Phone/Fax: (615) 322-3458 and [2]Tohoku Pharmaceutical University, 4-4-1, Komatsushima, Aoba-ku, Sendai 981-8558, Japan

Email:
Piotr Kaszynski[*] - piotr.kaszynski@vanderbilt.edu

* Corresponding author

Abstract

The effect of the phenyl–alkyl connecting group on mesogenic properties of several series of isostructural compounds containing *p*-carborane (**A** and **B**), bicyclo[2.2.2]octane (**C**), and benzene (**D**) was investigated using thermal and optical methods. Results demonstrated that mesophase stability in the series containing **A**–**D** follows the order $(Alk)CH_2CH_2– < (Alk)OOC– < (Alk)CH_2O– < (Alk)COO–$. Surprisingly, the connecting groups $(Alk)CH_2CH_2–$ and $(Alk)OOC–$ destabilize the mesophase significantly stronger for carboranes (**A** and **B**) than for carbocyclic derivatives (**C** and **D**). Analysis indicates that this effect may have quadrupolar and conformational origin.

Introduction

During the past decade, we have been investigating mesogenic derivatives of *p*-carboranes **A** and **B** (Figure 1) in the context of fundamental and applied studies of liquid crystals and development of new materials for electrooptical applications [1-23]. *p*-Carboranes belong to an extensive family of *closo*-boranes and are characterized by 3-dimensional σ-aromaticity and high-order symmetry axis [23]. Therefore, it is of interest to understand how the electronic properties of the two clusters and their

unusual molecular symmetry and size affect bulk properties of mesogens. Through extensive comparison of isostructural mesogenic derivatives of *p*-carboranes (**A** and **B**), bicyclo[2.2.2]octane (**C**), and benzene (**D**), we have been probing fundamental aspects of structure-property relationships in liquid crystals such as the effect of conformational properties [1,2], the structure of the linking group [5], and tail fluorination [18,19] on mesophase stability, and also the effectiveness of
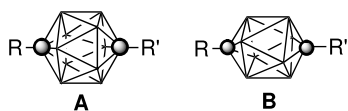
Figure 1: The molecular structures of 1,12-dicarba-*closo*-dodecaborane (12-vertex *p*-carborane, **A**) and 1,10-dicarba-*closo*-decaborane (10-vertex *p*-carborane, **B**). Each vertex corresponds to a BH fragment and the sphere represents a carbon atom.

shielding of a lateral substituent [8,16,20] and chirality transfer phenomena [17]. Results of these studies are important for the design of new materials and optimizing of their properties for applications.

During our investigation of structurally related series of mesogens containing rings **A–D** (Figure 2), it became apparent that the benzene ring–alkyl chain connection has a distinctly different impact on phase stability in derivatives of *p*-carborane (**A**) than in their isostructural carbocycles. For instance, a larger stabilization of the nematic phase, upon $CH_2 \rightarrow O$ replacement, was observed in *p*-carborane mesogens relative to benzene analogues. Thus, in series **1–4**, the nematic phase is stabilized by about 14 K more for the pairs **1A/2A** and **3A/4A**, than for terphenyl (**D**) and bicyclo[2.2.2]octane (**C**) analogues (Figure 2). Similarly high values for phase stabilization of about 34 K are observed in pairs of alkyl and alkoxy dioxane derivatives **5[n]** and **6[n]** [4], as compared to similar benzene mesogens [24]. Also in series **7–11** the introduction of the connecting oxygen atom gives a larger increase in mesophase stability by an average of 6 ± 2 K for the 12-vertex *p*-carborane derivatives than for their benzene analogues [5]. However, in series **12** and

13 the effect of incorporation of the O atom as the connecting group is practically the same for all ring systems [15].

A recently developed series of isostructural mesogens allows to analyze the effect of the replacement of an alkoxy in **14[6]** with an ester group in **15[6]**. The $CH_2O \rightarrow OOC$ exchange dramatically destabilized the nematic phase for the 10- and 12-vertex *p*-carborane derivatives, while a much smaller effect was observed for the carbocycles [25]. Series **14** and **15** [25] and also diesters **17** [2] provide an opportunity for further investigation of this interesting phenomenon. Therefore, we focused on series **14–16** to investigate the CH_2O, COO, OOC connecting groups, and also on series **17–20** to study the CH_2O, CH_2CH_2, COO, OOC groups.

Here we describe the preparation of an isostructural series of diesters **16[6]** and **18B**, and also tetraesters **19** and **20**, and a detailed comparative analysis focusing on the impact of the connecting group on mesogenic properties. The analysis is aided by molecular modeling of the pertinent molecular fragments. In addition, we report two homologues of **16A[6]**, diesters **16A[5]** and **16A[7]**.

Results
Synthesis

Diesters **16[n]** were prepared from diphenols **21** and appropriate carboxylic acid chlorides in the presence of a base as shown in Scheme 1. The requisite diphenols **21** were obtained in nearly quantitative yields by treating the corresponding dimethoxy derivatives **14[0]** with BBr_3. This procedure represents a significant improvement to the original preparation of
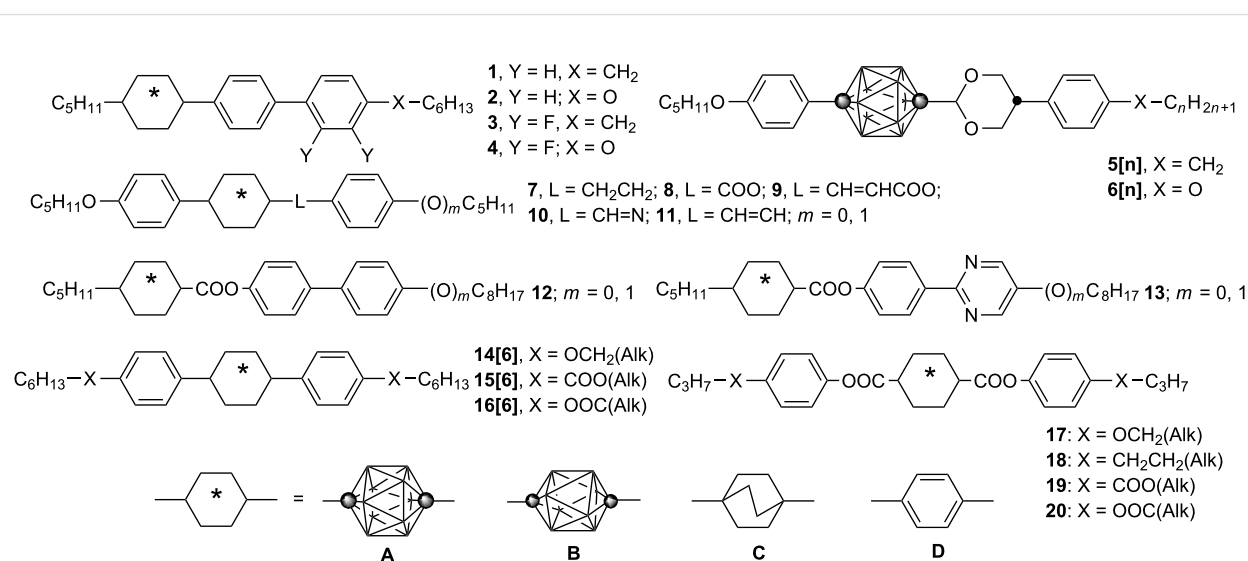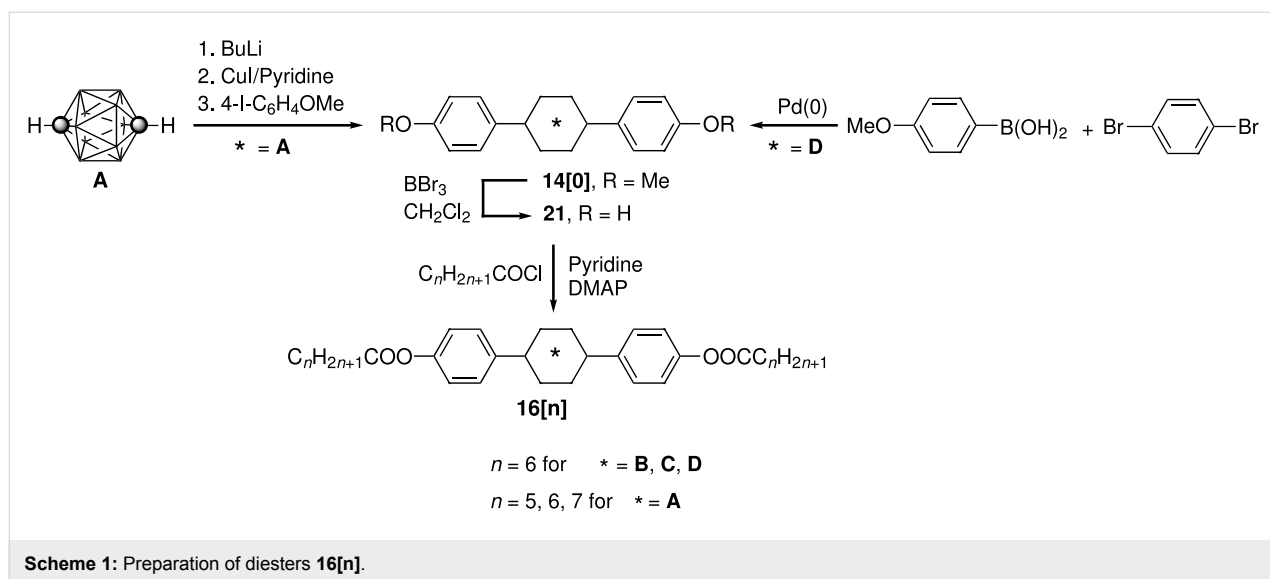

Figure 2: The molecular structures of derivatives **1–20**.

Scheme 1: Preparation of diesters **16[n]**.

1,12-bis(4-hydroxyphenyl)-*p*-carborane (**21A**) from **14A[0]** [26] and 1,4-bis(4-hydroxyphenyl)benzene (**21D**) [27]. The preparation of diphenol **21C** will be described elsewhere [25]. The dimethoxy carborane derivative **14A[0]** was obtained using the Wade's arylation procedure [28] of *p*-carborane (**A**) with 4-iodoanisole as described before [26]. The 10-vertex analogue **14B[0]** was prepared in a similar way and will be described elsewhere [25]. 4,4''-Dimethoxyterphenyl **14D[0]** was prepared in 84% yield from 1,4-dibromobenzene and (4-methoxyphenyl)boronic acid using the Suzuki coupling procedure [29]. This method is comparable to other Pd(0)-assisted methods for the synthesis of **14D[0]** [30-32].

The 10-vertex *p*-carborane diester **18B** was obtained from the corresponding dicarboxylic acid **22B** [33] and 4-pentylphenol (Scheme 2) according to a recently described procedure [2]. The two series of tetraesters **19** and **20** were prepared from the appropriate dicarboxylic acid **22** and phenols **23** and **24**, respectively. *p*-Carborane-1,12-dicarboxylic acid **22A** and terephthalic acid (**22D**) were converted to the corresponding acid chlorides using PCl$_5$ and then reacted with phenols in the presence of a base. The previously described method [2] for the preparation of esters of bicyclo[2.2.2]octane-1,4-dicarboxylic acid (**22C**) was unsuccessful and the desired esters **19C** and **20C** were obtained from the diacid and appropriate phenol using the classical Mitsunobu procedure [34]. A similar procedure was used for the preparation of tetraester **20B**, while **19B** was prepared more efficiently using the acid chloride method. Ester **19D** has been reported in the literature [35].

Phenol **24** was prepared by acylation of 4-benzyloxyphenol with butyryl chloride followed by removal of the protective benzyl group under reductive conditions as described in the literature [36] (Scheme 3).

Scheme 2: Preparation of esters **18–20**.

Scheme 3: Preparation of phenol **24**.
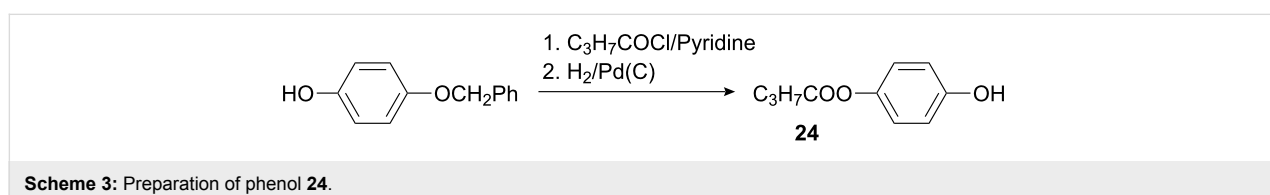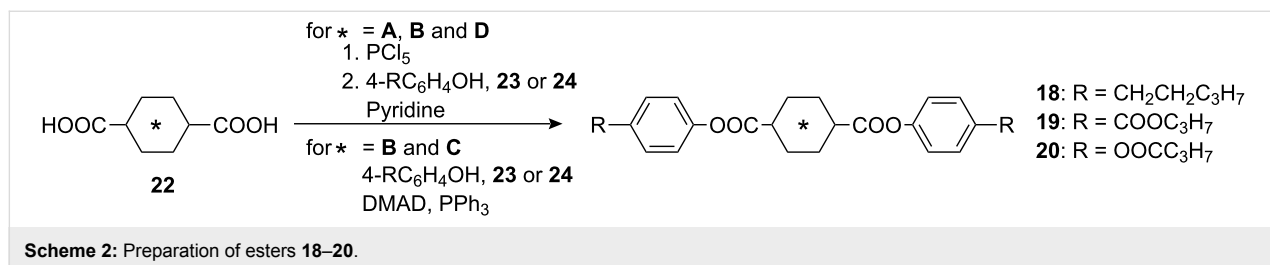
Mesogenic properties

Transition temperatures and enthalpies of the newly prepared compounds were determined by differential scanning calorimetry (DSC). The phase types were assigned by comparison of microscopic textures observed in polarized light with those published for reference compounds [37-39]. Results for these and also their structural analogues are shown in Table 1 and Table 2.

All *p*-carborane derivatives in series **14–20** exhibit exclusively the nematic phase. Similar nematic behavior is observed for carbocycles in series **17–20** with the exception of **19D**, which exhibits a SmA phase in addition to a N phase. In contrast, most carbocyclic derivatives in series **14[6]–16[6]** display only smectic and soft crystalline polymorphs. The bicyclo[2.2.2]octane derivative **16C[6]** is the only exception and exhibits a narrow range nematic phase above a soft crystalline phase designated as L or E on the basis of viscosity, ability to supercool, and optical textures. In general, bicyclo[2.2.2]octane derivatives **14C[6]–16C[6]** exhibit orthogonal phases (SmA and SmB), while the terphenyl analogues display a rich smectic polymorphism involving mainly tilted phases. The terphenyl derivatives **14D[6]** and **16D[6]** exhibit the most interesting polymorphism in the series with 4 smectic phases and possibly a soft crystalline modification such as a G phase below the SmF phase in the latter. A DSC trace for

Table 2: Transition temperatures (°C) for **16A[n]**.[a]

$C_nH_{2n+1}COO$—〈 〉—⬡—〈 〉—$OOCC_nH_{2n+1}$

n	Transition temperatures
5	Cr$_1$ 66 Cr$_2$ 120 N 155 I
6	Cr 108 N 132 I
7	Cr$_1$ 76 Cr$_2$ 92 N 124 I

[a]Obtained on heating; Cr: crystal, N: nematic, I: isotropic. Transition enthalpies are listed in the SI.

16D[6] is shown in Figure 3, and representative textures of its mesophases are presented in Figure 4. The tilted phases in both terphenyl compounds were identified by the appearance and subsequent characteristic changes of the Schlieren textures in the homeotropic regions of the SmA phase upon cooling.

In general, the order of phase stability for all five series follows **A ~ B < C < D**. Derivatives of both *p*-carboranes **A** and **B** exhibit similar stability of the nematic phase, with the exception of **15[6]** and **19** for which the monotropic nematic phase of the 10-vertex carborane derivatives is significantly less stable (<20 K) than that of the 12-vertex analogues.

Table 1: Transition temperatures (°C) for selected liquid crystals.[a]

	*	A	B	C	D
	X	C_6H_{13}–X–〈 〉–*–〈 〉–X–C_6H_{13}			
14[6]	–CH$_2$O–(Ph)	Cr 96 N 98 I[b]	Cr 73 N 105 I[b]	Cr 98 SmB 161 SmA 179 I[b]	Cr[c] 182 SmF 218 SmI 219 SmC 232 SmA 235 I[b]
15[6]	–OOC–(Ph)	Cr 112 (N 31) I[b]	Cr 65 (N 11) I[b]	Cr[d] 114 SmA 148 I[b]	Cr 134 SmC 143 SmA 183 I[b]
16[6]	–COO–(Ph)	Cr 108 N 132 I	Cr[e] 102 N 136 I	Cr[f] 102 X 205 N 207 I	Cr 66 X 96 SmF 226 SmI 232 SmC[g] 250 SmA 251 I
		C_3H_7–X–〈 〉–OOC–*–COO–〈 〉–X–C_3H_7			
17	–CH$_2$O–(Ph)	Cr 137 N 182.6 I[h]	Cr[i] 111 N 183.4 I[h]	Cr 112 N 229.5 I[h]	Cr 189 N 235 I[j]
18	–CH$_2$CH$_2$–(Ph)	Cr 106 N 118 I[k]	Cr 85 N 110 I	Cr 98 N 173 I[l]	Cr 155 N 181 I[m]
19	–OOC–(Ph)	Cr 203 (N 139) I[g]	Cr 160 (N 128) I	Cr 121 N 195 I	Cr 130 SmA 207 N 221 I[n]
20	–COO–(Ph)	Cr 133 N 230 I	Cr 120 N 234 I	Cr 133 N 275 I	Cr 230 N 287 I

[a]Obtained on heating; Cr: crystal, Sm: smectic, N: nematic, I: isotropic, X: unidentified phase. Transition enthalpies for new compounds are listed in the SI. [b]Ref. [25]. [c]Cr – Cr transition at 108 °C. [d]Cr – Cr transition at 100 °C. [e]Cr – Cr transition at 73 °C (14.9 kJ/mol). [f]Cr – Cr transition at 33 °C (11.6 kJ/mol). [g]Optical determination obtained on cooling .[h]Ref. [2]. [i]Cr – Cr transition at 70 °C. [j]Ref. [40]. [k]Previously reported Cr 104 N 114 I, ref. [21]. [l]Ref. [41]. [m]Ref. [42]. [n]Ref. [35].
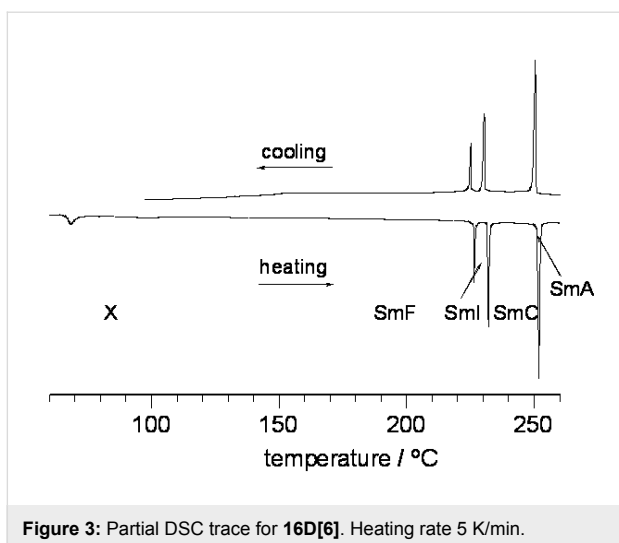
Figure 3: Partial DSC trace for **16D[6]**. Heating rate 5 K/min.

Figure 4: Optical textures of **16D[6]** obtained for the same region of the sample upon cooling: (a) SmA growing from isotropic (251 °C), (b) focal-conic texture of SmC (242 °C), (c) SmI (229 °C), and (d) broken focal-conic texture of SmF (211 °C). Magnification × 60.

Analysis of three homologues **16A[n]** demonstrated the decreasing stability of the nematic phase with increasing chain length from T_{NI} of 155 °C for $n = 5$ to 124 °C for $n = 7$ (Table 2). Investigation of the 4,4″-dimethoxyterphenyl **14D[0]** revealed a high temperature nematic phase (Cr 277 N 295 I), which is in disagreement with the original literature report [43].

Comparative Analysis

Mesogenic properties of structurally analogous pairs were compared, and the results are presented in Figure 5 and Figure 6.

The –OCH$_2$– → –CH$_2$CH$_2$– substitution

A comparison of T_{NI} for compounds in series **17** [2] versus their isostructural analogues **18**, in which the linking oxygen atom is replaced with –CH$_2$–, demonstrates that the presence of the oxygen atom increases the phase stability by about 55 K (or 27 K per alkoxyphenyl group) for the carbocyclic compounds.
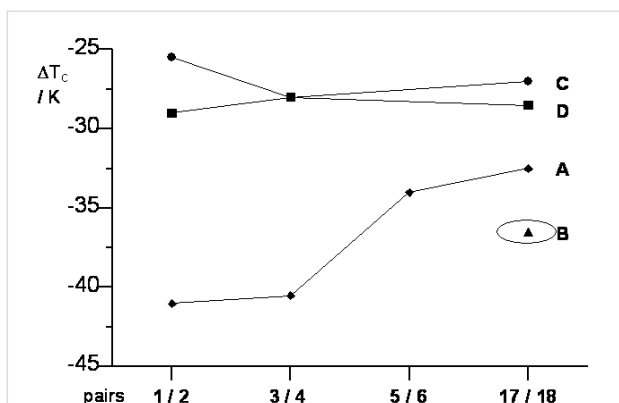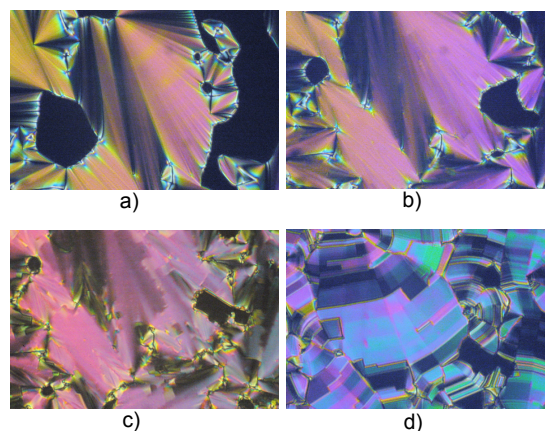
In contrast, the difference in T_{NI} is larger by 10 K for *p*-carborane **A** and 18 K for *p*-carborane **B** (Figure 5 and Figure 6). These results are consistent with earlier findings for pairs **1/2**, **3/4**, and **5/6** (Figure 5) in which a particularly large impact of the –OCH$_2$– → –CH$_2$CH$_2$– substitution on T_{NI} is observed for the rigid biphenyl derivatives **1–4**.

The –OCH$_2$– → –OOC– and –OCH$_2$– →–COO– substitution

Data in Table 1 demonstrate that the replacement of the heptyloxy group with heptanoyloxy in **14[16]**/**16[6]** and butoxy with butanoyloxy in **17/20** results in an increase of the T_{NI} by about 30 K and 45 K, respectively, for all structural units **A–D**. The only exception is the pair **14D[6]**/**16D[6]** for which the change in T_{NI} is only 16 K. The larger change of T_{NI} for pairs

Figure 5: The change in the clearing temperature ΔT_c upon substitution –OCH$_2$– → –CH$_2$CH$_2$– in selected pairs of compounds. The lines are guides for the eye.
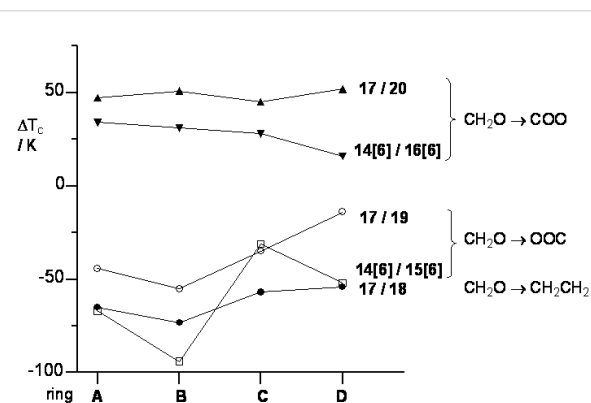

Figure 6: The change in the clearing temperature ΔT_c upon replacing of the –OCH$_2$– connecting group with another in selected pairs of compounds. The lines are guides for the eye.

17/20 than for **14[6]/16[6]** is consistent with attenuation of the substitution effect by the shorter alkyl chain in the latter (–C$_3$H$_7$ vs –C$_6$H$_{13}$).

In contrast, replacement of the oxymethylene linking group with a carboxy group of reversed orientation relative to the core (pairs **14[6]/15[6]** and **17/19**) leads to significant destabilization of the mesophase, and the magnitude of the effect markedly depends on the nature of the central structural element (Figure 6). Thus, for derivatives of carbocycles **C** and **D**, T_c decreases less than 55 K for **14[6]/15[6]** and less than 40 K for **17/19**, while for the *p*-carboranes the decrease is larger, reaching a value of 94 K for the pair **14B[6]/15B[6]**.

Data in Table 1 also allow for assessment of the impact of the orientation of the connecting carboxyl group on T_{NI} as a function of the central structural element. Thus, in pairs **16[6]/15[6]** and **20/19**, the change of carbonyloxy to oxycarbonyl leads to a marked phase destabilization for all structural elements **A–D**. Consistent with our previous analysis, the effect is much stronger for *p*-carboranes (>90 K) than for carbocycles (<80 K) with the typical order: **D**, **C** < **A** < **B**.

Molecular Modeling

For a better understanding of the terminal substituent's impact on the conformational ground state of the molecules, four benzene derivative models, **25**–**28**, were optimized at the B3LYP/6-31G(d) level of theory, and their equilibrium geometries are presented in Figure 7. Results show that the replacement of the oxygen atom with a –CH$_2$– group reorients the terminal chain from co-planar, in the conformational ground state of ethoxybenzene (**25**), to the orthogonal position relative to the benzene ring plane in propylbenzene (**26**). Replacement of the –CH$_2$O– fragment with the –COO– group leads to an increase of angle θ between the ring and substituent planes to about 50° in phenyl acetate (**27**). Reversing the connectivity of the ester group (–COO– → –OOC–) results in return to the co-planar orientation of the substituent in benzoate **28**. The computational results are consistent with experimental findings for anisole [44] and ethylbenzene [45], and solid-state structures for compounds containing fragments **25**–**28** [46].
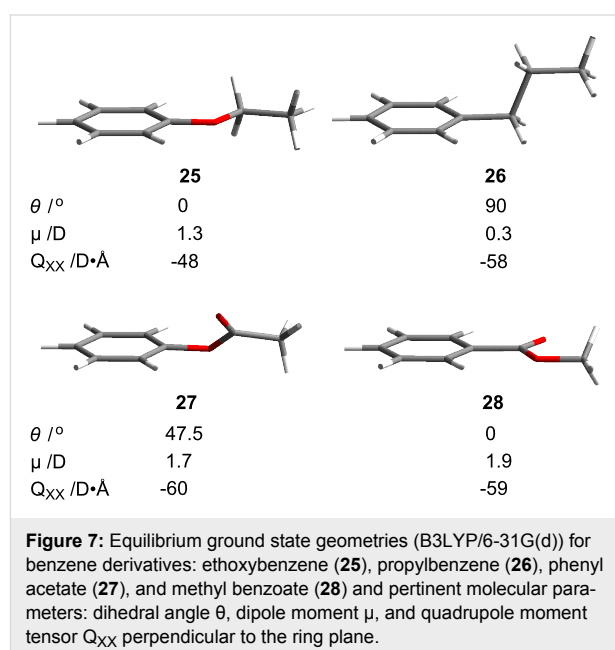
Overall, the interplanar angle θ between the ring and substituent increases in the series **25**, **28** < **27** < **26** or –OR, –C(O)OR < –OOCR < –CH$_2$R.

Further analysis of the computational results demonstrates that molecular dipole moment μ increases in the following order: **26** < **25** < **27** < **28**. The quadrupole moment tensor Q$_{XX}$ perpendicular to the benzene ring is larger for the esters than for alkyl or alkoxy derivatives.

Discussion and Conclusion

Results presented in Table 1 are in agreement with general trends [47,48] and demonstrate that the replacement of –OCH$_2$– with –OOC– increases T_{NI}, while replacement with –CH$_2$CH$_2$– or –COO– decreases T_{NI}. Overall, the effectiveness of the connecting group in mesophase stabilization follows the order: –OOC(Alk) > –OCH$_2$(Alk) > –COO(Alk) > –CH$_2$CH$_2$(Alk). The magnitude of the effect for the –OCH$_2$– → –OOC– replacement is practically independent of the central structural element **A–D**. In contrast, the decrease in T_{NI} upon substitution of –OCH$_2$– with –CH$_2$CH$_2$– or –COO– is stronger for *p*-carborane derivatives (**A** and **B**) than for their carbocyclic analogues. This effect is observed for compounds in which the *p*-carborane is connected directly to the substituted benzene ring (**1–4**, **14–16**) or through a spacer (**5**, **6**, **17–20**).

The origin of the observed relative effectiveness of the connecting groups (–OOC(Alk) > –OCH$_2$(Alk) > –COO(Alk) > –CH$_2$CH$_2$(Alk)) is unclear at the moment. In general, the phase stability is related to packing fraction, and for more compact anisometric molecules (high packing fraction) the clearing temperature is higher [49]. Thus, it can be expected that compounds with substituents preferring coplanar orientation with the aryl ring (–OR and –COOR) would exhibit higher mesophase stability than those with non-coplanar orientation (–CH$_2$R and –OOCR). While this simple steric argument is consistent with data for pairs –CH$_2$R/–OR, the effect of orientation of the carboxy group on mesophase stability is opposite. Therefore, steric arguments alone cannot explain the observed trend for these analogues.

	25	**26**
θ /°	0	90
μ /D	1.3	0.3
Q$_{XX}$ /D·Å	-48	-58

	27	**28**
θ /°	47.5	0
μ /D	1.7	1.9
Q$_{XX}$ /D·Å	-60	-59

Figure 7: Equilibrium ground state geometries (B3LYP/6-31G(d)) for benzene derivatives: ethoxybenzene (**25**), propylbenzene (**26**), phenyl acetate (**27**), and methyl benzoate (**28**) and pertinent molecular parameters: dihedral angle θ, dipole moment μ, and quadrupole moment tensor Q$_{XX}$ perpendicular to the ring plane.

Electronic effects also cannot sufficiently explain the observed trend in mesophase stability and the poor performance of the carboxyl group. Thus, the observed trend is inconsistent with the order of dipole moments calculated for the relevant molecular fragments **25**–**28** (Figure 7). According to the computational results, esters **27** and **28** have similar, and also the largest molecular dipole and quadrupole moments. Therefore, compounds containing these fragments would be expected to exhibit both similar and high mesophase stability. The data show otherwise and a large difference in T_C is observed for the isomeric esters (e.g. for **19B/20B** $\Delta T_{NI} = 80$ K; for other examples see LiqCryst database [50]).

The origin of the observed excessive mesophase destabilization in *p*-carborane derivatives by the –COO(Alk) and –CH$_2$CH$_2$(Alk) substituents is even more puzzling. Data in Table 1 show that mesophase of *p*-carborane derivatives containing electron rich benzene rings (with the –OR and –OOCR substituents) is excessively stabilized relative to those containing either weakly donating (–CH$_2$CH$_2$R) or electron-withdrawing (–COOR) substituents. This suggests that inter-molecular quadrupolar interactions between *p*-carborane and benzene ring may be responsible for the observed phase stabilization. Support for this hypothesis is provided by the finding that the connecting group affects bulk properties whether *p*-carborane is connected to the benzene ring directly or through a spacer. The observed larger effect of the –CH$_2$CH$_2$– → –OCH$_2$– replacement in pairs **1A/2A** and **3A/4A** as compared to **17A/18A** suggests a role for the molecular dipole moment in phase stabilization. Since *p*-carboranes are moderately electron withdrawing substituents, the alkoxy derivatives have a larger dipole moment than the alkyl derivatives [16]. Alternatively, the effect can be due to higher rigidity of **1-4**, which attenuates the effect as compared to the more conformationally flexible diesters.

Overall, the analysis cannot distinguish one particular factor responsible for the impact of structural elements (**A**–**D**) on phase stabilization. Instead, a combination of conformational properties of structural elements **A**–**D** and substituents, their relative sizes [51], and electronic properties of the benzene ring bearing the substituent dictate mesogenic properties.

The present report concentrates on the systematic variation of the connecting group between the alkyl and phenyl ring, and its effect on phase stability. For completeness, we also mention one example of variation of the carborane–alkyl connecting group, and its impact on T_c. Thus, a replacement of –CH$_2$CH$_2$– → –C≡C– destabilized the T_{NI} by over 150 K in bi-carborane derivatives, while a similar transformation in the biphenyl analogue leads to an increase of the clearing temperature [1,7].

This dramatic effect has been attributed to conformational properties of molecules in the condensed phase.

A more complete understanding of the impact of structural modification on bulk properties will emerge through further research on structure-property relationships and studying of other examples of structurally similar mesogens containing the four ring systems **A**–**D**.

Experimental

Optical microscopy and phase identification were performed using a PZO "Biolar" polarized microscope equipped with a HCS400 Instec hot stage. Thermal analysis was obtained using a TA Instruments 2920 DSC. Transition temperatures (onset) and enthalpies were obtained using small samples (1–2 mg) and a heating rate of 5 K min^{-1} under a flow of nitrogen gas. For DSC and microscopic analyses, each compound was additionally purified by dissolving in CH$_2$Cl$_2$, filtering to remove particles, evaporating and recrystallization typically from hexanes or toluene/heptane mixture. The resulting crystals were dried in vacuum overnight at ambient temperature. 10- and 12-vertex *p*-carboranes (**A** and **B**) were purchased from Katchem s. r. o. (Prague, Czech Republic).

Supporting Information

Synthetic procedures for compounds **14D[0]**, **16[n]**, **18B**, **19**, **20**, **24**, and analytical details are provided.

Supporting Information File 1
General methods and synthetic procedures
[http://www.beilstein-journals.org/bjoc/content/supplementary/1860-5397-5-83-S1.pdf]

Acknowledgements

References

1. Kaszynski, P.; Pakhomov, S.; Tesh, K. F.; Young, V. G., Jr. *Inorg. Chem.* **2001**, *40*, 6622–6631. doi:10.1021/ic010663x
2. Kaszynski, P.; Januszko, A.; Ohta, K.; Nagamine, T.; Potaczek, P.; Young, V. G., Jr.; Endo, Y. *Liq. Cryst.* **2008**, *35*, 1169–1190. doi:10.1080/02678290802409775
3. Nagamine, T.; Januszko, A.; Ohta, K.; Kaszynski, P.; Endo, Y. *Liq. Cryst.* **2005**, *32*, 985–995. doi:10.1080/02678290500291756

4. Nagamine, T.; Januszko, A.; Kaszynski, P.; Ohta, K.; Endo, Y. *J. Mater. Chem.* **2006,** *16,* 3836–3843. doi:10.1039/b608012j

5. Nagamine, T.; Januszko, A.; Ohta, K.; Kaszynski, P.; Endo, Y. *Liq. Cryst.* **2008,** *35,* 865–884. doi:10.1080/02678290802245450

6. Ohta, K.; Januszko, A.; Kaszynski, P.; Nagamine, T.; Sasnouski, G.; Endo, Y. *Liq. Cryst.* **2004,** *31,* 671–682. doi:10.1080/02678290410001670584

7. Piecek, W.; Kaufman, J. M.; Kaszynski, P. *Liq. Cryst.* **2003,** *30,* 39–48. doi:10.1080/0267829021000039669

8. Ringstrand, B.; Vroman, J.; Jensen, D.; Januszko, A.; Kaszynski, P.; Dziaduszek, J.; Drzewinski, W. *Liq. Cryst.* **2005,** *32,* 1061–1070. doi:10.1080/02678290500291699

9. Douglass, A. G.; Czuprynski, K.; Mierzwa, M.; Kaszynski, P. *Chem. Mater.* **1998,** *10,* 2399–2402. doi:10.1021/cm980089w

10. Douglass, A. G.; Mierzwa, M.; Kaszynski, P. Liquid Crystals Containing p-Carborane. In *Liquid Crystals: Chemistry and Structure;* Tykarska, M.; Dabrowski, R.; Zielinski, J., Eds.; Zakopane, 1998; Vol. 3319, pp 59–62.

11. Czuprynski, K.; Douglass, A. G.; Kaszynski, P.; Drzewinski, W. *Liq. Cryst.* **1999,** *26,* 261–269. doi:10.1080/026782999205407

12. Douglass, A. G.; Both, B.; Kaszynski, P. *J. Mater. Chem.* **1999,** *9,* 683–686. doi:10.1039/a807596d

13. Czuprynski, K.; Kaszynski, P. *Liq. Cryst.* **1999,** *26,* 775–778. doi:10.1080/026782999204877

14. Douglass, A. G.; Czuprynski, K.; Mierzwa, M.; Kaszynski, P. *J. Mater. Chem.* **1998,** *8,* 2391–2398. doi:10.1039/a804322a

15. Januszko, A.; Kaszynski, P.; Wand, M. D.; More, K. M.; Pakhomov, S.; O'Neill, M. *J. Mater. Chem.* **2004,** *14,* 1544–1553. doi:10.1039/b311140g

16. Januszko, A.; Glab, K. L.; Kaszynski, P.; Patel, K.; Lewis, R. A.; Mehl, G. H.; Wand, M. D. *J. Mater. Chem.* **2006,** *16,* 3183–3192. doi:10.1039/b600068a

17. Januszko, A.; Kaszynski, P.; Drzewinski, W. *J. Mater. Chem.* **2006,** *16,* 452–461. doi:10.1039/b512319d

18. Januszko, A.; Kaszynski, P. *Liq. Cryst.* **2008,** *35,* 705–710. doi:10.1080/02678290802120281

19. Januszko, A.; Glab, K. L.; Kaszynski, P. *Liq. Cryst.* **2008,** *35,* 549–553. doi:10.1080/02678290802015713

20. Jasinski, M.; Jankowiak, A.; Januszko, A.; Bremer, M.; Pauluth, D.; Kaszynski, P. *Liq. Cryst.* **2008,** *35,* 343–350. doi:10.1080/02678290701817318

21. Kaszynski, P.; Huang, J.; Jenkins, G. S.; Bairamov, K. A.; Lipiak, D. *Mol. Cryst. Liq. Cryst.* **1995,** *260,* 315–332. doi:10.1080/10587259508038705

22. Kaszynski, P.; Douglass, A. G. *J. Organomet. Chem.* **1999,** *581,* 28–38. doi:10.1016/S0022-328X(99)00088-1

23. Kaszynski, P. *closo*-Boranes as π Structural Elements for Advanced Anisotropic Materials. In *Anisotropic Organic Materials-Approaches to Polar Order;* Glaser, R.; Kaszynski, P., Eds.; ACS Symposium Series: Washington, D.C., 2001; Vol. 798, pp 68–82. And references therein.

24. Villiger, A.; Leenhouts, F. *Mol. Cryst. Liq. Cryst.* **1991,** *209,* 297–307. doi:10.1080/00268949108036205

25. Kaszynski, P.; Kulikiewicz, K. K.; Januszko, A.; Douglass, A. G.; Tilford, R. W.; Pakhomov, S.; Patel, M. K.; Ke, Y.; Radziszewski, G. J.; Young, V. G., Jr. Submitted.

26. Fox, M. A.; MacBride, J. A. H.; Peace, R. J.; Wade, K. *J. Chem. Soc., Dalton Trans.* **1998,** 401–412. doi:10.1039/a707154j

27. Price, C. C.; Mueller, G. P. *J. Am. Chem. Soc.* **1944,** *66,* 632–634. doi:10.1021/ja01232a038

28. Coult, R.; Fox, M. A.; Gill, W. R.; Herbertson, P. L.; McBride, J. A. H.; Wade, K. *J. Organomet. Chem.* **1993,** *462,* 19–29. doi:10.1016/0022-328X(93)83337-U

29. Miyaura, N.; Yanagi, Y.; Suzuki, A. *Synth. Commun.* **1981,** *11,* 513–519. doi:10.1080/00397918108063618

30. Chaumeil, H.; Le Drian, C.; Defoin, A. *Synthesis* **2002,** 757–760. doi:10.1055/s-2002-25773

31. Sinclair, D. J.; Sherburn, M. S. *J. Org. Chem.* **2005,** *70,* 3730–3733. doi:10.1021/jo050105q

32. Tao, X.; Zhao, Y.; Shen, D. *Synlett* **2004,** 359–361. doi:10.1055/s-2003-44992

33. Garrett, P. M.; Smart, J. C.; Hawthorne, M. F. *J. Am. Chem. Soc.* **1969,** *91,* 4707–4709. doi:10.1021/ja01045a021

34. Mitsunobu, O. *Synthesis* **1981,** 1–28. doi:10.1055/s-1981-29317

35. Leblanc, J. P.; Tessier, M.; Judas, D.; Friedrich, C.; Noël, C.; Maréchal, E. *Macromolecules* **1993,** *26,* 4391–4399. doi:10.1021/ma00069a001

36. Neubert, M. E.; Wildman, P. J.; Zawaski, M. J.; Hanlon, C. A.; Benyo, T. L.; De Vries, A. *Mol. Cryst. Liq. Cryst.* **1987,** *145,* 111–158. doi:10.1080/00268948708080217

37. Demus, D.; Richter, L. *Textures of Liquid Crystals,* 2nd ed.; VEB Deutscher Verlag für Grundstoffindustrie: Leipzig, 1980.

38. Gray, G. W.; Goodby, J. W. G. *Smectic Liquid Crystals-Textures and Structures;* Leonard Hill: Philadelphia, 1984.

39. Dierking, I. *Smectic Liquid Crystals Textures and Structures;* Wiley-VCH: Weinheim, 2003. doi:10.1002/3527602054

40. Kelker, H.; Scheurle, B. *J. Phys. (Paris)* **1969,** *30-C4,* 104–108. doi:10.1051/jphyscol:1969425

41. Compound ID # 37494 in *LiqCryst 4.6* database.

42. Neubert, M. E.; Stahl, M. E.; Cline, R. E. *Mol. Cryst. Liq. Cryst.* **1982,** *89,* 93–117. doi:10.1080/00268948208074472

43. Compound ID # 21727 in *LiqCryst 4.6* database.

44. Onda, M.; Toda, A.; Mori, S.; Yamaguchi, I. *J. Mol. Struct.* **1986,** *144,* 47–51. doi:10.1016/0022-2860(86)80166-1

45. Scharfenberg, P.; Rozsondai, B.; Hargittai, I. *Z. Naturforsch., A* **1980,** *35,* 431–436.

46. Haase, W.; Athanassopoulou, M. A. Crystal Structures of LC Mesogens. In *Structure and Bonding;* Mingos, D. M. P., Ed.; Springer: Berlin, 1999; Vol. 94, pp 139–197.

47. Toyne, K. J. Liquid Crystal Behavior in Relation to Molecular Structure. In *Thermotropic Liquid Crystals;* Gray, G. W., Ed.; Wiley: New York, 1987; pp 28–63.

48. Demus, D. Chemical Structure and Mesogenic Properties. In *Handbook of Liquid Crystals;* Demus, D.; Goodby, J. W.; Gray, G. W.; Spiess, H.-W.; Vill, V., Eds.; Wiley-VCH: New York, 1998; Vol. 1, pp 133–187.

49. Demus, D.; Hauser, A. Molecular structure and thermodynamic properties of nematic liquid crystals. In *Selected Topics In Liquid Crystal Research;* Koswig, H.-D., Ed.; Akademie-Verlag: Berlin, 1990; pp 19–44.

50. Vill, V. *LiqCryst 4.6* database (LCI Publisher GmbH, Hamburg, Germany, www.lci-publisher.com) and references therein.

51. Effective diameter *d* for the four structural elements: **A**, *d* = 7.43 Å; **B**, *d* = 7.17 Å; **C**, *d* = 6.72 Å; **D**, *d* = 5.03 Å. For details see footnote 33 in reference 16.

License and Terms

Competition between local disordering and global ordering fields in nematic liquid crystals

Matej Cvetko[*1,2], Milan Ambrožič[2] and Samo Kralj[2,3]

Full Research Paper

Open Access

Address:
[1]Regional Development Agency Mura Ltd, Lendavska 5a, 9000 Murska Sobota, Slovenia, [2]Laboratory of Physics of Complex Systems, Faculty of Natural Sciences and Mathematics, University of Maribor, Koroška 160, 2000 Maribor, Slovenia and [3]Condensed Matter Physics Department, Jožef Stefan Institute, Jamova 39, 1000 Ljubljana, Slovenia

Email:
Matej Cvetko[*] - Matej.Cvetko@rra-mura.si

* Corresponding author

Abstract

We study the influence of external electric or magnetic field B on orientational ordering of nematic liquid crystals or of other rod-like objects (e.g. nanotubes immersed in a liquid) in the presence of random anisotropy field type of disorder. The Lebwohl–Lasher lattice type of semi-microscopic approach is used at zero temperature. Therefore, results are valid well below the transition into the isotropic phase. We calculate the correlation function of systems as a function of B, concentration p of impurities imposing random anisotropy field disorder, the disorder strength W and system dimensionality (2D and 3D systems). In order to probe memory effects we calculate correlation length ξ for random and homogeneous initial configurations. We determine the crossover fields $B_c(p)$ separating roughly the ordered and disordered regime. Memory effects are apparent only in the latter case, i.e. for $B < B_c$.

PACS numbers: 47.51.+a, 47.54.-r, 07.05.Tp, 61.30.-v

Introduction

For years there has been a strong interest in the phase and structural behavior of randomly perturbed liquid crystals (LCs) [1]. Such systems could be used in various electro-optical applications. On the other hand they represent also an adequate testing ground [2] to study fundamental questions concerning the impact of disorder [3-6] on various phase and structural transitions.

Most studies so far have been carried out in thermotropic nematic LC phases, which exhibit long range orientational order [7]. To enforce disorder to LC ordering one either confines LC to various porous matrices [8-12] (e.g., aerogels, Controlled-pore glass, Vycor glass) or mixes LCs with nanoparticles. For the latter purpose aerosil nanoparticles [13-15] are particularly adequate. They form random networks, the structure of which

can be altered by varying the concentration of nanoparticles. At least three qualitatively different regimes can be realized [16].

Studies so far have mainly focused on structural and phase behavior [8-18]. It has been shown that the isotropic nematic phase transition is typically replaced by the paranematic–nematic (PN–N) phase transition. The transition temperature in most cases decreases with increased disorder strength. If disorder is strong enough the transition can disappear. In the nematic phase memory effects can be observed revealing to some extent glass-like features.

To our knowledge none of the studies so far have systematically explored the effect of external ordering field (*B*) in such systems. This is the topic of our paper. We consider the competition between local disordering fields and the global external magnetic or electric ordering field. Local random fields can be in practice imposed geometrically. Experimental examples are LCs confined to a porous matrix [1], mixtures of LCs and aerosil nanoparticles [12-15], binary mixtures of different rodlike objects which tend to be oriented perpendicularly [19], and nanotubes immersed in liquid crystals [20,21]. We focus on *B* induced erasing of memory effects in such systems using the Lebwohl–Lasher [22] type lattice model deep in the nematic phase.

The structure of the article is as follows. First we present the semi-microscopic lattice model that we use. Then the results are presented and discussed. In the following section we summarize our results. Some numerical details are summarized in the last section.

Model

We consider an orthogonal cubic lattice with $N = N_0^d$ cylindrically symmetric particles positioned at equidistant sites in the space with *d* dimensions. The nearest neighbour's distance is taken as a unit, thus the side of the cell has the length $L = N_0$. Local orientation of a particle at the site with index α is given by a unit vector – director $\boldsymbol{S}_\alpha$. We further set at randomly chosen sites of concentration *p* cylindrically symmetric quenched impurities enforcing orientational ordering along $\boldsymbol{e}_\alpha$. The orientations of impurities are randomly chosen without any preferred global orientation. We also impose a homogeneous external (e.g., electric or magnetic) ordering field $\boldsymbol{B} = B\boldsymbol{e}_B$, which tends to reorient the director field along $\boldsymbol{e}_B$. Systems with the head-to-tail invariance, where $\pm\boldsymbol{S}_\alpha$ orientations are equivalent, are taken into account. This property is characteristic for most LC molecules (where several structural details are averaged out via relatively fast molecular rotations) or nanotubes. The corresponding interaction energy of the system can be expressed as [6,8,23]

$$F = -\frac{J}{2}\sum_{\alpha,\beta}\left(\boldsymbol{S}_\alpha \cdot \boldsymbol{S}_\beta\right)^2 - W\sum_\alpha p_\alpha\left(\boldsymbol{S}_\alpha \cdot \boldsymbol{e}_\alpha\right)^2 - B^2\sum_\alpha\left(\boldsymbol{S}_\alpha \cdot \boldsymbol{e}_B\right)^2. \quad (1)$$

The parameter $J > 0$ describes the ordering interaction among neighbouring molecules tending to orient directors parallel. The index α in the double sum counts all the particles, and the indices β run over the 1st nearest neighbours of the α-th particle. At randomly chosen sites of concentration *p* we additionally place rigid impurities which are coupled with surrounding directors by the random anisotropy type interaction [24,25] of anchoring strength $W > 0$. At the sites with impurities $p_\alpha = 1$ while at remaining sites $p_\alpha = 0$.

We describe ordering in the Cartesian coordinate frame (*x,y,z*), whose axes point along unit vectors $\boldsymbol{e}_x$, $\boldsymbol{e}_y$ and $\boldsymbol{e}_z$, respectively. The external field is oriented along a chosen axis, e.g., *x*-axis. We consider behaviour in two and three dimensions, to which we henceforth refer as 2D and 3D, respectively.

For latter convenience we scale quantities in Equation 1 with respect to *J*: $\widetilde{F} = F / J$, $\widetilde{W}_i = W_i / J$, $\widetilde{B} = B / \sqrt{J}$, i.e. we set $J = 1$ in (1). We henceforth omit the tildes. Some details of the minimization of the total energy Equation 1 are given in the numerical approach section. We have neglected the role of thermal fluctuations and consider configurations at zero temperature. In case of nematic ordering in liquid crystals such assumption is sensible deep in the nematic phase (i.e. well below the isotropic-nematic LC phase transition temperature).

In simulations we either originate from randomly distributed orientations of directors, or from homogeneously aligned samples along a symmetry breaking direction. In the latter case the directors are initially homogeneously aligned along $\boldsymbol{e}_x$. We henceforth refer to these cases as the i) random and ii) homogeneous samples, respectively. The i) random case can be experimentally realized by quenching the system from the isotropic phase to the ordered phase without an external field (i.e., $B = 0$). This can be achieved either via a sudden decrease of temperature or sudden increase of pressure. The ii) homogeneous case can be realized by applying first a strong homogeneous external field $\boldsymbol{B}$ along a symmetry breaking direction. After a well enough alignment is achieved the field is switched off.

In order to diminish the influence of statistical variations we carry out several simulations (typically $N_{rep} \approx 10$) for a given set of parameters (i.e., *W*, *p* and a chosen initial condition).

From obtained configurations we calculate the orientational correlation function $G(r)$. It measures orientational correlation of LC directors as a function of their mutual separation *r* (*r* = 1

for nearest neighbours). We define it in two dimensional (2D) ensembles as

$$G(r) = \left\langle 2\left(\boldsymbol{S}_\alpha \cdot \boldsymbol{S}_\beta\right)^2 - 1\right\rangle, \qquad (2)$$

and in three dimensions (3D) as

$$G(r) = \frac{1}{2}\left\langle 3\left(\boldsymbol{S}_\alpha \cdot \boldsymbol{S}_\beta\right)^2 - 1\right\rangle \qquad (3)$$

The brackets $\langle\cdots\rangle$ denote the average over all lattice sites that are separated for a distance r. If the directors are completely homogeneously aligned along a single direction it follows $G(r) = 1$. On the other hand $G(r) = 0$ reflects completely uncorrelated directors. Since each director is parallel with itself, it holds $G(0) = 1$. The correlation function is a decreasing function of the distance r.

In order to obtain structural details from a calculated $G(r)$ dependence we use the ansatz

$$G(r) = (1-s)e^{-(r/\xi)^m} + s, \qquad (4)$$

with adjustable parameters ξ, m, and s. The correlation length ξ estimates the average domain in which directors are significantly correlated. The parameter m measures the distribution width of ξ values. Presence of a single correlation length in the system is reflected in $m \approx 1$. A value of s reveals the degree of ordering within the system. The case $s = 0$ indicates the short range order (SRO). A finite value of s reveals either the long range order (LRO) or quasi long range order (QLRO). To distinguish between these two cases a finite size analysis $s(L)$ must be carried out where L represents the typical linear size of the system. If $s(L)$ saturates at a finite value the system exhibits LRO. If $s(L)$ dependence exhibits algebraic dependence on L the system possesses QLRO.

Results

We study the influence of an external ordering field on nematic ordering which is orientationally perturbed by randomly distributed impurities of concentration p. We vary the history of samples, concentration p of impurities, anchoring strength W between LC molecules and impurities, dimensionality of the system and the external field strength B. We consider 2D and 3D systems. Concerning histories we either originate from initially homogeneously aligned directors or from completely disordered configuration.

For a given set of control parameters we calculate a configuration of the system by minimizing the interaction energy. The configuration reflects the interplay among elastic, external ordering field and surface disordering tendencies. The external ordering (B) and impurities introduce additional characteristic scales into the system. The relative strength of elastic and external ordering field contribution is measured by the external field extrapolation length [7] $\xi_B \approx \sqrt{J/B}$. In the case of ordered LC-substrate interfaces the relative importance of surface anchoring term is measured by the surface extrapolation length [7] $d_e \approx J/W$. The external ordering field is expected to override the surface anchoring tendency in the limit $d_e/\xi >> 1$. However, if LC-substrate interfaces introduce a disorder into the system, then instead of d_e the so called Imry-Ma scale ξ_{IM} characterizes the ordering of the system. It expresses the relative importance of elastic ordering and surface disordering term. It roughly holds [26]

$$\xi_{IM} \propto W_{dis}^{\frac{2}{d-4}} \qquad (5)$$

where $W_{dis} \propto W$ measures the disorder strength.

From obtained orientational ordering we calculate the correlation function $G(r)$. From it we extract the average correlation length ξ using Equation 4. In case that the disorder dominates the system behavior one expects $\xi \approx \xi_{IM}$. On the contrary, the dominance of B is reflected in $\xi \approx \xi_B$.

Note that for cases studied we obtain qualitatively similar results for 2D and 3D systems. Consequently, we carry out more detailed simulations for 2D systems which demand less computational time.

A typical $G(r)$ dependence in 2D and 3D is shown in Figure 1a and Figure 1b, respectively. We plot $G(r)$ for both homogeneous and random initial configuration in the presence of external field and without it. For $B = 0$ it holds $\xi^{(hom)} > \xi^{(ran)}$, where superscripts (hom) and (ran) denote correlation lengths in homogeneous and random samples, respectively. The reason behind this are stronger elastic frustrations in random samples, as analyzed in more detail in our previous paper [25]. Furthermore, $\xi^{(ran)}$ roughly obeys the Imry-Ma scaling for low enough external fields (i.e. $\xi^{(ran)} << \xi_B$), suggesting $\xi^{(ran)} \approx \xi_{IM}$. The presence of B becomes apparent when $\xi \approx < \xi_{IM}$, which is shown in Figure 1.

We also note that in random samples $s = G(r\to\infty)$ always equals zero [25] for $B = 0$ indicating short range order. On the contrary in homogeneous samples we obtain a finite value of s if the disorder strength is not too large. In Figure 1 we see that the presence of external field can enforce a finite value of s also in random samples.
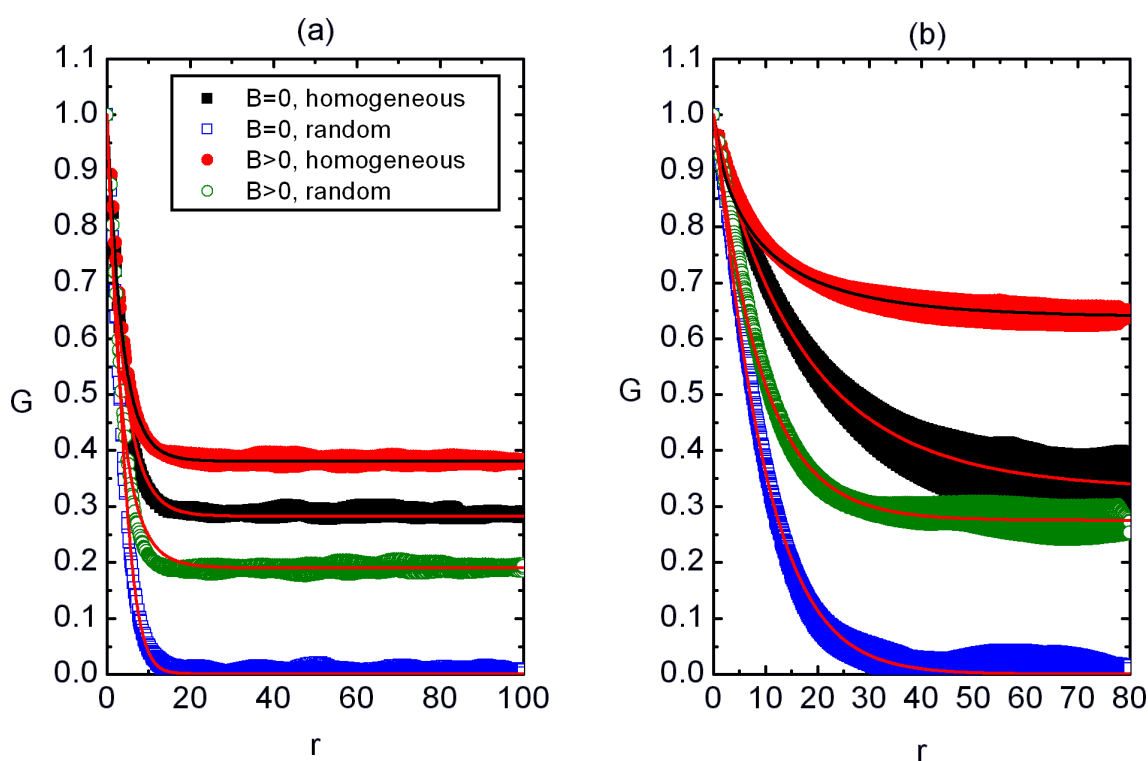
Figure 1: The orientational correlation function as a function of separation *r* between LC molecules for (a) 2D and (b) 3D systems. In random samples $G(r)$ vanishes for large enough values of *r* for *B* = 0 while in homogeneous samples it could saturate at a finite plateau *s* (if *p* or *W* are low enough). For *B* > 0 a finite plateau can be observed also in random samples. (a) $p = 0.3$, $W = 2.5$, $N_0 = 260$; (b) $p = 0.3$, $W = 2.5$, $N_0 = 100$. At $r = 1$ the first neighbors are placed in the cubic cell. The legend is shown in (a).

In Figure 2 we plot ξ as a function of $1/B$ for both homogeneous and random samples. For strong enough magnetic fields one expects $\xi \approx \xi_B \propto 1/B$. On the other hand for a weak enough *B* the value of ξ is dominantly influenced by the disorder strength. Indeed, we observe a crossover behavior in $\xi(B)$ dependence on varying *B*. The crossover between two qualitatively different regimes roughly takes place at the crossover field B_c. We define it as the field below which the difference between $\xi^{(ran)}$ and $\xi^{(hom)}$ is apparent. Below B_c the disordered regime takes place, where ξ exhibits weak dependence on *B*, i.e. $\xi \approx \xi_{IM}$. Above B_c the ordered regime exists, where $\xi \approx \xi_B \propto 1/B$. Therefore, for $B > B_c$ it holds $\xi^{(ran)} \approx \xi^{(hom)} \approx \xi_B$ and in the random regime one observes $\xi^{(hom)} \approx \xi^{(ran)} \approx \xi_{IM}$.

The corresponding $s(B)$ dependence is shown in Figure 3. As expected *s* monotonously increases on increasing *B*, because the external field tends to increase the degree of ordering. Note that in random samples $s(B = 0) = 0$ and the presence of *B* gives rise to $s > 0$.

In Figure 4 we show the $m(B)$ dependence. For weak enough fields ($B << B_c$) one typically observes $m^{(ran)} > m^{(hom)} > 1$. Therefore, in random samples we have larger dispersion of ξ values than in homogeneous samples. With the increasing external field both $m^{(ran)}$ and $m^{(hom)}$ asymptotically approach towards $m = 1$. In the latter case the distribution of ξ vales is sharply centered at $\xi \approx \xi_B$.

The crossover field B_c as a function of *p* is shown in Figure 5. Indicated lines roughly separate ergodic ($B > B_c$) and nonergodic regimes ($B < B_c$). With increasing *p* the degree of frustration within the system increases. Consequently larger values of *B* are needed to erase disorders induced memory effects. Note that B_c is larger in 2D than in 3D systems because in the former case the LC molecules are effectively more constrained by impurities (i.e., in 3D the additional degree of freedom is present).
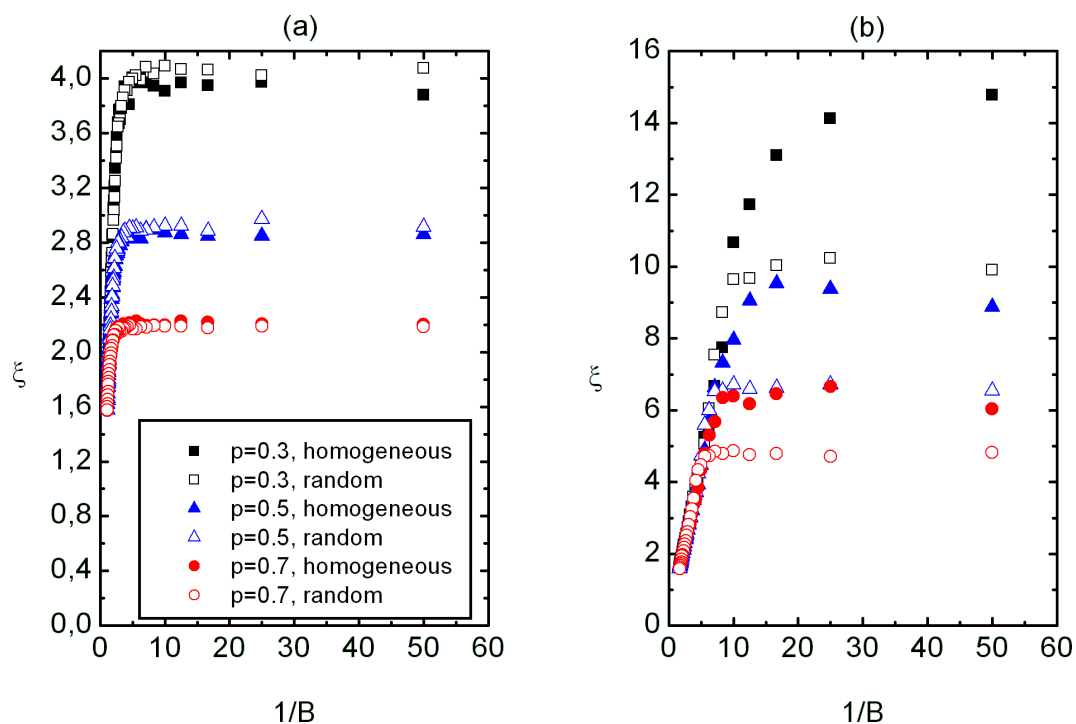
Figure 2: Correlation length ξ as a function of $1/B$ for homogeneous and random samples for three different concentrations of impurities in (a) 2D and (b) 3D. The $\xi_B(B)$ dependence displays a crossover between the disordered and ordered regime. The disordered regimes extends at ($B < B_c$), where $\xi^{(hom)} > \xi^{(ran)}$. In the ordered regime ($B > B_c$) one observes $\xi^{(ran)} \approx \xi^{(hom)} \approx \xi_B$. (a) $W = 2.5$, $N_0 = 260$; (b) $W = 2.5$, $N_0 = 100$. The legend is shown in (a).
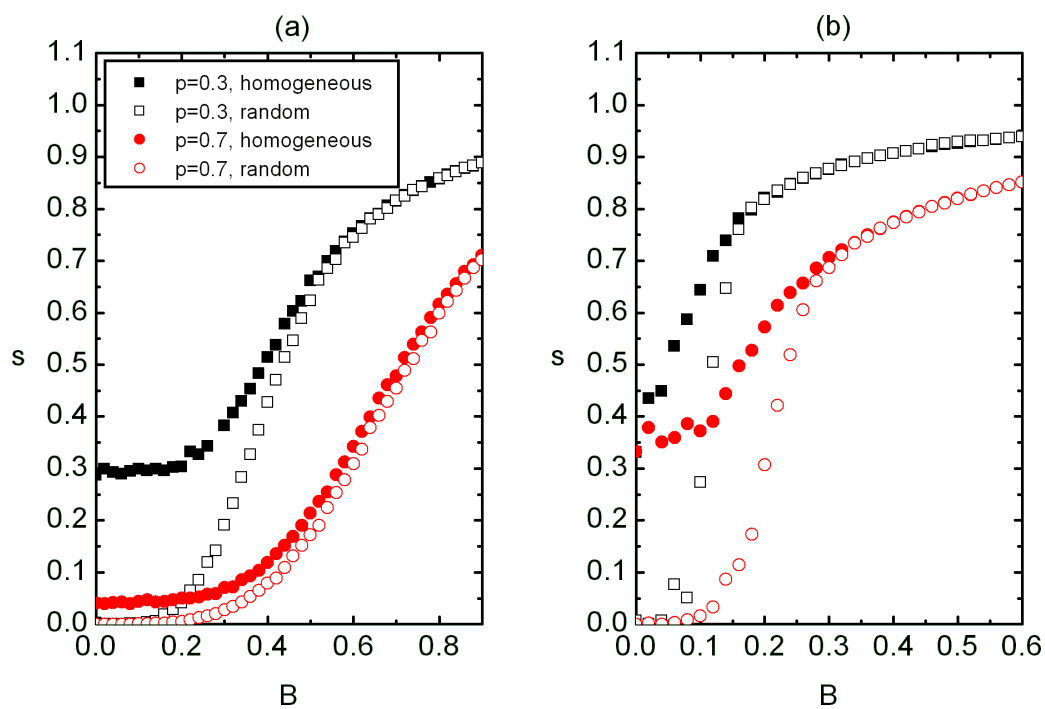
Figure 3: The $s(B)$ dependence for homogeneous and random samples for two different p in (a) 2D and (b) 3D. For $s(B = 0)$ we obtain $s^{(ran)} = 0$. In the disordered regime it holds $s^{(hom)} > s^{(ran)}$ and $s^{(hom)} \approx s^{(ran)}$ in the ordered regime. (a) $W = 2.5$, $N_0 = 260$; (b) $W = 2.5$, $N_0 = 100$. The legend is shown in (a).
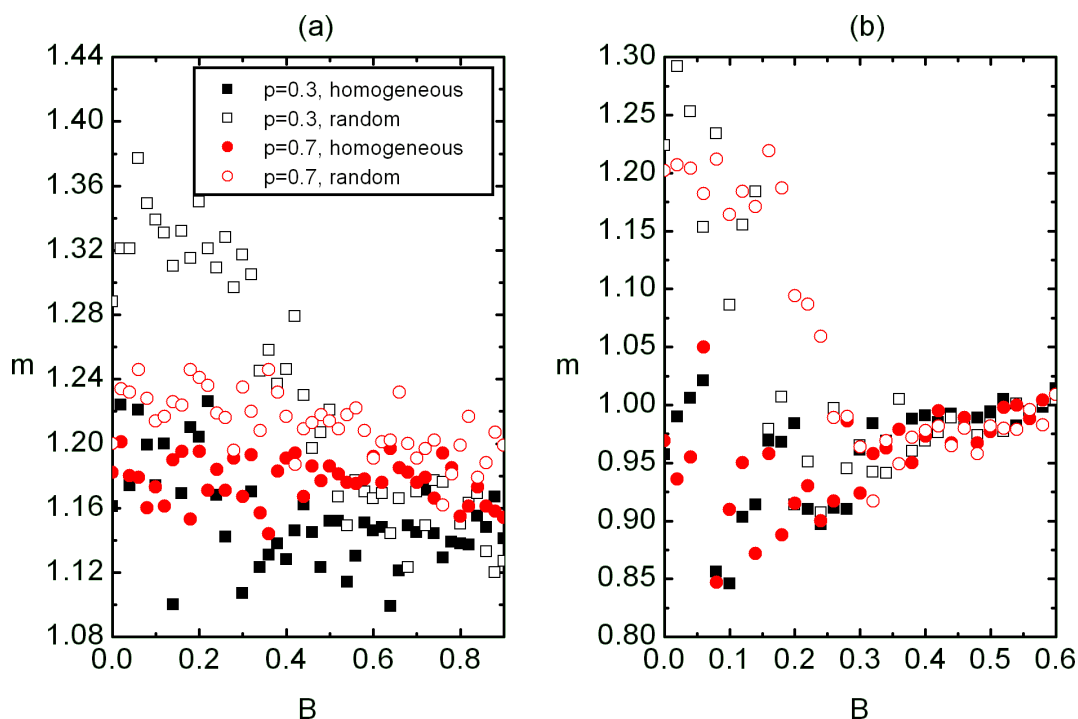
Figure 4: The $m(B)$ dependence r homogeneous and random samples for two different p in (a) 2D and (b) 3D. In the disordered regime it holds $m^{(ran)} > m^{(hom)} > 1$. In the ordered regime we obtain $m^{(ran)} \approx m^{(hom)} > 1$ which asymptotically approach one on increasing B. (a) $W = 2.5$, $N_0 = 260$; (b) $W = 2.5$, $N_0 = 100$. The legend is shown in (a).
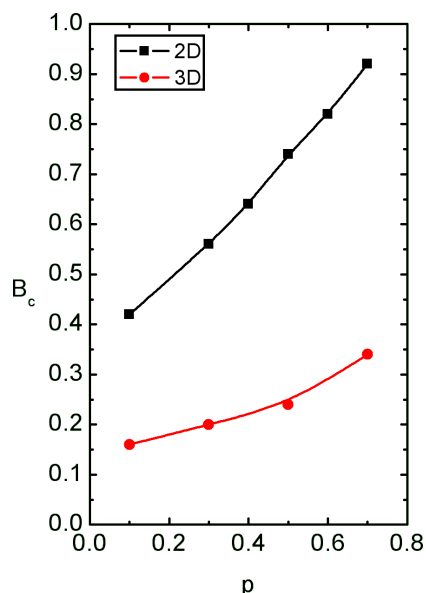

Figure 5: The crossover field B_c on varying p. Indicated lines roughly separate ergodic ($B > B_c$) and nonergodic regimes ($B < B_c$). With increasing p one the degree of frustration within the system increases. Consequently larger values of B are needed to erase disorder induced memory effects. The points are calculated and the lines serve as guides for the eye. (a) $W = 2.5$, $N_0 = 260$; (b) $W = 2.5$, $N_0 = 100$.

Conclusions

We have studied the influence of external ordering electric or magnetic field B on systems of rod-like objects (e.g. nematic liquid crystals or a dispersion of nano-rods in a liquid environment [20,21]) in the presence of random anisotropic type of disorder. We express the interaction energy F of the system using the Lebwohl–Lasher type semi-microscopic description. The orientational order is described in terms of the uniaxial director field exhibiting head-to-tail invariance. We calculate configurations of director fields by minimizing F at temperature zero. Therefore, our results are reasonable deep in the nematic phase, where the long range orientational order is observed in absence of random fields. In addition we neglect biaxial states [27,28] which might be present in strongly elastically perturbed systems. For a given set of parameters (i.e. concentration p of impurities imposing random anisotropy disorder, disorder anchoring strength W, system dimensionality, history of systems and B) we calculate the orientational correlation function $G(r)$ of the system. From it we extract the average size of correlated regions and distribution of ξ values measured via the distribution parameter m.

Our main interest was to determine the magnetic field regime in which random-field driven memory effects are erased by a

strong enough magnetic field. For this purpose we monitored ξ dependence on B for random and homogeneous initial configurations. These states represent two extreme conditions and consequently yield relatively strong memory effects for weak enough values of B. On increasing B values of m are approaching towards $m = 1$. This signifies that the single peak distribution of ξ values is narrowing. On varying B we distinguish between two qualitatively different regimes. The *disorded* regime, where random field effects are apparent, exists below B_c. In it we find $\xi^{(hom)} > \xi^{(ran)}$. In the ordered regime $B > B_c$ the average length ξ is dominated by external field B and $\xi \approx \xi_B \propto 1/B$. The crossover values B_c are larger in 2D systems, and monotonously increase on increasing p.

The results of our studies suggest regimes in which memory effects are expected. Our settings well mimic for example mixtures of LCs and aerosil particles [13-15] or LCs confined to porous matrices [10-12], or randomly perturbed nanotubes in a liquid environment [20,21]. Our results might be of use for electro-optic applications, where switching between different optical states (i.e. global orientational ordering) is achieved via external electric or magnetic fields in advanced soft nano-composites or soft hybrid systems.

Numerical approach

The system consists of a lattice of $N_0 \times N_0 \times N_0$ sites with unit directors

$$\boldsymbol{S}_{ijk} = \boldsymbol{e}_x S_x^{(ijk)} + \boldsymbol{e}_y S_y^{(ijk)} + \boldsymbol{e}_z S_z^{(ijk)} \tag{6}$$

In 2D we set $S_Z = 0$. We express the total interaction energy functional as the sum over all sites $F = \sum_{ijk} F_{ijk}$ where the term F_{ijk} consists of three parts:

$$F_{ijk} = -\frac{1}{2} \sum_{i'j'k'} (\boldsymbol{S}_{ijk} \cdot \boldsymbol{S}_{i'j'k'})^2 - W p_{ijk} (\boldsymbol{S}_{ijk} \cdot \boldsymbol{e}_{ijk})^2 - B^2 (\boldsymbol{S}_{ijk} \cdot \boldsymbol{e}_x)^2 \tag{7}$$

$J = 1$. The indices i', j', k' run over the first neighbors of the point described by the indices I, j, k. With respect to denotation of indices in Equation 1 these sets of indices correspond to $\alpha = (I,j,k)$ and $\beta = (i',j',k')$. The parameter p_{ijk} has the value either 1 or 0, while the orientation of the unit vector $\boldsymbol{e}_{ijk}$ is random spatially distributed, we set these by random-number generator.

The equilibrium director configuration is obtained by minimizing the total interaction energy with respect to all the directors by taking into account the normalization condition $\boldsymbol{S}_{ijk}^2 = 1$. The resulting potential to be minimized reads $F^* = \sum_{ijk} F_{ijk}^*$, where

$$F_{ijk}^* = \lambda_{ijk}(S_{ijk}^2 - 1) + F_{ijk} \tag{8}$$

and λ_{ijk} are Lagrange multipliers. We minimize the potential F^* and obtain the following set of N_0^d equations which are solved numerically:

$$\sum_{i'j'k'} \boldsymbol{g}(\boldsymbol{S}_{ijk}, \boldsymbol{S}_{i'j'k'}) + w p_{ijk} \boldsymbol{g}(\boldsymbol{S}_{ijk}, \boldsymbol{e}_{ijk}^{(ran)}) + B^2 \boldsymbol{g}(\boldsymbol{S}_{ijk}, \boldsymbol{e}_x) = 0 \tag{9}$$

where the vector function $\boldsymbol{g}$ is defined as

$$\boldsymbol{g}(\boldsymbol{v}_1, \boldsymbol{v}_2) = (\boldsymbol{v}_1 \cdot \boldsymbol{v}_2)\left[\boldsymbol{v}_2 - (\boldsymbol{v}_1 \cdot \boldsymbol{v}_2)\boldsymbol{v}_1\right] \tag{10}$$

The system of Equation 9 is solved by overrelaxation method which has been proved fast and reliable. At cell boundaries we impose the periodic boundary conditions.

Acknowledgements

References

1. *Liquid Crystals in Complex Geometries Formed by Polymer and Porous Network;* Crawford, G. P.; Žumer, S., Eds.; Oxford University Press: London, 1996.
2. Kurik, M. V.; Lavrentovich, O. D. *Usp. Fiz. Nauk* **1988**, *154*, 381.
3. Radzihovsky, L.; Toner, J. *Phys. Rev. Lett.* **1997**, *79*, 4214–4217. doi:10.1103/PhysRevLett.79.4214
4. Feldman, D. E. *Phys. Rev. Lett.* **2000**, *84*, 4886–4889. doi:10.1103/PhysRevLett.84.4886
5. Popa-Nita, V.; Romano, S. *Chem. Phys.* **2001**, *264*, 91–99. doi:10.1016/S0301-0104(00)00340-2
6. Cleaver, D. J.; Kralj, S.; Sluckin, T. J.; Allen, M. P. The random anisotropy nematic spin model. In *Liquid Crystals in Complex Geometries Formed by Polymer and Porous Networks;* Crawford, G. P.; Žumer, S., Eds.; Oxford University Press: London, 1996; pp 467–481.
7. Kleman, M.; Lavrentovich, O. D. *Soft Matter Physics;* Springer-Verlag: Berlin, 2002.
8. Aliev, F. M.; Breganov, M. N. *Sov. Phys. JETP* **1989**, *68*, 70–68.
9. Tripathi, S.; Rosenblatt, C.; Aliev, F. M. *Phys. Rev. Lett.* **1994**, *72*, 2725–2729. doi:10.1103/PhysRevLett.72.2725
10. Bellini, T.; Clark, N. A.; Muzny, C. D.; Wu, L.; Garland, C. W.; Schaefer, D. W.; Oliver, B. J. *Phys. Rev. Lett.* **1992**, *69*, 788–791. doi:10.1103/PhysRevLett.69.788
11. Kralj, S.; Zidanšek, A.; Lahajnar, G.; Muševič, I.; Žumer, S.; Blinc, R.; Pintar, M. M. *Phys. Rev. E* **1996**, *53*, 3629–3638. doi:10.1103/PhysRevE.53.3629
12. Kutnjak, Z.; Kralj, S.; Lahajnar, G.; Žumer, S. *Phys. Rev. E* **2003**, *68*, No. 021705. doi:10.1103/PhysRevE.68.021705

13. Sinha, G.; Leys, J.; Glorieux, C.; Thoen, J. *Phys. Rev. E* **2005,** *72,* No. 051710. doi:10.1103/PhysRevE.72.051710
14. Bellini, T.; Buscaglia, M.; Chiccoli, C.; Mantegazza, F.; Pasini, P.; Zannoni, C. *Phys. Rev. Lett.* **2000,** *85,* 1008–1011. doi:10.1103/PhysRevLett.85.1008 And references therein.
15. Cordoyiannis, G.; Kralj, S.; Nounesis, G.; Žumer, S.; Kutnjak, Z. *Phys. Rev. E* **2006,** *73,* No. 031707. doi:10.1103/PhysRevE.73.031707
16. Iannacchione, G. S.; Garland, C. W.; Mang, J. T.; Rieker, T. P. *Phys. Rev. E* **1998,** *58,* 5966–5981. doi:10.1103/PhysRevE.58.5966
17. Popa-Nita, V. *Eur. Phys. J. B* **1999,** *12,* 83–90. doi:10.1007/s100510050981
18. Popa-Nita, V. *Chem. Phys.* **1999,** *246,* 247–253. doi:10.1016/S0301-0104(99)00184-6
19. Cvetko, M.; Krasna, M.; Ambrožič, M.; Kutnjak, Z.; Kralj, S., in press. In preparation.
20. Dierking, I.; Scalia, G.; Morales, P. *J. Appl. Phys.* **2005,** *97,* No. 044309. doi:10.1063/1.1850606
21. Lagerwall, J.; Scalia, G.; Haluska, M.; Dettlaff-Weglikowska, U.; Roth, S.; Giesselmann, F. *Adv. Mater.* **2007,** *19,* 359–364. doi:10.1002/adma.200600889
22. Lebwohl, P. A.; Lasher, G. *Phys. Rev. A* **1972,** *6,* 426–429. doi:10.1103/PhysRevA.6.426
23. Romano, S. *Int. J. Mod. Phys. B* **2002,** *16,* 2901–2915. doi:10.1142/S0217979202009986 And references therein.
24. Harris, R.; Plischke, M.; Zuckerman, M. J. *Phys. Rev. Lett.* **1973,** *31,* 160–162. doi:10.1103/PhysRevLett.31.160
25. Cvetko, M.; Ambrožič, M.; Kralj, S. *Liq. Cryst.* **2009,** *36,* 33–41. doi:10.1080/02678290802638431
26. Imry, Y.; Ma, S. *Phys. Rev. Lett.* **1975,** *35,* 1399–1401. doi:10.1103/PhysRevLett.35.1399
27. Cruz, C.; Figueirinhas, J. L.; Filip, D.; Feio, G.; Ribeiro, A. C.; Frere, Y.; Meyer, T.; Mehl, G. H. *Phys. Rev. E* **2008,** *78,* No. 051702. doi:10.1103/PhysRevE.78.051702
28. Ambrožič, M.; Bisi, F.; Virga, E. G. *Continuum Mech. Thermodyn.* **2008,** *20,* 193–218. doi:10.1007/s00161-008-0077-x

Self-assembled ordered structures in thin films of HAT5 discotic liquid crystal

Piero Morales[1], Jan Lagerwall[2], Paolo Vacca[3,§], Sabine Laschat[4]
and Giusy Scalia[*3]

Full Research Paper

Open Access

Address:
[1]ENEA, C. R. Casaccia, Via Anguillarese 301, I-00060 S. Maria di Galeria (Roma), Italy, [2]Institute of Chemistry – Physical Chemistry, Martin-Luther-University Halle-Wittenberg, Von-Danckelmannplatz 4, D-06120 Halle, Germany, [3]ENEA, C. R. Portici, P.le E. Fermi, I-80055 Portici (Naples) Italy and [4]Institute of Organic Chemistry, University of Stuttgart, Pfaffenwaldring 55, D-70569 Stuttgart, Germany

Email:
Piero Morales - piero.morales@enea.it; Jan Lagerwall - jan.Lagerwall@lcsoftmatter.com; Paolo Vacca - vacca.paolo@gmail.com; Sabine Laschat - Sabine.Laschat@oc.uni-stuttgart.de; Giusy Scalia[*] - giusy.scalia@solcanta.com

* Corresponding author
§ Affiliation of this author when his contribution to this work was given

Keywords:
AFM; discotic liquid crystals; hexapentyloxytriphenylene; self-organization; thin films

Abstract

Thin films of the discotic liquid crystal hexapentyloxytriphenylene (HAT5), prepared from solution via casting or spin-coating, were investigated by atomic force microscopy and polarizing optical microscopy, revealing large-scale ordered structures substantially different from those typically observed in standard samples of the same material. Thin and very long fibrils of planar-aligned liquid crystal were found, possibly formed as a result of an intermediate lyotropic nematic state arising during the solvent evaporation process. Moreover, in sufficiently thin films the crystallization seems to be suppressed, extending the uniform order of the liquid crystal phase down to room temperature. This should be compared to the bulk situation, where the same material crystallizes into a polymorphic structure at 68 °C.

Introduction

Discotic liquid crystals are an interesting type of organic semiconductors that allow long-range charge transport thanks to the spontaneous formation of channels as a result of molecular self-organization into columns and the orbital overlap of neighboring molecules [1,2]. In particular, columnar phases are very appealing for applications since the transport of charges occurs along the columns, which then behave like molecular wires. Their good performance makes them promising for use as tran-

sistors [3] in electronic circuits, for light emitting diodes [4] and in solar cells [5,6]. Liquid crystals (LCs) possess a long range, even if imperfect, order that is beneficial for creating a macroscopic common molecular orientation which can be potentially controlled, thus making it possible to choose the direction of charge flow. Moreover, the degree of molecular order affects the charge transport efficiency, which improves with increasing order.

Efforts to improve the electronic performance of such systems have focused not only on the synthesis of optimized molecules but also on the aligning methods. In fact while rod-like (calamitic) LCs can be easily aligned along chosen directions by the use of treated surfaces or electric or magnetic fields, these treatments are almost always ineffective for discotic LCs. Without a macroscopic, uniform alignment the excellent properties of discotic LCs cannot be expressed at their best. Moreover, the ability to select the direction of the column alignment is also desirable since the optimum direction depends on the application [7]. Use of discotics as transistors requires LC columns bridging the electrodes, usually parallel to the substrates. This corresponds to the so-called planar alignment with the molecular planes perpendicular to the substrate and the columnar axis parallel to it. On the other hand, for solar cells or OLEDs the columns should be perpendicular to the electrode coated substrate, in what is referred to as homeotropic alignment, with the molecules lying flat on the substrate surface. While some progress has been made in identifying alignment methods, these are not generally effective for all types of discotics, with some materials aligning as expected and others not. Methods to align discotics include the use of treated surfaces [8,9], the Langmuir–Blodgett technique [10], zone-casting processes [11] or the use of magnetic fields [12]. With the above methods planar alignment is mostly achieved and often fibrillar structures are observed. Uniform homeotropic alignment in thin films is rarer and often difficult to achieve. The properties of the discotic thin films are also important for applications since the uniformity of the alignment on macroscopic scale and the stability of the alignment with the temperature are fundamental for the actual implementation of discotics in devices.

In the present work we study thin films of hexapentyloxytriphenylene, known as HAT5 for short (Scheme 1), a historically important discotic molecule which allowed the proof of photoconductivity in discotic LCs [13]. Besides exhibiting high charge mobility this material is, unlike many other discotic LCs, relatively easy to align uniformly in a homeotropic configuration between two glass plates, thus allowing time-of-flight measurements of photoconductivity. While most of the studies are with such geometry, which is obtained by confining the LC

between indium tin oxide (ITO)-coated glass plates at micrometer distance, very little is known about the organization of HAT5 in films of submicrometer thickness and their characteristics. Such films, produced by drop-casting and spin-coating, are the focus of this study.

Scheme 1: Hexapentyloxytriphenylene (HAT5).
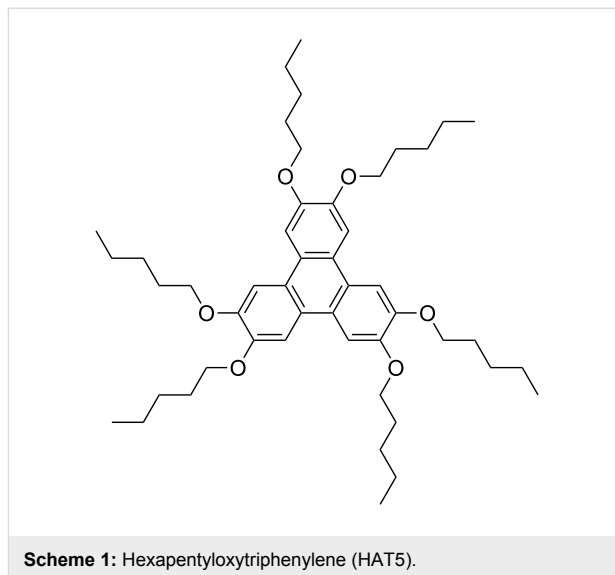
Results and Discussion

Different preparation techniques obviously produce films of different thicknesses and uniformity; drop-casting yields thicker and less uniform samples as compared to those prepared by spin-coating. The former were thick enough to show birefringence, thus making them suitable for optical microscopy investigations. As can be seen in Figure 1a, the sample has a striped texture, which is uncharacteristic of columnar phases studied in standard sample cells (typical thickness of several microns), with long fibers aligned locally along a common direction. The alignment of the director (the average orientation of the main molecular symmetry axis) is planar, as evidenced by the non-zero birefringence, with the column axes parallel to the substrate. The film was heated to study the phase sequence, which revealed that the temperatures of the transitions were somewhat shifted from those of bulk samples (crystal 69 °C Col_h 122 °C isotropic). A first change in texture was observed around 75 °C (Figure 1b), corresponding to melting into the columnar liquid crystalline phase (Col_h). The new texture retained the striped character but broke up into many small domains. At 125 °C (Figure 1c) the disappearance of birefringence revealed the transition to the isotropic phase.

The textures were also monitored on cooling and showed the liquid crystal phase formation at about 110 °C with the texture now typical of a discotic columnar phase with the characteristic bright dendritic features in a black background (Figure 1d). The
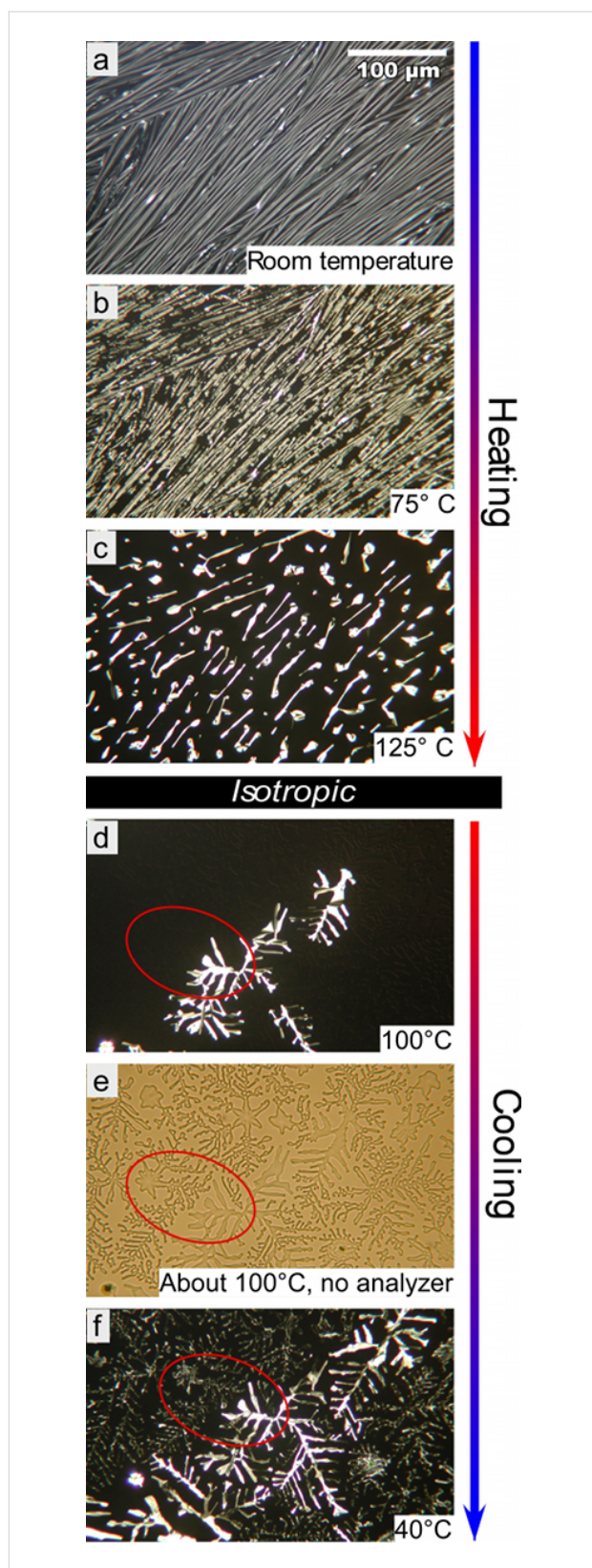
Figure 1: Optical microscopy textures of a film prepared by drop-casting on heating to the isotropic phase and subsequent cooling. All images were taken with crossed polarizers, except (e) which was taken with the analyzer removed.

area in the red oval includes bright and dark regions in the polarizing microscopy image. Observing the same area without the analyzer (Figure 1e) revealed a different, non-birefringent dendritic regime, suggesting a homeotropic LC alignment. At crystallization (Figure 1f), the alignment within each regime was partially lost, resulting in the previously non-birefringent homeotropic areas becoming visible between crossed polarizers.

The striking difference between the initial and final texture after the thermal treatment demonstrates that the starting arrangement must have been strongly influenced by the preparation process, the flow direction of the solution and the assembly during solvent evaporation probably being critical for the development of the fibrillar structure (we will propose a more detailed explanation below). However, this alignment is apparently not stable in this relatively thick film and when the LC is heated into the isotropic phase this organization is lost. On subsequent cooling into the columnar phase this instead forms according to the interaction with the surface, resulting in a standard homeotropic alignment configuration typical of bulk samples.

The samples prepared by spin-coating resulted in a thinner layer of material as suggested by a basically black appearance in the polarizing microscope. In some cases some birefringent lines with planar alignment, with widths in the range 2–3 μm, could be detected (Figure 2). Other samples prepared with settings that ensured thinner films had a uniformly black aspect. The origin of the black background is the extremely small thickness of the LC film, giving negligible effective birefringence, even for a director in planar orientation. The analysis of these regions thus relied mainly on atomic force microscopy (AFM, Figure 3–Figure 9). This technique confirmed that the black background observed by optical microscopy is not simply the uncovered substrate but it shows a fibrillar structure reminiscent of the optical microscopy textures from the thicker films produced by casting.

It is thus reasonable to deduce that the LC is also aligned planarly in these thin films. Indeed, the linear structures that could also be detected optically in the spin-coated films were birefringent with a well-defined optical axis, such that they appeared and disappeared upon rotation of the sample; an example is shown in the red ellipse in the top and bottom pictures of Figure 2. It was possible to localize these structures by AFM as shown in Figure 3. Here an example with overall diameter in the order of 1.5–2 μm (similar to the lines detected optically) is shown, together with small elongated aggregates. The substrate roughness, evaluated as the root mean square of the AFM topographic values of representative areas of the image is 1.6 nm.
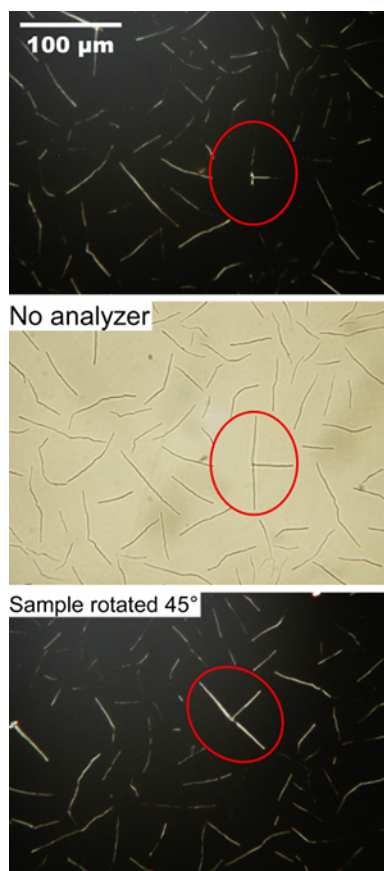
Figure 2: Optical microscopy images of a spin-coated sample with linear structures thick enough to be detected optically. Since their birefringence depends on the relative orientation of the optical axis and the polarizers, we have used a reference area, enclosed in the red oval, for demonstrating the uniform, planar alignment of the director in the linear structures. The upper and lower images were obtained with crossed polarizers while the middle one was taken without the analyzer to show the complete sample morphology.
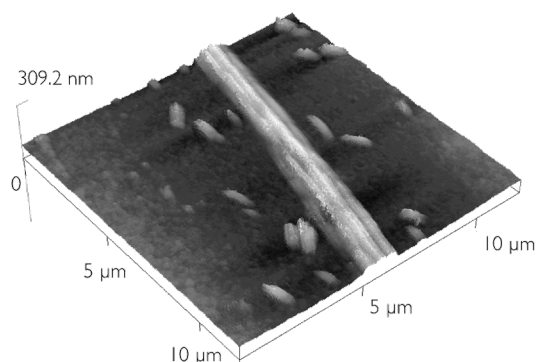

Figure 3: AFM scan of a thick rope, of similar size to the linear structures observed by optical microscopy. AFM shows that they are actually composed of several thinner fibers.

The structure actually appears to be a kind of rope, formed by thinner fibers, each of diameter in the order of 0.5 μm. In other regions it was possible to observe the thinner fibers, of dimensions comparable to the ones constituting the thicker rope, not in aggregates but lying separately on the substrate as can be seen in Figure 4. These thinner fibers can also be very long, at least tens of micrometers.
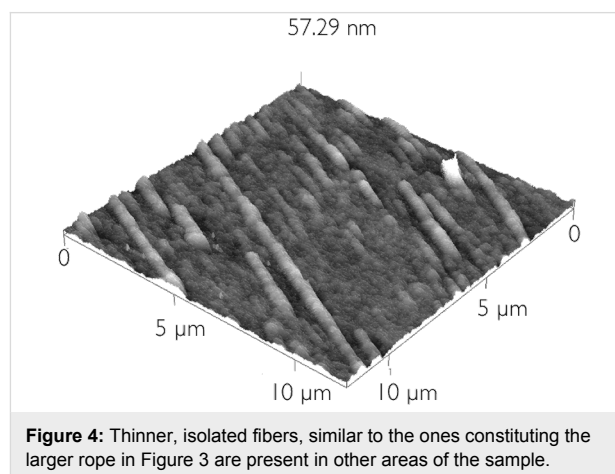

Figure 4: Thinner, isolated fibers, similar to the ones constituting the larger rope in Figure 3 are present in other areas of the sample.

The phase transition behavior in the thin spin-coated films could be studied in the thick linear structures as these were observable by optical microscopy. Interestingly, this revealed a drastic difference from the drop-cast sample. In the ropes of the spin-coated film no phase transition was detected upon heating from room temperature up to 129 °C, when the material became isotropic. Therefore only one transition was visible, presumably the liquid crystalline–isotropic transition, demonstrating a dramatic stabilization of the LC order over a much larger temperature range than in bulk samples. While we cannot rule out that the sample is in a glassy state at low temperatures, the important observation is that the large-scale order is retained. The increase in the temperature range of the ordered state is an effect of the confinement of the molecules into a very thin structure, analogous to the observations made in liquid crystal confined in electrospun polymeric microtubules [14]. Moreover, the spatial confinement gives also stabilization of the alignment. Indeed, after heating the spin-coated sample to the isotropic phase and then cooling it to the LC state, the original alignment was preserved and the texture appeared unchanged from the initial state, in contrast to the observations made on the thicker drop-cast samples. Thus, these two different preparation methods lead to a great difference in the stability of molecular alignment and in the temperature behavior of the material, even starting from the same solution. This behavior is important for applications since it may allow large-scale uniform alignment over a substantially wider temperature range compared to the bulk LC.

Because of the close resemblance between the fibers in the ropes, visible by optical microscopy due to their birefringence, and the non-aggregated and optically invisible fibers observable only by AFM, we can infer that the alignment in the latter is also planar. Moreover, if the stabilization of the planar alignment occurs in the larger structures, the effect ought to be even more enhanced in smaller arrangements. Besides these fibers that can be extremely long, areas with densely packed "elongated droplets" can also be found, as shown in Figure 5. These have a width in the order of hundreds of nanometers while the length is in the micron range. Moreover, they are locally ordered along the same direction, but over the sample area this direction changes smoothly, producing a pattern strongly reminiscent of nematic organization.
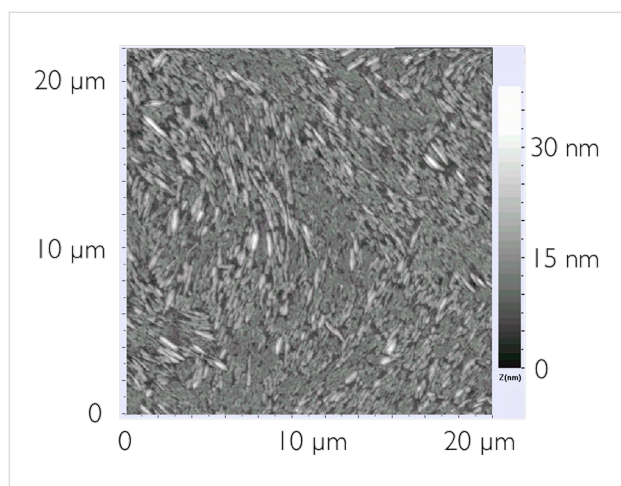

Figure 5: Small, elongated aggregates form a nematic-like texture, possibly due to the formation of a lyonematic phase during solvent evaporation.

One explanation for the formation of planar alignment in thin films (generally thicker than those studied here, however) has been proposed by Grelet and Bock [15] in terms of the difference in surface tension at the different interfaces. In that case the stable LC order in the films appears only upon thermal annealing. While the same process might be occurring in our system, the evidence of nematic order – absent in the phase sequence of HAT5 – is difficult to explain following this scenario, suggesting that another or additional mechanism plays a role. One possible explanation could be that, as the solvent evaporates a concentration is reached at which aggregates of columnar stacks exhibit an organized phase of lyomesomorphic type, like the soft columnar nematic phases of diluted discotics described in other works [16-18]. Discotic molecules aggregate in small columnar stacks in dodecane and at a certain concentration these stacks behave as molecules in a calamitic nematic phase, aligning accordingly. In reference [19] it is reported that aggregation of the discotic molecules already starts when they

are in solution. This assembly can remain or influence the final structure together with processing conditions. When all the solvent has evaporated, the organization into molecular stacks and their super-organization in nematic order may be frozen in, explaining the peculiar texture shown by AFM (Figure 5) as well as the non-standard initial textures of the drop-cast sample observed by optical microscopy. The tendency to form organized structures even on the small scale is striking, and it is clearly important to understand how to control and tune a desired assembly.

We therefore carried out investigations to study the impact of the change in the concentration of HAT5 in toluene at the same settings for the deposition on substrates of equal size via spin-coating. Three concentrations were examined: 6 mg/ml, 3 mg/ml and 1.5 mg/ml. The fibrillar texture appeared in all cases, rendering the assessment of the film thickness more difficult due to the uneven surface. We found that for the highest concentration, 6 mg/ml, the layer thickness ranges between 30 and 50 nm. An example of the surface roughness is shown in the lower part of Figure 6. The surface is characterized by fiber-like structures that are locally aligned although the alignment changes in different domains. Arrows have been drawn as a guide to the eye to identify the local alignment. Unlike the arrangement of Figure 4, no "particle-like" units could be identified but only rather long fibers that smoothly bend together with neighboring fibers. It is not easy to identify the individual fibers and quantify the dimensions because they are closely
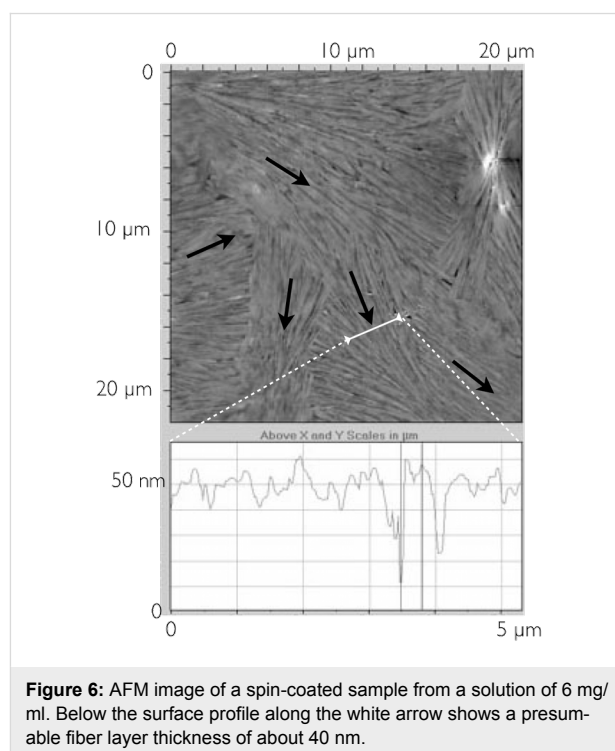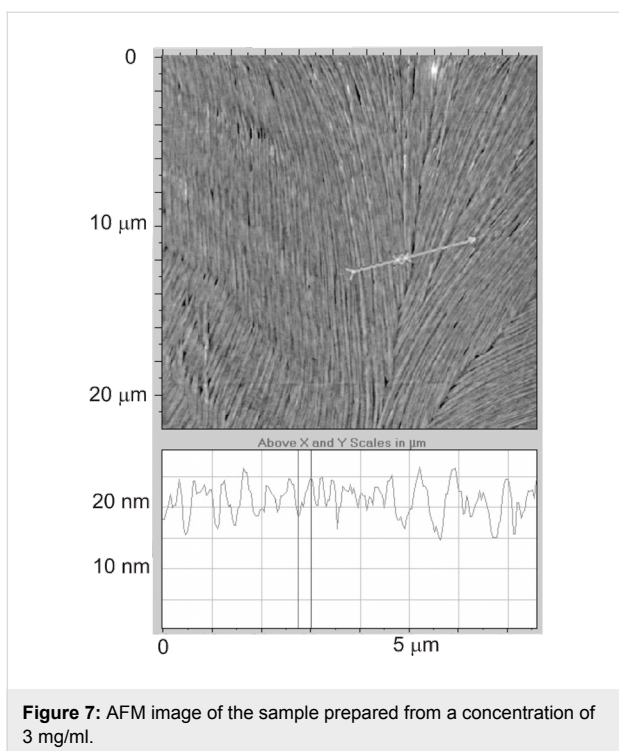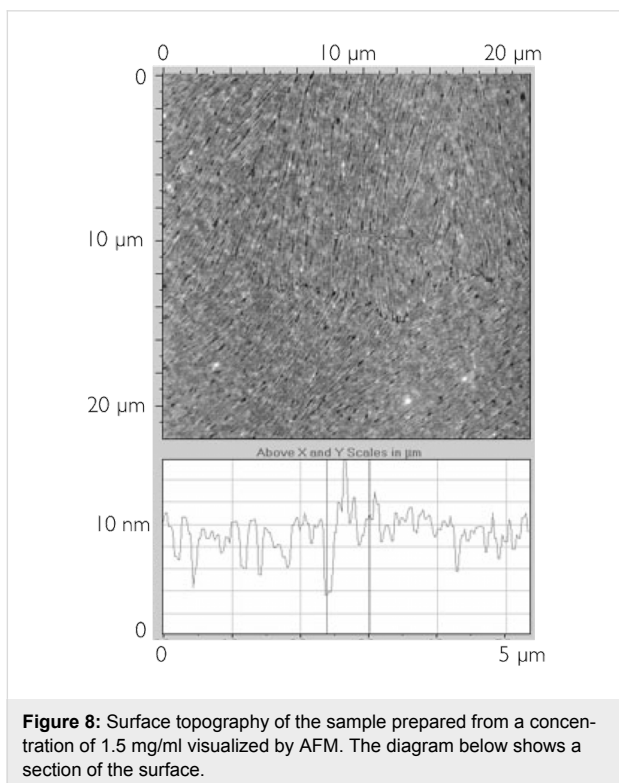

Figure 6: AFM image of a spin-coated sample from a solution of 6 mg/ml. Below the surface profile along the white arrow shows a presumable fiber layer thickness of about 40 nm.

Figure 7: AFM image of the sample prepared from a concentration of 3 mg/ml.

packed together. They appear quite thick even although the section of the surface given by the AFM identifies also some thinner features, suggesting that the thick structures may be thin fibers aggregating into superstructures.

Figure 8: Surface topography of the sample prepared from a concentration of 1.5 mg/ml visualized by AFM. The diagram below shows a section of the surface.

As expected reducing the concentration decreases the film thickness to values in the range of 10–20 nm for the sample produced from the 3 mg/ml solution, cf. Figure 7. Interestingly, the fibrils now seem to align easier with each other, forming larger areas of uniform alignment compared to the more concentrated samples. While it is apparent that the area of uniform alignment is larger than in the thicker sample, the most striking feature is the thinning of the fibers that appear more distinct and almost continuous from the top of the scan to the bottom thus indicating a length of at least 20 μm.

For the even smaller concentration of 1.5 mg/ml, the resulting film thickness ranges between 5 and 10 nm. The AFM investigation of Figure 8 shows a structure of quite thin fibers still largely with a common orientation. Measurement of the lateral fibril dimension here is difficult, but they appear thinner that those in the previous samples, and the surface profile shows more subtle features.

In Figure 9, a higher resolution image of the fiber structure for this lower concentration sample is shown. The width of these fibers appears to be in the order of hundreds of nanometers and their self-assembly renders small parts of the substrate visible. In the region shown, the alignment of the group of fibers changes abruptly by about 20° (the two arrows show the local director orientations). At the change point the fibers break, giving rise to what looks like a long trench from the top centre to the lower left-hand corner.

Figure 9: Higher resolution scans of the fiber structure of the low concentration sample.
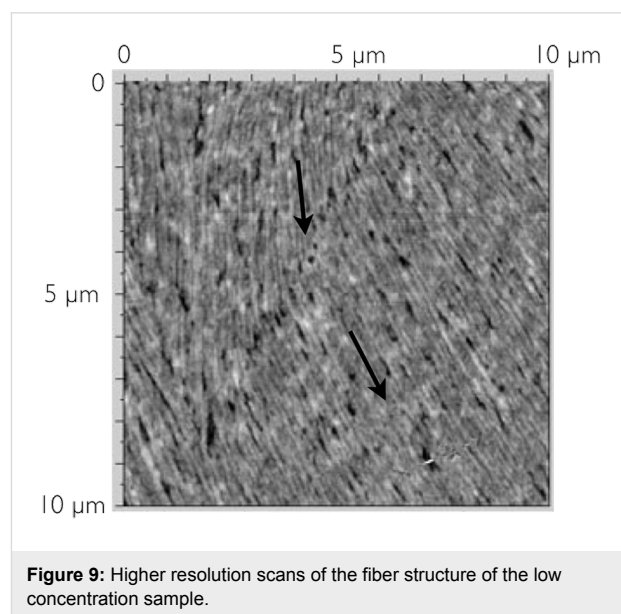
An overview of the results obtained for cast and spin-coated samples, in comparison with bulk samples, is provided in Table 1.

Table 1: Overview of results for the different films compared to bulk samples.

Sample	Bulk	Cast	Spin-coated
Thickness	Typically a few μm	Enough for optical birefringence	5–50 nm
Phase sequence	crystal 69 °C Col$_h$ 122 °C isotropic	crystal 75 °C Col$_h$ 125 °C isotropic	glass (?) 129 °C isotropic
Typical alignment and structure on ITO glass slides	Homeotropic, columnar	Planar and homeotropic, (metastable) fiber-like structure	Planar, stable fibers and ropes

Conclusion

The discotic liquid crystal HAT5 showed the tendency to form fiber-like structures in films prepared from solution using different methods. In the thicker samples prepared by drop-casting this texture is however not stable, heating to the isotropic phase and subsequent cooling resulted in the typical alignment of HAT5 known from sandwich cells. For all thinner samples, prepared by spin-coating, a fiber-like texture was observed, persistent after thermal treatment and stable over a larger temperature range. The most common arrangement observed is one of very long fibers that appear thinner at the lower concentrations of the starting solution, resulting in generally thinner films. Further studies employing techniques such as X-ray scattering are needed for the elucidation of the definite molecular arrangements. However, the preference to form long fiber structures and the columnar hexagonal phase possessed by HAT5 in bulk suggest that this phase may be present in the observed fibers.

We conclude that even a simple technique such as spin-coating allows organization of discotic liquid crystals in micrometer-sized regions of uniform planar alignment. The self-organizing nature of discotics is thus a powerful and promising tool for creating controlled nanometric or micrometric structures.

Experimental

HAT5 was dissolved in toluene at different concentrations and deposited on square glass substrates of 2.5 cm side length, coated with indium tin oxide (ITO). The deposition of the solution was performed by drop-casting or spin-coating, the latter at a speed of 500 rpm for 10 s. A starting concentration of 7.2 mg/ml was initially chosen to ensure a macroscopic coverage of the substrate surface. All the samples were then kept for 2 h at 56 °C in a vacuum oven to ensure complete evaporation of the solvent.

The investigations of the deposited layers were performed by polarizing optical microscopy and by atomic force microscopy. An Olympus BH-2 optical microscope equipped with an Instec temperature controller allowed the characterization of the phase transitions and the assessment of the orientation of the molecules in thicker samples. AFM investigations were carried out with Quesant Nomad atomic force microscope in tapping mode with super-sharp silicon probes of force constant 5 N/m. All AFM scans were performed at room temperature.

References

1. Laschat, S.; Baro, A.; Giesselmann, F.; Haegele, C.; Scalia, G.; Steinke, N.; Judele, R.; Tosoni, M.; Kapatsina, E.; Schreivogel, A.; Sauer, S. *Angew. Chem., Int. Ed.* **2007,** *46,* 4832–4887. doi:10.1002/anie.200604203
2. Sergeyev, S.; Pisula, W.; Geerts, Y. H. *Chem. Soc. Rev.* **2007,** *36,* 1902–1929. doi:10.1039/b417320c
3. Pisula, W.; Menon, A.; Stepputat, M.; Lieberwirth, I.; Kolb, U.; Tracz, A.; Sirringhaus, H.; Pakula, T.; Muellen, K. *Adv. Mater.* **2005,** *17,* 684–689. doi:10.1002/adma.200401171
4. Christ, T.; Glusen, B.; Greiner, A.; Kettner, A.; Sander, R.; Stumpflen, V.; Tsukruk, V.; Wendorff, J. H. *Adv. Mater.* **1997,** *9,* 48–52. doi:10.1002/adma.19970090110
5. Schmidt-Mende, L.; Fechtenkotter, L.; Mullen, K.; Moons, E.; Friend, R. H.; Mackenzie, J. D. *Science* **2001,** *293,* 1119–1122. doi:10.1126/science.293.5532.1119
6. Hassheider, T.; Benning, S. A.; Lauhof, M. W.; Kitzerow, H. S.; Bock, H.; Watson, M. D.; Mullen, K. *Mol. Cryst. Liq. Cryst.* **2004,** *413,* 461–472. doi:10.1080/15421400490439103
7. Simpson, C.; Wu, J.; Watson, M. D.; Mullen, K. *J. Mater. Chem.* **2004,** *14,* 494–504. doi:10.1039/b312789c
8. Zimmermann, S.; Wendorff, J. H.; Weder, C. *Chem. Mater.* **2002,** *14,* 2218–2223. doi:10.1021/cm010932h
9. Van de Craats, A. M.; Stutzmann, N.; Bunk, O.; Nielsen, M. M.; Watson, M.; Muellen, K.; Chanzy, H. D.; Sirringhaus, H.; Friend, R. H. *Adv. Mater.* **2003,** *15,* 495–499. doi:10.1002/adma.200390114
10. Henderson, P.; Beyer, D.; Jonas, U.; Karthaus, O.; Ringsdorf, H.; Heiney, P. A.; Maliszewskyj, N. C.; Ghosh, S. S.; Mindyuk, O. Y.; Josefowics, J. Y. *J. Am. Chem. Soc.* **1997,** *119,* 4740–4748. doi:10.1021/ja964036w
11. Tracz, A.; Jeszka, J. K.; Watson, M. D.; Pisula, W.; Muellen, K.; Pakula, T. *J. Am. Chem. Soc.* **2003,** *125,* 1682–1683. doi:10.1021/ja028945z
12. Lee, J.-H.; Kim, H.-S.; Pate, B. D.; Choi, S.-M. *Physica B* **2006,** *385–386,* 798–800. doi:10.1016/j.physb.2006.06.087

13. Adam, D.; Closs, F.; Frey, T.; Funhoff, D.; Haarer, D.; Ringsdorf, H.; Schuhmacher, P.; Siemensmeyer, K. *Phys. Rev. Lett.* **1993,** *70,* 457–460. doi:10.1103/PhysRevLett.70.457

14. Lagerwall, J.; McCann, J. T.; Formo, E.; Scalia, G.; Xia, Y. *Chem. Commun.* **2008,** *42,* 5420–5422. doi:10.1039/b810450f

15. Grelet, E.; Bock, H. *EPL* **2006,** *73,* 712–718. doi:10.1209/epl/i2005-10459-5

16. Krüerke, D.; Rudquist, P.; Lagerwall, S. T.; Sawade, H.; Heppke, G. *Ferroelectrics* **2000,** *243,* 207–220. doi:10.1080/00150190008008022

17. Usol'tseva, N.; Hauck, G.; Koswig, H. D.; Praefcke, K.; Heinrich, B. *Liq. Cryst.* **1996,** *20,* 731–739. doi:10.1080/02678299608033166

18. Palmans, A. R. A.; Vekemans, J. A. J. M.; Hikmet, R. A.; Fischer, H.; Meijer, E. W. *Adv. Mater.* **1998,** *10,* 873–876. doi:10.1002/(SICI)1521-4095(199808)10:11<873::AID-ADMA873>3.0. CO;2-H

19. Duzhko, V.; Shi, H. F.; Singer, K. D.; Semyonov, A. N.; Twieg, R. J. *Langmuir* **2006,** *22,* 7947–7951. doi:10.1021/la060763l

Beilstein Journal
of Organic Chemistry

Symmetry breaking and structure of a mixture of nematic liquid crystals and anisotropic nanoparticles

Marjan Krasna[*1,2], Matej Cvetko[1,3] and Milan Ambrozic[1]

Full Research Paper

Open Access

Address:
[1]University of Maribor, Faculty of Natural Sciences and Mathematics, Koroška cesta 160, 2000 Maribor, Slovenia, [2]University of Maribor, Faculty of Arts, Koroška cesta 160, 2000 Maribor, Slovenia and [3]Regional Development Agency Mura Ltd. Lendavska 5a, 9000 Murska Sobota, Slovenia

Email:
Marjan Krasna[*] - marjan.krasna@uni-mb.si;
Matej Cvetko - matej.cvetko@rra-mura.si;
Milan Ambrozic - milan.ambrozic@uni-mb.si

* Corresponding author

Abstract

Orientational ordering of a homogeneous mixture of uniaxial liquid crystalline (LC) molecules and magnetic nanoparticles (NPs) is studied using the Lebwohl–Lasher lattice model. We consider cases where NPs tend to be oriented perpendicularly to LC molecules due to elastic forces. We study domain-type configurations of ensembles, which are quenched from the isotropic phase. We show that for large enough concentrations of NPs the long range uniaxial nematic ordering is replaced by short range order exhibiting strong biaxiality. This suggests that the impact of NPs on orientational ordering of LCs for appropriate concentrations of NPs is reminiscent to the influence of quenched random fields which locally enforce a biaxial ordering.

Introduction

The past decade has witnessed an increased interest in the study of two-component mixtures consisting of nanoparticles (NPs) in a host material [1-5]. A characteristic feature of a nanoparticle is that at least one of its dimensions is of the order of nanometers. Such systems are expected to play an important role in the emerging field of nanotechnology and also in composites with extraordinary material properties. These mixtures can, in general, exhibit properties which are not encountered in either of the isolated components, thus opening the door to new applications.

Of particular interest are cases where the host component is a soft material [6]. These materials can then exhibit relatively strong responses, even to local low-energy excitations. Typical representatives of soft materials, with great application potential, are various liquid crystals phases [6]. Their soft character is due to continuous symmetry breaking by which LC phases are reached, giving rise to Goldstone excitation modes. LCs are also optically anisotropic and transparent, whose structure can be readily controlled by the confining surfaces and by applying an external electric or magnetic field. LCs exhibit a rich pallet

of different structures and phases that can display almost all physical phenomena. In addition, the chemistry of LCs is relatively well developed; therefore the synthesis of LC molecules with the desired behavior can be achieved with a certain degree of ease. As a result of these properties, even pure LC systems have found several applications, in particular in the electro-optics industry.

We henceforth limit our attention to rod-like LC molecules and to thermotropic LCs in which liquid crystal phases are induced by lowering the temperature from the ordinary liquid (isotropic) phase. The nematic configuration represents the simplest liquid crystal phase [6]. In the bulk nematic phase LC molecules tend to be oriented homogeneously along a single symmetry breaking direction. At the mesoscopic level the average local orientational ordering is commonly described by the nematic director field $\bar{n}$. The directions $\pm\bar{n}$ of this unit vector field are physically equivalent, reflecting the so called head-to tail invariance of LC phase on the mesoscopic scale.

If ensembles are suddenly quenched from the isotropic to the lower symmetry nematic phase, then unavoidably a domain pattern forms [7]. The reason behind this is continuous symmetry breaking and causality (i.e., the finite speed at which information spreads in a system). Generality of this mechanism gives rise to a broad universality of the phenomenon. The basic features of domain pattern dynamics in a pure bulk are described by the Kibble–Zurek mechanism [8,9] which was originally introduced to explain the formation of topological defects in the early universe following the big bang [8]. For the latter purposes, we summarize main features of this universal mechanism for the case of the isotropic–nematic (I–N) phase transition. In the I–N quench the continuous orientational symmetry is broken. A randomly chosen configuration of the symmetry breaking field $\bar{n}$ is established in causally disconnected parts [7]. This choice is based on local fluctuation mediated preferences. Consequently, a domain structure appears, which is well characterized by a single domain length ξ_d. At the domain walls topological defects form. Such a structure is energetically costly due to the high concentration of domain walls and defects. The costs on average domain growth with time can be reduced by mutual annihilation of defects [10,11]. In the pure bulk system a spatially homogeneous structure is gradually attained. However, if impurities are present, they can pin the defects [12-14]. Consequently, the domain structure can be stabilized.

In this contribution we study numerically a mixture of uniaxial nematic liquid crystals and rod-like NPs using a Lebwohl–Lasher [15,16] lattice model. We consider cases where NPs and LC molecules tend to be oriented perpendicular

to each other and show that in such systems NPs induce strong biaxiality [17] in LC ordering. Furthermore, we demonstate that NPs can stabilize the domain pattern giving rise to short range ordering in the nematic LC phase [18,19].

Results and Discussion
Model
The three-dimensional (3D) spin model simultaneously describes the orientational field of a LC *molecule* and the dimensionless magnetization of the magnetic component. We henceforth refer to these elements as *nematic spins* and *magnetic spins*, respectively. Here a *molecule* might represent a small group of real LC molecules. The system is represented by a rectangular simulation cell consisting a lattice of $N = N_x \times N_y \times N_z$ sites. Each site is enumerated by a set of indices (i, j, k), where $1 \le i \le N_x$, $1 \le j \le N_y$ and $1 \le k \le N_z$, and is occupied either by nematic or magnetic spin $\bar{S}(i,j,k) \equiv \bar{S}_{ijk}$, which may point in any direction. At the mesoscopic level, nematic spins represent the conventional nematic director field. Neighboring alike spins tend to align in parallel directions, whilst nematic and magnetic spins tend to be perpendicular to each other. The probability for a specific site to contain the magnetic component (instead of LC) is x, yielding on average xN magnetic spins in the cell. The parameter x is set in advance, and then the computer random generator is used to insert randomly magnetic spins into the cell according to the probability x. During the simulation (relaxation of spins approaching equilibrium) this positional configuration of magnetic and nematic spins remains unchanged.

The total energy of the system is given by:

$$F = \sum_{ijk} f_{ijk} \qquad (1)$$

where the energy term f_{ijk} equals:

$$f_{ijk} = -\frac{1}{2}\sum_{n.n.} J_{ijk}(\bar{S}_{ijk} \cdot \bar{S}_{n.n.})^\mathrm{a}$$

The six terms include the spin interactions between the nearest neighbors (denotation *n.n.*): the spin $\bar{S}(i, j, k)$ interacts with $\bar{S}(i+1, j, k)$, $\bar{S}(i-1, j, k)$, $\bar{S}(i, j+1, k)$, $\bar{S}(i, j-1, k)$, $\bar{S}(i, j, k+1)$ and $\bar{S}(i, j, k-1)$, respectively. The factor 1/2 is included because each neighboring spin pair is counted twice in the double sum. The interaction J_{ijk} is equal to a constant, $J_{\mathrm{LC-LC}}$ or $J_{\mathrm{LC-NP}}$ or $J_{\mathrm{NP-NP}}$, reflecting the cases where an interacting pair is a LC–LC spin, LC–magnetic spin or magnetic–magnetic spin, respectively. We scale the system into a dimensionless form by setting $J_{\mathrm{LC-LC}} = 1$. The parameter ($J_{\mathrm{NP-NP}}$) is taken as positive since neighbouring magnetic spins tend to align parallel. By

contrast, we set $J_{LC-NP} < 0$, tending to orient LC molecules and NP perpendicularly. In the simulations we take $J_{LC-LC} = J_{NP-NP} = 1$, and J_{LC-NP} is either set to -1, -2 or -4. The exponent a is equal to 1 for magnetic–magnetic coupling while for nematic–nematic or nematic–magnetic coupling it has the value 2. The different values for exponent a for the different kinds of spins reflects their different symmetry properties. Unlike magnetic spins, nematic spins are insensitive to an inversion operation: $\bar{S} \equiv -\bar{S}$.

The equilibrium spin configuration is obtained by minimizing the total interaction energy with respect to all the spins. Therefore, we neglect thermal fluctuations. Consequently, our approach is sensible, deep in the nematic LC phase region, i.e. well below the isotropic–nematic phase transition. In order to satisfy the normalization of the spin vectors, $\bar{S}_{ijk}^2 = 1$, the "operational" total interaction energy must be rewritten as:

$$F^* = \sum_{ijk} f_{ijk}^* \tag{2}$$

where:

$$f_{ijk}^* = \lambda_{ijk}(S_{ijk}^2 - 1) + f_{ijk}$$

with Lagrange multipliers λ_{ijk}, which must also be evaluated in order to solve the system.

From the obtained spin configurations, we calculate various quantities which reflect the structural properties of the system. One of these is the equilibrium total energy which is conveniently normalized to one spin site:

$$<f> = \frac{F}{N} \tag{3}$$

and represents the average energy term per spin.

The orientational ordering of the LC part of the system can be characterized by the traceless symmetric order parameter tensor with 3×3 components:

$$Q_{mn} = \frac{3}{2}<S_{ijk,m}S_{ijk,n}> -\frac{1}{2}I \tag{4}$$

where $S_{ijk,m}$ is the m-th component of the LC spin $\bar{S}_{ijk}$. The brackets $<...>$ denote the average of the quantity through the simulation cell and I is the identity matrix.

The degree of biaxiality of the LC component is measured with the *biaxiality parameter* [20,21]

$$\beta^2 = 1 - \frac{6\left(TrQ^2\right)^3}{\left(TrQ^3\right)^2} \tag{5}$$

where $0 \leq \beta^2 \leq 1$. The uniaxial states are characterized by $\beta^2 = 0$, and the states exhibiting maximal biaxiality by $\beta^2 = 1$.

Average structural characteristics of the system can be inferred from the orientational correlation function:

$$G(r) = \frac{3}{2}<(\bar{S}_{ijk} \cdot \bar{S}_{mnl})^2> -\frac{1}{2} \tag{6}$$

Here $<...>$ denotes averaging over spin pairs separated by a distance r. Due to the isotropic character of our ensembles, the relationship $G(\bar{r}) = G(r)$ holds.

The correlation function is calculated numerically in the following manner. First, the "vector index difference" (Δi, Δj, Δk) is chosen, for instance (2, 1, -3), giving the vector relative position of correlated spin pairs in units of the nearest neighbor distance a_0. Next, the pairs r and G, corresponding to (Δi, Δj, Δk), are calculated:

$$r = \sqrt{(\Delta i)^2 + (\Delta j)^2 + (\Delta k)^2}$$

$$G = \frac{1}{N}\sum_{i,j,k}(\frac{3}{2}(\bar{S}_{ijk} \cdot \bar{S}_{i+\Delta i, j+\Delta j, k+\Delta k})^2 - \frac{1}{2})$$

Averaging of individual pair correlations over the spin lattice is used. To avoid technical difficulties, periodic boundary conditions are performed when one of the indices exceeds the limit. For example, if $i = N_x$ and $\Delta i = 3$, we take $i + \Delta i = 3$ instead of $N_x + 3$. This is in accordance with the periodic boundary condition used in the evaluation of the spins themselves (for instance, in Equation 2 the "right" nearest neighbor of the spin on the right border of simulation cell with index $i = N_x$ has the corresponding index $i = 1$).

The "vector index difference" (Δi, Δj, Δk) is systematically varied to obtain the $G(r)$ dependence, and the data pairs (r, G) are sorted by increasing distance r. However, the same r may correspond to different combinations of index differences (Δi, Δj, Δk), for instance in all sign combinations of ($\pm\Delta i$, $\pm\Delta j$, $\pm\Delta k$). By inspecting of the results of numerical simulations, we find that G is indeed equal in cases with the same r, except for small

unimportant statistical variations which are subsequently annulled by averaging G for data pairs (r, G) with the same r.

To extract structural details from a calculated $G(r)$ dependence, we fit it with the ansatz [22]

$$G(r) = (1-s)e^{-(r/\xi)^m} + s \qquad (7)$$

where ξ, m and s are adjustable parameters. Distances are scaled with respect to the nearest neighbour distance a_0. The *nematic domain length* ξ estimates the average length over which LC molecules are relatively well correlated. The distribution width of ξ values is measured by the *domain dispersion parameter m*. Dominance of a single coherence length in the system is signalled by $m \approx 1$. A magnitude and system size dependence of the *range parameter s* reveals the degree of ordering within the system. The case $s = 0$ indicates short range ordering (SRO), whilst a finite value of s is consistent with either long range ordering (LRO) or quasi long range ordering (QLRO). To distinguish between these two cases a finite size analysis $s(N)$ must be carried out. If $s(N)$ saturates at a finite value, the system exhibits LRO. If $s(N)$ dependence exhibits algebraic dependence on N then the system possesses QLRO. In our study the correlation function was calculated only for the LC component of the system.

Results

We consider homogeneous mixtures of nematic LCs (*nematic spins*) and elongated NPs (*magnetic spins*). For sufficiently large concentrations x of NPs, such a system could undergo phase separation. In order to estimate roughly concentrations of NPs which are well soluble in a LC solvent, we focus on the chemical potential μ of NPs in the mixture. It can be expressed as [23]

$$\mu(x) = \mu(1) + k_B T \ln(x) + F_b \qquad (8)$$

where $x = N_{NP}/(N_{LC} + N_{NP})$, N_{NP} (i.e., N_{LC}) represents the number of NPs (i.e., LC molecules) in the system, $\mu(1)$ is the chemical potential in the solid phase, k_B is the Boltzmann constant, T is the temperature and F_b is the average binding energy of a NP with its surroundings. We further assume that the chemical potential in a diluted and solid NP state are comparable (depending on the chemical composition of both phases) and consequently, the system does not possess a tendency for phase separation. With this in mind we obtain $k_B T \ln(x) + F_b \approx 0$. From this expression we get an estimate for the upper concentration x_{max} of NPs for which a homogeneous distribution is preserved:

$$x_{max} \approx e^{-F_b/(k_B T)} \qquad (9)$$

Therefore, high solubility is preferred by low binding energies and high temperatures. In order to discern the influence of geometrical details of NPs we consider dilute mixtures, where

$$\varphi = \frac{N_{NP}v_{NP}}{N_{NP}v_{NP} + N_{LC}v_{LC}} \approx x \frac{v_{NP}}{v_{LC}}$$

holds, where φ is the volume fraction of NPs and v_{NP} (i.e., v_{LC}) is the volume of an average nanoparticle (i.e., LC molecule). Therefore, the upper volume fraction φ_{max} of NPs in a homogeneous mixture can be expressed as

$$\varphi_{max} \approx \frac{v_{NP}}{v_{LC}} e^{-F_b/(k_B T)} \qquad (10)$$

We next consider a mixture of a nematic LC phase and ferromagnetic NPs. Such mixtures are of interest for the development of LC materials with pronounced magnetic properties. It was shown [24] that in such materials orientational ordering is predominantly influenced by elastic interactions, which are several orders of magnitude greater than magnetic interactions. To demonstrate that we estimate at the mesoscopic level the typical energy changes related to the reorientation of the nematic director $\vec{n}$ from the direction along the local effective magnetic field $\vec{B}$ towards the perpendicular direction. Here we assume that $\vec{B} = \mu_0 \vec{M}$ originates from magnetic NPs, where μ_0 is the magnetic permittivity constant and $\vec{M} \approx \vec{p}_m / v_{NP}$ represents the magnetization of NPs due to the magnetic dipole moment $\vec{p}_m$. The resulting quadrupolar magnetic field free energy density change Δf_B is approximately given by

$$\Delta f_B \approx \frac{|\Delta\chi|B^2}{2\mu_0} \approx \frac{\mu_0|\Delta\chi|p_m^2}{2\mu_0 v_{NP}^2}$$

where $\Delta\chi$ is the magnetic anisotropy of LC molecules [6] (which can be either positive or negative). Furthermore, introducing an elongated NP of length d into a LC, which via surface anchoring enforces elastic distortion in LC medium, typically gives rise to free energy penalties of the order $\Delta F_e \approx Kd$, where K is the characteristic Frank nematic elastic constant. Typical nematic material constants are approximately given by $K \approx 10^{-12}$ J/m, $|\Delta\chi| \approx 10^{-10}$, and for rod like NPs of radius $r = 1$ nm we set $d/r = 10$ and $p_m \approx emu$. From this choice of parameters we obtain $\Delta F_e >> eV$, $v_{NP}\Delta f_B << eV$ and consequently, $v_{NP}\Delta f_B/\Delta F_e << 1$. Therefore, elastic forces predominantly influence orientational ordering of LC molecules that are surrounded by magnetic NPs.

Consequently, we henceforth limit the discussion to elastic interactions between LCs and NPs. In order to obtain qualitatively new features, we consider the case where NP and LC molecules tend to orient themselves perpendicular to each other. Such conditions are often encountered in other studies of mixtures of nematic LCs and magnetic inclusions reported in the literature [25-27]. On the other hand, we set it that isolated components possess the tendency for parallel orientation. We study structural and phase properties as a function of concentration of NPs in the diluted regime (i.e., $x \ll 1$) and of the interaction strength $|J_{LC-NP}|$ between NP and LC molecules. We monitor quasi stable nematic configurations after quenching the system from the isotropic phase.

In Figure 1 we plot the correlation function $G(r)$ measuring the degree of orientational order of LC molecules for different concentrations x. One sees that for sufficiently low concentrations the nematic long range order is preserved, which is manifested in a finite value of s. However, with increasing x the value of s decreases monotonously. Our numerical simulations suggest, that above a threshold value $x = x_c$ long range ordering is replaced by short range ordering. Therefore, for a sufficiently large concentration the degree of disorder introduced by randomly distributed elongated nanoparticles is large enough to destroy the LRO favoured by the pure LC component.
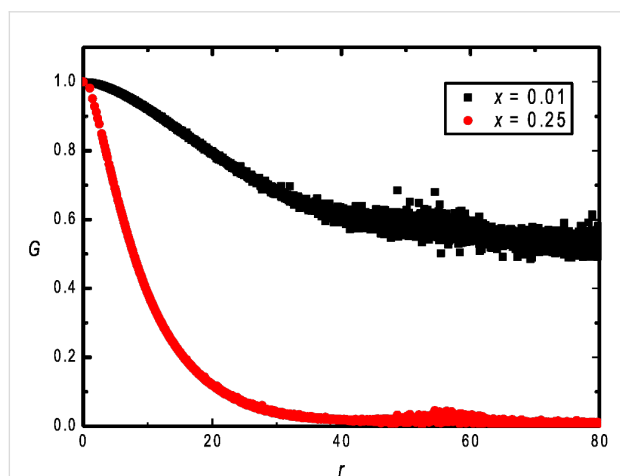

Figure 1: Nematic orientational correlation function $G(r)$ for different values of x ($x = 0.01$ and 0.25), $N = 80 \times 80 \times 80$, $J_{LC-NP} = -1$, $J_{LC-LC} = J_{NP-NP} = 1$.

More details of this phenomenon are presented in Figure 2 where the average behaviour of systems, extracted by fitting Equation 7, is shown on increasing x for different interaction strengths $|J_{LC-NP}|$. We plotted the *nematic domain length* ξ (Figure 2a), the *domain dispersion parameter m* (Figure 2b), and the *range parameter s* (Figure 2c). As intuitively expected, ξ decreases monotonously with x, see Figure 2a. Our simula-

tions suggest $\xi \propto x^{-n}$, where $n = 0.33 \pm 0.03$. The values of m are strongly scattered around the average value $\bar{m} \approx 1.4 \pm 0.2$, where a systematic trend on varying x is not observed as it is evident from Figure 2b. On the other hand, Figure 2c yields strong evidence that the LRO (or QLRO) is destroyed above a critical value x_c. For $s|J_{LC-NP}| = 1$ we obtain $x_c \approx 0.1$. To test
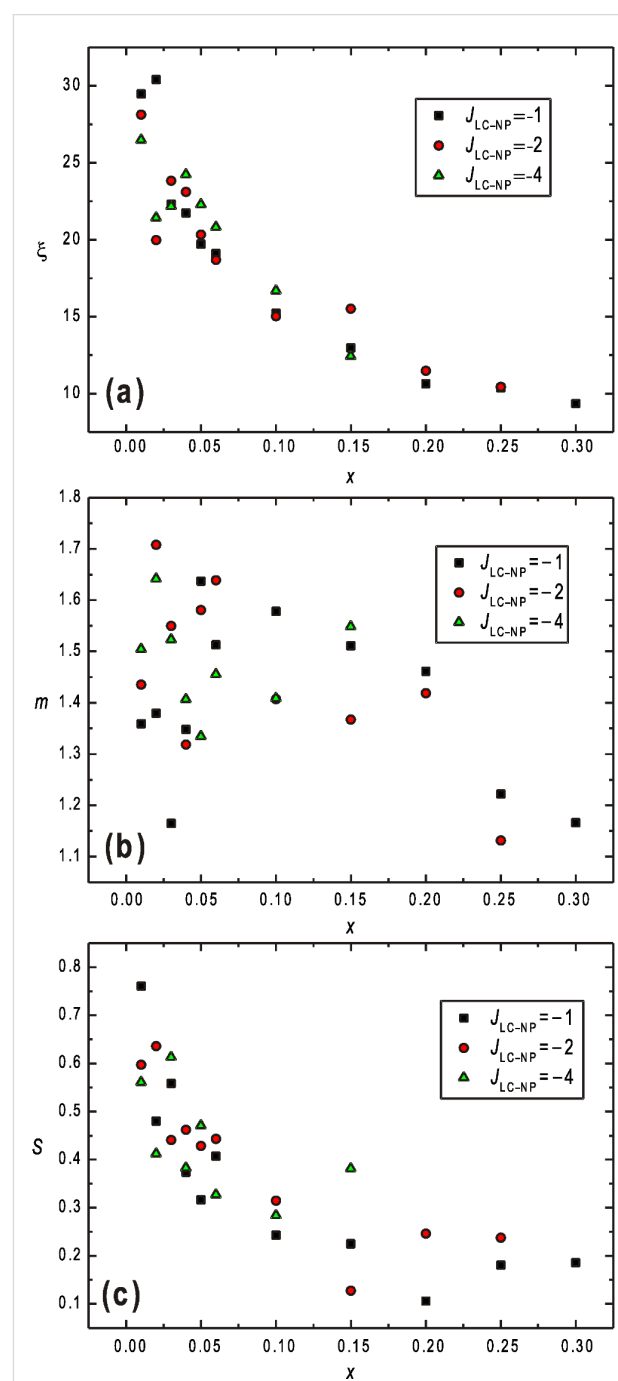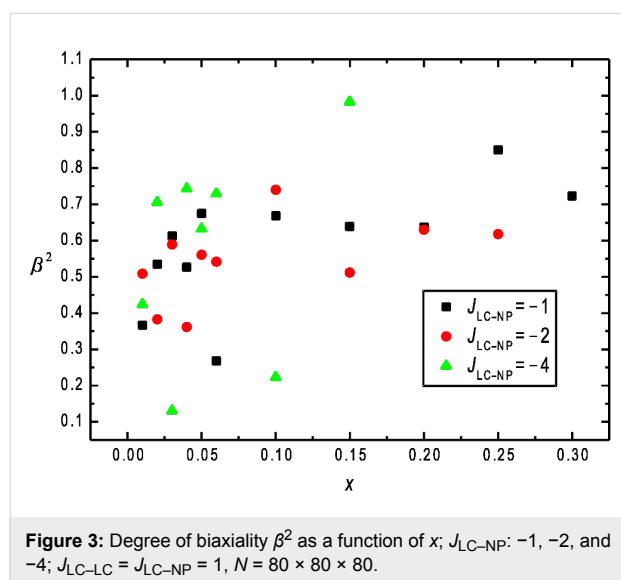

Figure 2: (a) The *nematic domain length* ξ, (b) the *domain dispersion parameter m*, and (c) the *range parameter s* as a function of x for different values of J_{LC-NP}: −1, −2, and −4; $J_{LC-LC} = J_{LC-NP} = 1$, $N = 80 \times 80 \times 80$.

the existence of LRO we performed finite size analysis for $x = x_c/2 \approx 0.05$. Our numerical results do not show any systematic decrease of s on increasing $L \propto N^{1/3}$. This suggests that the systems exhibit LRO if $x \lll x_c$.

We next focus on degree of biaxiality within the ensembles studied. For this purpose we calculate the biaxiality parameter β^2 as a function of x (Figure 3). It can be seen that the degree of biaxiality is surprisingly strong, even for relatively low values of x. The average degree of biaxiality β^2 is larger than 0.5 above $x = 0.05$, which is surprisingly large. The reason behind this is the local tendency of NPs to reorient LC molecules perpendicular to them. This tendency is similar to that of an external electric or magnetic field acting on LCs with negative field anisotropy which tends to orient LC molecules perpendicularly to the field direction [6,28]. In such LC materials an external field imposes a finite degree of biaxiality.

Figure 3: Degree of biaxiality β^2 as a function of x; $J_{\text{LC–NP}}$: −1, −2, and −4; $J_{\text{LC–LC}} = J_{\text{LC–NP}} = 1$, $N = 80 \times 80 \times 80$.

Conclusion

We studied numerically structural characteristics of a diluted mixture of nematic liquid crystals and ferromagnetic nanoparticles. The concentration x of NPs is low enough in order to avoid a phase separation process [29]. We consider cases where both LC molecules and NPs are elongated and tend to be oriented perpendicularly to each other [25-27]. For simulation we use a Lebwohl–Lasher lattice type model [15]. LC molecules and NPs tend to orient perpendicularly to each other. In actual samples such conditions could be realized for so called homeotropic [6] surface anchoring at the NP–LC interface of elongated NPs providing that $Wd/K > 1$. Here W is the anchoring strength, K is the characteristic nematic elastic constant and d is the length of a nanoparticle. We typically consider ensembles of $N = 80 \times 80 \times 80$ elements (i.e., LC

molecules and NPs). In simulations we quench the systems from an isotropic phase, where orientations of all particles are randomly distributed.

Our simulations reveal that NPs act effectively as nematic domain pinning centres [30]. After quenching, nematic domains form due to continuous symmetry breaking. In a bulk system the domains would gradually grow in order to get rid of energetically expensive domain walls [7]. However, the presence of NPs stabilizes the domain pattern. We find that the average domain walls scales as $\xi \propto x^{-n}$, where $n = 0.33 \pm 0.03$. Furthermore, for sufficiently large concentrations ($x_c \approx 0.1$) the LRO (or QLRO) appears to be replaced by SRO. Our results also show that NPs strongly support biaxial states [17,31]. Even at relatively low concentrations the degree of biaxiality is surprisingly high. We obtain $\beta^2 > 0.5$ above $x \approx 0.05$.

One of calculated LC (blue) and NP (red) spin patterns in three perpendicular planes (x−y, y−z, and x−z) cutting the centre of simulation cube cell is presented in the graphical abstract. The lengths of lines representing individual spins in the pattern vary because one of spin components is perpendicular to the plane of view.

Acknowledgements

References

1. Lynch, M. D.; Patrick, D. L. *Nano Lett.* **2002,** *2,* 1197–1201. doi:10.1021/nl025694j
2. Dierking, I.; Scalia, G.; Morales, P. *J. Appl. Phys.* **2005,** *97,* 044309. doi:10.1063/1.1850606
3. Lagerwall, J.; Scalia, G.; Haluska, M.; Dettlaff-Weglikowska, U.; Roth, S.; Giesselmann, F. *Adv. Mater.* **2007,** *19,* 359–364. doi:10.1002/adma.200600889
4. Schoot, P.; Popa-Nita, V.; Kralj, S. *J. Phys. Chem. B* **2008,** *112,* 4512–4518. doi:10.1021/jp712173n
5. Kralj, S.; Bradac, Z.; Popa-Nita, V. *J. Phys.: Condens. Matter* **2008,** *20,* 244112. doi:10.1088/0953-8984/20/24/244112
6. De Gennes, P. G.; Prost, J. *The Physics of Liquid Crystals;* Oxford University Press: Oxford, 1993.
7. Bradač, Z.; Kralj, S.; Žumer, S. *Phys. Rev. E* **2002,** *65,* 021705. doi:10.1103/PhysRevE.65.021705
8. Kibble, T. W. B. *J. Phys. A: Math. Gen.* **1976,** *9,* 1387–1398. doi:10.1088/0305-4470/9/8/029
9. Zurek, W. H. *Nature* **1985,** *317,* 505–508. doi:10.1038/317505a0
10. Bradač, Z.; Kralj, S.; Svetec, M.; Žumer, S. *Phys. Rev. E* **2003,** *67,* 050702(R). doi:10.1103/PhysRevE.67.050702
11. Svetec, M.; Kralj, S.; Bradač, Z.; Žumer, S. *Eur. Phys. J. E* **2006,** *20,* 71–79. doi:10.1140/epje/i2005-10120-9
12. Pires, D.; Fleury, J. B.; Galerne, Y. *Phys. Rev. Lett.* **2007,** *98,* 247801. doi:10.1103/PhysRevLett.98.247801

13. Kralj, S.; Rosso, R.; Virga, E. G. *Phys. Rev. E* **2008,** *78,* 031701.
    doi:10.1103/PhysRevE.78.031701
14. Kralj, S.; Rosso, R.; Virga, E. G. *Phys. Rev. E* **2010,** *81,* 021702.
    doi:10.1103/PhysRevE.81.021702
15. Lebwohl, P. A.; Lasher, G. *Phys. Rev. A* **1972,** *6,* 426–429.
    doi:10.1103/PhysRevA.6.426
16. Romano, S. *Int. J. Mod. Phys. B* **2002,** *16,* 2901–2915.
    doi:10.1142/S0217979202009986
    And references therein.
17. Cruz, C.; Figueirinhas, J. L.; Filip, D.; Feio, G.; Ribeiro, A. C.; Frère, Y.;
    Meyer, T.; Mehl, G. H. *Phys. Rev. E* **2008,** *78,* 051702.
    doi:10.1103/PhysRevE.78.051702
18. Popa-Nita, V. *Eur. Phys. J. B* **1999,** *12,* 83–90.
    doi:10.1007/s100510050981
19. Popa-Nita, V.; Gerlič, I.; Kralj, S. *Int. J. Mol. Sci.* **2009,** *10,* 3971–4008.
    doi:10.3390/ijms10093971
20. Kaiser, P.; Wiese, W.; Hess, S. *J. Non-Equilib. Thermodyn.* **1992,** *17,*
    153–169. doi:10.1515/jnet.1992.17.2.153
21. Kralj, S.; Virga, E. G. *J. Phys. A: Math. Gen.* **2001,** *34,* 829–838.
    doi:10.1088/0305-4470/34/4/309
22. Cvetko, M.; Ambrožič, M.; Kralj, S. *Liq. Cryst.* **2009,** *36,* 33–41.
    doi:10.1080/02678290802638431
23. Popa-Nita, V.; Kralj, S. *J. Chem. Phys.* **2010,** *132,* 024902.
    doi:10.1063/1.3291078
24. Brochard, F.; Gennes, P. G. D. *J. Phys. (Paris)* **1970,** *31,* 691.
25. Burylov, S. V.; Raikher, Yu. L. *Phys. Rev. E* **1994,** *50,* 358–367.
    doi:10.1103/PhysRevE.50.358
26. Zadorozhnii, V. I.; Reshetnyak, V. Yu.; Kleshchonok, A. V.;
    Sluckin, T. J.; Thomas, K. S. *Mol. Cryst. Liq. Cryst.* **2007,** *475,*
    221–231. doi:10.1080/15421400701732019
27. Zadorozhnii, V. I.; Vasilev, A. N.; Reshetnyak, V. Yu.; Thomas, K. S.;
    Sluckin, T. J. *EPL* **2006,** *73,* 408–414. doi:10.1209/epl/i2005-10406-6
28. Kralj, S.; Virga, E. G.
    Phys. Rev. E: Stat. phys. plasmas fluids relat. Interdiscip topics **2002,**
    66, 021703-1–021703-9.
29. Popa-Nita, V.; Kralj, S. *Phys. Rev. E* **2006,** *73,* 041705.
    doi:10.1103/PhysRevE.73.041705
30. Cleaver, D. J.; Kralj, S.; Sluckin, T. J.; Allen, M. P. In *Liquid Crystals in
    Complex Geometries Formed by Polymer and Porous Networks;*
    Crawford, G. P.; Žumer, S., Eds.; Oxford University Press: London,
    1996; pp 467–481.
31. Ambrožič, M.; Bisi, F.; Virga, E. G. *Continuum Mech. Thermodyn.*
    2008, *20,* 193–218. doi:10.1007/s00161-008-0077-x